

Exame de qualificação de doutorado: Poeira, metalicidade e formação estelar: estimando fração de gás.

Eduardo Alberto Duarte Lacerda

Orientador:

Prof. Dr. Roberto Cid Fernandes Jr.

Coorientadora:

Rosa M. Gonzalez Delgado

• • •

Universidade Federal de Santa Catarina
Centro de Ciências Físicas e Matemáticas
Programa de Pós-Graduação em Física

Florianópolis (SC) – 7 de março de 2016

Resumo

Neste trabalho estamos estudando a conversão do coeficiente de extinção por poeira em densidade superficial de massa de gás em discos de galáxias espirais. Para tal finalidade estamos utilizando uma amostra de 184 galáxias do projeto CALIFA, um *survey* astronômico de espectroscopia de campo integrado (*Integral Field Spectroscopy - IFS*). Utilizando as medidas de linhas de emissão provenientes dos espectros residuais da síntese de populações estelares, calculamos o coeficiente de extinção através do decremento de Balmer (τ_V^{neb}) de maneira a compará-lo com aquele proveniente da síntese (τ_V^*). Construímos um objeto em `PYTHON` que organiza essas medidas, facilitando a utilização desses resultados juntamente com os resultados da síntese.

Selecionamos apenas zonas pertencentes aos discos de galáxias e que possuam formação estelar, juntamente com um controle de qualidade. Neste processo, o corte mais brusco em nossa amostra é devido a baixa relação sinal-ruído da linha de [O III] ($(S/N)_{[\text{O III}]} < 3$) em 91142 zonas. Nossa amostra final engloba 16479 zonas reamostradas em ~ 4500 anéis radiais (elípticos) em uma unidade natural da galáxia (raio no qual abarca metade da luz - HLR).

Em paralelo estamos trabalhando em duas frontes. Na primeira estamos buscando o sentido real de τ_V^* utilizando um modelo proposto juntamente com τ_V^{neb} de maneira que possamos encontrar os coeficientes diretamente ligados ao meio interestelar e às nuvens formadoras de estrelas (regiões HII). A segunda, de certa forma, depende da primeira, pois estamos fazendo a conversão de poeira em gás, portanto τ_V influencia diretamente nosso resultado. Nessa etapa investigamos relação entre formação estelar e poeira, de maneira a reproduzir uma relação como a de Kennicutt-Schmidt (KS), encontrando uma correlação entre ambos. Através dos resíduos desta relação (que neste trabalho chamamos de *pseudo* KS) vimos que algumas propriedades estão correlacionadas com o espalhamento desta relação, na qual, a mais forte parece ser com a densidade superficial de massa estelar (μ_*). Também utilizamos tanto τ_V^* quanto τ_V^{neb} para calcular Σ_{gas} , elemento que nos falta para calcular frações de gás, ingrediente muito importante na evolução química de galáxias.

Sumário

1	Introdução	1
1.1	O GAS-UFSC e o IAA-CSIC	1
1.2	Gás, estrelas e poeira nas galáxias	2
1.3	De poeira para gás	3
1.4	Este trabalho	4
2	Linhas de emissão	7
2.1	EmLinesDataCube	7
2.1.1	Extinção estimada através do decremento de Balmer	8
2.1.2	Metalicidade Nebular	10
2.1.3	Exemplo de utilização	11
2.2	Taxa de formação estelar	13
3	Amostra de galáxias	17
3.1	Artigo - CALIFA, the Calar Alto Legacy Field Area survey III. Second public data release.	17
3.2	Definição da amostra deste trabalho	18
3.2.1	Mascarando elementos e removendo <i>outliers</i>	18
3.2.2	Classificação Morfológica	19

3.3	Perfis radiais	22
4	Comparações entre propriedades estelares e propriedades nebulares	27
4.1	Comparação entre as taxas de formação estelar	27
4.2	Comparação entre os coeficientes de extinção	31
4.3	Comparação entre as metalicidades	33
4.3.1	Metais em galáxias - $\langle \log Z_\star \rangle_M$ e $\log (O/H)$	33
4.3.2	Artigo - Insights on the Stellar Mass-Metallicity Relation from the CALIFA Survey.	33
4.3.3	Artigo - The CALIFA Survey across the Hubble sequence. Spatially resolved stellar population properties in galaxies	37
5	Extinção diferencial	39
5.1	Estudo empírico	39
5.1.1	Comparação direta entre os coeficientes	39
5.1.2	O papel de x_Y e de b/a	40
5.2	Modelagem e interpretação	45
5.2.1	O modelo	45
5.3	Próximos passos	47
5.3.1	Comparação com os dados.	47
5.3.2	Perfis radiais vs. propriedades integradas	48
6	Estimando frações de gás	49
6.1	Um modelo simples de evolução química	49
6.2	Relação de Kennicut-Schmidt e a pseudo-KS	51
6.2.1	Resíduos da pseudo-KS	51
6.3	Conversão de poeira em gás.	56

6.3.1	Analisando a conversão	57
6.4	Perspectivas e próximos passos.	63
A	Artigos publicados	65
A.1	CALIFA, the Calar Alto Legacy Integral Field Area survey. III. Second public data release	65
A.2	Insights on the stellar mass-metallicity relation from the CALIFA Survey . .	97
A.3	The CALIFA survey across the Hubble sequence. Spatially resolved stellar population properties in galaxies	104
Referências Bibliográficas		I

Lista de Figuras

2.1	Exemplo de ajuste de linha de emissão.	8
2.2	Calibração da abundância de oxigênio no gás	11
2.3	Exemplo de programa utilizando o EmLinesDataCube.	12
2.4	Diagrama BPT da galáxia NGC2916.	13
2.5	Evolução temporal do número e da taxa de fótons H-ionizantes em unidades da massa formada.	16
3.1	Histogramas: densidade superficial de massa, idade média, fração de populações jovens e relação axial.	20
3.2	Classificação por morfologia.	21
3.3	Imagen e exemplos de mapas e perfis radiais.	23
3.4	Perfis radiais das propriedades físicas.	25
3.5	Histogramas dos perfis radiais das propriedades físicas.	26
4.1	Comparação entre Σ_{SFR}^* e $\Sigma_{\text{SFR}}^{\text{neb}}$ em bins radiais para diversas idades.	29
4.2	Comparação entre as SFR.	30
4.3	Comparação entre os coeficientes de extinção.	32
4.4	Comparação entre os coeficientes de extinção da amostra selecionada.	32
4.5	$\langle \log Z_\star \rangle_M$ vs. $\log(O/H)$ - perfis radiais	34
4.6	Relação μZR e comparação entre as metalicidades.	36

5.1	Comparação τ_V^* e histogramas de \mathcal{D}_τ e \mathcal{R}_τ .	40
5.2	\mathcal{D}_τ , x_Y e φ .	42
5.3	\mathcal{R}_τ , x_Y e φ .	43
5.4	\mathcal{D}_τ , x_Y e φ no SDSS.	44
5.5	\mathcal{R}_τ , x_Y e φ no SDSS.	44
5.6	Modelo para extinção diferencial.	46
5.7	Histogramas de τ_{BC} , τ_{ISM} e ρ .	48
6.1	A_V/μ_\star vs. $\langle \log Z \rangle_M$	50
6.2	Relação pseudo-KS.	52
6.3	Resíduos da <i>pseudo-KS</i> .	53
6.4	Resíduos da <i>pseudo-KS</i> removendo o espalhamento com $\left(\frac{(O/H)}{(O/H)_\odot}\right)$.	54
6.5	Resíduos da <i>pseudo-KS</i> removendo o espalhamento com μ_\star .	55
6.6	A <i>pseudo-KS</i> sem os principais causadores de espalhamento.	55
6.7	Calibração das metalicidades.	58
6.8	Perfil radial de δ_{DGR} .	59
6.9	Perfis radiais de Σ_{gas} e f_{gas} .	60
6.10	Histogramas de Σ_{gas} e f_{gas} .	60
6.11	Propriedades físicas e Σ_{gas} .	61
6.12	Propriedades físicas e f_{gas} .	62
6.13	Relação de Kennicut-Schmidt.	62
6.14	Tempo de depleção do gás.	64

Capítulo 1

Introdução

Com a criação e difusão em massa de dados gerados com os grandes projetos astronômicos atuais, nossa forma de enxergar o mundo vem se tornando cada vez menos ingênuas quanto ao Universo. Com diferentes faixas espectrais (desde raios- γ até micro-ondas), diferentes fontes de dados (spectros de galáxias integradas, espectroscopia de campo, imagens, monitoramento temporal) e diferentes objetivos, os *surveys* astronômicos¹ permeiam por diferentes fenômenos astrofísicos. Além de estarem formando um imenso legado de informações para futuros astrofísicos, são basilares para o desenvolvimento de novas ideias e resolução dos desafios atuais da área.

1.1 O GAS-UFSC e o IAA-CSIC

Nos últimos anos nosso grupo de Astrofísica (GAS-UFSC) aqui na Universidade Federal de Santa Catarina vem trabalhando com dados de diversos *surveys*. Nossa grupo foi pioneiro no estudo das propriedades físicas das populações estelares de aproximadamente um milhão de galáxias do *SDSS* através do projeto SEAGal/*STARLIGHT*² publicando diversos artigos importantes e amplamente citados (e.g., Cid Fernandes et al. 2005; Mateus et al. 2006; Stasińska et al. 2006; Asari et al. 2007; Stasińska et al. 2008; Cid Fernandes et al. 2011).

Atualmente participamos de um projeto entre nosso grupo de populações estelares aqui no GAS com pesquisadores do Instituto de Astrofísica de Andalucía (IAA), na cidade de Granada, Comunidade autônoma de Andalucía, ao sul da Espanha. Esse instituto pertence ao

¹Um *survey* astronômico é um levantamento de informações ou mapeamento de regiões do céu utilizando telescópios e detectores.

²<http://starlight.ufsc.br>

Consejo Superior de Investigaciones Científicas (CSIC), o maior órgão público (estatal) de pesquisas científicas na Espanha, e o terceiro maior da Europa. Conta com pesquisadores participantes do CALIFA (Sánchez et al. 2012), funcionando como centro físico do projeto. A pesquisadora Rosa M. González Delgado, coorientadora deste trabalho, uma das principais líderes do projeto e que também atua como Pesquisadora Visitante Especial (PVE-CsF) aqui na UFSC; Rubén García Benito, que faz parte do grupo de redução dos dados do *survey*; e Enrique Pérez, do grupo de populações estelares, já trabalham em nossa parceria e possuem conhecimento e domínio das técnicas exploradas por nosso projeto, além de participarem ativamente do desenvolvimento do CALIFA. Durante os últimos três anos nosso grupo de populações estelares no CALIFA publicou diversos artigos (e.g., Pérez et al. 2013; González Delgado et al. 2014b,a, 2015), e mais dois já foram submetidos. Paralelamente participamos de diversos congressos e conferências publicando nossos resultados.

1.2 Gás, estrelas e poeira nas galáxias

Galáxias são formadas por uma complexa mistura de gás, poeira, estrelas e matéria escura, distribuídas em discos, bulbos e halos. O gás é o combustível da formação estelar. As nuvens de gás molecular, formadas pelo esfriamento de gás do meio interestelar, se fragmentam formando estruturas menores e cada vez mais densas, que são chamadas *clumps*. A formação estelar acontece quando o centro dessas massas de gás colapsam devido ao desbalanceamento entre pressão e gravidade. Essas regiões, que podem ser pequenas ou se estenderem a gigantes berçários estelares, estão geralmente cobertas por uma densa camada de poeira. Gerada pelo próprio processo de formação estelar, a poeira funciona como uma cortina que modifica a energia dos fótons que chegam até nossos detectores. Isso acontece pois os grãos de poeira absorvem e reemitem radiação com diferentes energias, modificando o espectro observado. Esse processo é chamado de extinção por poeira. Apesar de modificar o espectro, a poeira pode também ser usada como sinalizadora de regiões aonde há intensa formação estelar. No final do ciclo de vida das estrelas, diversos elementos são jogados no meio interestelar através das explosões de supernovas, alterando assim a composição química do gás disponível para produção de novas estrelas.

Schmidt (1959) foi o primeiro a propor a existência de uma lei de potências que liga a taxa de formação estelar (SFR - *star formation rate*) e o gás. Anos depois, Kennicutt (1998) estuda essa relação observationalmente, utilizando diversos indicadores de formação estelar em diferentes faixas espectrais. Em seu trabalho, Kennicutt estabelece a ligação entre a den-

sidade superficial do gás e da SFR. Hoje em dia essa é comumente chamada de relação de Kennicut-Schmidt (KS) ou lei de formação estelar. A equação parametrizada por Kennicutt foi:

$$\Sigma_{\text{SFR}} = (2.5 \pm 0.7) \times 10^{-4} \left(\frac{\Sigma_{\text{gas}}}{M_{\odot} \text{ pc}^{-2}} \right)^{1.4 \pm 0.15} M_{\odot} \text{ yr}^{-1} \text{ kpc}^{-2}. \quad (1.1)$$

Utilizando a síntese de populações estelares aplicada às galáxias do CALIFA poderíamos estimar Σ_{gas} através de uma equação como (1.1) mas, além de não ser uma maneira independente de Σ_{SFR}^* , esta equação foi parametrizada para valores integrados de galáxias, diferentemente da área típica das regiões que estamos observando (regiões de galáxias com tamanhos típicos de $\sim 1 \text{kpc}$). Com a síntese é possível também obter a história de formação estelar através da fração de populações estelares com distintas idades (Asari et al. 2007), não necessitando assim prender-se às zonas das galáxias onde o espectro tenha relação sinal ruído (S/N) suficiente para a medida de todas as linhas espectrais necessárias para os cálculos sobre o gás e poeira. Nos falta, porém, uma medida da quantidade de gás de forma independente da formação estelar, o que nos levou a buscar uma conversão que utilize uma ou mais propriedades provenientes da síntese com o STARLIGHT.

1.3 De poeira para gás

Dentro da astrofísica extragaláctica, um dos grandes temas ainda incômodo é a determinação de massas de gás. A quantidade de gás de uma galáxia define o processo de formação estelar, portanto, é peça fundamental no entendimento da sua evolução. O gás atômico (formado majoritariamente por átomos de hidrogênio) geralmente está nas partes de fora das regiões de formação estelar, aonde a temperatura já está alta o suficiente para quebrar a ligação entre os hidrogênios. O gás molecular é associado diretamente com a formação estelar, porém a molécula de H₂ não possui um observável direto. A baixa massa da molécula não permite que nenhum grau de liberdade rotacional seja excitado, pois a temperatura nessas regiões é muito baixa, necessitando ser traçado através de outros elementos presentes ali. Geralmente o que se usa são as transições entre os níveis energéticos do monóxido de carbono (CO) pois suas linhas são bem fortes (fácil de observar). Bolatto et al. (2013) revisam o tema mostrando um panorama geral sobre a conversão de intensidade da linha de CO e a densidade superficial do gás.

Avermelhamento (medido através de índices de cores) e extinção da luz das estrelas são te-

mas discutidos e utilizados como evidência da existência de “*núvens interestelares*”. Barnard (1908), através da análise de imagens dos objetos Messier 8, 17 e 18, discute a presença de “buracos ou manchas” entre as estrelas, e a existência de estrelas no meio de “nebulosidades”. Esse artigo foi escrito inclusive antes da famosa discussão de Sharpless e Curtis em 1920, e do artigo de Hubble (1925) que definiu que as “nebulosas espirais” eram objetos que estavam a distâncias muito maiores que a dimensão da Via Láctea. Atualmente, trabalhos como a revisão de Draine (2003) nos ajudam a entender as propriedades físicas, a natureza dos grãos de poeira e de como ela afeta a luz que a atravessa.

Uma das formas de se mapear e determinar quantidades de gás em galáxias é utilizando a presença de poeira. Devido a presença de poeira nas regiões de formação estelar, podemos utilizá-la como maneira indireta de estimar a densidade superficial do gás oculto através da introdução de um fator de conversão:

$$\Sigma_{\text{gas}} = \frac{\Sigma_{\text{gas}}}{\Sigma_d} \times \Sigma_d = \kappa \times \Sigma_d. \quad (1.2)$$

O índice d designa poeira (*dust*, em inglês) e as densidades superficiais são dadas em $M_\odot pc^{-2}$. Diversos artigos discutem a calibração e os *caveats* deste tipo de conversão e também problemas de degenerescência na conversão CO-H₂ (Guiderdoni & Rocca-Volmerange 1987; Leroy et al. 2011, 2013; Rémy-Ruyer et al. 2014), mas quase todos eles utilizam medidas de infravermelho (IR) para estimar Σ_d , onde os grãos de poeira geralmente re-emitem a luz absorvida em outras frequências. Já Brinchmann et al. (2013, BR13 daqui em diante) desenvolvem uma conversão de poeira para gás utilizando medidas da poeira em absorção, e não em emissão, como os estudos em IR, para as galáxias formadoras de estrelas³ do sétimo lançamento público de dados (*data release*) do SDSS (Abazajian et al. 2009, DR7). Segundo BR13, esse é um método é sensível ao gas total da galáxia (soma do gás molecular com o gás atômico). Na busca por traçadores de gás, escolhemos a poeira em absorção (na faixa do espectro óptico) para tal objetivo pois é uma quantidade à qual temos acesso, tanto via síntese espectral como por meio de linhas de emissão.

1.4 Este trabalho

Nessa primeira etapa do doutorado estamos procurando entender melhor a natureza das propriedades físicas estelares e nebulares e suas diferenças nas galáxias do CALIFA. No Cap.

³Galáxias *star-forming* (SF) - com formação estelar ativa.

2 descrevemos o processo de medidas das propriedades nebulares. A seleção da amostras, suas ressalvas e exemplos de perfis radiais são discutidos no Cap. 3. Comparações entre algumas das propriedades nebulares e àquelas provenientes da síntese são discutidas no Cap. 4. De maneira e melhor entender a relação entre o coeficiente de extinção proveniente da síntese e do decremento de Balmer e suas relações com a extinção do meio interestelar (*interstellar medium - ISM*) e das núvens formadoras de estrelas (*birth-clouds - BC*) desenvolvemos uma discussão mais pontualmente no Cap. 5. Por fim, no Cap. 6, desenvolvemos a conversão de poeira em absorção para gás utilizando o método de BR13, juntamente com algumas proposições para os próximos passos deste projeto. Permeando os capítulos, quando pertinente, descrevo minha participação em artigos nestes últimos dois anos.

Capítulo 2

Linhas de emissão

Espectros observados carregam uma mistura de luz provenientes de distintas componentes das galáxias (estrelas, gás, poeira, etc). Com a síntese de populações estelares pode-se modelar os espectros proveniente das estrelas de diferentes idades e composições químicas (metalicidade), além da correção pela aplicação de uma lei de extinção por poeira. Subtraindo os espectros observados dos espectros modelados obtém-se os espectros residuais, compostos basicamente pelas linhas de emissão. Essas linhas são geradas principalmente através das ionizações e recombinações de átomos dos elementos encontrados no meio interestelar, e mais densamente, nas nuvens de gás. Neste capítulo descrevo um módulo em `PYTHON` que desenvolvemos para incluir medidas de linhas de emissão (e seus subprodutos) derivados em nossa plataforma geral de análise dos cubos de dados do CALIFA.

2.1 EmLinesDataCube

Dentre os diversos produtos indiretos da síntese de populações estelares, a medida dos fluxos integrados das linhas de emissão é peça fundamental em nosso projeto. Rubén García Benito, nosso colaborador e membro no projeto CALIFA, desenvolveu um programa que, utilizando-se dos espectros residuais ajusta perfis gaussianos para as linhas possibilitando então a medida dos fluxos integrados das linhas de emissão além de estimar os erros envolvidos neste processo. Um exemplo desse processo pode ser observado na Fig. 2.1. Nela vemos a linha de H β na zona central do objeto UGC00148 e o ajuste feito pelo programa. Provavelmente essas medidas sejam liberadas para a comunidade científica assim que o último lançamento público de dados do CALIFA for feito (DR3).

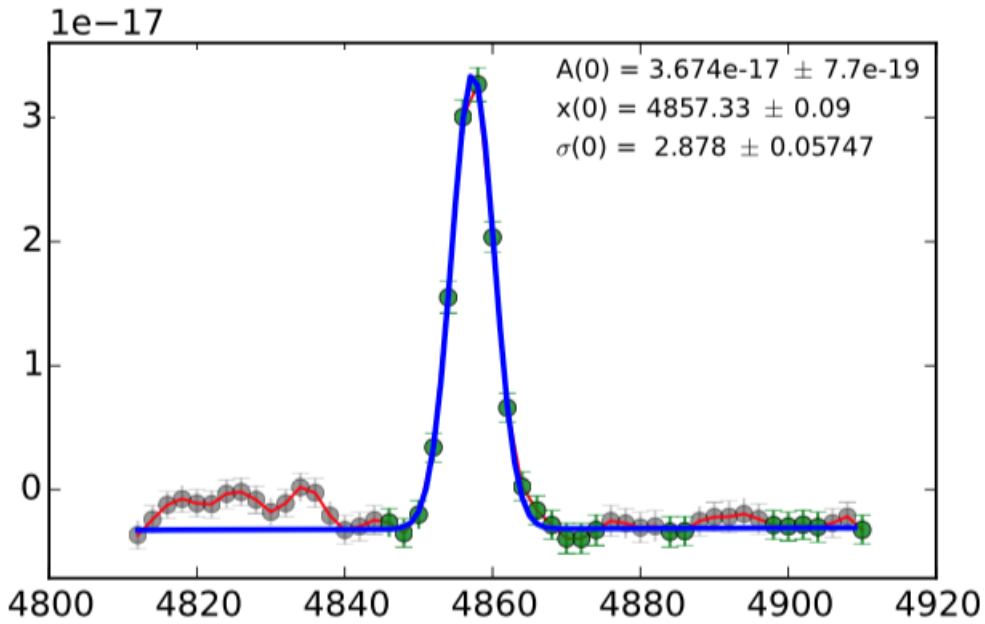


Figura 2.1: Espectro na região da linha de $H\beta$ em emissão para a zona central da galáxia UGC00148 (objeto CALIFA 12) juntamente com o melhor ajuste. Em destaque a amplitude (A), o comprimento de onda central (x) e o desvio padrão neste ajuste (σ).

Feitas as medidas, temos o arcabouço para calcularmos várias propriedades nebulares. Escrevemos um objeto em PYTHON (cujo nome titula esta seção) que, além de organizar os resultados provenientes do programa de medida das linhas de emissão, também calcula a abundância de oxigênio, índice que usamos como metalicidade nebulosa ($\log(O/H)$), o coeficiente de extinção para as regiões nebulosas (τ_V^{neb}), larguras equivalentes das linhas, assim como os erros propagados em cada cálculo. Esse objeto foi adicionado ao PyCASSO¹ (Cid Fernandes et al. 2013) para que os demais membros do projeto possam utilizá-lo. Nele também encontram-se as medidas dos fluxos em diversas linhas de emissão, a posição central das linhas medidas, amplitudes, desvios padrão, coeficientes para reconstrução do contínuo em cada linha de emissão, os erros nestas medidas, além das propriedades mencionadas anteriormente e seus erros propagados.

2.1.1 Extinção estimada através do decremento de Balmer

Em um modelo que assume que entre o observador e a fonte de energia existe uma camada difusa, como uma cortina, que extingue a luz diferentemente em cada comprimento de onda,

¹Python CALIFA Stellar Synthesys Organizer - <http://minerva.ufsc.br/~andre/PyCASSO-0.9.3/intro.html>

temos:

$$F_{\lambda}^{obs} = F_{\lambda}^{int} e^{-\tau_{\lambda}} \quad (2.1)$$

onde F_{λ}^{int} é o fluxo intrínseco (F_{λ}^{obs} , o observado) em cada comprimento de onda, τ_{λ} é a profundidade óptica para o comprimento de onda λ (neste trabalho também o chamamos de coeficiente de extinção). O modelo de extinção de Cardelli et al. (1989) nos dá uma calibração empírica da razão entre os coeficientes de extinção em um comprimento de onda e na banda V, e com isso podemos desenvolver (2.1) de maneira que possamos escrever uma equação para τ_V :

$$F_{\lambda}^{obs} = F_{\lambda}^{int} e^{-(\frac{\tau_{\lambda}}{\tau_V})\tau_V} \quad (2.2)$$

$$q_{\lambda} \equiv \frac{\tau_{\lambda}}{\tau_V} \quad (2.3)$$

$$F_{\lambda}^{obs} = F_{\lambda}^{int} e^{-q_{\lambda}\tau_V} \quad (2.4)$$

$$\frac{F_{\lambda}^{obs}}{F_{\lambda'}^{obs}} = \frac{F_{\lambda}^{int} e^{-q_{\lambda}\tau_V}}{F_{\lambda'}^{int} e^{-q_{\lambda'}\tau_V}} \quad (2.5)$$

$$\ln\left(\frac{F_{\lambda}^{obs}}{F_{\lambda'}^{obs}}\right) = \tau_V(q_{\lambda'} - q_{\lambda}) \ln\left(\frac{F_{\lambda}^{int}}{F_{\lambda'}^{int}}\right) \quad (2.6)$$

$$\tau_V = \frac{1}{(q_{\lambda'} - q_{\lambda})} \left[\ln\left(\frac{F_{\lambda}^{obs}}{F_{\lambda'}^{obs}}\right) - \ln\left(\frac{F_{\lambda}^{int}}{F_{\lambda'}^{int}}\right) \right] \quad (2.7)$$

Nessa equação, os q_{λ} são provenientes da curva de extinção adotada.

Utilizando (2.7) podemos calcular qual o coeficiente de extinção para essas regiões nebulares. Para este cálculo utilizamos o fato de que a razão entre os fluxos intrínsecos das duas primeiras linhas da série de Balmer, H α e H β , varia muito um pouco com a metalicidade, a densidade e a temperatura. Usamos aqui esse valor como constante e igual a 2.86 (densidade eletrônica de $n = 100 \text{ cm}^{-3}$ e temperatura eletrônica $T_e = 10^4 \text{ K}$; Osterbrock & Ferland 2006). Também utilizamos $q_{H\alpha} = 0.81775$ e $q_{H\beta} = 1.16427$ (valores da calibração empírica feita por Cardelli et al.). Com isso temos:

$$\tau_V^{\text{neb}} = 2.886 \ln\left(\frac{F_{H\alpha}^{obs}/F_{H\beta}^{obs}}{2.86}\right). \quad (2.8)$$

Como veremos mais adiante (Sec. 4.2, Fig. 3.5 - painel i) τ_V^{neb} varia tipicamente entre 0.6

e 0.65 (média e mediana) nas regiões aqui estudadas. O erro propagado para τ_V^{neb} é:

$$\tau_V^{\text{neb}} \equiv \tau_V^{\text{neb}}(F_{\text{H}\alpha}^{\text{obs}}, F_{\text{H}\beta}^{\text{obs}}) \quad (2.9)$$

$$\epsilon(\tau_V^{\text{neb}}) = \sqrt{\left(\frac{\partial \tau_V^{\text{neb}}}{\partial F_{\text{H}\alpha}^{\text{obs}}}\right)^2 \epsilon(F_{\text{H}\alpha}^{\text{obs}})^2 + \left(\frac{\partial \tau_V^{\text{neb}}}{\partial F_{\text{H}\beta}^{\text{obs}}}\right)^2 \epsilon(F_{\text{H}\beta}^{\text{obs}})^2} \quad (2.10)$$

$$\frac{\partial \tau_V^{\text{neb}}}{\partial F_{\text{H}\alpha}^{\text{obs}}} = \frac{1}{F_{\text{H}\alpha}^{\text{obs}}(q_{\text{H}\beta} - q_{\text{H}\alpha})} \quad (2.11)$$

$$\frac{\partial \tau_V^{\text{neb}}}{\partial F_{\text{H}\beta}^{\text{obs}}} = -\frac{1}{F_{\text{H}\beta}^{\text{obs}}(q_{\text{H}\beta} - q_{\text{H}\alpha})} \quad (2.12)$$

$$\epsilon(\tau_V^{\text{neb}}) = \frac{1}{(q_{\text{H}\beta} - q_{\text{H}\alpha})} \sqrt{\left(\frac{\epsilon(F_{\text{H}\alpha}^{\text{obs}})}{F_{\text{H}\alpha}^{\text{obs}}}\right)^2 + \left(\frac{\epsilon(F_{\text{H}\beta}^{\text{obs}})}{F_{\text{H}\beta}^{\text{obs}}}\right)^2} \quad (2.13)$$

Os termos de dentro da raiz em (2.13) são o inverso das relações sinal-ruído (S/N) de $\text{H}\alpha$ e $\text{H}\beta$. Como $\text{H}\beta$ é sempre a mais ruidosa das duas, podemos aproximar a incerteza em τ_V^{neb} por:

$$\epsilon(\tau_V^{\text{neb}}) \approx \frac{2.886}{(S/N)_{\text{H}\beta}} \quad (2.14)$$

com valor típico ~ 0.14 .

2.1.2 Metalicidade Nebular

Todos os elementos, além do hidrogênio e do hélio, são considerados metais em astrofísica. Um método direto para medir a abundância de oxigênio é através do cálculo da temperatura eletrônica das regiões HII. Este método necessita a medida da linha de [O III] $\lambda 4363$ que é muito fraca e quase impossível de ser detectada em regiões com alta metalicidade. Os indicadores de metalicidade nebulosa geralmente são baseados em métodos de linhas fortes (*strong-line methods*; Pagel et al. 1979), principalmente os que utilizam as razões das linhas de [O III] $\lambda 5007$ e [N II] $\lambda 6584$ buscando correlações com a abundância relativa de oxigênio. As calibrações destes indicadores que estão sendo utilizadas pelo CALIFA foram feitas por Marino et al. (2013, M13 daqui em diante) de forma empírica utilizando medidas de temperatura eletrônica de 603 regiões HII e mais medidas nebulares de 3423 regiões HII mapeadas por Sánchez et al. (2013). O indicador que estamos utilizando para esse projeto é aquele que calibra a fração relativa de oxigênio utilizando a razão entre as linhas de [O III] e [N II]. A

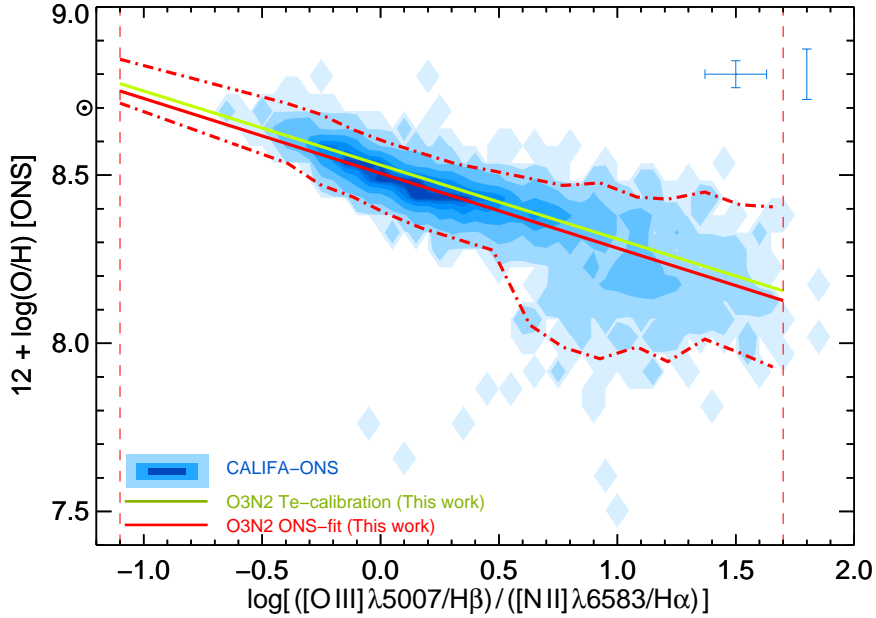


Figura 2.2: Calibração da abundância de oxigênio nebuloso para 3423 regiões HII mapeadas por Sánchez et al. (2013). Figura retirada de Marino et al. (2013)

parametrização encontrada pelos autores foi:

$$12 + \log(O/H) = 8.533[\pm 0.012] - 0.214[\pm 0.012] \times O3N2 \quad (2.15)$$

onde O3N2 vem da razão entre os fluxos intrínsecos de [O III], H β , [N II] e H α :

$$O3N2 \equiv \log\left(\frac{[O_{III}]\lambda 5007}{H\beta} \times \frac{H\alpha}{[N_{II}]\lambda 6584}\right). \quad (2.16)$$

A Fig. 2.2 mostra o resultado da calibração por M13. As regiões estudadas nesse trabalho possuem abundâncias relativas de oxigênio nebuloso em torno de 0.6 (O/H) $_{\odot}$.

2.1.3 Exemplo de utilização

Com a criação do objeto `EmLinesDataCube` e sua adição ao `pyCASSO`, o processo de análise e produção de gráficos torna-se extremamente simples. Um exemplo de programa para produzir um gráfico BPT (Baldwin et al. 1981) utilizando os fluxos de quatro linhas de emissão (H α , H β , [O III] λ 5007 e [N II] λ 6584) pode ser visto na Fig. 2.3. Primeiro carregam-se os arquivos de dados utilizando o `pyCASSO` e o `EmLinesDataCube` então todas as informações já estão prontas para serem utilizadas. Calculam-se então as razões entre as linhas e, por último, o gráfico é

```

1 import numpy as np
2 from matplotlib import pyplot as plt
3 from pycasso import fitsQ3DataCube
4
5 CALIFASuperFits='K0277.fits'
6 EmLinesFits='K0277.EML.fits'
7 # Carregando arquivos FITS
8 K = fitsQ3DataCube(CALIFASuperFits)
9 K.loadEmLinesDataCube(EmLinesFits)
10 # Agora todos as informacoes sobre as linhas de
11 # emissao estao instanciadas em K.EL
12
13 # Indices dos vetores aonde estao armazenados os
14 # fluxos de cada linha
15 Ha_obs__z = K.EL.flux[K.EL.lines.index('6563'), :]
16 Hb_obs__z = K.EL.flux[K.EL.lines.index('4861'), :]
17 N2_obs__z = K.EL.flux[K.EL.lines.index('6583'), :]
18 O3_obs__z = K.EL.flux[K.EL.lines.index('5007'), :]
19 # Razao entre os fluxos de N2/Ha e O3/Hb
20 N2Ha__z = np.log10(N2_obs__z) - np.log10(Ha_obs__z)
21 O3Hb__z = np.log10(O3_obs__z) - np.log10(Hb_obs__z)
22
23 # Grafico
24 f = plt.figure()
25 ax = f.gca()
26 sc = ax.scatter(N2Ha__z, O3Hb__z, c = K.zoneDistance_HLR,
27                  cmap = 'viridis_r', marker = 'o', s = 10,
28                  alpha = 0.8, edgecolor = 'none')
29 ax.set_xlabel(r'$\log\ [NII]/H\alpha$')
30 ax.set_ylabel(r'$\log\ [OIII]/H\beta$')
31 cb = plt.colorbar(sc, ticks = [0, 0.5, 1, 1.5, 2])
32 cb.set_label('R [HLR]')
33 plt.axis([-0.6, 0.3, -1.5, 1])
34 f.savefig('%s-BPT.pdf' % K.califaID)

```

Figura 2.3: Exemplo de programa utilizando os fluxos de $H\alpha$, $H\beta$, $[O III] \lambda 5007$ e $[N II] \lambda 6584$ para construção de um gráfico BPT utilizando o objeto `EMLINESDATACUBE` juntamente com o `PYCASSO`.

feito utilizando a biblioteca gráfica `MATPLOTLIB`².

Na Fig. 2.4 podemos ver uma imagem produzida por um programa como o do exemplo anterior. Neste caso utilizamos os dados da galáxia NGC2916 (objeto CALIFA 277). Clasificada com tipo morfológico Sb, é considerada uma galáxia azul e com massa intermediária ($\sim 10^{11} M_\odot$). Todas as zonas neste gráfico possuem S/N maior que 3 em todas as quatro linhas do BPT ($H\beta$, $[O III]$, $H\alpha$ e $[N II]$). Podemos ver que as zonas mais próximas ao núcleo da galáxia estão distribuídas na ponta da asa direita no plano BPT, lado associado aos núcleos ativos. Já do outro lado do gráfico, local associado às regiões de formação estelar, se encontram as zonas pertencentes ao disco da galáxia ($R > 0.7HLR$).

² <http://matplotlib.org/>

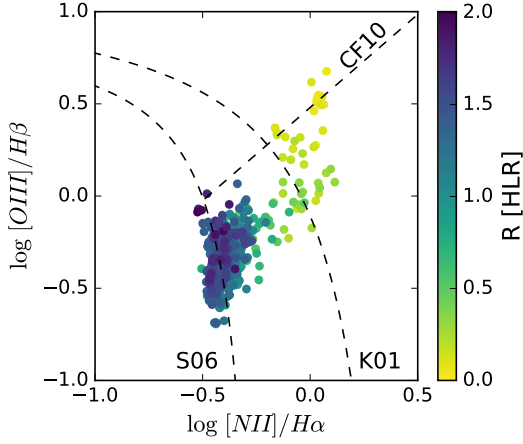


Figura 2.4: Diagrama BPT para as regiões com $S/N > 3$ nas linhas H β , [O III] $\lambda 5007$, H α e [N II] $\lambda 6584$, da galáxia NGC2916 (objeto CALIFA 277) produzida por um programa como o do exemplo da Fig. 2.3. As cores marcam a distância ao centro da galáxia em unidades do raio que contém metade da luz (HLR). As linhas são definidas por Kewley et al. (2001, K01), Stasińska et al. (2006, S06) e Cid Fernandes et al. (2010, CF10).

2.2 Taxa de formação estelar

Um dos métodos mais utilizados para medida de taxa de formação estelar (*Star Formation Rate - SFR*) recente utiliza a linha de emissão de H α . Nesse método assume-se que a formação estelar é constante nos últimos t anos, que deve englobar pelo menos o tempo de vida das estrelas massivas ionizantes, que produzem basicamente todos os fótons que geram a linha de emissão de H α .

Nós queremos calibrar a luminosidade da linha de H α ($L_{\text{H}\alpha}$) como um indicador de SFR usando uma relação linear:

$$\text{SFR}_{\text{H}\alpha} = k \times L_{\text{H}\alpha}. \quad (2.17)$$

Portanto, nosso trabalho é encontrar k . Faremos isso investigando a natureza dos fótons H-ionizantes.

Chamamos Λ o valor total de luz (I) que recebemos de estrelas que se formaram t anos atrás. $I(t)$ pode ser qualquer função que descreve a evolução temporal de qualquer fonte radiativa genérica *por unidade de massa formada* de uma população estelar simples (*Simple Stellar Population - SSP*). Como depende da massa formada fica claro que essa quantidade é

dependente da Função de Massa Inicial (*Initial Mass Function - IMF*):

$$\Lambda(t) = \int_0^t l(t') dM(t'). \quad (2.18)$$

Para obter Λ nos falta saber como a massa em estrelas cresce no tempo, ou seja, saber como a SFR varia no tempo:

$$dM(t) = \text{SFR}(t) dt \quad (2.19)$$

$$(2.20)$$

Integrando (2.18) dentro do tempo do Universo ($T_U \sim 14$ bilhões de anos) teremos hoje um total de luz:

$$\Lambda = \Lambda(t = T_U) = \int_0^{T_U} l(t) dM(t) \quad (2.21)$$

$$\Lambda(T_U) = \int_0^{T_U} \text{SFR}(t) l(t) dt \quad (2.22)$$

Assumindo o caso B de recombinação do hidrogênio, um em cada 2.226 fótons ionizantes produzem um fóton de H α (Osterbrock & Ferland 2006). Esse número não varia muito em função da temperatura e da densidade nas regiões HII. Portanto:

$$L_{H\alpha} = h\nu_{H\alpha} \frac{Q_H}{2.226}, \quad (2.23)$$

onde Q_H é a taxa de fótons H-ionizantes. Em todo este processo assume-se que nenhuma radiação ionizante escapa da nuvem e, apesar de $L(H\alpha)$ estar corrigido por extinção, também assume-se que a poeira não absorve muito os fótons com $h\nu > 13.6$ eV. Escrevemos dQ_H como a equação (2.18).

$$Q_H(t) = \int dQ_H = \int q_H(t) dM(t) \quad (2.24)$$

Nas equações acima, q_H (que assume o mesmo papel de $l(t)$ em (2.18)) é a taxa de fótons H-ionizantes por unidade de massa formada. Considerando os fótons que possam ionizar o hidrogênio ($h\nu \geq 13.6$ eV ou $\lambda \leq 912\text{\AA}$) escrevemos:

$$q_H(t) = \int_0^{912\text{\AA}} \frac{l_\lambda \lambda}{hc} d\lambda. \quad (2.25)$$

Nesta equação, l_λ é a luminosidade por unidade de massa formada e comprimento de onda em unidades solares [$L_\odot/\text{ÅM}_\odot$] para uma SSP³. Com isso, nós ainda precisamos analisar como a integração de q_H evolui com o tempo, para então obter a SFR. Integrando q_H de hoje até T_U nós obtemos o número de fótons H-ionizantes produzidos pelas fontes que emitem a luz l :

$$\mathcal{N}_H = \int_0^{T_U} q_H(t) dt \quad (2.26)$$

Utilizamos a base de populações estelares de Bruzual & Charlot (2003) com as isócronas de Padova 2000, juntamente com a IMF de Salpeter (1955). Neste caso, podemos ver na Fig. 2.5 a evolução temporal de \mathcal{N}_H em valores absolutos (painei superior esquerdo) e relativamente ao total de \mathcal{N}_H (painei superior direito). Em Cid Fernandes et al. (2011, Fig. 2b) nós podemos ver a evolução temporal de q_H sob todas as idades e metalicidades⁴. A mesma figura é reproduzida no painel inferior. É notável que o número de fótons H-ionizantes rapidamente converge ao máximo perto de $t = 10^7$ anos. Também fica claro que \mathcal{N}_H é dependente da metalicidade, portanto o valor de k em (2.17) também⁵. Utilizando (2.20) em (2.24) e com uma simplificação graças a SFR constante dentro desta escala temporal ($SFR(t) \rightarrow SFR$), podemos reescrever (2.24) usando (2.26):

$$Q_H = SFR \mathcal{N}_H(t = 10^7 \text{ anos}, \text{IMF}, Z_\star). \quad (2.27)$$

Substituindo (2.27) em (2.23) podemos escrever:

$$SFR_{H\alpha} = \frac{2.226}{\mathcal{N}_H h\nu_{H\alpha}} \times L_{H\alpha} \quad (2.28)$$

Este método resulta em uma SFR recente, em termos de que usamos o valor de \mathcal{N}_H para $t = 10^7$ anos. Finalmente, resolvendo (2.28) encontramos o valor para k em (2.17):

$$SFR_{H\alpha} [\text{M}_\odot \text{ yr}^{-1}] = 3.13 \times \left(\frac{L_{H\alpha}}{10^8 L_\odot} \right) = 8.1 \times 10^{-42} L_{H\alpha} [\text{ergs s}^{-1}] \quad (2.29)$$

Em Kennicutt (1998) esse coeficiente é calculado utilizando diferentes modelos estelares mas utilizando a mesma IMF. Nossa valor é bem próximo daquele obtido no artigo ($7.9 \times$

³Apesar de não escritas aqui, existem dependências com Z , IMF e isócronas em l_λ (portanto, também em q_H e todos os seus produtos)

⁴Naquele estudo, o grupo SEAGal/STARLIGHT utilizou as isócronas de Padova 1994 com a IMF de Chabrier (2003).

⁵O valor de k em nossa análise varia de 2.00 até 3.13 de acordo com a metalicidade indo de $0.02Z_\odot$ a $1.58Z_\odot$.

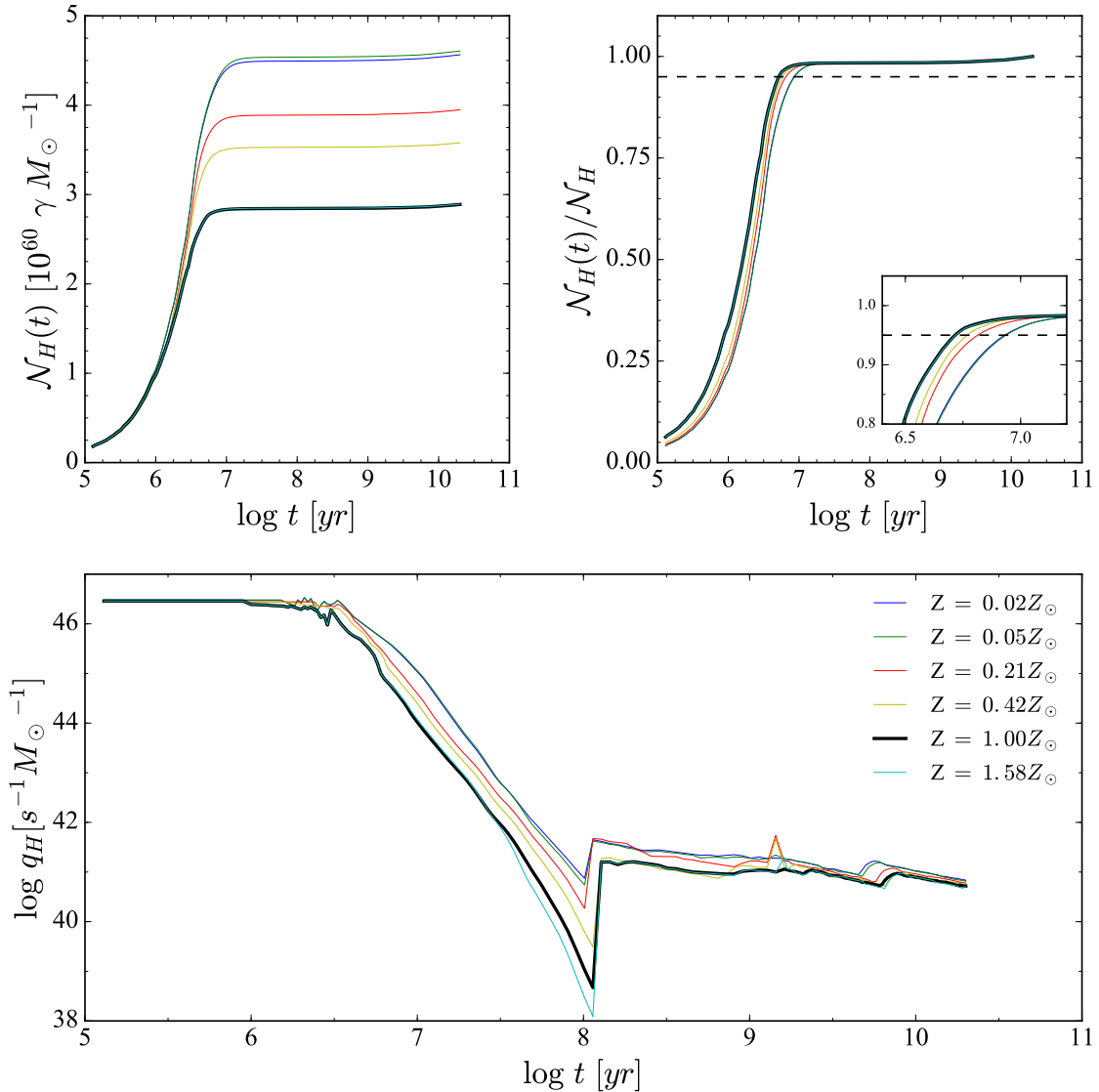


Figura 2.5: *Painel superior esquerdo:* A evolução no tempo do número de fótons (\mathcal{N}_H) para 6 metalicidades (de $0.02 Z_\odot$ até $1.58 Z_\odot$) que compoem nossos modelos de SSP. A linha preta grossa representa a evolução utilizando metalicidade solar. *Painel superior direito:* O mesmo que o *painel superior esquerdo* mas normalizado pelo valor total de \mathcal{N}_H . A linha pontilhada representa 95% do total de \mathcal{N}_H . Em destaque a região ao redor de 10 milhões de anos. *Painel inferior:* Evolução da taxa de fótons H-ionizantes em unidades da massa formada. Também mostra o valor seguindo o código de cores para as mesmas metalicidades.

10^{-42}).

Capítulo 3

Amostra de galáxias

Nem todas as regiões das galáxias que estudamos têm medidas das linhas espectrais necessárias para este estudo. Essa falta não é um defeito de observação e sim uma característica intrínseca de determinada região. As linhas em emissão geralmente estão ligadas ao gás e nem todas as partes da galáxia possuem gás. Nesse capítulo vamos descrever todas as características e máscaras impostas em nossa amostra. Faremos um breve comentário sobre a classificação morfológica destas galáxias, além de calcular e exemplificar os perfis radiais que utilizaremos em nossas discussões futuras.

3.1 Artigo - CALIFA, the Calar Alto Legacy Field Area survey III. Second public data release.

Esse artigo (Apêndice A.1) descreve uma amostra de 200 galáxias que tiveram seus dados liberados no segundo *data release* do CALIFA (DR2) passando por todas as configurações de observação, procedimentos de redução dos dados, avaliação de erros e controle de qualidade. Nosso grupo de populações estelares se encarregou de escrever alguns programas de análise e gerar as imagens nas quais nos embasamos para avaliar a qualidade da síntese de populações estelares com o STARLIGHT em 170670 espectros para distintas posições em cada galáxia, além de realizarmos uma comparação com os resultados para a amostra do DR1 (Husemann et al. 2013). Durante esse trabalho notamos que os resíduos reduziram sensivelmente desde a última versão. Esta mesma análise nos ajudou a melhorar a máscara de remoção de linhas telúricas¹ dos espectros. Também verificamos que os erros relacionados aos espectros obser-

¹Linhas provenientes de fenômenos que ocorrem na Terra.

vados possuem uma distribuição muito próxima a uma gaussiana. Todas os dados presentes nesse trabalho receberam o mesmo pré-processamento detalhado neste artigo.

3.2 Definição da amostra deste trabalho

A amostra de galáxias deste trabalho faz parte da amostra total de galáxias do CALIFA. Os dados passaram pelos mesmos pré-processamento e controle de qualidade daqueles liberados pelo DR2, porém possui dados que ainda não foram disponibilizados publicamente, abarcando 226176 regiões (zonas) de 305 galáxias espirais. Cada uma dessas zonas dessa é composta por um ou mais pixels, com um espectro resultante da soma dos espectros destes, para que tenhamos relação sinal-ruído maior ou igual a 20 na janela de normalização deste espectro. Esse procedimento, conhecido como *Voronoi binning*, está detalhado, juntamente com o procedimento de derivação das propriedades estelares através do código STARLIGHT para cada uma das regiões destas galáxias, em Cid Fernandes et al. (2013).

3.2.1 Mascarando elementos e removendo *outliers*

Para que possamos focar nossos estudos nas regiões de formação estelar, aplicamos uma máscara nos dados selecionando as regiões que possuam:

- medidas do fluxo integrado das linhas de H β , [O III], H α e [N II] com relação sinal-ruído maior do que 3;
- medidas para as seis propriedades comparadas neste capítulo:
 - coeficiente de extinção proveniente da síntese - τ_V^* ;
 - coeficiente de extinção estimado através do decremento de Balmer - τ_V^{neb} ;
 - densidade superficial da taxa de formação estelar calculado através da síntese - Σ_{SFR}^* ;
 - densidade superficial da taxa de formação estelar calculado através da luminosidade de H α - $\Sigma_{\text{SFR}}^{\text{neb}}$;
 - metalicidade média das populações estelares, pesada pela massa estelar - $\langle \log Z_\star \rangle_M$;
 - metalicidade nebulosa - $\log(O/H)$.
- fração de luz proveniente de populações estelares jovens maior que 0.05 (5%) ($x_Y > 0.05$);
- τ_V e τ_V^{neb} maiores que 0.05;

- mais do que cinco zonas contribuindo para o cálculo dos perfis radiais;
- distância ao núcleo maior que 70% do raio que contém metade da luz (*half-light radius* - HLR).

O que aqui chamamos de população jovem discutiremos um pouco mais adiante, na Sec. 4.1. A última imposição é feita para que não haja contaminação por zonas do bojo da galáxia (partes centrais onde as linhas são produzidas por diferentes fenômenos físicos, relacionados a um núcleo ativo). Esse valor (0.7 HLR) foi definido por nossos colaboradores analisando as curvas de brilho das galáxias e representa um valor máximo para localização de zonas centrais.

Na Fig. 3.1 podemos ver os histogramas normalizados (a integral dentro do intervalo do histograma é 1) de algumas propriedades de modo que evidencie os efeitos da máscara que forma nossa amostra. Em vermelho temos as 226176 regiões em 305 galáxias e, em azul, as 16479 zonas de 184 galáxias (19 Sa, 38 Sb, 59 Sbc, 55 Sc e 13 Sd). É notável que nossa seleção busca zonas mais densas e mais jovens (maior fração de populações jovens diminuindo a idade média). O corte mais brusco em nossa amostra é devido a baixa relação sinal-ruído da linha de [O III] ($(S/N)_{[O\text{ III}]} < 3$) em 91142 zonas.

3.2.2 Classificação Morfológica

Com tipos morfológicos variando entre Sa e Sd, massas estelares entre 10^9 e $10^{11.5} M_\odot$ e populações estelares com idades médias entre 10^8 e 10^{10} anos, podemos ver na Fig. 3.2 que as galáxias se ordenam de forma interessante quando agrupadas por tipo morfológico, antecorrelacionando com a idade média estelar e a massa estelar (M_\star e t_\star) e correlacionando com a fração de luz proveniente das populações jovens ($x_Y \equiv x_Y(t_\star < 32 \times 10^6 \text{ anos})$). Cada galáxia contribui com um ponto em cada painel deste gráfico, ou seja, são propriedades integradas. Os intervalos entre primeiro e terceiro quartil quase não se sobreponem quando analisamos as classes morfológicas por idade média.

Esse resultado parece ser interessante visto que a classificação morfológica foi feita por colaboradores do CALIFA totalmente através de inspeção visual das imagens na banda-r do SDSS das mesmas galáxias. Vemos também que as galáxias tipo Sd possuem as populações estelares mais jovens e menos massivas na média. Por ser um fenômeno apenas de posição do referencial de observação não deveríamos ver preferência por valor de relação axial (b/a) quando dividimos em classes morfológicas, o que realmente acontece.

Estamos em fase de finalização de um artigo em que comparamos a relação entre a taxa de

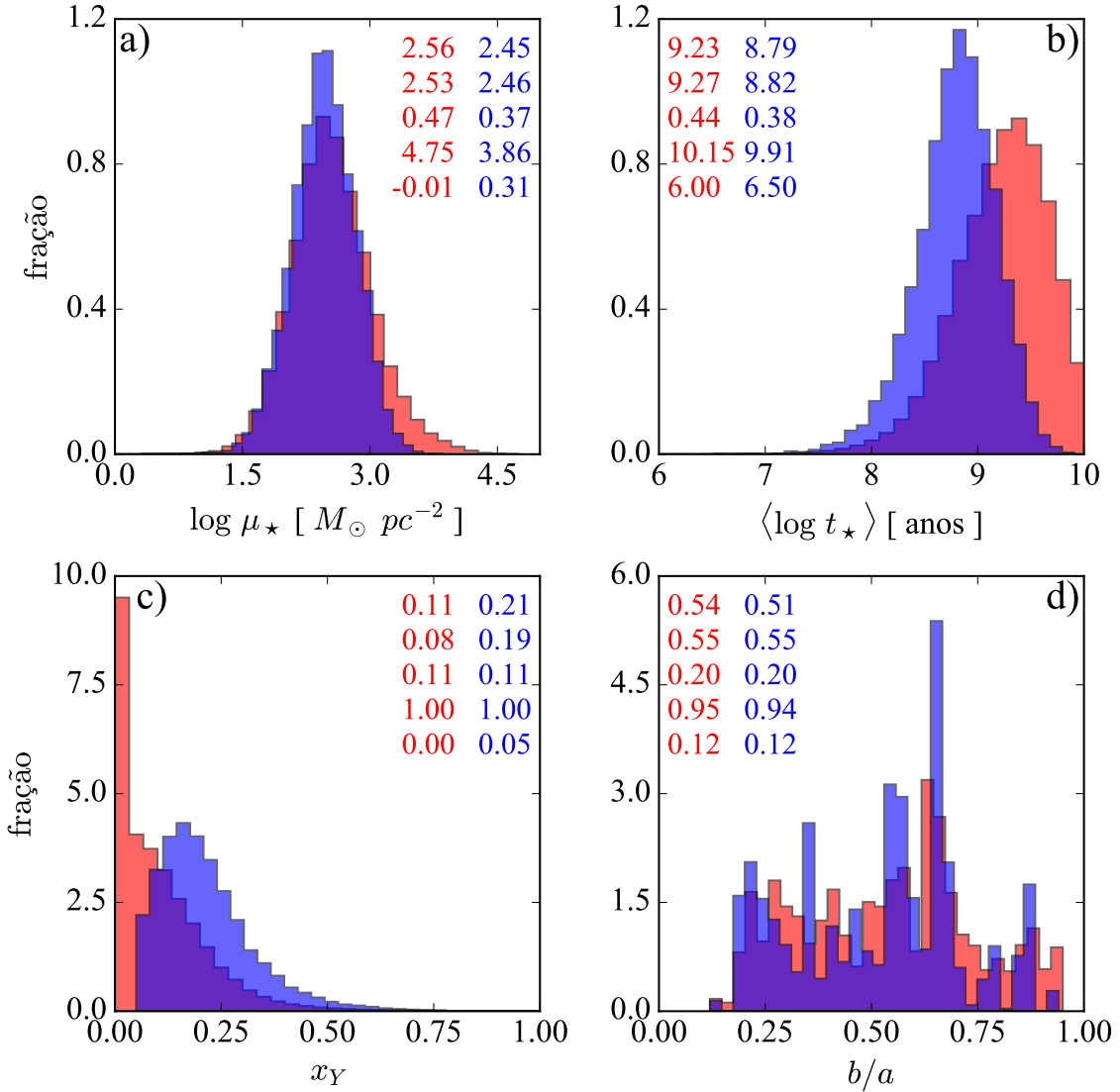


Figura 3.1: Histogramas da densidade superficial de massa (*painel a*), idade média das populações estelares (*painel b*), fração de populações jovens (*painel c*) e relação axial (*painel d*). Em vermelho temos a distribuição de valores de 226176 regiões em 305 galáxias e, em azul, a de 16525 zonas de 184 galáxias resultantes da seleção. Em cada gráfico temos os valores da média, mediana, desvio padrão, máximo e mínimo de cada distribuição.

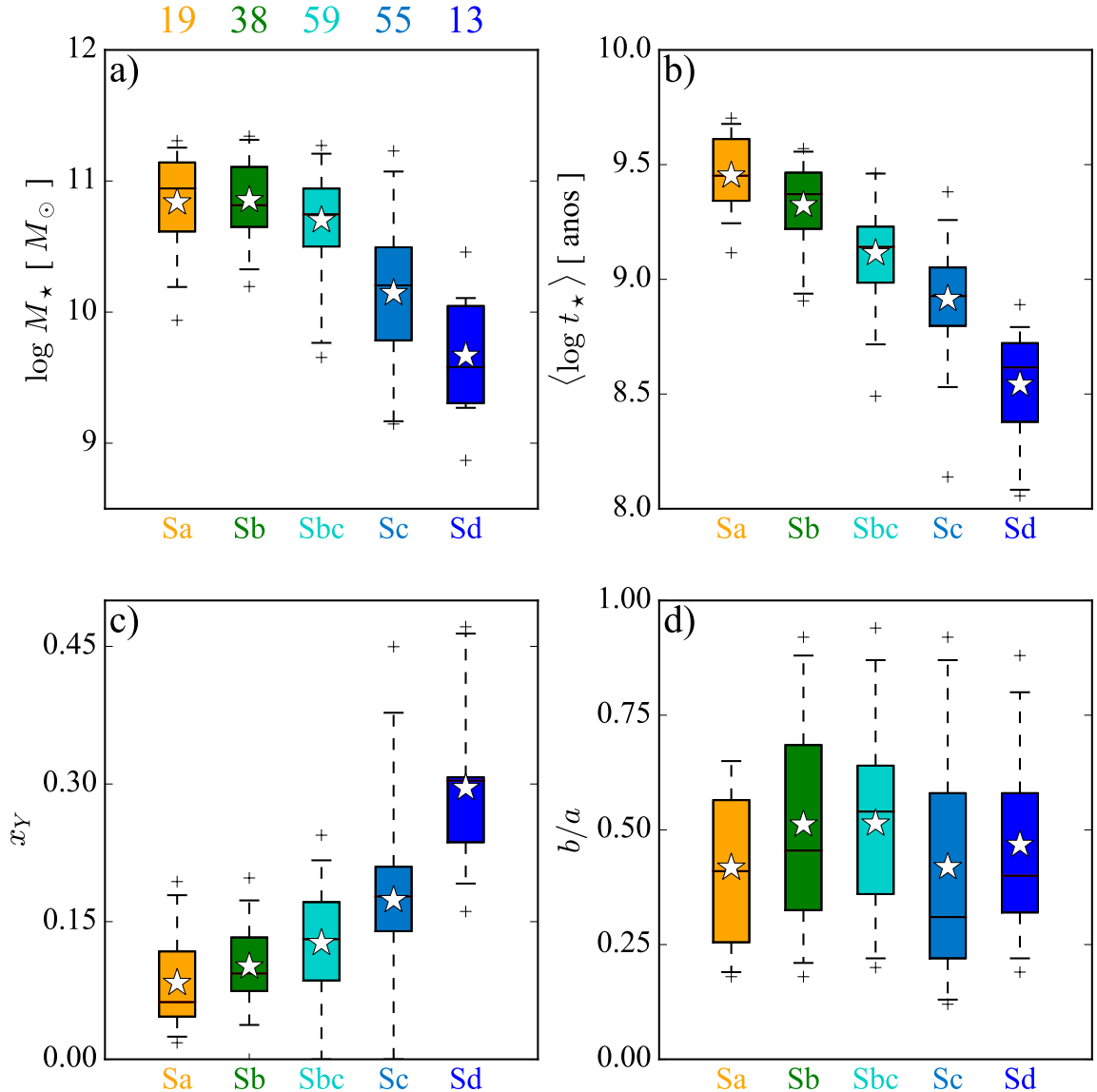


Figura 3.2: Algumas propriedades separadas em classes morfológicas. Massa estelar (*painel a*), idade estelar média (*painel b*), fração de luz proveniente das populações jovens (*painel c*, $x_Y \equiv x_Y(t_\star < 32 \times 10^6$ anos)) e inclinação (*painel d*) de 305 galáxias espirais da amostra observada do CALIFA. No primeiro painel, os valores que ficam fora do intervalo de 3σ são marcados por uma cruz vermelha.

formação estelar e a massa para diferentes classes morfológicas. Esse artigo já foi submetido e deve sair logo agora no início de 2016.

3.3 Perfis radiais

Uma maneira interessante de analisar galáxias é produzir perfis radiais para as propriedades físicas. Esse tipo de média azimutal (tanto em classes definidas por anéis circulares quanto em anéis elípticos) diminui o espalhamento dos pontos. Para a análise individual de cada galáxia também permite estudo da evolução das propriedades ao longo do raio. Quando colocamos todas as galáxias na mesma análise, a vantagem dos *bins* radiais vem do平衡amento da influência de cada galáxia quando analisamos todas juntas. Para que seja possível este “empilhamento” de galáxias, estas médias radiais são feitas definindo-se um raio efetivo para cada galáxia. No nosso caso utilizamos como raio efetivo aquele que comporta metade da luz da galáxia (HLR) e definimos 30 anéis com espessura de 0.1 HLR (ou seja, indo até 3 HLR) partindo do pixel central de cada galáxia.

No artigo de González Delgado et al. (2014b) os autores discutem as estruturas radiais de algumas propriedades estelares, aplicando este tipo de estudo para 107 galáxias no CALIFA. Nele são derivados os raios de metade da luz (HLR) e de metade da massa (*half-mass radius* - HMR) e deste resultado concluem que as galáxias são em geral 15% mais compactas em massa do que em luz. Também mostram que algumas propriedades, como idade estelar média, extinção por poeira e densidade superficial de massa estelar são bem representados pelo seus valores medidas a 1 HLR.

Escolhemos utilizar perfis radiais em anéis elípticos neste trabalho, calculando a média entre todas as zonas não mascaradas dentro de cana anel. Como um exemplo, podemos observar na Fig. 3.3 três exemplos de mapas e perfis radiais (x_Y , τ_V^* e τ_V^{neb}) da galáxia NGC1667 (objeto CALIFA 140). Em destaque (azul) temos o valor integrado para a galáxia. Dentro de nosso trabalho utilizamos as medidas em zonas, em perfis radiais e quando necessário, integradas (resolvendo para o disco ou para a galáxia completa), nos possibilitando portanto verificar diferenças nestes tipos de abordagens.

O perfil radial (entre 0.7 e 3 HLR) médio das principais propriedades utilizadas neste trabalho podem ser vistas na Fig. 3.4 juntamente com seus histogramas na Fig. 3.5. Elas são muito importantes em todos os aspectos que abordaremos: formação estelar, poeira e a conversão de densidade superficial de poeira em densidade superficial de gás em discos de galáxias es-

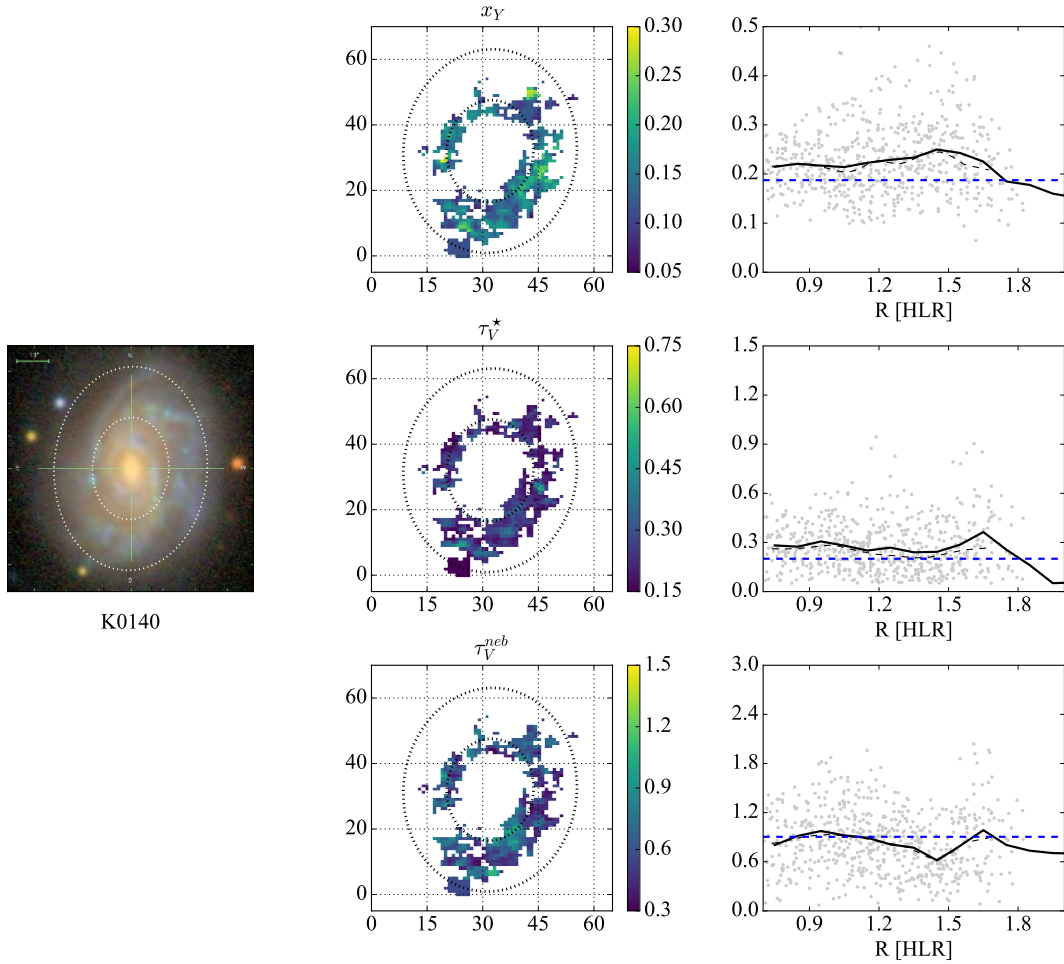


Figura 3.3: Imagem do *SDSS* da galáxia NGC1667 (CALIFA 140). Em cada fileira aparece o mapa e o perfil radial da fração de luz proveniente das populações jovens (x_Y - primeira fileira), do coeficiente de extinção resultante da síntese de populações estelares (τ_V^* - segunda fileira) e do coeficiente de extinção por decremento de Balmer (τ_V^{neb} - terceira fileira). Nos mapas duas elipses concêntricas marcam 1 e 2 HLR. Em cada gráfico do perfil radial aparece no fundo em cinza os valores para as zonas, em linha tracejada preta a mediana da distribuição ao longo do raio e em azul tracejado o valor integrado para a galáxia, além do perfil radial (linha preta contínua).

pirais. Podemos ver que existem alguns gradientes negativos (crescem de fora para dentro) bem definidos de densidade superficial da taxa de formação estelar (Σ_{SFR}), a metalicidade nebulosa, ($\log O/H$), densidade superficial de massa estelar (μ_*). Outras propriedades parecem não variar muito dentro do disco. Alguns perfis mudam de tendência ao passar de 2 HLR, mas vale ressaltar que na maioria das distribuições, os pontos acima de 2 HLR ultrapassam 1σ da distribuição. Embora não seja tão forte, existe um gradiente positivo na fração em luz de populações jovens.

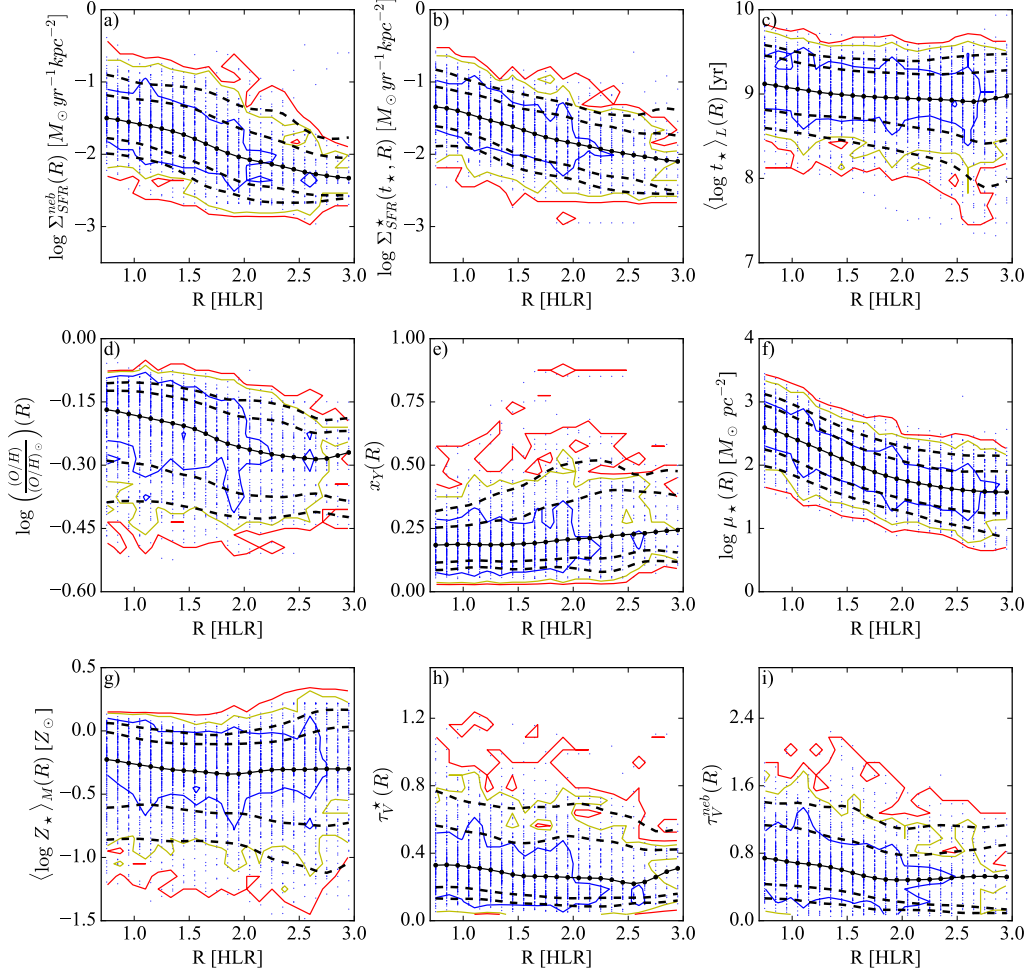


Figura 3.4: Perfis radiais médios (entre 0.7 e 3 HLR) das principais propriedades físicas abordadas neste trabalho. Densidade superficial da taxa de formação estelar detectada por $H\alpha$ e pela síntese (painéis *a* e *b*), idade média das populações estelares (painel *c*), metalicidade nebular (painel *d*), fração em luz de populações jovens (painel *e*), densidade superficial de massa estelar (painel *f*), metalicidade média das populações estelares (painel *g*), coeficiente de extinção da síntese e do decremento de Balmer (painéis *h* e *i*). Em cada painel vemos também os contornos definindo 1σ , 2σ e 3σ da distribuição. As linhas marcam a mediana (linha contínua) e os 5, 16, 64, 95 percentis (linhas tracejadas).

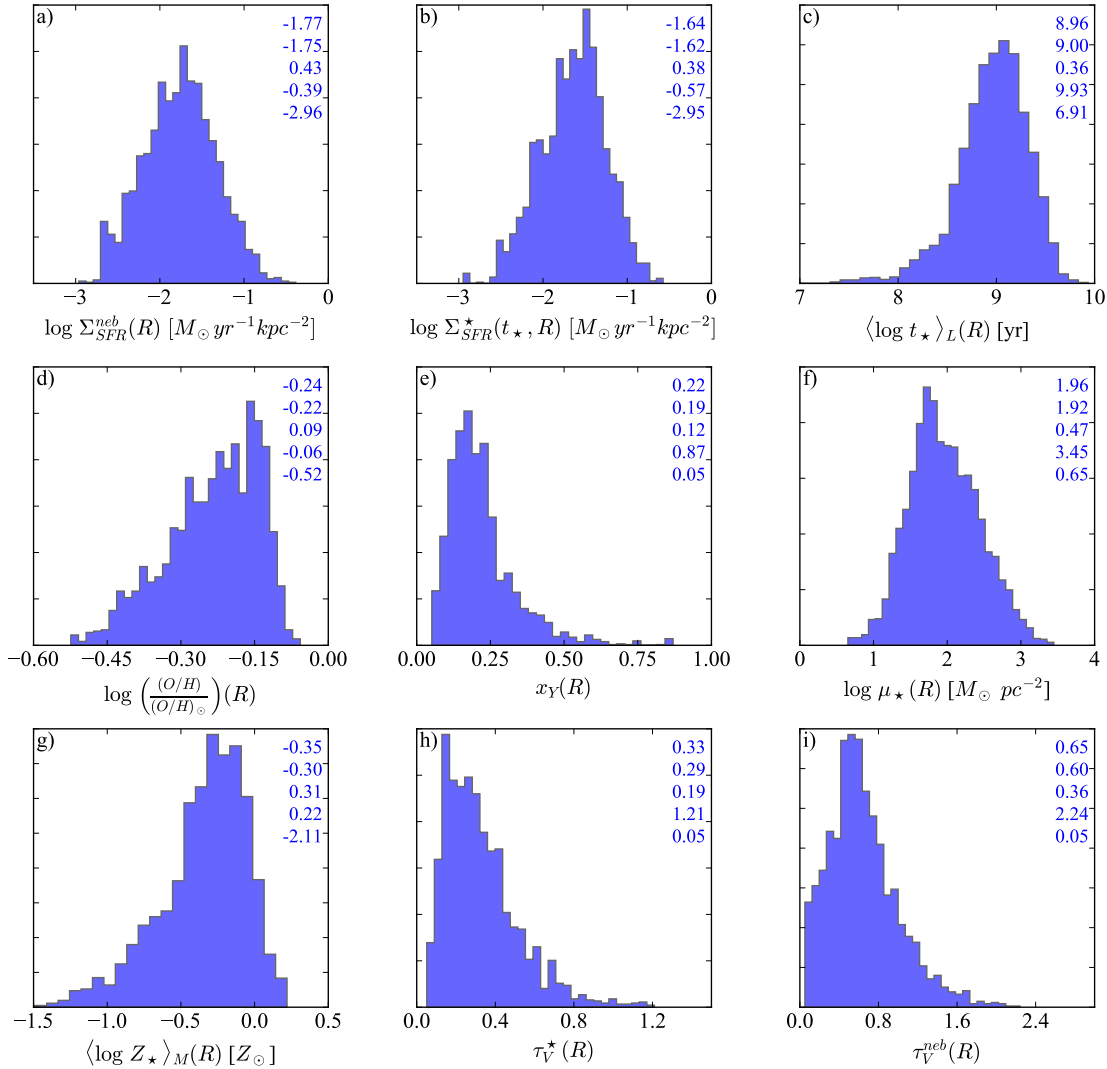


Figura 3.5: Histogramas normalizados de todas as propriedades físicas da Fig. 3.4. Os valores no canto superior direito marcam a média, mediana, desvio padrão, máximo e mínimo das distribuições.

Capítulo 4

Comparações entre propriedades estelares e propriedades nebulares

Precisamos entender as diferenças entre as propriedades que obtemos através da síntese espectral e aquelas calculadas com as linhas de emissão. As propriedades da síntese são relacionadas às populações estelares e comparações com as nebulares podem nos ajudar a entender melhor a história de formação estelar de cada região. Durante os últimos anos esses estudos cruzados entre propriedades sintéticas e nebulares de quase um milhão de galáxias do *SDSS* renderam ótimos resultados para o GAS-UFSC. Nesse capítulo faremos esse tipo de comparação utilizando as propriedades mais importantes diretamente para a conversão de poeira em gás: taxa de formação estelar, coeficiente de extinção por poeira e metalicidade.

4.1 Comparação entre as taxas de formação estelar

Com a síntese de populações estelares podemos calcular a história de formação estelar utilizando o vetor cumulativo de massa ($\eta_\star(t_\star)$), que integra a fração total de massa convertida em estrelas para cada idade das populações da base (μ_j). Então podemos calcular uma taxa de formação dentro de um intervalo de tempo:

$$\eta_\star(t_\star) = \sum_{t_{\star,j} < t_\star} \mu_j \quad (4.1)$$

$$\overline{\text{SFR}}_\star(t_\star) = M_\star \frac{(1 - \eta_\star(t_\star))}{t_\star}, \quad (4.2)$$

onde M_\star é a massa total convertida em estrelas durante toda a história de formação estelar de uma galáxia.

Como explicado na Sec. 2.2, podemos medir a taxa de formação estelar recente medindo a luminosidade intrínseca de H α . Com as duas taxas de formação estelar, uma referente às estrelas com idade menor que 10 milhões de anos e estimada pela linha de emissão de H α (2.29), outra proveniente da síntese de populações estelares, que pode ser avaliada em diferentes tempos t_\star em (4.2). Geramos diversas figuras como a Fig. 4.1 para encontrar a idade que melhor relaciona as duas medidas (aqui a chamamos de t_{SF}). Em todos os painéis vemos a comparação das duas densidades superficiais da taxa de formação estelar, em *bins* radiais, para diferentes valores de t_\star , além de um ajuste *OLS bisector* e os coeficiente de correlação de Spearman e Pearson (números abaixo da idade no canto superior esquerdo). Neste gráfico há apenas os cortes removendo as zonas aonde não há S/N suficiente nas quatro linhas do BPT. Vemos que entre 12 e 56 milhões de anos o coeficiente de correlação quase não muda, chegando ao máximo (0.7880 em 31.62 milhões de anos), ou seja, não há muita diferença escolher idades neste intervalo nessa amostra, portanto escolhemos $t_{SF} = 31.62$ milhões de anos. Escolhemos fazer este tipo de análise utilizando as correlações entre densidades superficiais pois são mais confiáveis já que removem o termo d^2 existente no cálculo da SFR, que induz uma correlação direta entre SFR_\star e $SFR_{H\alpha}$. Esse valor de t_{SF} não está muito distante da escala de tempo de vida das estrelas que produzem a maioria dos fótons capazes de produzirem a linha de H α ($\sim 10^7$ anos).

No primeiro painel da Fig. 4.2 vemos o que comentamos anteriormente sobre a pouca variação do coeficiente de Spearman no intervalo entre 12 e 56 milhões de anos. Apesar de que os cortes definidos na Sec. 3.2.1 com relação a idade e coeficiente de extinção mínimos não estão aplicados, como mencionado anteriormente, o resultado não quase não altera muito quando aplicamos os cortes. O que acontece com a aplicação da máscara é que a correlação para idades mais baixas que nosso t_{SF} escolhido aumentam e o desvio quadrático diminui. Nos painéis de baixo vemos a correlação entre as densidades superficiais da taxa de formação estelar por zonas e em *bins* radiais, calculando $\overline{SFR_\star}(t_\star)$ utilizando $t_\star = t_{SF} = 31.62$ milhões de anos. Juntamente ao ajuste *OLS* (em vermelho), adiciono um ajuste forçando que o coeficiente angular seja 1 (em azul). A comparação utilizando os *bins* radiais possuem desvio *rms* 0.390 contra 0.465 quando compararmos o ajuste *OLS*.

Este procedimento de comparação foi feito também em Asari et al. (2007), no qual os autores encontraram t_{SF} igual a 25 milhões de anos, para 82302 galáxias do *SDSS*. A síntese de populações estelares foi realizada utilizando o *STARLIGHT*, mas com uma diferente IMF. Apesar dessa diferença a concordância entre os resultados é boa.

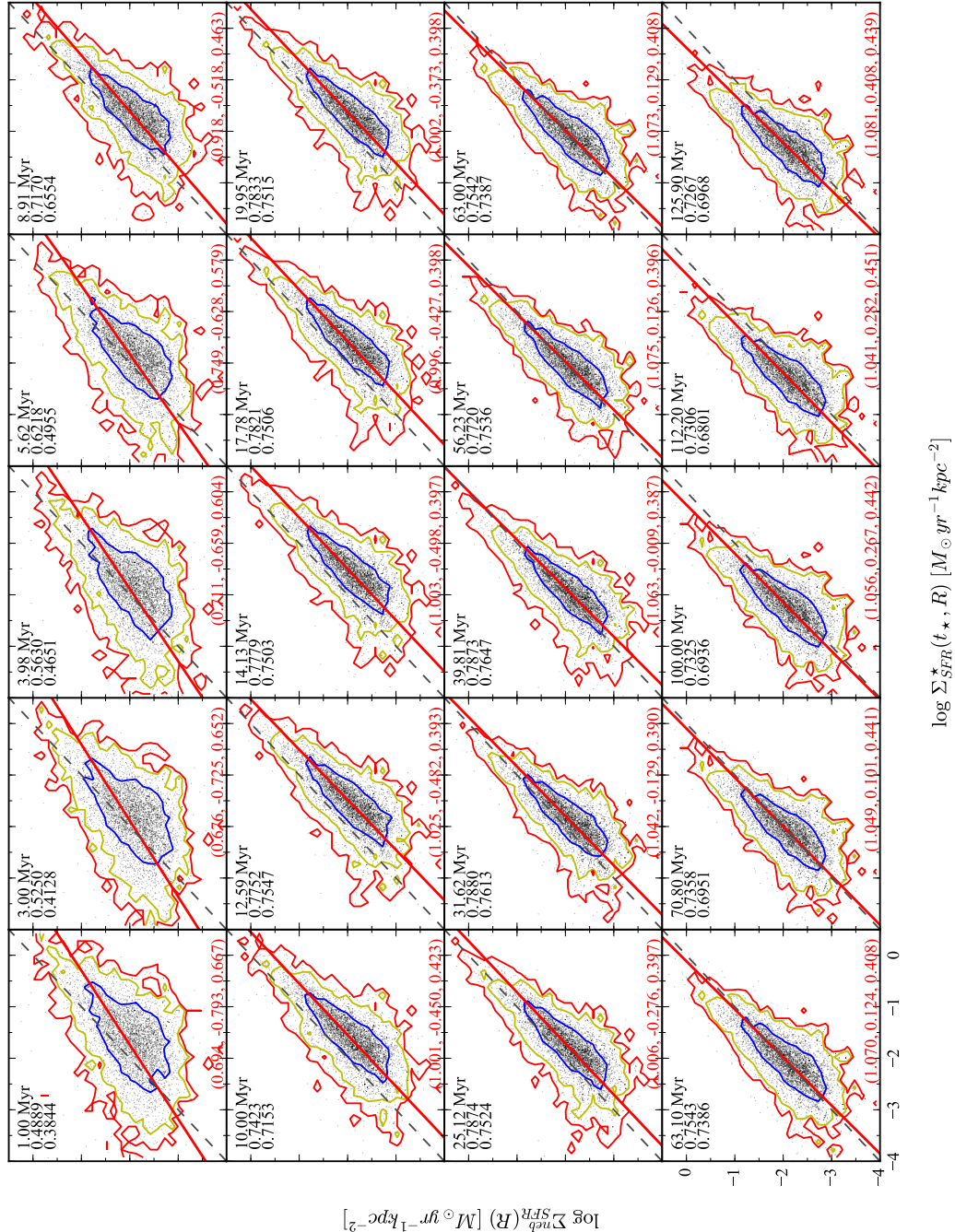


Figura 4.1: comparação das duas densidades superficiais da taxa de formação estelar em bins radiais, para diferentes valores de t_\star . Em cada gráfico temos os contornos em 1σ (azul), 2σ (verde) e 3σ (vermelho) da distribuição. A linha vermelha indica o ajuste *OLS bisector*, e os números em vermelho são o coeficiente angular, o ponto de interceptação com o eixo x e o valor *rms* em torno do ajuste. No canto superior esquerdo está indicado t_\star , o coeficiente de correlação de Spearman e o de Pearson.

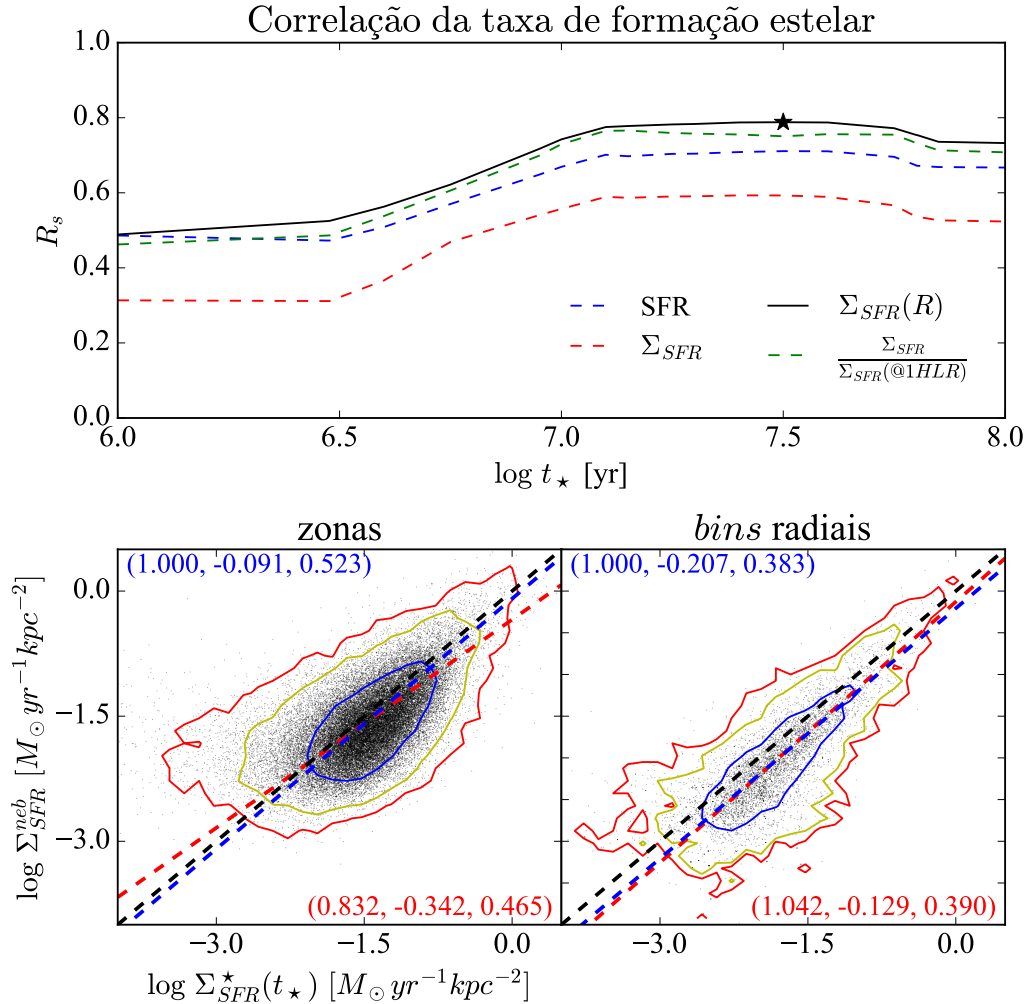


Figura 4.2: Painel superior: o coeficiente de correlação de Spearman entre as SFR para diferentes t_\star . Para cada cor temos um tipo de cálculo de SFR e em linha preta contínua temos os valores do coeficiente de Spearman para os perfis radiais de Σ_{SFR} , que possui o valor de idade que utilizamos para ser nossa escala de tempo de formação estelar (t_{SF}) (marcado por uma estrela preta). Painéis inferiores: comparação entre as densidades superficiais da SFR utilizando $t_\star = t_{SF} = 3.2 \times 10^7$ para zonas e bins radiais. Em cada painel a linha pontilhada vermelha é o ajuste linear utilizando *OLS bisector*, em azul é o ajuste forçando que o coeficiente angular seja 1 e em preto é a bissetriz ($x = y$). Os números no canto inferior direito de cada painel temos o coeficiente angular, a interceptação da reta com o eixo vertical, e a média quadráticas dos desvios em relação ao ajuste.

4.2 Comparação entre os coeficientes de extinção

A síntese de populações estelares realizadas pelo STARLIGHT adota o mesmo modelo de extinção por poeira explicado em 2.1.1, onde todas as populações são atenuadas pelo mesmo fator $e^{-\tau_A}$. Essa simplificação contraria tanto evidências observacionais quanto estudos teóricos, que caminham para um cenário onde populações mais jovens são mais atenuadas pela poeira que populações mais velhas. Calzetti et al. (1994) encontraram evidências diretas de que a extinção em regiões HII é aproximadamente duas vezes maior do que a das estrelas ($\tau_V^* \sim 0.44\tau_V^{neb}$). Charlot & Fall (2000) propõe um modelo onde populações jovens são atenuadas por poeira na nuvem de gás que a gerou e encontra que o coeficiente de extinção das *birth-clouds* (BC) é cerca de 3 vezes maior que do meio interestelar (ISM). Kreckel et al. (2013) através de dados de espectrografia de campo integrado do KINGFISH (Kennicutt et al. 2011) calculam a densidade superficial de poeira dessas galáxias e chegam a conclusão que o coeficiente de extinção derivados do contínuo estelar não correlaciona com a quantidade total de massa de poeira, diferentemente daquele derivado do decremento Balmer.

Apesar do modelo de extinção ser o mesmo, o coeficiente calculado por cada um dos procedimentos é diferente, como podemos ver através dos resultados da Fig. 4.3. Esta figura apresenta a comparação entre os coeficientes de extinção para zonas e também para os perfis radiais. O coeficiente que vem do STARLIGHT é calculado no processo de ajuste espectral, já o do decremento de Balmer representa melhor as regiões onde existem os observáveis necessários para seu cálculo, ou seja, regiões onde existam linhas de H α e H β , portanto, regiões mais jovens. Verificamos que a medida que vamos sendo mais exigentes com a fração de luz proveniente das populações jovens (x_Y), valor mínimo de τ_V^* e τ_V^{neb} , e distância radial de cada zona considerada na comparação (ver Fig. 4.4), as diferenças entre os dois coeficientes diminui, iluminando um caminho que vamos nos aprofundar um pouco melhor no próximo capítulo e que pode nos ajudar a um melhor entendimento do significado de τ_V^* .

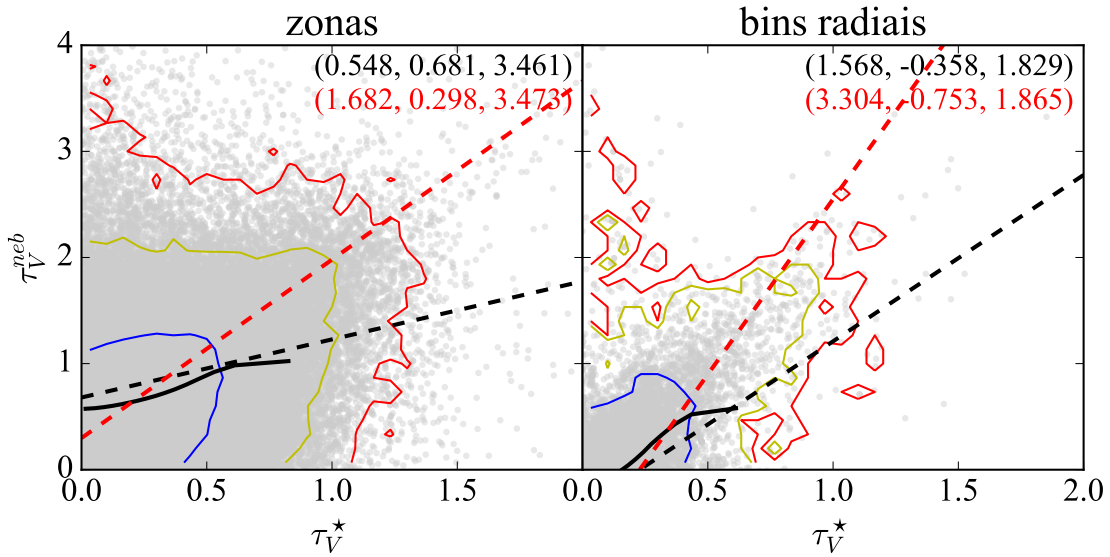


Figura 4.3: Comparação entre os coeficientes de extinção por poeira provenientes da síntese (τ_V^*) e do decremento de Balmer (τ_V^{neb}). Os contornos azul, amarelo e vermelho representam os intervalos de confiança (1σ , 2σ e 3σ). A linha preta representa a mediana e as linhas pontilhadas representam o ajuste utilizando *OLS bisector* (vermelha) e mínimos quadrados (preta). Como em todos os gráficos com ajustes lineares, em detalhe temos o coeficiente angular, a interceptação da reta com o eixo vertical, e a média quadráticas dos desvios em relação a cada ajuste. Este gráfico não possui a máscara da definição da amostra aplicada.

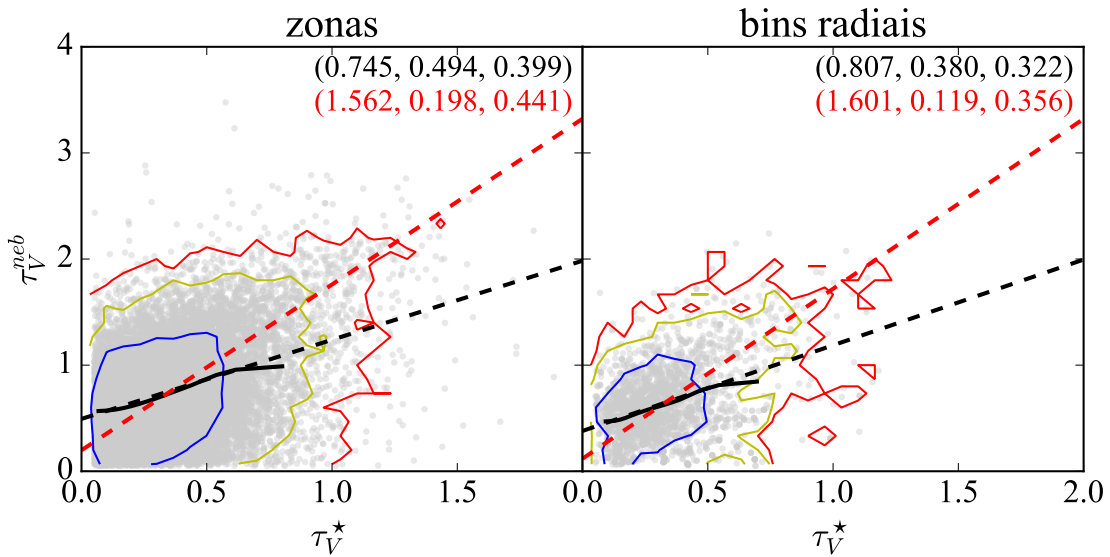


Figura 4.4: Igual a Fig. 4.3 mas com a aplicação dos cortes definidos em 3.2.1.

4.3 Comparação entre as metalicidades

4.3.1 Metais em galáxias - $\langle \log Z_\star \rangle_M$ e $\log(O/H)$

Como citado em 2.1.2, com a calibração de M13 temos a metalicidade nebular para aquelas regiões aonde temos medidas para todas as linhas envolvidas no processo ($H\beta$, [O III], $H\alpha$ e [N II]). A metalicidade estelar para cada pixel (par x, y) é calculada segundo a equação:

$$\langle \log Z_\star \rangle_{M,xy} = \frac{\sum_{tZ} M_{\star,tZ,xy} \times \log Z}{\sum_{tZ} M_{\star,tZ,xy}}. \quad (4.3)$$

onde $M_{\star,tZ,xy}$ representa a massa em estrelas com idade t e metalicidade Z no pixel xy .

Na Fig. 4.5 vemos em detalhe a comparação entre as metalicidades estelar e nebular para os perfis radiais e das galáxias de nossa amostra. A comparação entre essas duas propriedades deve ser analisada com cuidado, porque estamos tratando de coisas bem diferentes derivadas de maneira completamente diferente, todavia a correlação existe e já foi identificada por diversos artigos (Cid Fernandes et al. 2005; Gallazzi et al. 2005; Cid Fernandes et al. 2007; Asari et al. 2007). Stasińska et al. (2006) enfatiza que esse método de derivação de metalicidade nebular utilizando *strong-line methods* são calibrados geralmente em gigantes regiões HII, portanto ainda são necessários estudos sobre os gradientes de metalicidades dentro de galáxias. Ainda sim, vejo uma boa correlação entre as duas medidas. Os valores para zonas possuem muito espalhamento, mas quando verificamos os valores os perfis radiais (e também os valores integrados, embora aqui não demonstrados) vemos que existe uma boa correlação entre as duas com um espalhamento pequeno (em todos os *bins* menor que 0.2 dex). Vemos também que temos uma tendência para que populações na parte mais interna do disco possuam metalicidades mais altas que nas partes externas. Essa discussão é muito interessante e precisa ser muito desenvolvida, mas não faz parte dessa nossa primeira etapa. Entretanto, a conversão de poeira para gás deve ser dependente de metalicidade, portanto, o tema surgirá nas próximas etapas deste trabalho.

4.3.2 Artigo - Insights on the Stellar Mass-Metallicity Relation from the CALIFA Survey.

No artigo de González Delgado et al. (2014a) (GD14 daqui em diante), cuja versão completa está no apêndice A.2, analisamos a relação entre massa estelar (M_\star - efeitos globais)

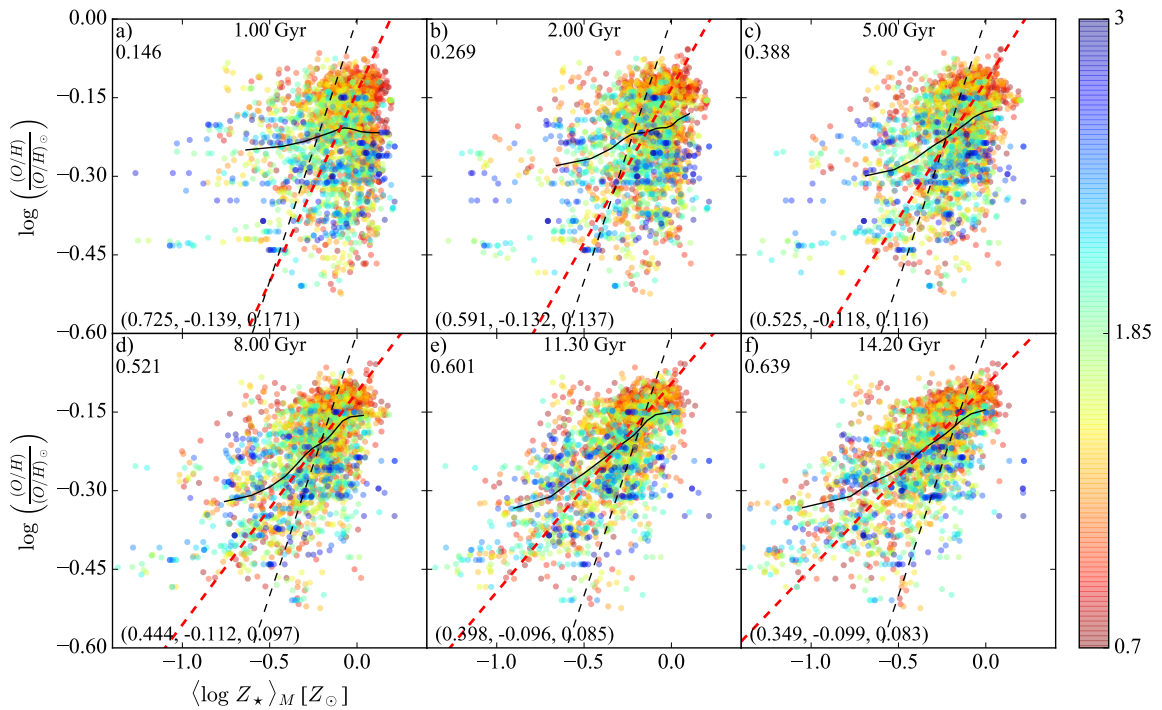


Figura 4.5: Comparação entre a metalicidade do gás ($\log (O/H)$) e metalicidade média das populações estelares ($\langle \log Z_\star \rangle_M$) calculada para diferentes intervalos de tempo (1, 2, 5, 8, 11.3 e 14.2 bilhões de anos). Em cada gráfico em vermelho o *OLS bisector* e a bissetriz em preto. Novamente em detalhe o coeficiente angular, a interceptação da reta com o eixo vertical, e a média quadráticas dos desvios em relação ao ajuste.

e a densidade superficial de massa estelar (μ_\star - efeitos locais) com a metalicidade estelar ($\langle \log Z_\star \rangle_M$) de uma amostra de 300 galáxias do CALIFA de todos os tipos morfológicos (desde E a Sd). Tremonti et al. (2004) investigam a mesma relação, embora para a metalicidade do gás (Z_{neb}) e apenas para galáxias SF. Essa relação é conhecida como relação massa-malicidade (*mass-metallicity relation - MZR*). Verificamos que a MZR estelar é mais inclinada e se estende em um intervalo muito maior comparando com aquela utilizando a metalicidade do gás pois esta última nos fornece informações sobre o estado atual do gás e a primeira, sobre toda a história de formação estelar da galáxia.

Sánchez et al. (2013) analisa essa relação para ~ 3000 regiões HII mapeadas em 150 galáxias do CALIFA. Comparando nossos resultados com os obtidos por Sánchez et al. (Fig. 2b em GD14) nestas regiões vemos que eles se distanciam conforme M_\star diminui. Após calcularmos a metalicidade estelar considerando apenas populações jovens ($t_\star \leq 2$ bilhões de anos) vemos que o resultado se aproxima melhor da tendência para as regiões HII.

Utilizando nossa amostra, vemos na Fig. 4.6 a relação entre a densidade superficial de massa estelar e a metalicidade nos três painéis de cima (zonas, anéis elípticos e galáxias integradas) e, na mesma sequência, temos a comparação entre a metalicidade nebular e estelar. Em cada gráfico aparecem as medianas para as metalicidades estelares calculadas para diferentes intervalos de idades (de 1 a 14 bilhões de anos) de modo a ilustrar a sequência de evolução química inferida a partir da síntese. A figura nos mostra que para mesmos valores de μ_\star a metalicidade estelar é mais alta para as estrelas mais jovens, o que parece ser um resultado coerente imaginando que o meio onde as novas estrelas nascem vai enriquecendo quimicamente com o passar do tempo, fazendo com que novas estrelas tenham maior metalicidade. A metalicidade nebular (marcada com uma linha tracejada preta) parece ser muito menos sensível às regiões mais massivas do que a metalicidade estelar. Zahid et al. (2014), analisando galáxias com $z \lesssim 1.6$, argumentam que esse achamento acontece quando $M_\star \gg M_{\text{gas}}$ ($f_{\text{gas}} \rightarrow 0$; ver Eq. 6.1), assim a quantidade de oxigênio presa dentro das estrelas (*lock-up fraction*) de baixa massa é da ordem daquela produzida pelas estrelas de alta massa. Os modelos de evolução química evoluíram bastante nos últimos anos (e.g., Lilly et al. 2013; Peng & Maiolino 2014; Ascacíbar et al. 2015; Peng et al. 2015) e esperamos que logo tenhamos melhores resultados nessa área. O tema é muito interessante e tem muito ainda a ser explorado, principalmente quanto aos efeitos locais, quando analisamos esta relação internamente nas galáxias e seus efeitos em parâmetros globais. Sobre o painel abaixo, o que vemos é que a variação da metalicidade estelar é muito maior do que a nebular e a correlação entre ambas vai aumentando à medida que vamos de zonas para galáxias integradas. O painel inferior central condensa todos os painéis da Fig. 4.5.

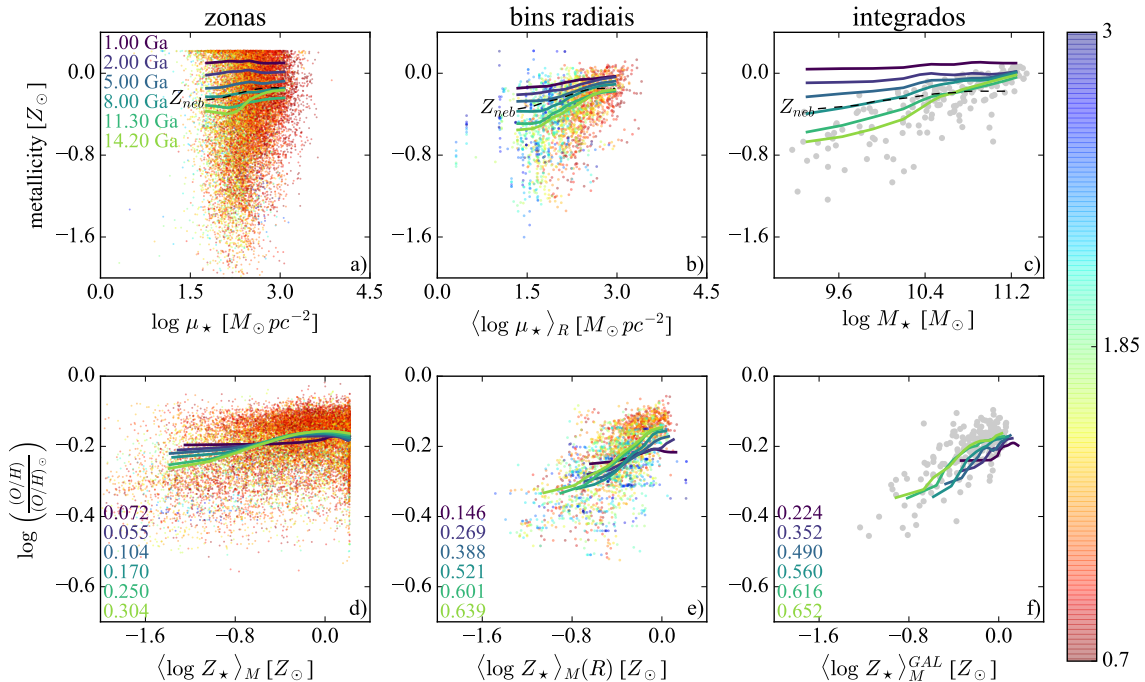


Figura 4.6: Relação μZR para zonas (painedel a), bins radiais (painedel b) e galáxias integradas (painedel c). Os pontos desenhados em cada gráfico representam $\langle \log Z_\star \rangle_M$ calculado para todas as populações com distintas idades, coloridos pela distância radial (barra de cores em HLR). Cada gráfico possui a mediana da distribuição de $\langle \log Z_\star \rangle_M$ para diferentes intervalos de população ($t_\star \leq 1, 2, 5, 8, 11.3$ e 14.2 bilhões de anos), além da mediana para Z_{neb} ($\log(O/H)$). Comparação $\langle \log Z_\star \rangle_M$ e Z_{neb} seguindo a mesma configuração acima (zonas (painedel d), raio (painedel e) e integrados (painedel f)) com as medianas por diferentes intervalos de população no cálculo de $\langle \log Z_\star \rangle_M$ também. Seguindo o mesmo padrão de cores para as medianas, abaixo de cada gráfico vemos o coeficiente de correlação de Spearmann entre $\langle \log Z_\star \rangle_M$ e Z_{neb} .

4.3.3 Artigo - The CALIFA Survey across the Hubble sequence. Spatially resolved stellar population properties in galaxies

Durante o tempo que estive no IAA tive participação em dois artigos. O segundo deles (González Delgado et al. 2015) (em anexo, A.3) é um artigo onde resolvemos espacialmente as propriedades estelares baseados na síntese com o STARLIGHT para 300 galáxias do CALIFA entre todos os tipos morfológicos. Verificamos que as galáxias mais massivas são mais densas, velhas, mais ricas em metais e menos extinguidas por poeira. Discutimos algumas como as propriedades se comportam em partes distintas da galáxia (bojo e disco) e o quanto essas propriedades variam quando dividimos em classes de massa, idade e tipo morfológico. Galáxias do tipo Sb-Sbc possuem gradientes de $\langle \log Z_\star \rangle_M$ compatíveis com aqueles medidos para a Via Láctea. Galáxias tipo Sc possuem gradientes mais planos, nos mostrando que a evolução química do disco contribui bastante com a evolução química das galáxias desta classe morfológica. Em uma visão geral, concluímos que o processo de parada de formação estelar¹ é geralmente independente da massa total da galáxia, enquanto metalicidade e a estrutura física da galáxia são influenciadas por processos que são dependentes da massa.

¹Geralmente conhecido como *quenching*.

Capítulo 5

Extinção diferencial

O objetivo deste trabalho é conseguir estimar fração de gás para nossas galáxias do CALIFA através da conversão de poeira em gás explorando uma conversão do tipo da Eq. 1.2. Para isso vamos tentar entender melhor a diferença entre os coeficientes de extinção por poeira adotados, realizando um procedimento parecido e fazendo algumas comparações com um estudo de nosso grupo de populações estelares, que ainda está para ser publicado, sobre extinção diferencial em galáxias do *SDSS*. Este estudo sobre extinção diferencial nas galáxias do *SDSS* é parte da tese de Marielli de Souza Schlickmann.

5.1 Estudo empírico

De maneira a explorar as diferenças entre os coeficientes de extinção, identificamos duas variáveis que nos ajudarão nesse processo:

$$\mathcal{D}_\tau \equiv \tau_V^{\text{neb}} - \tau_V^\star \quad (5.1)$$

$$\mathcal{R}_\tau \equiv \frac{\tau_V^{\text{neb}}}{\tau_V^\star} \quad (5.2)$$

5.1.1 Comparação direta entre os coeficientes

Neste capítulo (e nos seguintes) nos atemos em uma discussão utilizando perfis radiais. Na Fig. 5.1 vemos a comparação direta entre os coeficientes, juntamente com os histogramas de \mathcal{D}_τ e \mathcal{R}_τ . O primeiro painel mostra a comparação entre os coeficientes como na Fig. 4.4 para

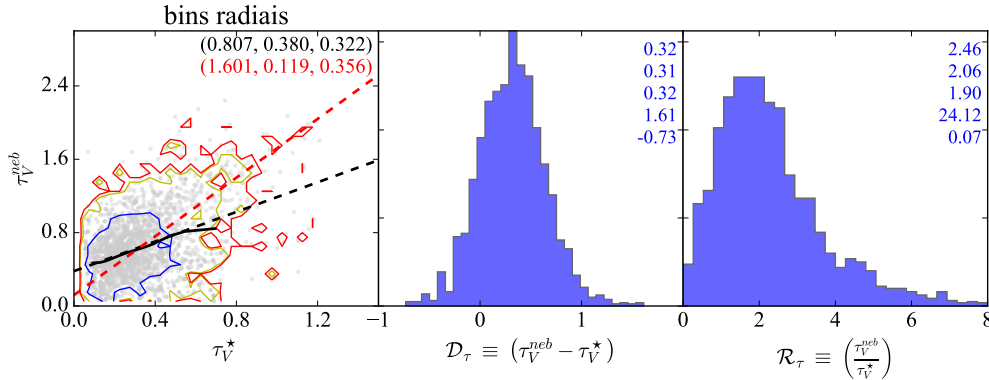


Figura 5.1: Painel esquerdo: Igual ao painel superior direito da Fig. 4.4. Painel central e direito: histogramas normalizado de \mathcal{D}_τ e \mathcal{R}_τ . Os valores no canto superior direito marcam a média, mediana, desvio padrão, máximo e mínimo das distribuições.

perfis radiais. Os dois histogramas são de \mathcal{D}_τ e \mathcal{R}_τ . Os valores da mediana (média) de \mathcal{D}_τ são 0.31 (0.32) e de \mathcal{R}_τ , 2.06 (2.46) e ambos mostram claramente a existência de uma extinção diferencial. Esse resultado aparece da mesma forma para zonas e para as galáxias integradas. No trabalho de Marielli (com 107231 espectros de galáxias integradas do SDSS-DR7) cabe lembrar que a síntese de populações estelares foi feita apenas para espectros integrados e com diferentes base de populações estelares e IMF, além do intervalo de normalização ser feito em uma janela diferente, portanto, alterando também o resultado de x_Y ; ainda sim encontramos valores que evidenciam o mesmo fenômeno e que servem de base para a discussão.

5.1.2 O papel de x_Y e de b/a

Pela relação entre os coeficientes vemos que há um espalhamento notável, entretanto, parece óbvio que a extinção diferencial existe. Ao estudar algumas propriedades, galáxia por galáxia, vimos que existe uma relação interessante entre as variáveis que criamos aqui (\mathcal{D}_τ e \mathcal{R}_τ), a fração de populações jovens (x_Y) e também a relação axial da galáxia (b/a). A primeira pela fato que relaciona regiões onde existam populações mais jovens, ou seja, mais relacionadas a regiões formadoras de estrelas, ajudando-nos a quebrar um pouco nessa ambiguidade nos valores de τ_V^* e a última pelo fato de afetar diretamente a forma de modelar a extinção por poeira.

Para utilizar a relação axial vamos fazer uma pequena correção para a projeção do disco

no plano do céu:

$$\varphi = \cos i = \begin{cases} \sqrt{\frac{(b/a)^2 - (0.13)^2}{1 - (0.13)^2}}, & \text{se } b/a > 0.13 \\ 0.05, & \text{se } b/a \leq 0.13 \end{cases} \quad (5.3)$$

onde i é o ângulo de inclinação da galáxia e 0.13 é o valor da relação axial intrínseca de uma galáxia mais frontal possível (*edge-on*). Valores com $b/a \leq 0.13$ recebem o valor da menor inclinação de nossa amostra (0.05) ao invés de 0 para não haver problemas matemáticos futuros. Esse é um refinamento que altera levemente o valor de b/a e praticamente só afeta as galáxias com $b/a < 0.4$.

Na Fig. 5.2 vemos como \mathcal{D}_τ se relaciona com φ e x_Y . Nos painéis a e c vemos as distribuições, e nos b e d vemos as medianas para diferentes classes da variável cruzada, isto é, distribuição contra x_Y com os pontos divididos em classes de φ e distribuição contra φ em classes de x_Y . É clara a tendência de $\mathcal{D}_\tau \rightarrow 0$ quando $x_Y \rightarrow 1$. Pelo painel a vemos que apesar da existência de uma anticorrelação entre \mathcal{D}_τ e x_Y , existe um espalhamento considerável. Dividimos nossa amostra em classes de φ e parece não haver dependência (painel b). Nos painéis c e d exploramos a relação \mathcal{D}_τ e φ . \mathcal{D}_τ não parece haver dependência com φ mas quando dividimos a amostra em classes de x_Y vemos que se confirma a anticorrelação.

Repetimos esse mesmo experimento para \mathcal{R}_τ na Fig. 5.3. Observando a mediana parece que $\mathcal{R}_\tau \rightarrow 1$ quando $x_Y \rightarrow 1$, com uma $\mathcal{R}_\tau \rightarrow 3 \sim 4$ quando $x_Y \rightarrow 0$. Vemos pelo painel d que a anticorrelação com x_Y segue, mas olhando o b vemos que parece haver um pequeno afastamento entre as medianas da distribuição quando dividimos nessas classes de φ . Esse resultado não é evidente quando olhamos o painel c . Quando fazemos o mesmo gráfico para as galáxias do SDSS esse resultado é muito mais evidente (Figs. 5.4 e 5.5), aparecendo uma correlação entre \mathcal{R}_τ . Em primeira estância creio que isso se deve ao poder da estatística dos dados do SDSS. Nossa estudo com valores integrados peca por estatística, pois temos apenas 184 pontos.

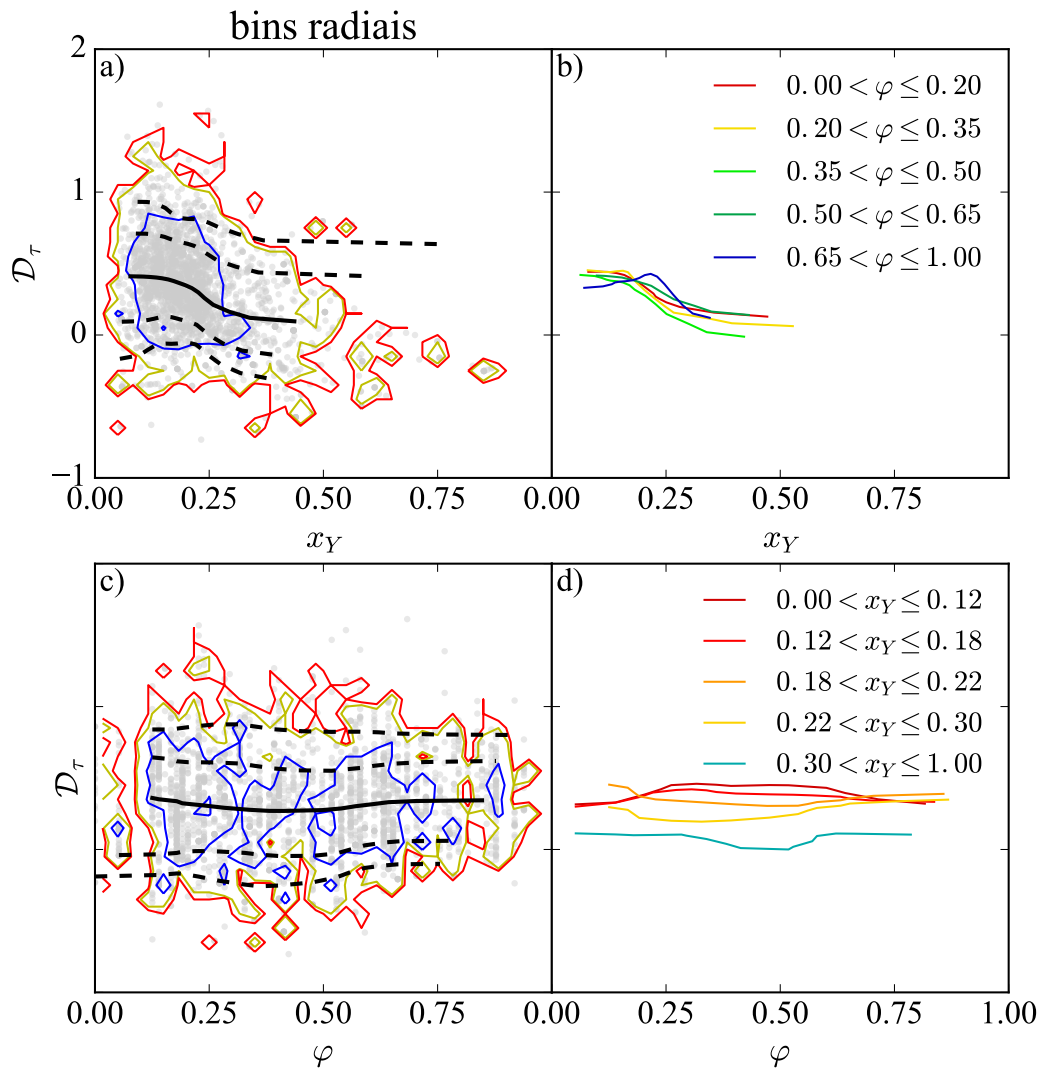


Figura 5.2: Painel a: \mathcal{D}_τ versus x_Y para nossa amostra. Os contornos definem 1 σ , 2 σ e 3 σ da distribuição. As linhas marcam a mediana (linha contínua) e os 5,16,64,95 percentis (linhas tracejadas). Painel b: as medianas da mesma distribuição quando dividimos nossa amostra em classes de φ . Os intervalos são criados para que contenham praticamente o mesmo número de pontos. Painel c: igual ao a mas versos φ . Painel d: igual ao b mas com a amostra dividida em classes de x_Y .

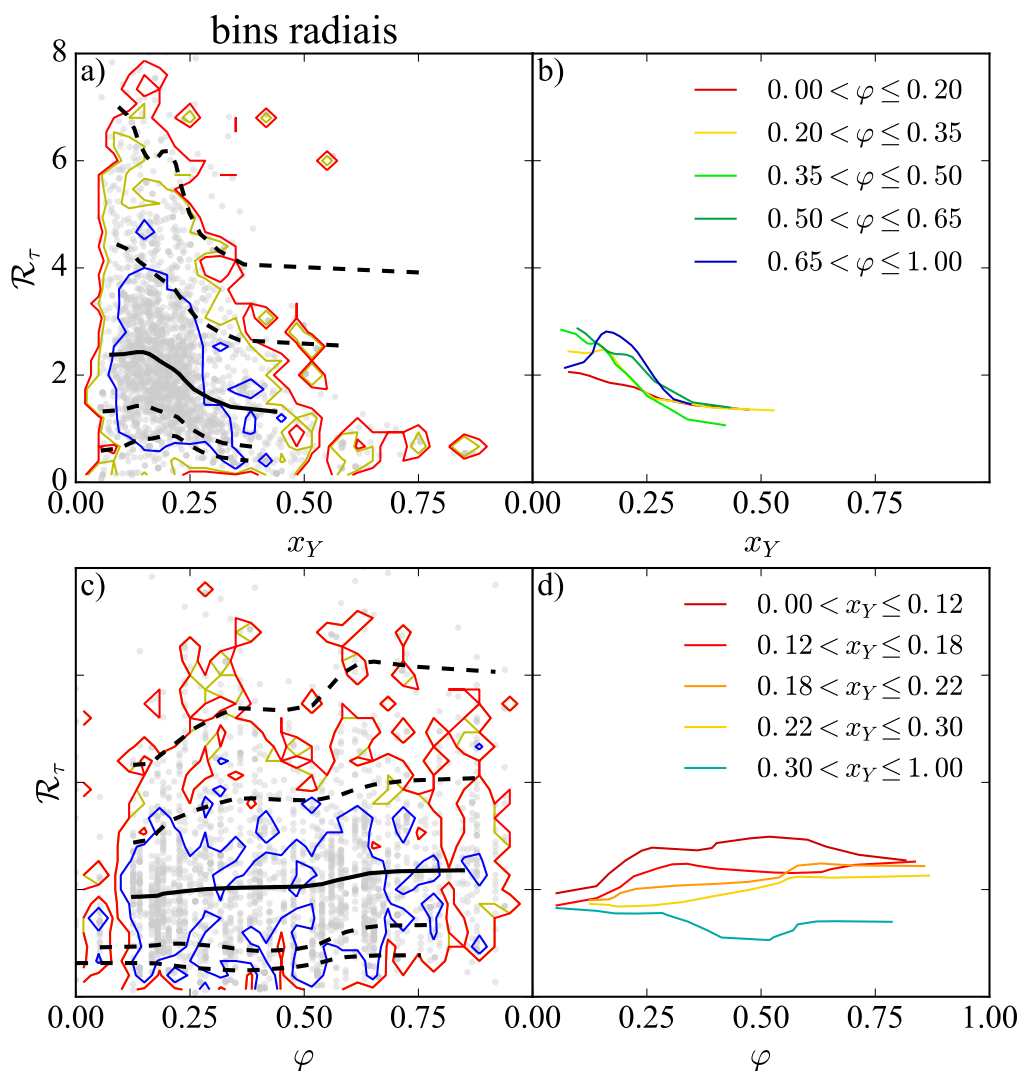


Figura 5.3: Igual a Fig. 5.2 mas com \mathcal{R}_τ .

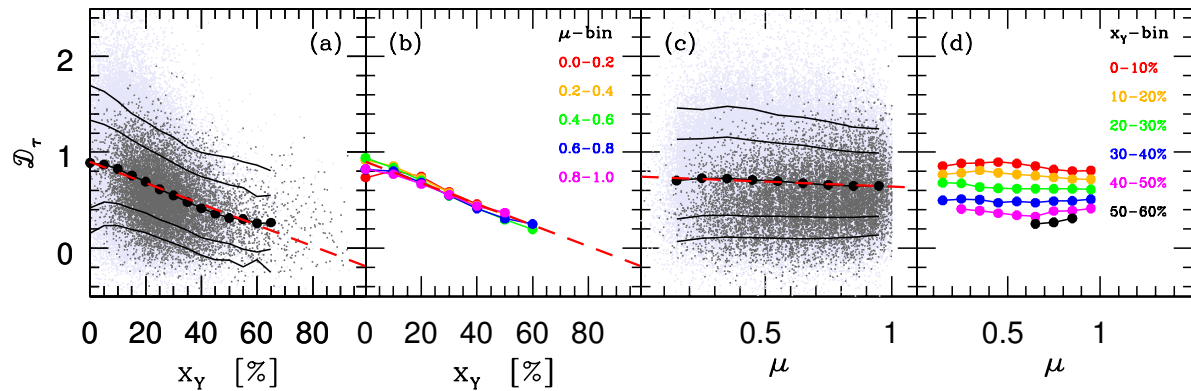


Figura 5.4: Igual a Fig. 5.2 mas para os dados do SDSS.

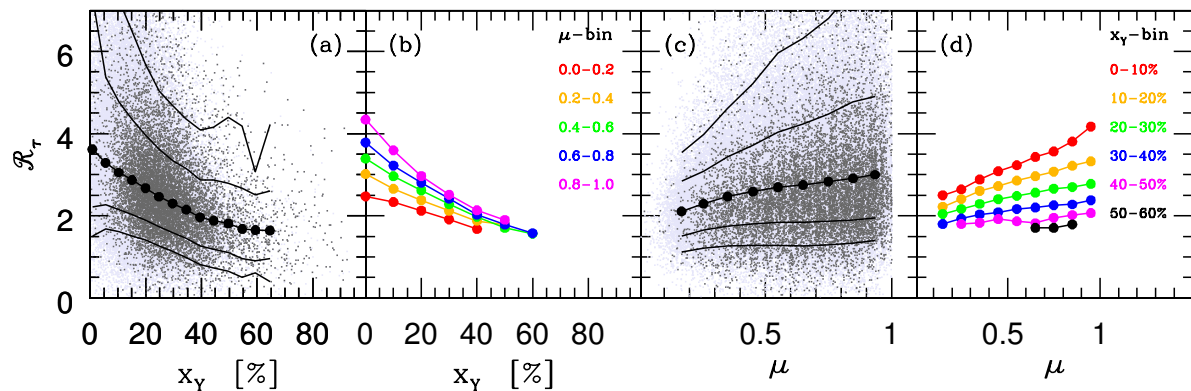


Figura 5.5: Igual a Fig. 5.3 mas para os dados do SDSS.

5.2 Modelagem e interpretação

Com esse cenário criado até agora neste capítulo, parece ser óbvio que x_Y é fundamental em nossa interpretação da extinção diferencial. O resultado da correlação entre \mathcal{R}_τ e φ não parece ser tão forte localmente quanto para valores integrados pois ele aparece muito melhor quando olhamos para a amostra do *SDSS*. Seguiremos aqui assumindo essa na linha de interpretação do trabalho de extinção diferencial nas galáxias do *SDSS*. Essa diferença esperamos discutir em um futuro próximo e entra na lista de coisas para fazer, portanto nesta seção vou apresentar o modelo proposto na tese de Marielli e utilizar a mesma modelagem com nossos dados.

5.2.1 O modelo

Segundo tudo que vimos até agora, nosso modelo deve levar em conta que a luz proveniente das populações jovens são atenuadas de maneira mais intensa que o meio interestelar. Além disso, deve levar em conta que existe algum tipo de relação entre a razão entre os coeficientes seja afetada diretamente pelo ângulo de inclinação da galáxia. Apesar de aqui estarmos utilizando $t_{SF} = 32$ milhões de anos, tanto na tese de Marielli quanto no artigo de Charlot & Fall (2000) são consideradas jovens todas as populações com idade menor que 10 milhões de anos. A interpretação da influência de φ foi relacionada a diferença entre geometria das regiões HII e a da galáxia. As estrelas jovens, assim como as velhas, possuem atenuações semelhantes a do ISM dos discos galáticos, mas as populações jovens possuem também a poeira de suas *birth clouds*. Ou seja, se modelarmos as regiões HII como esfericamente simétricas, o coeficiente de extinção não deve se alterar quando mudamos a linha de visada entre o observador e a galáxia. Já para o ISM parece se alterar bastante, portanto a razão entre os coeficientes deve se alterar no mesmo passo que a inclinação se altera. Na Fig. 5.6 fica melhor explicado.

Essa figura juntamente com as considerações acima nos levam a identificar um coeficiente de extinção para as populações jovens e outro para as velhas da seguinte maneira:

$$\tau_O = \frac{\tau_{ISM}}{\varphi} \quad (5.4)$$

$$\tau_Y = \frac{\tau_{ISM}}{\varphi} + \alpha \tau_{BC} \quad (5.5)$$

onde α entra para corrigir as possíveis diferenças entre a extinção para as populações jovens e para as suas regiões HII associadas.

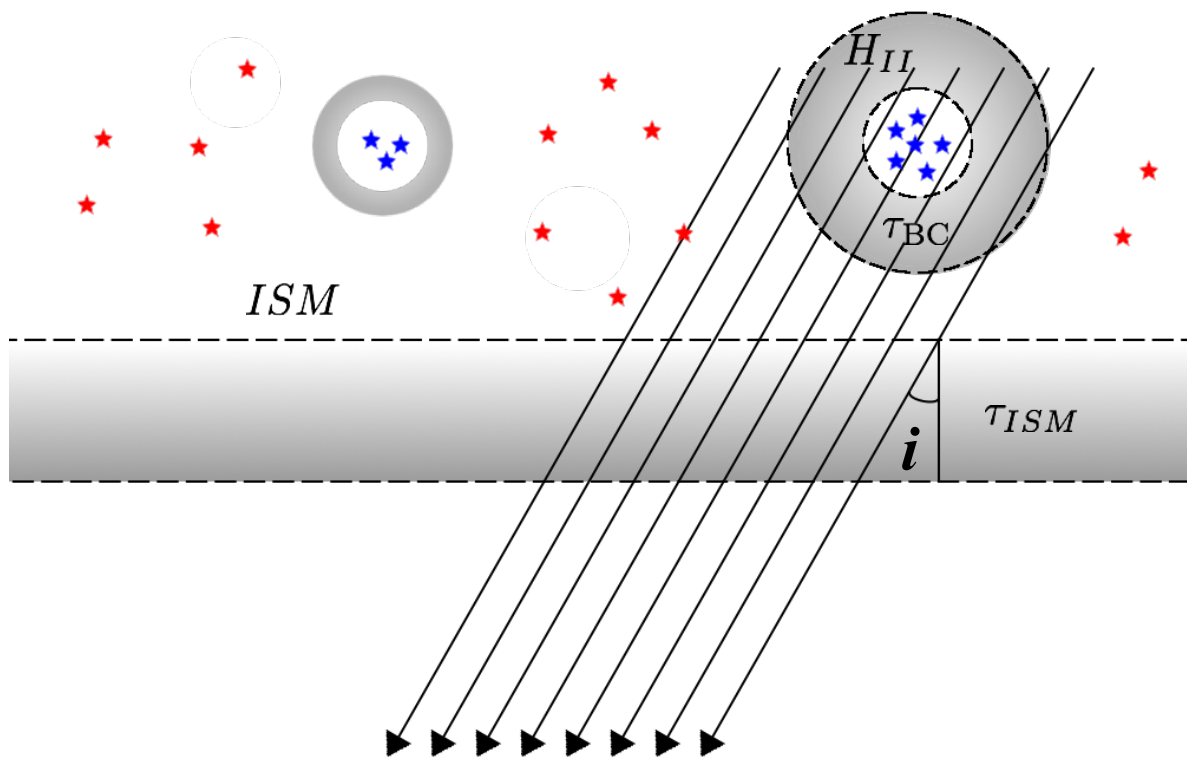


Figura 5.6: Figura mostrando o modelo criado. As setas apontam para o observador. São indicados também o ângulo de inclinação da galáxia, assim como as regiões que delimitam τ_{BC} e τ_{ISM} . Estrelas azuis significam estrelas jovens e vermelhas estrelas velhas. As camadas de poeira estão pintadas em cinza.

Para relacionar essas variáveis com nossos observáveis, começamos identificando τ_Y como τ_V^{neb} . Como comentamos na Sec. 4.2 x_Y parece funcionar distribuindo os pesos entre τ_O e τ_Y na interpretação de τ_V^* , assim, podemos aproximar τ_V^* como:

$$\tau_V^* \approx \tilde{\tau} \equiv x_Y \tau_Y + (1 - x_Y) \tau_O. \quad (5.6)$$

Com essa última equação fechamos nosso sistema e podemos escrever equações para τ_{ISM} e τ_{BC} , além de trazer uma interpretação para o real significado de τ_V^* . Trabalhando com (5.5), (5.5) e (5.6) e identificando $\tau_Y = \tau_V^{\text{neb}}$ obtemos:

$$\tau_{\text{BC}} = \frac{\tau_V^* - \tau_V^{\text{neb}}}{1 - \alpha x_Y} \quad (5.7)$$

$$\tau_{\text{ISM}} = \varphi \frac{\tau_V^* - \alpha x_Y \tau_V^{\text{neb}}}{1 - \alpha x_Y} \quad (5.8)$$

5.3 Próximos passos

Ainda temos muito mais a fazer nessa direção. Ainda temos que comparar este modelo com os dados para posteriormente podermos discutir as diferenças entre a aplicação deste modelo de extinção diferencial para galáxias integradas e para perfis radiais (e consequentemente, para zonas também).

5.3.1 Comparação com os dados.

O primeiro passo no sentido da comparação deste modelo proposto com os dados é identificando as nossas variáveis \mathcal{D}_τ e \mathcal{R}_τ no contexto da Fig. 5.6:

$$\mathcal{D}_\tau = (1 - \alpha x_Y) \tau_{\text{BC}} \quad (5.9)$$

$$\mathcal{R}_\tau = \frac{\varphi^{-1} \tau_{\text{ISM}} + \alpha \tau_{\text{BC}}}{\varphi^{-1} \tau_{\text{ISM}} + \alpha x_Y \tau_{\text{BC}}} \equiv \frac{1 + \alpha \varphi \rho}{1 + \alpha \varphi x_Y \rho} \quad (5.10)$$

onde $\rho = \frac{\tau_{\text{BC}}}{\tau_{\text{ISM}}}$.

Pelo histogram dessas variáveis (Fig. 5.7) vemos que o cenário de extinção diferencial persiste, com valores característicos (mediana) para τ_{BC} de 0.39 e de τ_{ISM} 0.08. A razão entre as medianas (médias) resulta em 4.9 (3.8). A mediana da razão nos leva a um valor um pouco

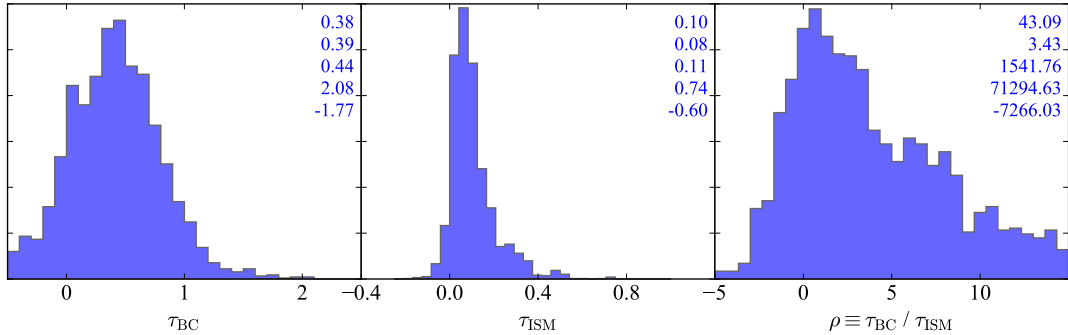


Figura 5.7: Nos três painéis vemos os histogramas de τ_{BC} , τ_{ISM} e ρ . Os intervalos se estendem para fora do gráfico, portanto, a última classe de cada histograma (em ambos os lados) contém todos os pontos que ficaram para fora. Os valores nos cantos são os mesmos encontrados em todos os histogramas deste trabalho: média, mediana, desvio padrão, máximo e mínimo.

mais baixo, 3.43, mas há espalhamento muito grande nesta variável (devido aos valores de τ_{BC} e τ_{ISM} que passam por zero).

5.3.2 Perfis radiais vs. propriedades integradas

Espectrografia de campo integrado está mudando a forma com que nós lidamos com os desafios atuais em astrofísica. Os dados de IFS do CALIFA nos possibilitam calcular como as propriedades físicas se alteram dentro de uma galáxia. Ao estudar as populações estelares quando observamos uma região de uma galáxia, ao invés de uma galáxia inteira, estamos olhando diferentes estágios de evolução química e formação estelar, inclusive com uma diferença muito maior entre os coeficientes de extinção dentro da mesma galáxia. As galáxias do CALIFA estão dentro do mesmo intervalo de redshift de forma que todas aproveitem o campo inteiro de observação, dessa forma, zonas possuem diâmetros variando entre 200pc a 1kpc. Quando temos valores integrados, estamos olhando valores que representam uma galáxia inteira (portanto uma “soma” de tudo o que acontece no bojo e no disco).

Capítulo 6

Estimando frações de gás

A fração de gás no modelo simples de evolução química (*closed-box model*) escala linearmente com a metalicidade do gás, onde a inclinação da reta é o *yield*, que representa o quanto de metais está sendo produzido e ejetado a cada geração de estrelas. Durante a pesquisa que nos levou a escrever o artigo que está no Apênd. A.2 encontramos uma relação interessante que serviu de pontapé inicial para explorarmos a conversão de poeira em gás. Nesse capítulo vamos comentar brevemente sobre nosso progresso e discutir quais os desafios enfrentados até agora e aqueles que estão por vir nas próximas etapas de nosso projeto.

6.1 Um modelo simples de evolução química

A relação da qual comentamos no preambulo deste capítulo pode ser vista na Fig. 6.1. A razão entre o coeficiente de extinção e a densidade superficial de massa estelar (A_V/μ_\star) parece relacionar de maneira interessante com a metalicidade média das populações estelares.

Podemos definir fração de gás como:

$$f_{\text{gas}} = \frac{M_{\text{gas}}}{M_\star + M_{\text{gas}}} = \frac{1}{1 + \left(\frac{M_\star}{M_{\text{gas}}}\right)} \equiv \frac{1}{1 + \left(\frac{\mu_\star}{\Sigma_{\text{gas}}}\right)} \quad (6.1)$$

onde M_{gas} é a massa total na forma de gás e M_\star é a massa total em estrelas e μ_\star e Σ_{gas} são as densidades superficiais de massa estelar e de massa de gás.

Em um modelo simples de evolução química assume-se:

- não existir nem *inflow* nem *outflow* de gás na galáxia (isolada em um sistema fechado

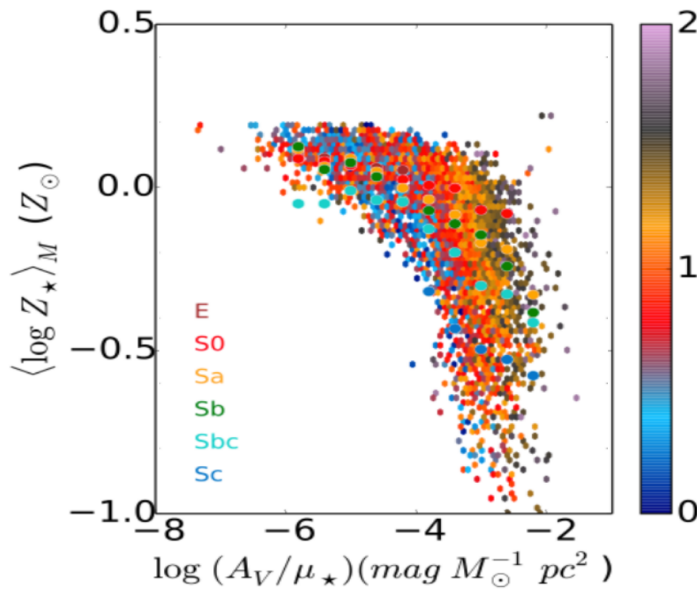


Figura 6.1: Relação entre metalicidade média das populações estelares e a razão entre o coeficiente de extinção (em magnitude) e a densidade superficial de massa estelar. Os pontos são aproximadamente 6000 bins radiais de 300 galáxias (de 0 a 2 HLR divididos em 20 bins por galáxia) e estão classificados em cores por tipo morfológico.

sem entrada nem saída de gás);

- seu gás inicial não possui metais (metalicidade inicial do sistema é zero);
- *Instantaneous Recycling Approximation* - IRA: todas as estrelas com mais de $1 M_\odot$ evoluem e morrem imediatamente e todas as estrelas com massa menor que $1 M_\odot$ vivem eternamente;
- a IMF é constante no tempo;
- o gás está sempre homogeneamente misturado.

Com estas simplificações, podemos escrever a metalicidade do gás como:

$$Z_{\text{gas}} = y \ln \left(\frac{1}{f_{\text{gas}}} \right), \quad (6.2)$$

onde y é o *yield* estelar (também conhecido como *true yield*). Invertendo (6.2) podemos definir o *yield* efetivo (y_{eff}), ou seja, aquele que um sistema teria caso se comportasse como dito modelo ao longo de toda a linha do tempo. Essa primeira equação foi derivada explicitamente pela primeira vez por Searle & Sargent (1972) ao estudar duas regiões HII gigantes, ditas “isoladas”. Garnett (2002), assumindo um *true yield* constante, calcula y_{eff} para 31 galáxias

espirais e 13 galáxias irregulares, encontrando valores distintos entre elas, o que o leva a concluir que o fluxo de gás (*outflow* e *inflow*) nestes sistemas são ambos processos muito importantes para a evolução química de uma galáxia. Tremonti et al. (2004) calculam o y_{eff} para ~ 55000 galáxias *star-forming* do SDSS, chegando a um valor de 0.0104. Ao adicionar outras medidas verifica que este valor varia em uma escala de ~ 10 vezes, o que falha com a assunção de um *yield* constante.

6.2 Relação de Kennicut-Schmidt e a pseudo-KS

Como explicado na Sec. 1.2, a quantidade de gás de uma galáxia e a taxa de formação estelar estão relacionadas através de uma lei de potências (KS). A relação entre poeira e formação estelar é um resultado de indireto desta lei já que vemos que existe a ligação entre poeira e gás e que ela possui dependência com a metalicidade nebular principalmente (Magdis et al. 2011; Leroy et al. 2011; Santini et al. 2014, e suas referências). Pensando nisso, vamos estudar a relação entre poeira e formação estelar (aqui chamada de pseudo-KS - *pKS*), que pode ser vista na Fig. 6.2. No painel esquerdo usamos τ_V^* como variável representante da poeira e no direito, τ_V^{neb} . O espalhamento nesta figura nos mostra que podemos explorar os resíduos em torno desse ajuste, mas é bastante claro que existe uma relação. A conversão de CO em gás também é dependente da metalicidade, mas utilizando o coeficiente de extinção em absorção não necessitamos medidas adicionais.

6.2.1 Resíduos da pseudo-KS

Primeiramente vamos definir o resíduo como:

$$\Delta(pKS) = \log \Sigma_{SFR}^* - (0.751 \log \tau_V^* - 1.209). \quad (6.3)$$

De todas as propriedades que vemos na Fig. 6.3 as maiores correlações com $\Delta(pKS)$ são com a densidade superficial de massa estelar, o raio, a metalicidade nebular e a fração em luz das populações jovens. Apesar da notável participação da metalicidade nebular no espalhamento da relação *pKS*, ela possui intervalo pequeno de variação (90% dos pontos ficam no intervalo entre -0.4 e -0.11 Z_\odot), além do resíduo ir para o lado contrário que imaginariamo assumindo que, para um τ_V^* fixo, com o aumento da metalicidade Σ_{gas} (e consequentemente, Σ_{SFR}^*) deveria diminuir (causando um resíduo na direção contrária). Em razão de seu largo intervalo (~ 3 ordens de grandeza), a densidade superficial de massa estelar parece ser a principal causadora

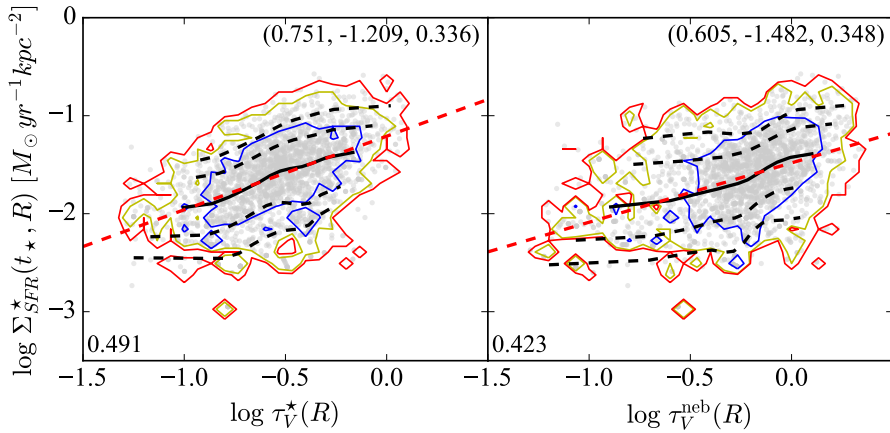


Figura 6.2: Relação entre a densidade superficial da taxa de formação estelar e o coeficiente de extinção proveniente da síntese (τ_V^* - painel esquerdo) e do decremento de Balmer (τ_V^{neb} - painel direito). Em ambos painéis as linhas pretas marcam a mediana (linha contínua) e os 5, 16, 64 e 95 percentis (linhas tracejadas). A linha tracejada em vermelho marca o ajuste linear da mediana e os valores marcam o coeficiente de correlação de Spearman (canto inferior esquerdo) e a inclinação, valor de y no qual há a interceção do eixo x e o valor do desvio médio quadrático da distribuição em torno do ajuste (canto superior direito).

do espalhamento na relação. A fração em luz de populações jovens também parece ter uma boa participação, entretanto, como apresentado no Cap. 5, x_Y (e também de b/a) possuem grande influência no cálculo de τ_V^* de maneira que nas regiões com fração de luz em populações jovens mais alta, τ_V^* se iguala (e em alguns casos é ultrapassa) o valor de τ_V^{neb} . A correlação com o raio parece refletir o comportamento de Σ_{SFR}^* que varia bastante dentro do disco, diferentemente de τ_V^* (veja na Fig. 3.4 o comportamento de Σ_{SFR}^* e). A metalicidade estelar média e a idade média das populações estelares parecem assumirem um papel pequeno no espalhamento da pKS. Não verificamos influência alguma da morfologia.

Como primeiro passo vamos tentar remover o espalhamento utilizando a regressão linear representada no primeiro painel da Fig. 6.3, ou seja, removendo o espalhamento causado pela metalicidade nebulosa. Dessa forma, vamos identificar as duas variáveis que utilizaremos:

$$\Delta_1 = 0.751 \log \tau_V^* + 1.188 \log \left(\frac{(O/H)}{(O/H)_\odot} \right) - 0.935 \quad (6.4)$$

Definimos então um novo $\Delta(pKS)$, alterando (6.3) utilizando Δ_1 :

$$\Delta(pKS) = \log \Sigma_{SFR}^* - \Delta_1. \quad (6.5)$$

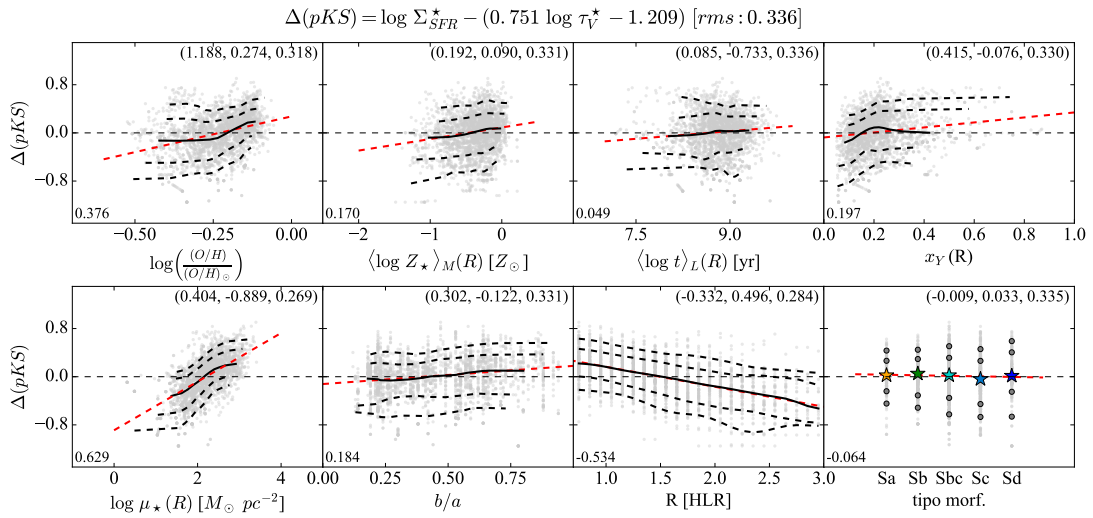


Figura 6.3: No eixo y de todos os painéis temos $\Delta(pKS) = \log \Sigma_{SFR}^* - (0.751 \log \tau_V^* - 1.209)$, onde, o termo entre parenteses é o ajuste linear da mediana no painel esquerdo da Fig. 6.2. No eixo x temos, na primeira fila, da esquerda para direita: metalicidade nebulosa ($\log(O/H)$), metalicidade estelar média pesada pela massa ($\langle \log Z_* \rangle_M$), idade média das populações estelares ($\langle \log t_* \rangle_L$), fração em luz das populações estelares jovens (x_Y); na última fila, na mesma ordem: densidade superficial de massa estelar ($\log \mu_*$), relação axial (b/a), raio e tipo morfológico. Em cada painel as linhas pretas marcam a mediana (linha contínua) e os 5, 16, 64 e 95 percentis (linhas tracejadas). A linha tracejada vermelha representa a regressão linear da mediana, cuja inclinação, o valor de y no qual há a interceptação do eixo x e o valor rms da distribuição estão no canto superior direito. O número no canto inferior esquerdo é o coeficiente de correlação de Spearman.

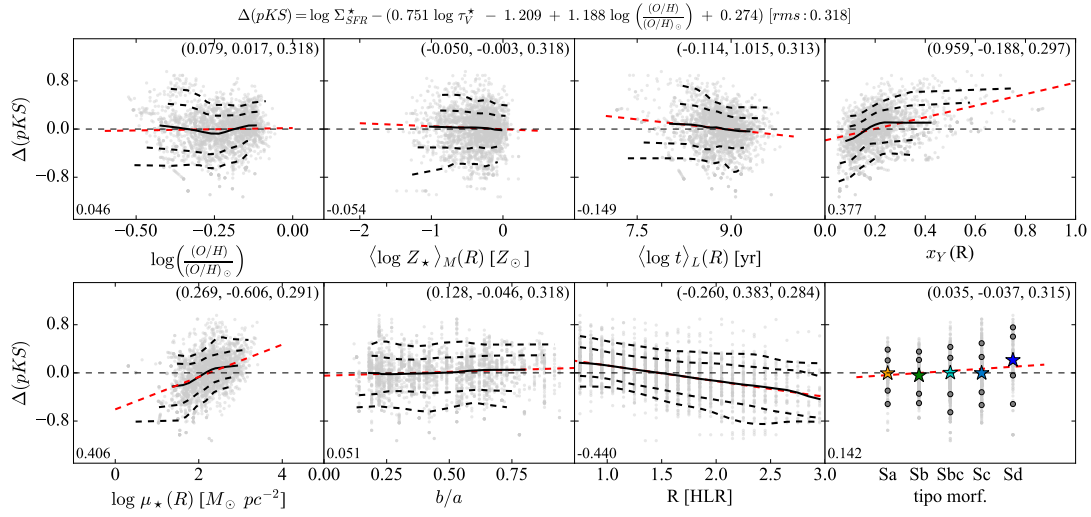


Figura 6.4: Igual a Fig. 6.3, mas removendo o espalhamento causado pela metalicidade nebular, conforme a dependência mostrada no seu primeiro painel.

Este resultado pode ser observado na Fig. 6.4. Vemos que apesar de diminuir em uma maneira geral o espalhamento, vemos que a densidade superficial de massa estelar continua cumprindo um papel importante nesta relação. Dessa forma, repetimos este último passo, mas agora removendo o espalhamento causado por μ_\star :

$$\Delta_2 = 0.751 \log \tau_V^\star + 0.404 \log \mu_\star - 2.098. \quad (6.6)$$

O novo valor de $\Delta(pKS)$ fica:

$$\Delta(pKS) = \log \Sigma_{\text{SFR}}^\star - \Delta_2. \quad (6.7)$$

Como podemos ver na Fig. 6.5, após este processo o espalhamento diminui consideravelmente na relação geral e em todas as outras variáveis, inclusive com a metalicidade nebular. Esta propriedade, assim como μ_\star , possui um gradiente no mesmo sentido em relação ao raio, e talvez esse seja o motivo pelo qual quando removemos o espalhamento causado por esta última resulte na diminuição do espalhamento causado pela primeira. Os efeitos com idade, fração em de populações jovens, b/a e morfologia serão estudados em um próximo passo de nosso trabalho, principalmente no contexto do Cap. 5. Parece que, em primeira ordem, encontramos o mais forte causador do espalhamento da Fig. 6.2, painel esquerdo. Na Fig. 6.6 vemos o resultado desse processo na pKS .

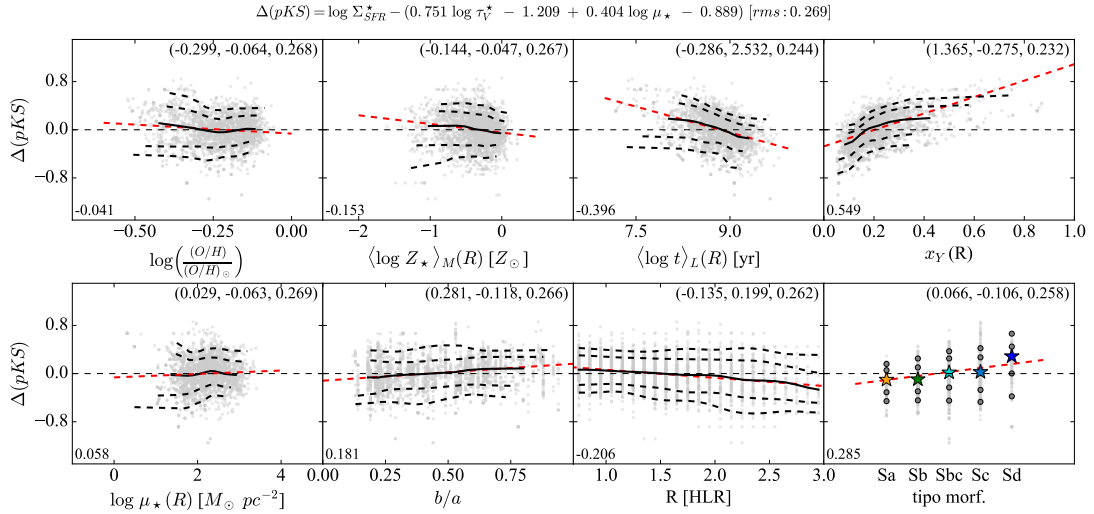


Figura 6.5: Igual a Fig. 6.4, mas removendo o espalhamento causado pela densidade superficial de massa estelar, conforme a dependência mostrada no primeiro painel da segunda fileira da Fig. 6.3.

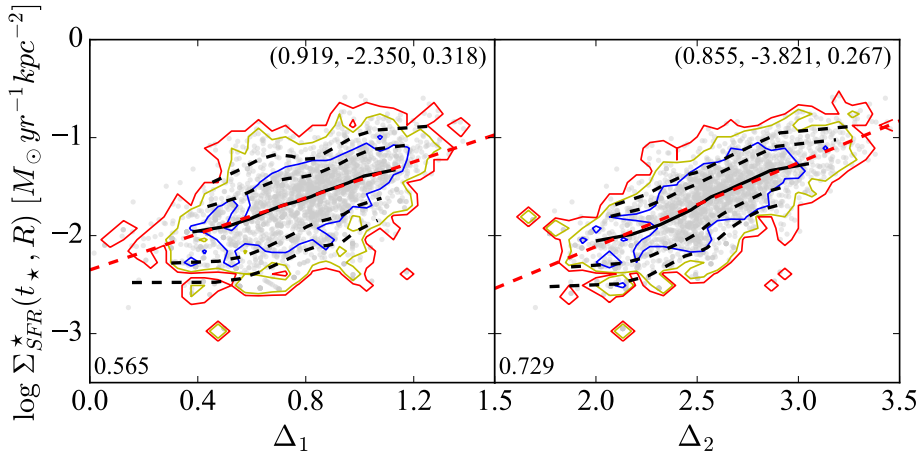


Figura 6.6: Igual a Fig. 6.2, mas agora usando no eixo x os valores de Δ_1 e Δ_2 , que se referem à remoção do espalhamento causado pela metalicidade nebular e pela densidade superficial de massa estelar respectivamente.

Diversos autores atualmente calculam e discutem a relação KS e a sua validade para diferentes resoluções espaciais (e.g., Kennicutt et al. 2007; Leroy et al. 2012; Calzetti et al. 2012; Lada et al. 2013; Tacconi et al. 2013; Casasola et al. 2015). A inclinação da KS ($N = 1.4$ em (1.1)) varia geralmente entre 1 e 2, dependendo da resolução espacial observada (regiões HII, perfis radiais, galáxias integradas) ou do tipo de gás usado (atômico, molecular ou a soma dos dois).

6.3 Conversão de poeira em gás.

Para converter poeira em gás primeiro precisamos da densidade superficial de poeira, que pode ser conseguida utilizando a equação:

$$\tau_d = \sigma_d \int n_d dz = \frac{\sigma_d}{m_d} \times \Sigma_d \quad (6.8)$$

$$\Sigma_d = \frac{m_d}{\sigma_d} \tau_d, \quad (6.9)$$

onde σ_d é área de um grão de poeira, n_d é o número de grãos de poeira ao longo de uma profundidade dz e m_d é a massa de um grão de poeira. Substituindo (6.9) em (1.2) e assumindo τ_v como τ_d obtemos:

$$\Sigma_{\text{gas}} = \kappa \times \frac{m_d}{\sigma_d} \tau_v. \quad (6.10)$$

A conversão de poeira em gás é dependente da metalicidade segundo podemos verificar em todas as referências sobre o assunto. Vamos explorar a conversão de poeira em gás em BR13, onde os autores seguem o modelo de extinção de Charlot & Fall (2000) e identificam algumas variáveis que vamos utilizar:

$$\xi = \frac{\Sigma_d}{\Sigma_Z} \quad (6.11)$$

$$Z = \frac{\Sigma_Z}{\Sigma_{\text{gas}}} \quad (6.12)$$

$$\delta_{\text{DGR}} = \frac{\Sigma_d}{\Sigma_Z} \frac{\Sigma_Z}{\Sigma_{\text{gas}}} = \frac{\Sigma_d}{\Sigma_{\text{gas}}} = \xi Z, \quad (6.13)$$

onde ξ é a razão poeira-metais (*dust-to-metals*), Z é a metalicidade do gás e o termo δ_{DGR} é igual a $1/\kappa$. Utilizando (6.13) em (6.10) e fazendo $m_d/\sigma_d \approx 0.2$, que corresponde ao tipo de

poeira Galáctica (BR13), temos:

$$\Sigma_{\text{gas}} \approx 0.2 \frac{\tau_V}{\delta_{\text{DGR}}} [M_\odot pc^{-2}]. \quad (6.14)$$

Neste artigo os autores utilizaram dados de ~ 70000 galáxias *star-forming* do SDSS-DR7 e parametrizam δ_{DGR} como a Eq. 28 de BR13:

$$\delta_{\text{DGR}} = (5.3 \times 10^{-3} - 1.1 \times 10^{-2}) \left(\frac{(O/H)}{(O/H)_\odot} \right), \quad (6.15)$$

onde os fatores que multiplicam a metalicidade representam um intervalo onde esta conversão é válida. O valor de δ_{DGR} foi parametrizado utilizando as metalicidades MPA/JHU¹ calculadas para o SDSS. Para que possamos utilizar essa conversão, calibraremos a abundância de oxigênio de M13 com aquela utilizada no trabalho de BR13. Podemos ver na Fig. 6.7 a calibração feita utilizando 4 ajustes. Escolhemos utilizar o ajuste linear, pois é aquele com menor desvio quadrático médio. Finalmente, nossa equação final para δ_{DGR} é:

$$\delta_{\text{DGR}} = (5.3 \times 10^{-3} - 1.1 \times 10^{-2}) \times 10^{(2.016x + 0.425)}, \quad (6.16)$$

onde $x = \log((O/H)/(O/H)_\odot)$ de M13. Podemos ver o perfil radial médio de δ_{DGR} para a amostra definida neste trabalho. Agora, substituindo (6.16) em (6.14) e utilizando este resultado em (6.1) podemos estimar frações de gás para galáxias do CALIFA.

6.3.1 Analisando a conversão

Como não possuímos medidas diretas de gás para comparar com os valores estimados aqui, vamos utilizar uma forma indireta invertendo (1.1) para calcular Σ_{gas} a partir da KS, desta forma obtemos:

$$\Sigma_{\text{gas}}^{\text{KS}} = \left(\frac{\Sigma_{\text{SFR}}^*}{2.5 \times 10^{-4}} \right)^{\frac{1}{1.4}} \quad (6.17)$$

$$f_{\text{gas}}^{\text{KS}} = \frac{1}{1 + \left(\frac{\mu_*}{\Sigma_{\text{gas}}^{\text{KS}}} \right)}. \quad (6.18)$$

Juntamente produzimos a mesma versão destas variáveis, mas substituindo os Σ_{SFR}^* e τ_V^* para $\Sigma_{\text{SFR}}^{\text{neb}}$ e τ_V^{neb} .

¹<http://wwwmpa.mpa-garching.mpg.de/SDSS/>

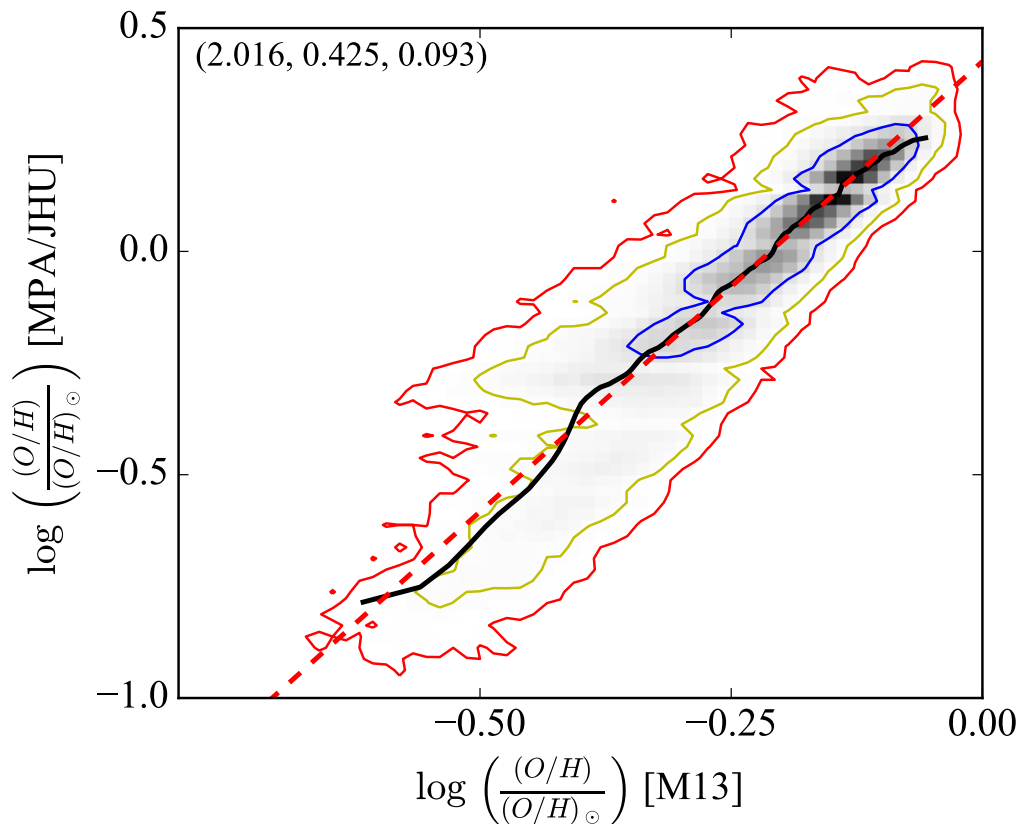


Figura 6.7: Calibração da metalicidade nebulosa (abundância relativa de oxigênio) do grupo MPA/JHU com a de M13. A linha preta contínua representa a mediana da distribuição, as outras linhas, pelas cores indicadas na legenda, são regressões polinomiais de 1^a, 2^a e 3^a ordem e o *OLS bisector* da distribuição. Os contornos marcam 1 σ , 2 σ e 3 σ respectivamente.

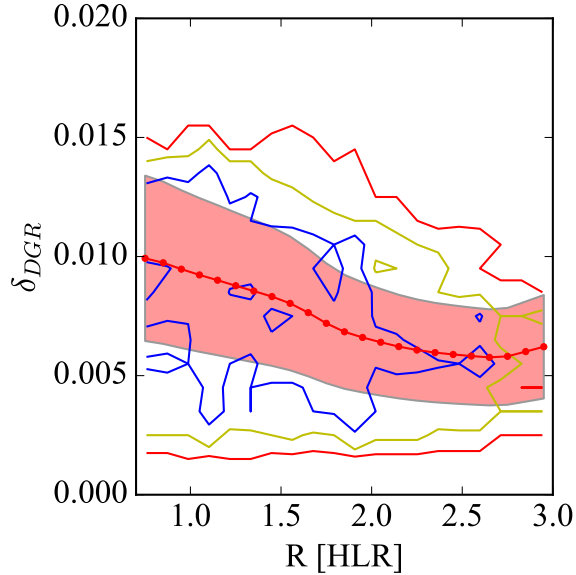


Figura 6.8: Perfil radial de δ_{DGR} definido pela em (6.16). A área rachurada representa δ_{DGR} calculado para os valores máximo e mínimo do intervalo definido por BR13. Os contornos marcam 1σ , 2σ e 3σ respectivamente.

A Fig. 6.9 nos mostra os perfis radiais de δ_{DGR} , Σ_{gas} e f_{gas} . Apesar da divergência entre os perfis de δ_{DGR} e Σ_{gas} quanto ao comportamento ao longo do raio, a fração de gás parece ser um resultado mais robusto, graças a influência de densidade superficial de massa estelar (μ_{\star}).

Na Fig. 6.10 os histogramas das variáveis calculadas nessa seção e nas Figs. 6.11 e 6.12 vemos Σ_{gas} e f_{gas} versus algumas propriedades. O código de cores em todos os gráficos segue àquele definido na Fig. 6.9. Para Σ_{gas} vemos que os resultados são bastante diferentes quando comparamos pelo método de conversão de poeira em absorção (utilizando um δ_{DGR}) e quando invertemos a lei de KS ((6.18) e (6.18)). Já quando observamos frações de gás vemos que os resultados são mais robustos.

Fechamos esta seção com a relação KS criada a partir dos valores de Σ_{gas} utilizando a conversão de BR13 (Fig. 6.13). Basicamente o resultado é: essa conversão não está “melhorando” os resultados na direção de uma relação mais inclinada do que a relação original (que seria o caso de ir em direção à relação de KS). Os resíduos de metalicidade na relação pKS (Fig. 6.3, primeiro painel na primeira fila) estão indo para a direção contrária a direção que deveria ter no caso de usar a conversão de poeira para gás assumindo (6.14) para chegar em uma relação de KS (1.1).

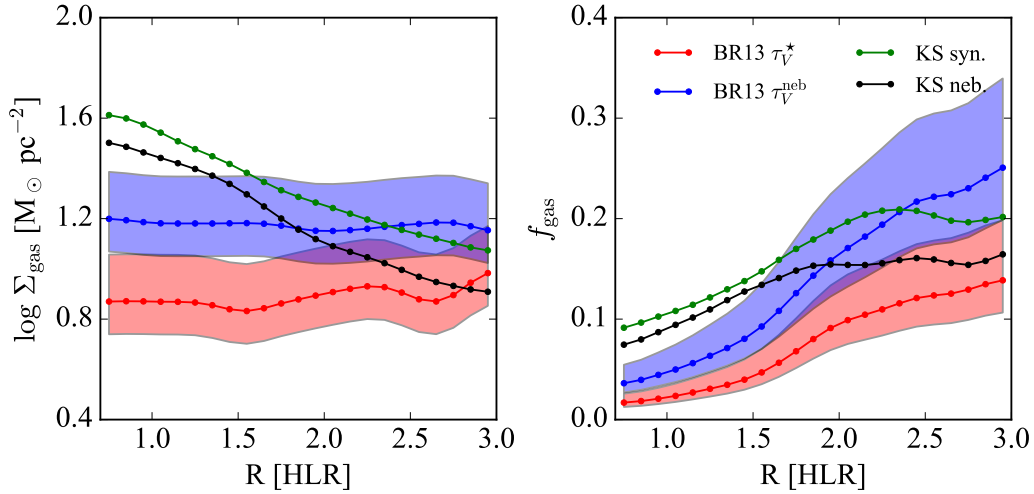


Figura 6.9: Perfis radiais para a razão poeira-gás (δ_{DGR}), densidade superficial de massa de gás (Σ_{gas}) e fração de gás (f_{gas}). A área hachurada representa o intervalo definido em (6.16). Em azul e vermelho temos a conversão de poeira em gás utilizando a conversão (6.14) com δ_{DGR} definido em (6.16), utilizando τ_V^{neb} e τ_V^* respectivamente. Em verde e preto temos as variáveis definidas no início desta seção, invertendo a lei de KS, utilizando Σ_{SFR}^* e $\Sigma_{\text{SFR}}^{\text{neb}}$ respectivamente.

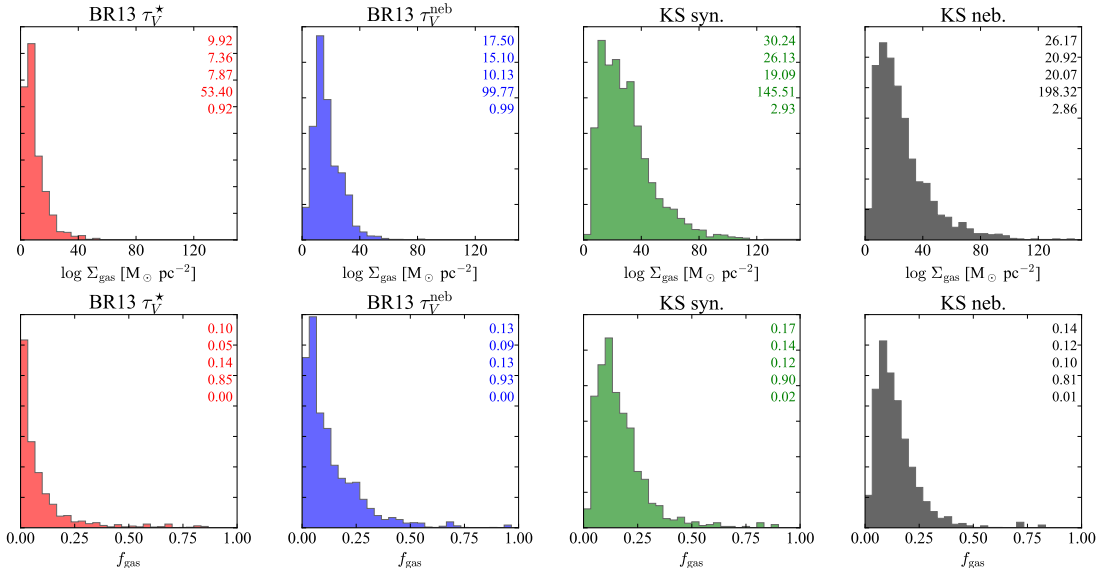


Figura 6.10: Histogramas de Σ_{gas} e f_{gas} calculadas das diferentes formas especificadas na Sec. 6.3.1. As cores de cada histograma seguem àquelas definidas na Fig. 6.9. Os valores nos cantos são os mesmos encontrados em todos os histogramas deste trabalho: média, mediana, desvio padrão, máximo e mínimo.

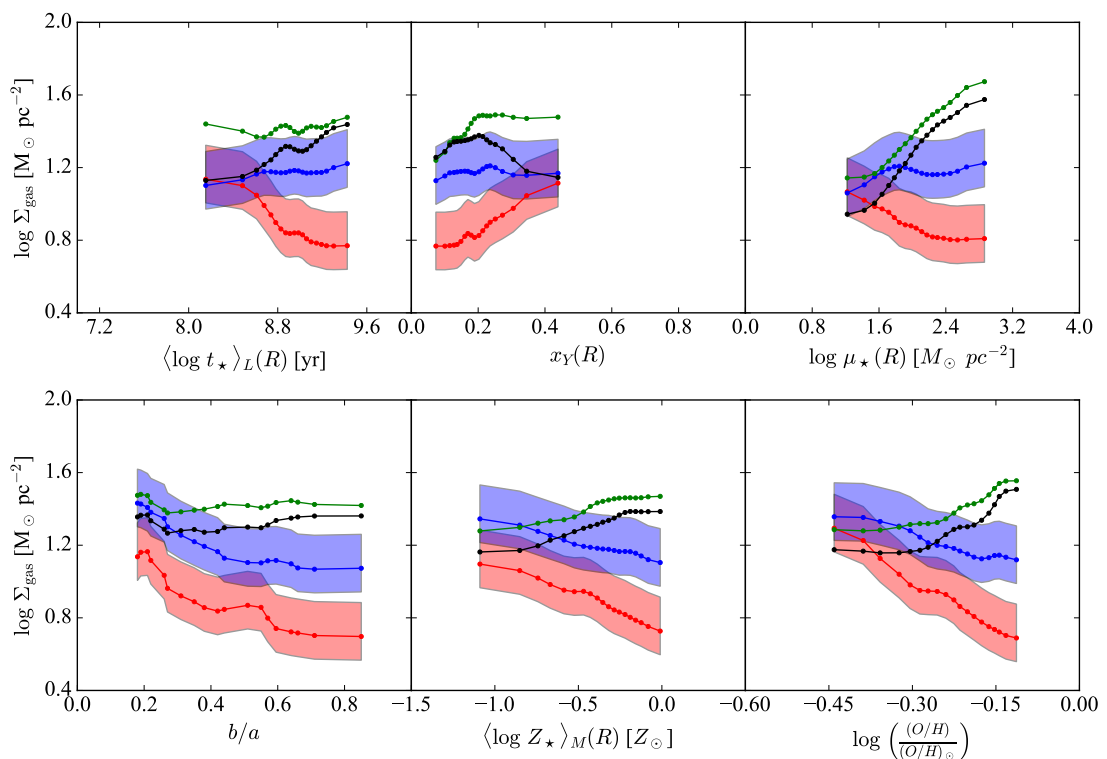


Figura 6.11: Densidade superficial de massa de gás (Σ_{gas}) contra idade média das populações estelares, fração em luz das populações jovens, densidade superficial de massa estelar, todos na primeira fileira e, na segunda fileira, relação de semi-eixos, metalicidade média das populações estelares pesada pela massa e metalicidade nebulosa.

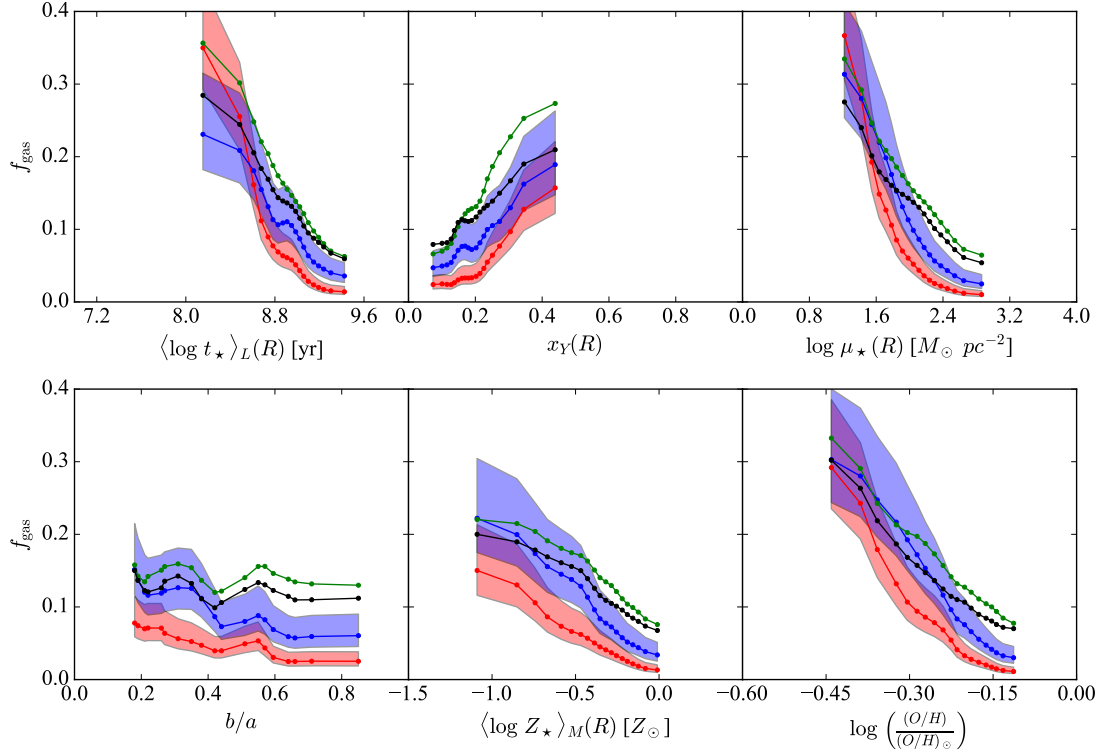


Figura 6.12: Igual a Fig. 6.11, mas para a fração de gás.

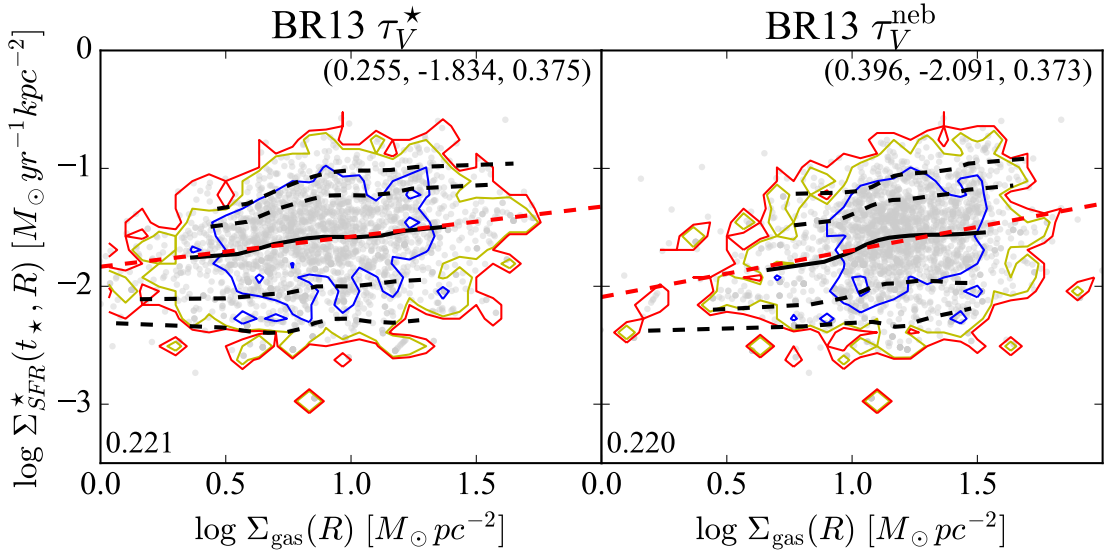


Figura 6.13: Igual a Fig. 6.2 mas substituindo o eixo x para o valor da densidade superficial de massa de gás calculado a partir da conversão de BR13 utilizando τ_V^* (painel esquerdo) e τ_V^{neb} (painel direito).

6.4 Perspectivas e próximos passos.

Nossa principal dificuldade nessa etapa é a falta de medidas diretas de gás para as mesmas regiões avaliadas, de forma a parametrizar uma conversão. A conversão de BR13 parece ter sido definida como somente dependente da metalicidade (6.15) mas na Sec. 6.2.1 verificamos que outras variáveis a pKS , principalmente a densidade superficial de massa estelar (μ_*). Precisamos estudar melhor esta relação também substituindo τ_V^* por τ_V^{neb} e também explorar as diferenças entre τ_V^* , τ_V^{neb} , τ_{ISM} e τ_{BC} e suas influências na relação pKS .

O desvio padrão da relação KS construída utilizando Σ_{gas} vindo da conversão de BR13 é próximo a 0.4 dex e, após a conversão, a inclinação da reta diminui, o que vai na direção contrária ao que imaginariam assumindo uma relação KS com inclinação ~ 1.4 .

Um próximo passo também é adotar um outro tipo de abordagem, considerando a eficiência da formação estelar (transformação de gás em estrelas), utilizando a relação:

$$SFE = \frac{\Sigma_{SFR}}{\Sigma_{gas}} = \frac{1}{t_{dep}}, \quad (6.19)$$

onde SFE vem de *star-formation efficiency* e t_{dep} , que é o inverso da eficiência, é o tempo de depleção do gás, que nos dá uma ideia da escala de tempo em que a galáxia consome todo o gás com a taxa em que está formando estrelas. Um exemplo desse tipo de análise pode ser visto na Fig. 6.14, onde utilizamos Σ_{gas} proveniente dos métodos utilizados nesse capítulo para verificar o tempo de depleção do gás, o qual nos diz o tempo médio no qual o gás é consumido.

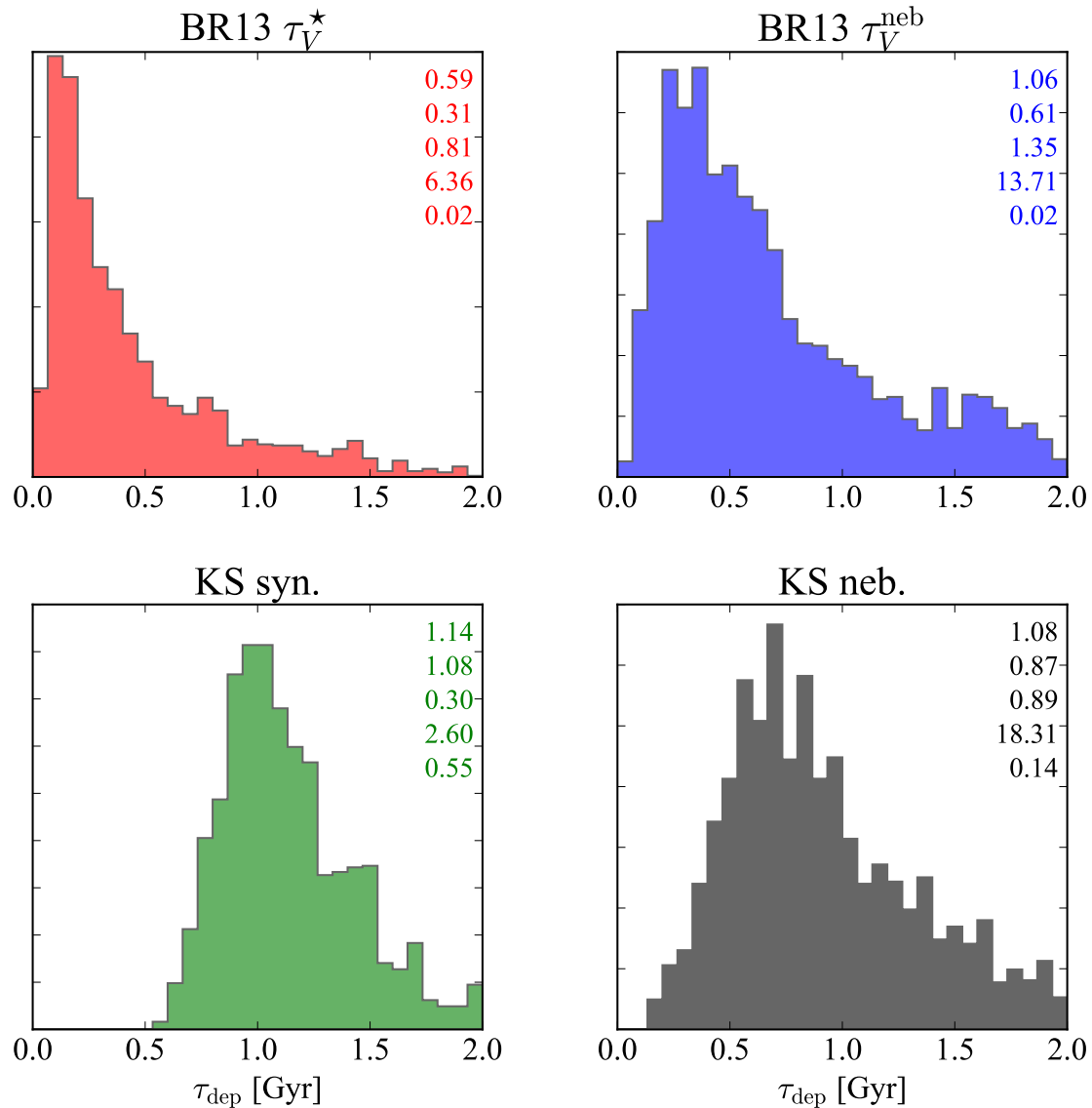


Figura 6.14: Histogramas de τ_{dep} para Σ_{gas} calculado como na Fig. 6.9. As cores e valores no canto superior direito de cada painel seguem o mesmo padrão da Fig. 6.10.

Apêndice A

Artigos publicados

A.1 CALIFA, the Calar Alto Legacy Integral Field Area survey. III. Second public data release

Artigo por García-Benito et al. (2015) ([doi:10.1051/0004-6361/201425080](https://doi.org/10.1051/0004-6361/201425080)). Também disponível em *pre-print* ([arXiv:1409.8302](https://arxiv.org/abs/1409.8302)).

CALIFA, the Calar Alto Legacy Integral Field Area survey

III. Second public data release^{★,★★}

R. García-Benito¹, S. Zibetti², S. F. Sánchez³, B. Husemann⁴, A. L. de Amorim⁵, A. Castillo-Morales⁶, R. Cid Fernandes⁵, S. C. Ellis⁷, J. Falcón-Barroso^{8,9}, L. Galbany^{10,11}, A. Gil de Paz⁶, R. M. González Delgado¹, E. A. D. Lacerda⁵, R. López-Fernandez¹, A. de Lorenzo-Cáceres¹², M. Lyubenova^{13,14}, R. A. Marino¹⁵, D. Mast¹⁶, M. A. Mendoza¹, E. Pérez¹, N. Vale Asari⁵, J. A. L. Aguerri^{8,9}, Y. Ascasibar¹⁷, S. Bekeraite¹⁸, J. Bland-Hawthorn¹⁹, J. K. Barrera-Ballesteros^{8,9}, D. J. Bomans^{20,21}, M. Cano-Díaz³, C. Catalán-Torrecilla⁶, C. Cortijo¹, G. Delgado-Inglada³, M. Demleitner²², R.-J. Dettmar^{20,21}, A. I. Díaz¹⁷, E. Florido^{13,33}, A. Gallazzi^{2,24}, B. García-Lorenzo^{8,9}, J. M. Gomes²⁵, L. Holmes²⁶, J. Iglesias-Páramo^{1,27}, K. Jahnke¹⁴, V. Kalinova²⁸, C. Kehrig¹, R. C. Kennicutt Jr²⁹, Á. R. López-Sánchez^{7,30}, I. Márquez¹, J. Masegosa¹, S. E. Meidt¹⁴, J. Mendez-Abreu¹², M. Mollá³¹, A. Monreal-Ibero³², C. Morisset³, A. del Olmo¹, P. Papaderos²⁵, I. Pérez^{23,33}, A. Quirrenbach³⁴, F. F. Rosales-Ortega³⁵, M. M. Roth¹⁸, T. Ruiz-Lara^{23,33}, P. Sánchez-Blázquez¹⁷, L. Sánchez-Menguiano^{1,23}, R. Singh¹⁴, K. Spekkens²⁶, V. Stanishev^{36,37}, J. P. Torres-Papaqui³⁸, G. van de Ven¹⁴, J. M. Vilchez¹, C. J. Walcher¹⁸, V. Wild¹², L. Wisotzki¹⁸, B. Ziegler³⁹, J. Alves³⁹, D. Barrado⁴⁰, J. M. Quintana¹, and J. Aceituno²⁷

(Affiliations can be found after the references)

Received 29 September 2014 / Accepted 24 February 2015

ABSTRACT

This paper describes the Second Public Data Release (DR2) of the Calar Alto Legacy Integral Field Area (CALIFA) survey. The data for 200 objects are made public, including the 100 galaxies of the First Public Data Release (DR1). Data were obtained with the integral-field spectrograph PMAS/PPak mounted on the 3.5 m telescope at the Calar Alto observatory. Two different spectral setups are available for each galaxy, (i) a low-resolution V500 setup covering the wavelength range 3745–7500 Å with a spectral resolution of 6.0 Å (FWHM); and (ii) a medium-resolution V1200 setup covering the wavelength range 3650–4840 Å with a spectral resolution of 2.3 Å (FWHM). The sample covers a redshift range between 0.005 and 0.03, with a wide range of properties in the color–magnitude diagram, stellar mass, ionization conditions, and morphological types. All the cubes in the data release were reduced with the latest pipeline, which includes improved spectrophotometric calibration, spatial registration, and spatial resolution. The spectrophotometric calibration is better than 6% and the median spatial resolution is 2''.4. In total, the second data release contains over 1.5 million spectra.

Key words. surveys – techniques: spectroscopic – galaxies: general

1. Introduction

The Calar Alto Legacy Integral Field Area (CALIFA) survey (Sánchez et al. 2012a, hereafter S12) is an ongoing large project of the Centro Astronómico Hispano-Alemán at the Calar Alto observatory (Almería, Spain) to obtain spatially resolved spectra for 600 galaxies in the local Universe by means of integral field spectroscopy (IFS). The CALIFA observations started in June 2010 with the Potsdam Multi Aperture Spectrograph (PMAS, Roth et al. 2005), mounted on the 3.5 m telescope, utilizing the large hexagonal field-of-view (FoV) offered by the PPak fiber bundle (Verheijen et al. 2004; Kelz et al. 2006). Each galaxy is observed using two different setups: one at intermediate spectral resolution (V1200, $R \sim 1650$) and the other at low resolution

(V500, $R \sim 850$). A diameter-selected sample of 939 galaxies was drawn from the 7th data release of the Sloan Digital Sky Survey (SDSS DR7, Abazajian et al. 2009), which is described in Walcher et al. (2014, hereafter W14). From this mother sample, the 600 target galaxies are randomly selected.

Combining the techniques of imaging and spectroscopy through optical IFS provides a more comprehensive view of individual galaxy properties than any traditional survey. CALIFA-like observations were collected during the feasibility studies (Mármol-Queraltó et al. 2011; Viironen et al. 2012) and the PPak IFS Nearby Galaxy Survey (PINGS, Rosales-Ortega et al. 2010), a predecessor of this survey. First results based on those data sets already explored their information content (e.g., Sánchez et al. 2011, 2012b; Rosales-Ortega et al. 2011, 2012; Alonso-Herrero et al. 2012). The CALIFA survey can therefore be expected to make a substantial contribution to our understanding of galaxy evolution in various aspects, including (i) the relative importance and consequences of merging and secular processes; (ii) the evolution of galaxies across the color–magnitude diagram; (iii) the effects of the environment on galaxies; (iv) the AGN-host galaxy

* Based on observations collected at the Centro Astronómico Hispano Alemán (CAHA) at Calar Alto, operated jointly by the Max-Planck-Institut für Astronomie (MPIA) and the Instituto de Astrofísica de Andalucía (CSIC).

** The second data release is available at <http://califa.caha.es/>
DR2

connection; (v) the internal dynamical processes in galaxies; and (vi) the global and spatially resolved star formation history and chemical enrichment of various galaxy types.

Compared with previous IFS surveys, e.g., Atlas3D (Cappellari et al. 2011) or the Disk Mass Survey (DMS) (Bershady et al. 2010), CALIFA covers a much wider range of morphological types over a large range of masses, sampling the entire color-magnitude diagram for $M_r > -19$ mag. While the recently started SAMI (Croom et al. 2012; Bryant et al. 2015) and MaNGA (Law & MaNGA Team 2014) surveys have a broad scope similar to CALIFA and aim to build much larger samples, CALIFA still has an advantage in terms of spatial coverage and sampling. For 50% of the galaxies, CALIFA provides data out to $3.5 r_e$, and for 80% out to $2.5 r_e$. At the same time, the spatial resolution of ~ 1 kpc is typically better than in either SAMI or MaNGA, revealing several of the most relevant structures in galaxies (spiral arms, bars, bulges, giant H α regions, etc.). The spectral resolution of CALIFA is lower than these two surveys in the red wavelength range, but is comparable for the blue wavelength range.

So far, a number of science goals have been addressed using the data from the CALIFA survey: (i) new techniques have been developed to understand the spatially resolved star formation histories (SFH) of galaxies (Cid Fernandes et al. 2013, 2014). We found solid evidence that mass-assembly in the typical galaxies happens from the inside-out (Pérez et al. 2013). The SFH and metal enrichment of bulges and early-type galaxies are fundamentally related to the total stellar mass, while for disk galaxies it is more closely related to the local stellar mass density (González Delgado et al. 2014b,a); (ii) we developed new tools to detect and extract the spectra of H α regions (Sánchez et al. 2012b), building the largest catalog currently available (~ 6000 H α regions and aggregations). This catalog has been used to define a new oxygen abundance calibrator, anchored to electron temperature measurements (Marino et al. 2013). From these, we explored the dependence of the mass-metallicity relation with star formation rate (Sánchez et al. 2013), and the local mass-metallicity relation (Rosales-Ortega et al. 2012). We found that all galaxies in our sample present a common gas-phase oxygen abundance radial gradient with a similar slope, when normalized to the effective radius (Sánchez et al. 2014). This agrees with an inside-out scenario for galaxy growth. This characteristic slope is independent of the properties of the galaxies, and, in particular, of the presence or absence of a bar, contrary to previous results. More recently, this result has been confirmed by the analysis of the stellar abundance gradient in the same sample (Sánchez-Blázquez et al. 2014); (iii) we explored the origin of the low intensity, LINER-like, ionized gas in galaxies. These regions are clearly not related to star formation activity, or to AGN activity. They are probably most closely related to post-AGB ionization in many cases (Kehrig et al. 2012; Singh et al. 2013; Papaderos et al. 2013); (iv) we explored the aperture and resolution effects on the data. The CALIFA survey provides a unique tool to understand the aperture and resolution effects in larger single-fiber (e.g., SDSS) and IFS surveys (e.g., MaNGA, SAMI). We explored the effects of the dilution of the signal in different gas and stellar population properties (Mast et al. 2014), and proposed a new empirical aperture correction for the SDSS data (Iglesias-Páramo et al. 2013); (v) we analyzed the local properties of the ionized gas and stellar population of galaxies where supernovae (SNe) have exploded. Core collapse SNe are found closer to younger stellar populations, while SNe Ia show no correlation to stellar age (Galbany et al. 2014); (vi) CALIFA is the first IFS survey that allows

gas and stellar kinematic studies for all morphologies with sufficient spectroscopic resolution to study (a) the kinematics of the ionized gas (García-Lorenzo et al. 2015); (b) the effects of bars in the kinematics of galaxies (Barrera-Ballesteros et al. 2014); (c) the effects of the interaction stage on the kinematic signatures (Barrera-Ballesteros et al., in prep.); (d) the bar pattern speeds in late-type galaxies (Aguerri et al. 2015); (e) the measurements of the angular momentum of galaxies to previously unexplored ranges of morphology and ellipticity (Falcón-Barroso et al., in prep.); and (vii) we explored the effects of a first stage merger on the gas and stellar kinematics, star formation activity and stellar populations of the Mice merging galaxies (Wild et al. 2014).

In this article, we introduce the second data release (DR2) of CALIFA, which grants public access to high-quality data for a set of 200 galaxies (400 datacubes). All the cubes in the data release have been reduced with the latest pipeline, which includes improved spectrophotometric calibration, spatial registration, and spatial resolution. This DR supersedes and increases the amount of data delivered in DR1 (Husemann et al. 2013, hereafter H13) by a factor of two.

The DR1 opened CALIFA to the community, and allowed for the exploration of several different scientific avenues not addressed by the collaboration (e.g., Holwerda & Keel 2013; De Geyter et al. 2014; Martínez-García et al. 2014; Davies et al. 2014). The properties of the galaxies in the DR2 sample are summarized in Sect. 2. We describe the observing strategy and setup (Sect. 3), processing (Sect. 4), structure (Sect. 5), and data (Sect. 6), which comprise essential information for any scientific analysis of the distributed CALIFA data. Several interfaces to access the CALIFA DR2 data are explained in Sect. 7.

2. The CALIFA DR2 sample

The CALIFA “mother sample” (MS) consists of 939 galaxies drawn from SDSS DR7. The main criteria for the target selection are: angular isophotal diameter ($45'' < isoA_r < 79.2''$) of the galaxies¹; redshift range $0.005 < z < 0.03$; cut in Galactic latitude to exclude the Galactic plane ($|b| > 20^\circ$); flux limit of $petroMag_r < 20$; and declination limit to $\delta > 7^\circ$. Redshift limits were imposed so that the sample would not be dominated by dwarf galaxies and to keep relevant spectral features observable within a fixed instrumental spectral setup. Redshift information was taken from SIMBAD for all galaxies where SDSS DR7 spectra were unavailable. The cut in declination was chosen to reduce problems due to differential atmospheric refraction (DAR) and PMAS flexure issues, but was not applied to the SDSS Southern area because of the sparsity of objects in this region. A comprehensive characterization of the CALIFA MS and a detailed evaluation of the selection effects implied by the chosen criteria is provided in W14. From the CALIFA MS, 600 galaxies are randomly selected for observation, based purely on visibility.

The 200 DR2 galaxies, which include the first 100 galaxies of DR1, were observed in both spectral setups between the start of observations in June 2010 and December 2013. We list these galaxies in Table 1 together with their primary characteristics. The distribution of galaxies in the sky follows the underlying SDSS footprint (Fig. 1). The number of galaxies in DR2 is not homogeneous as a function of right ascension, $\alpha(J2000)$,

¹ The $isoA_r$ parameter is the isophote major axis at 25 mag per square arcsecond in the r -band. For the meaning of other SDSS pipeline parameters, refer to the DR7 webpage: <http://skyserver.sdss.org/dr7/en/help/browser/browser.asp>

Table 1. CALIFA DR2 galaxies and their characteristics.

Name	ID ^a	α (J2000) ^b	δ (J2000) ^b	z ^c	m_g ^d	m_z ^d	$m_u - m_z$ ^d	Type ^e	Bar ^f	b/a ^g
IC 5376	001	00:01:19.779	+34:31:32.409	0.0168	14.24	12.60	3.48	Sb	A	0.27
UGC 00005	002	00:03:05.643	-01:54:49.804	0.0243	13.88	12.53	2.95	Sbc	A	0.54
NGC 7819	003	00:04:24.505	+31:28:19.228	0.0167	14.06	13.01	2.12	Sc	A	0.53
IC 1528	005	00:05:05.377	-07:05:36.204	0.0128	13.46	12.52	2.43	Sbc	AB	0.36
UGC 00036	007	00:05:13.882	+06:46:19.306	0.0210	14.12	12.46	3.55	Sab	AB	0.60
NGC 0001	008	00:07:15.860	+27:42:29.096	0.0151	13.46	12.01	2.97	Sbc	A	0.80
NGC 0036	010	00:11:22.298	+06:23:21.667	0.0203	13.46	12.01	3.23	Sb	B	0.65
MCG-02-02-030	013	00:30:07.309	-11:06:49.066	0.0118	13.41	12.08	2.91	Sb	AB	0.34
UGC 00312	014	00:31:23.922	+08:28:00.232	0.0145	13.76	13.07	1.52	Sd	B	0.35
UGC 00335NED02	017	00:33:57.323	+07:16:05.781	0.0183	14.27	12.82	3.42	E4(x)	A	0.63
NGC 0169	022	00:36:51.608	+23:59:27.501	0.0154	14.04	11.74	4.50	Sab(x)	A	0.42
NGC 0171	023	00:37:21.552	-19:56:03.210	0.0131	13.21	11.73	3.29	Sb	B	0.63
NGC 0180	025	00:37:57.703	+08:38:06.588	0.0177	13.51	11.98	3.00	Sb	B	0.64
NGC 0192	026	00:39:13.414	+00:51:50.968	0.0140	13.37	11.72	3.23	Sab	AB	0.31
NGC 0216	027	00:41:27.170	-21:02:40.826	0.0052	13.55	12.78	1.78	Sd	A	0.27
NGC 0237	030	00:43:27.841	-00:07:29.747	0.0139	13.52	12.38	2.44	Sc	B	0.57
IC 1652	037	01:14:56.277	+31:56:54.606	0.0173	14.08	12.72	3.13	S0a	A	0.31
NGC 0444	039	01:15:49.562	+31:04:50.245	0.0161	14.47	13.48	2.20	Scd	A	0.24
UGC 00809	040	01:15:51.837	+33:48:38.532	0.0140	14.81	13.74	2.52	Scd	A	0.19
UGC 00841	041	01:19:10.028	+33:01:50.248	0.0186	14.91	13.73	2.55	Sbc	A	0.25
NGC 0477	042	01:21:20.483	+40:29:17.332	0.0196	14.43	13.09	2.66	Sbc	AB	0.66
IC 1683	043	01:22:38.929	+34:26:13.654	0.0162	14.11	12.63	2.98	Sb	AB	0.59
NGC 0499	044	01:23:11.496	+33:27:36.683	0.0146	12.76	11.19	3.49	E5	A	0.61
NGC 0496	045	01:23:11.595	+33:31:45.386	0.0201	13.92	12.93	2.25	Scd	A	0.58
NGC 0528	050	01:25:33.571	+33:40:17.198	0.0161	13.51	11.89	3.58	S0	A	0.49
UGC 01057	053	01:28:53.253	+13:47:37.674	0.0212	14.54	13.26	2.66	Sc	AB	0.30
NGC 0774	072	01:59:34.729	+14:00:29.536	0.0154	13.52	11.88	3.50	S0	A	0.72
NGC 0776	073	01:59:54.525	+23:38:39.392	0.0164	13.52	12.06	3.19	Sb	B	0.69
NGC 0810	076	02:05:28.562	+13:15:05.867	0.0257	13.70	11.93	3.74	E5(x)	A	0.69
NGC 0825	077	02:08:32.329	+06:19:25.200	0.0113	13.63	12.04	3.29	Sa	A	0.33
UGC 01938	088	02:28:22.137	+23:12:52.655	0.0213	14.70	13.31	2.90	Sbc	AB	0.25
NGC 1056	100	02:42:48.312	+28:34:26.961	0.0052	13.00	11.41	3.02	Sa	A	0.57
UGC 02222	103	02:45:09.676	+32:59:22.935	0.0166	13.76	12.29	3.32	S0a(x)	AB	0.51
UGC 02229	104	02:45:27.567	+00:54:51.657	0.0244	14.16	12.48	3.49	S0a(x)	A	0.57
UGC 02403	115	02:55:57.257	+00:41:33.378	0.0137	14.15	12.41	3.44	Sb	B	0.28
NGC 1349	127	03:31:27.512	+04:22:51.241	0.0220	13.34	11.80	3.45	E6	A	0.89
NGC 1542	131	04:17:14.172	+04:46:54.239	0.0125	13.60	12.14	3.00	Sab	AB	0.38
UGC 03107	133	04:37:21.852	+09:32:40.747	0.0283	14.89	13.35	3.19	Sb	A	0.24
NGC 1645	134	04:44:06.400	-05:27:56.414	0.0163	13.46	11.97	3.38	S0a	B	0.64
IC 2095	141	04:48:45.881	-05:07:28.668	0.0095	15.59	15.23	1.28	Sc	AB	0.15
UGC 03253	146	05:19:41.885	+84:03:09.432	0.0138	13.69	12.27	3.07	Sb	B	0.62
NGC 2253	147	06:43:41.836	+65:12:22.950	0.0120	13.26	11.79	2.97	Sbc	B	0.87
UGC 03539	148	06:48:54.003	+66:15:41.885	0.0110	14.95	14.13	2.31	Sc	AB	0.19
NGC 2347	149	07:16:04.087	+64:42:40.776	0.0149	13.18	11.65	3.08	Sbc	AB	0.64
UGC 03899	150	07:32:37.749	+35:36:52.125	0.0130	14.99	14.46	1.47	Sd	A	0.43
NGC 2410	151	07:35:02.261	+32:49:19.566	0.0156	13.37	11.78	3.29	Sb	AB	0.32
UGC 03969	153	07:41:14.343	+27:36:50.635	0.0275	15.03	13.42	3.21	Sb	A	0.18
UGC 03995	155	07:44:09.128	+29:14:50.751	0.0159	13.48	11.92	3.58	Sb	B	0.46
NGC 2449	156	07:47:20.299	+26:55:48.708	0.0163	13.70	12.22	3.37	Sab	AB	0.50

Notes. ^(a) CALIFA unique ID number for the galaxy. ^(b) Equatorial coordinates of the galaxies as provided by NED. ^(c) Redshift of the galaxies based on SDSS DR7 spectra or complemented with SIMBAD information if SDSS spectra are not available. ^(d) Petrosian magnitudes as given by SDSS DR7 database corrected for Galactic extinction. ^(e) Morphological type from our own visual classification (see W14 for details). “(x)” indicates ongoing mergers. ^(f) Bar strength of the galaxy as an additional outcome of our visual classification. A stands for non-barred, B for barred and AB if unsure. ^(g) Ratio between the semi-minor and semi-major axis based on a detailed re-analysis of the SDSS images (see W14 for details). ^(h) Morphological classification of this particular galaxy NGC 4676B from Wild et al. (2014).

and has three clear peaks at around $\alpha \sim 15^\circ$, 255° , and 345° . All three peaks are located in the same observing semester, in the period from April to October. As noted in H13, there was a downtime of the 3.5 m telescope from August 2010 until April 2011 due to operational reasons at the observatory, which delayed the survey roughly by eight months. In addition to this, because of scheduling matters, a large part of the granted time was allocated

in summer seasons. Regardless of the observing time issue, the distribution of physical properties for DR2 is nearly random, as expected, and covers galaxies with a wide range of properties as discussed below.

Figure 2 shows the distribution of galaxies in the color-magnitude diagram. The DR2 sample covers nearly the full range of the CALIFA MS. On average, the DR2 targets

Table 1. continued.

Name	ID ^a	α (J2000) ^b	δ (J2000) ^b	z ^c	m_g ^d	m_z ^d	$m_u - m_z$ ^d	Type ^e	Bar ^f	b/a ^g
UGC 04132	165	07:59:13.046	+32:54:52.822	0.0174	13.80	12.23	3.17	Sbc	AB	0.26
UGC 04722	231	09:00:24.130	+25:36:53.079	0.0058	15.16	15.07	1.25	Sdm	A	0.19
NGC 2730	232	09:02:15.824	+16:50:17.841	0.0128	13.93	13.13	1.95	Scd	B	0.64
NGC 2880	272	09:29:34.567	+62:29:26.052	0.0051	12.40	10.99	3.21	E7	AB	0.71
IC 2487	273	09:30:09.166	+20:05:27.042	0.0145	13.94	12.58	2.90	Sc	AB	0.22
IC 0540	274	09:30:10.338	+07:54:09.903	0.0069	14.24	12.76	3.17	Sab	AB	0.30
NGC 2906	275	09:32:06.218	+08:26:30.367	0.0071	12.89	11.46	3.37	Sbc	A	0.51
NGC 2916	277	09:34:57.601	+21:42:18.940	0.0124	13.37	11.86	3.16	Sbc	A	0.59
UGC 05108	278	09:35:26.279	+29:48:45.439	0.0271	14.35	12.73	3.35	Sb	B	0.77
UGC 05358	306	09:58:47.135	+11:23:19.318	0.0097	15.12	14.41	1.79	Sd	B	0.33
UGC 05359	307	09:58:51.647	+19:12:53.918	0.0283	14.74	13.43	2.93	Sb	B	0.37
UGC 05396	309	10:01:40.485	+10:45:23.140	0.0181	14.43	13.24	2.66	Sbc	AB	0.27
NGC 3106	311	10:04:05.251	+31:11:07.653	0.0207	13.41	12.01	3.31	Sab	A	0.93
UGC 05498NED01	314	10:12:03.658	+23:05:07.590	0.0210	14.65	12.95	3.48	Sa(x)	A	0.24
NGC 3160	319	10:13:55.115	+38:50:34.534	0.0229	14.64	12.92	3.63	Sab	AB	0.29
UGC 05598	326	10:22:14.004	+20:35:21.879	0.0188	14.80	13.52	2.77	Sb	A	0.30
NGC 3303	340	10:37:00.088	+18:08:09.194	0.0200	14.24	12.55	3.56	S0a(x)	AB	0.60
UGC 05771	341	10:37:19.340	+43:35:15.321	0.0248	14.10	12.43	3.58	E6	A	0.71
NGC 3381	353	10:48:24.818	+34:42:41.078	0.0054	13.41	12.68	1.82	Sd	B	0.71
UGC 06036	364	10:55:55.261	+36:51:41.468	0.0218	14.14	12.47	3.65	Sa	A	0.29
IC 0674	381	11:11:06.361	+43:37:58.812	0.0251	14.07	12.57	3.40	Sab	B	0.65
NGC 3614	388	11:18:21.332	+45:44:53.408	0.0077	13.60	12.37	2.90	Sbc	AB	0.72
NGC 3811	436	11:41:16.630	+47:41:26.920	0.0102	13.48	12.06	3.00	Sbc	B	0.62
NGC 3991	475	11:57:30.959	+32:20:13.289	0.0108	14.08	13.52	1.42	Sm	A	0.22
NGC 3994	476	11:57:36.866	+32:16:39.426	0.0103	13.46	11.98	2.87	Sbc	AB	0.47
NGC 4003	479	11:57:59.033	+23:07:29.636	0.0219	13.96	12.39	3.29	S0a	B	0.42
UGC 07012	486	12:02:03.146	+29:50:52.737	0.0102	14.41	13.81	1.73	Sed	AB	0.54
NGC 4149	502	12:10:32.849	+58:18:14.884	0.0103	13.86	12.30	3.10	Sa	AB	0.19
NGC 4185	515	12:13:22.192	+28:30:39.468	0.0130	13.27	12.01	3.03	Sbc	AB	0.64
NGC 4210	518	12:15:15.842	+65:59:07.156	0.0091	13.44	12.03	2.99	Sb	B	0.73
IC 0776	528	12:19:03.120	+08:51:22.153	0.0081	14.74	14.42	1.25	Sdm	A	0.56
NGC 4470	548	12:29:37.778	+07:49:27.129	0.0079	12.96	12.12	1.84	Sc	A	0.66
NGC 4644	569	12:42:42.664	+55:08:43.897	0.0165	14.41	13.02	3.00	Sb	A	0.45
NGC 4676A	577	12:46:10.107	+30:43:54.899	0.0222	14.78	13.08	2.99	Sdm(x)	AB	0.28
NGC 4874	592	12:59:35.709	+27:57:33.339	0.0239	12.89	11.37	3.42	E0	A	0.88
UGC 08107	593	12:59:39.778	+53:20:28.203	0.0277	14.30	12.71	3.45	Sa(x)	A	0.39
UGC 08231	606	13:08:37.555	+54:04:27.737	0.0083	14.44	13.97	1.45	Sd	AB	0.37
UGC 08234	607	13:08:46.505	+62:16:18.099	0.0270	13.45	12.23	2.92	S0	A	0.63
NGC 5000	608	13:09:47.487	+28:54:24.993	0.0187	13.94	12.50	2.97	Sbc	B	0.60
UGC 08250	609	13:10:20.138	+32:28:59.479	0.0176	15.17	14.03	2.39	Sc	A	0.19
UGC 08267	610	13:11:11.334	+43:43:34.787	0.0242	14.87	13.14	3.39	Sb	AB	0.20
NGC 5205	630	13:30:03.571	+62:30:41.624	0.0059	13.45	12.12	2.92	Sbc	B	0.67
NGC 5216	633	13:32:06.896	+62:42:02.392	0.0098	13.58	12.12	3.27	E0	A	0.91
UGC 08733	657	13:48:38.994	+43:24:44.830	0.0078	14.70	13.63	1.83	Sdm	B	0.49
IC 0944	663	13:51:30.868	+14:05:31.959	0.0234	13.67	11.95	3.59	Sab	A	0.30
UGC 08778	664	13:52:06.669	+38:04:01.273	0.0108	14.20	12.90	2.89	Sb	A	0.21
UGC 08781	665	13:52:22.745	+21:32:21.669	0.0253	13.92	12.49	3.31	Sb	B	0.52
NGC 5378	676	13:56:51.013	+37:47:50.055	0.0100	13.53	12.12	3.23	Sb	B	0.63
NGC 5394	680	13:58:33.201	+37:27:13.118	0.0114	14.39	13.59	2.29	Sbc(x)	B	0.74
NGC 5406	684	14:00:20.120	+38:54:55.528	0.0180	13.37	11.84	3.46	Sb	B	0.88
NGC 5485	708	14:07:11.349	+55:00:05.933	0.0064	12.41	10.88	3.42	E5	A	0.81
UGC 09067	714	14:10:45.458	+15:12:33.858	0.0262	14.29	13.09	2.61	Sbc	AB	0.45
NGC 5520	715	14:12:22.811	+50:20:54.309	0.0063	13.31	12.05	2.71	Sbc	A	0.57
NGC 5614	740	14:24:07.588	+34:51:31.869	0.0130	12.68	11.03	3.56	Sa(x)	A	0.95

comprise $\sim 37\%$ of each color-magnitude bin of the total 600 objects in the full CALIFA sample. The deficit of low-luminosity galaxies with intermediate colors, noted in DR1, has improved. Fluctuations can be explained by the effect of low-number statistics, especially within those color-magnitude bins in which the MS contains fewer galaxies. This point is highlighted in Fig. 2 and emphasizes the need to eventually observe the full CALIFA sample to obtain a sufficient number of galaxies in each bin for a meaningful multi dimensional statistical analysis.

Figure 3 compares the redshift distribution of the CALIFA galaxies in the DR2 and DR1, as a percentage of the CALIFA MS. Except for a few particular bins, the redshift distribution is homogeneous with respect to the MS.

One important test to be made is whether the number density of galaxies estimated from the DR2 sample is not biased with respect to the MS. Figure 4 shows the r -band luminosity function (LF) of the DR2 sample as compared to the MS and the reference SDSS sample of Blanton et al. (2005). We refer to W14 for all technical details on how the LFs are obtained and for the

Table 1. continued.

Name	ID ^a	α (J2000) ^b	δ (J2000) ^b	z ^c	m_g ^d	m_z ^d	$m_u - m_z$ ^d	Type ^e	Bar ^f	b/a ^g
NGC 5630	749	14:27:36.610	+41:15:27.919	0.0089	13.60	13.04	1.62	Sdm	B	0.32
NGC 5682	758	14:34:44.978	+48:40:12.831	0.0076	14.39	13.64	1.74	Scd	B	0.31
NGC 5720	764	14:38:33.281	+50:48:54.874	0.0260	14.13	12.72	3.18	Sbc	B	0.65
UGC 09476	769	14:41:32.029	+44:30:45.978	0.0109	13.63	12.61	2.31	Sbc	A	0.63
NGC 5784	778	14:54:16.450	+42:33:28.452	0.0181	13.20	11.69	3.45	S0	A	0.81
UGC 09665	783	15:01:32.465	+48:19:10.928	0.0085	14.30	12.83	3.12	Sb	A	0.23
NGC 5888	789	15:13:07.372	+41:15:52.666	0.0291	13.84	12.25	3.47	Sb	B	0.54
NGC 5908	791	15:16:43.191	+55:24:34.461	0.0112	13.12	11.15	3.97	Sa	A	0.24
NGC 5930	795	15:26:07.950	+41:40:33.829	0.0088	13.53	11.76	3.27	Sab(x)	AB	0.84
UGC 09873	797	15:29:50.651	+42:37:44.104	0.0188	15.19	13.95	2.63	Sb	A	0.21
UGC 09892	798	15:32:51.947	+41:11:29.282	0.0189	14.80	13.51	2.78	Sbc	A	0.29
NGC 5966	806	15:35:52.108	+39:46:08.047	0.0151	13.24	11.76	3.36	E4	A	0.60
IC 4566	807	15:36:42.162	+43:32:21.545	0.0186	13.84	12.35	3.39	Sb	B	0.69
NGC 5987	809	15:39:57.356	+58:04:46.249	0.0100	12.76	11.07	3.62	Sa	A	0.39
NGC 6004	813	15:50:22.720	+18:56:21.386	0.0128	13.55	12.22	3.02	Sbc	B	0.94
NGC 6020	815	15:57:08.137	+22:24:16.492	0.0144	13.40	11.94	3.40	E4	A	0.73
NGC 6021	816	15:57:30.685	+15:57:21.766	0.0158	13.63	12.10	3.45	E5	A	0.78
NGC 6032	820	16:03:01.124	+20:57:21.330	0.0145	13.97	12.56	2.94	Sbc	B	0.30
UGC 10205	822	16:06:40.181	+30:05:56.651	0.0219	13.89	12.29	3.32	S0a	A	0.58
NGC 6063	823	16:07:12.993	+07:58:44.368	0.0095	13.63	12.53	2.56	Sbc	A	0.60
IC 1199	824	16:10:34.347	+10:02:25.322	0.0158	13.97	12.59	2.86	Sb	AB	0.41
NGC 6081	826	16:12:56.858	+09:52:01.580	0.0171	13.62	11.93	3.65	S0a	A	0.46
UGC 10331	828	16:17:21.123	+59:19:12.466	0.0152	14.50	13.60	2.11	Sc(x)	AB	0.26
NGC 6125	829	16:19:11.536	+57:59:02.899	0.0154	12.91	11.39	3.43	E1	A	0.91
NGC 6132	831	16:23:38.840	+11:47:10.459	0.0166	14.18	13.09	2.38	Sbc	A	0.36
NGC 6146	832	16:25:10.331	+40:53:34.325	0.0292	13.28	11.80	3.40	E5	A	0.77
NGC 6154	833	16:25:30.483	+49:50:24.934	0.0199	13.81	12.39	3.33	Sab	B	0.65
UGC 10380	834	16:25:49.911	+16:34:33.827	0.0292	14.89	13.18	3.57	Sb	AB	0.28
NGC 6150	835	16:25:49.966	+40:29:19.419	0.0292	13.92	12.35	3.49	E7	A	0.48
UGC 10384	837	16:26:46.685	+11:34:48.968	0.0165	14.70	13.22	2.82	Sb	A	0.22
UGC 10388	838	16:27:02.974	+16:22:56.031	0.0154	14.03	12.67	3.15	Sa	AB	0.40
NGC 6173	840	16:29:44.875	+40:48:41.965	0.0294	13.16	11.61	3.49	E6	A	0.65
NGC 6168	841	16:31:20.834	+20:11:08.298	0.0086	14.70	13.58	2.30	Sc	AB	0.18
UGC 10650	843	17:00:14.583	+23:06:22.839	0.0099	15.35	16.29	0.04	Scd	A	0.20
UGC 10693	845	17:04:53.020	+41:51:55.764	0.0280	13.45	12.00	3.41	E7	AB	0.68
UGC 10695	846	17:05:05.574	+43:02:35.360	0.0280	13.98	12.42	3.50	E5	A	0.67
UGC 10710	847	17:06:52.522	+43:07:19.961	0.0280	14.35	12.75	3.31	Sb	A	0.25
NGC 6310	848	17:07:57.480	+60:59:24.569	0.0114	13.72	12.29	3.24	Sb	A	0.22
NGC 6314	850	17:12:38.716	+23:16:12.297	0.0221	13.52	12.12	3.09	Sab	A	0.51
NGC 6338	851	17:15:22.976	+57:24:40.284	0.0274	13.33	11.70	3.66	E5	A	0.66
UGC 10796	852	17:16:47.725	+61:55:12.433	0.0102	14.28	13.74	1.44	Scd	AB	0.49
UGC 10811	854	17:18:43.726	+58:08:06.433	0.0291	14.55	13.02	3.30	Sb	B	0.42
IC 1256	856	17:23:47.285	+26:29:11.482	0.0159	13.91	12.70	2.60	Sb	AB	0.59
NGC 6394	857	17:30:21.423	+59:38:23.613	0.0284	14.53	13.06	3.05	Sbc	B	0.29
UGC 10905	858	17:34:06.438	+25:20:38.290	0.0265	13.68	12.15	3.37	S0a	A	0.53
NGC 6411	859	17:35:32.849	+60:48:48.255	0.0123	12.73	11.37	3.34	E4	A	0.68
NGC 6427	860	17:43:38.599	+25:29:38.178	0.0108	13.28	11.82	3.30	S0	AB	0.61
UGC 10972	861	17:46:21.921	+26:32:37.681	0.0155	14.10	12.78	2.91	Sbc	A	0.22
NGC 6478	862	17:48:37.742	+51:09:13.683	0.0227	14.16	12.83	2.59	Sc	A	0.42
NGC 6497	863	17:51:17.966	+59:28:15.149	0.0105	13.73	12.26	3.41	Sab	B	0.65
NGC 6515	864	17:57:25.195	+50:43:41.242	0.0228	13.52	12.10	3.27	E3	A	0.78
UGC 11228	865	18:24:46.260	+41:29:33.853	0.0194	13.78	12.26	3.43	S0	B	0.57
UGC 11262	866	18:30:35.698	+42:41:33.704	0.0186	14.89	13.75	2.65	Sc	A	0.39

explanation of the turnover of the LF at $M_r \approx -18.6$. The DR2 sample already reproduces the CALIFA MS LF very closely for most of the magnitude bins.

An important characteristic of the CALIFA MS is that it contains galaxies of all morphological types. Galaxy morphologies were inferred by combining the independent visual classifications of several collaboration members as described in W14. Figure 5 shows a histogram of bar strength as well as the percentage of DR2 galaxies with respect to the CALIFA MS distribution

for different morphological types grouped into elliptical, lenticular, and spiral galaxies (and subtypes). A more detailed classification of ellipticals (from 0 to 7) is available, but we do not distinguish between them here because of the low number of galaxies per elliptical subtype within DR2. From 200 galaxies in DR2, 18 have been classified as ongoing mergers² (of any type). As clearly seen in Fig. 5, the percentage of DR2 galaxies with respect to the CALIFA MS is almost constant for all

² According to our visual classification.

Table 1. continued.

Name	ID ^a	α (J2000) ^b	δ (J2000) ^b	z ^c	m_g ^d	m_z ^d	$m_u - m_z$ ^d	Type ^e	Bar ^f	b/a^g
NGC 6762	867	19:05:37.090	+63:56:02.791	0.0098	13.81	12.37	3.29	Sab	A	0.49
MCG-02-51-004	868	20:15:39.858	-13:37:19.227	0.0188	13.88	12.47	2.93	Sb	A	0.37
NGC 6941	869	20:36:23.474	-04:37:07.459	0.0208	13.47	12.06	3.14	Sb	B	0.73
NGC 6978	871	20:52:35.435	-05:42:40.041	0.0199	13.48	11.95	3.27	Sb	AB	0.39
UGC 11649	872	20:55:27.620	-01:13:30.879	0.0127	13.47	12.06	3.19	Sab	B	0.88
NGC 7025	874	21:07:47.336	+16:20:09.224	0.0166	12.85	11.25	3.57	S0a	A	0.72
UGC 11717	877	21:18:35.413	+19:43:07.397	0.0212	14.20	12.45	3.60	Sab	A	0.47
MCG-01-54-016	878	21:25:59.971	-03:48:32.267	0.0098	14.90	14.26	1.56	Scd	A	0.13
UGC 11792	880	21:42:12.700	+05:36:55.333	0.0160	14.82	13.30	3.08	Sbc	A	0.20
NGC 7194	881	22:03:30.938	+12:38:12.414	0.0272	13.55	12.01	3.47	E3	A	0.79
UGC 11958	883	22:14:46.882	+13:50:27.132	0.0262	14.02	12.47	3.44	S0(x)	A	0.74
UGC 11982	884	22:18:52.939	-01:03:31.254	0.0162	15.24	14.09	2.68	Scd	A	0.23
UGC 12054	885	22:29:32.454	+07:43:33.685	0.0070	14.62	13.82	1.89	Sc	A	0.24
NGC 7311	886	22:34:06.797	+05:34:13.166	0.0150	12.60	11.18	3.25	Sa	A	0.49
NGC 7321	887	22:36:28.022	+21:37:18.354	0.0238	13.58	12.29	2.98	Sbc	B	0.69
UGC 12127	888	22:38:29.421	+35:19:46.894	0.0275	13.46	11.94	3.53	E1	A	0.85
UGC 12185	890	22:47:25.063	+31:22:24.672	0.0222	14.16	12.75	3.21	Sb	B	0.47
UGC 12224	891	22:52:38.364	+06:05:37.045	0.0118	13.89	12.86	2.60	Sc	A	0.83
NGC 7436B	893	22:57:57.546	+26:09:00.012	0.0246	13.40	11.80	3.59	E2(x)	A	0.90
UGC 12274	894	22:58:19.600	+26:03:42.974	0.0255	14.21	12.59	3.63	Sa	A	0.36
UGC 12308	895	23:01:18.684	+14:20:22.466	0.0076	14.69	14.01	1.82	Scd	A	0.25
NGC 7466	896	23:02:03.464	+27:03:09.342	0.0251	14.22	12.76	3.00	Sbc	A	0.53
NGC 7489	898	23:07:32.695	+22:59:53.127	0.0208	13.70	12.61	2.42	Sbc	A	0.55
NGC 7549	901	23:15:17.271	+19:02:30.437	0.0157	13.98	12.62	2.76	Sbc	B	0.75
NGC 7563	902	23:15:55.928	+13:11:46.040	0.0143	13.33	11.80	3.45	Sa	B	0.68
NGC 7562	903	23:15:57.495	+06:41:15.151	0.0120	12.10	10.56	3.43	E4	A	0.68
NGC 7591	904	23:18:16.260	+06:35:08.860	0.0165	13.39	11.80	3.24	Sbc	B	0.59
UGC 12519	909	23:20:02.769	+15:57:10.028	0.0146	14.24	12.90	2.87	Sc	AB	0.21
UGC 12518	910	23:20:12.737	+07:55:55.915	0.0093	14.74	12.91	3.67	Sb	A	0.23
NGC 7625	913	23:20:30.139	+17:13:32.034	0.0054	13.03	11.47	3.03	Sa	A	0.78
NGC 7631	914	23:21:26.675	+08:13:03.463	0.0125	13.40	12.05	3.00	Sb	A	0.44
NGC 7653	915	23:24:49.358	+15:16:32.165	0.0142	13.17	11.88	3.00	Sb	A	0.88
NGC 7671	916	23:27:19.336	+12:28:02.673	0.0135	13.14	11.56	3.56	S0	A	0.65
NGC 7683	917	23:29:03.823	+11:26:42.607	0.0124	13.00	11.38	3.61	S0	A	0.62
UGC 12688	922	23:35:26.096	+07:19:19.554	0.0174	14.53	13.47	2.29	Scd(x)	AB	0.29
NGC 7716	924	23:36:31.450	+00:17:50.179	0.0085	13.03	11.60	3.25	Sb	A	0.71
NGC 7738	927	23:44:02.058	+00:30:59.838	0.0228	13.94	12.17	3.56	Sb	B	0.31
UGC 12816	930	23:51:50.691	+03:04:57.909	0.0178	14.09	13.16	2.08	Sc	A	0.62
NGC 7783NED01	932	23:54:10.078	+00:22:58.299	0.0262	13.62	12.06	3.43	Sa(x)	A	0.46
UGC 12864	935	23:57:23.921	+30:59:31.456	0.0156	14.24	13.25	2.19	Sc	B	0.32
MCG-01-01-012	936	23:59:10.803	-04:11:29.763	0.0193	14.64	12.83	4.07	Sab	AB	0.26
NGC 7800	937	23:59:36.753	+14:48:25.043	0.0058	13.35	13.16	1.11	Ir	AB	0.40
NGC 5947	938	15:30:36.595	+42:43:01.732	0.0198	14.07	12.81	2.80	Sbc	B	0.83
NGC 4676B ^h	939	12:46:11.235	+30:43:21.871	0.0218	17.00	15.31	3.44	Sb(x)	B	0.82

types, implying that the DR2 coverage seems to be consistent with a random selection. Axis ratios (b/a) were measured from the SDSS r -band image using growth curve analysis, by calculating light moments after proper sky subtraction and masking of foreground stars (see W14 for details). The axis ratios can be used as a proxy of the inclination of spiral galaxies. Figure 6 shows that the DR2 sample covers the same range of axis ratios as the MS. A Kolmogorov-Smirnov test gives a <5% confidence that the DR2 sample is drawn from a different distribution than the underlying MS.

In Fig. 7, we present the distribution of stellar masses for the DR2 galaxies. Galaxy stellar masses are from González Delgado et al. (2014a), and they have been estimated following the process described in Pérez et al. (2013), Cid Fernandes et al. (2013, 2014), and González Delgado et al. (2014b). These masses account for spatial variations in both M/L ratio and stellar extinction. In short, we use the code (Cid Fernandes et al. 2005) to fit each spectrum extracted from the datacube with a combination of SSP models from the Granada

(González Delgado et al. 2005) and MILES (Vazdekis et al. 2010) libraries, that cover the full metallicity range of the MILES models ($\log Z/Z_{\odot}$ from -2.3 to $+0.22$), and ages from 0.001 to 14 Gyr. We assume a Salpeter IMF. The DR2 galaxies cover intermediate to high-mass galaxies, including at least ten galaxies per 0.25 dex bin between 10^{10} and $10^{11.75} M_{\odot}$ and a median value close to $10^{11} M_{\odot}$. The asymmetric distribution is expected from the distribution in absolute magnitudes (see Fig. 2) and is inherited from the CALIFA MS because of its selection criteria (see W14 for details).

A more general “panoramic view” of the DR2 sample characteristics is presented in Fig. 8. Several of the main properties observable in 2D are highlighted for 169 randomly-selected galaxies, shown individually in hexagons that together form the shape of a CALIFA-like FoV. The galaxies have been ordered by r -band absolute magnitude, from top right (brightest absolute magnitude) to bottom left (faintest absolute magnitude). The highlighted properties derive from several different analysis pipelines developed within the collaboration. Stellar properties,

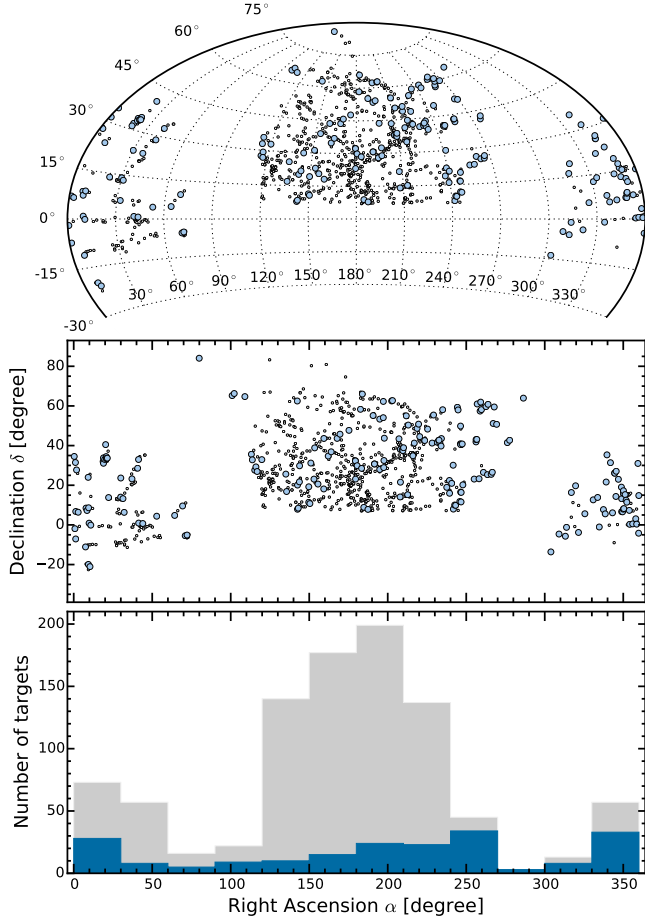


Fig. 1. Distribution on the sky of galaxies in the CALIFA mother sample (small open circles) and CALIFA DR2 sample (blue filled symbols). The *upper panel* shows the distribution in an Aitoff projection in J2000 Equatorial Coordinates (cut off at $\delta = -30^\circ$, below which the sample does not extend), while the *middle panel* is plotted in the Cartesian system. The *lower panel* shows both samples as a function of right ascension. The number distribution in bins of 30° along the right ascension is shown for the mother sample (gray area) and the DR2 sample (blue area).

like ages and mass surface density, were measured with the code (see references in the preceding paragraph describing the distribution of stellar masses in the sample) while gas properties and emission lines were measured using FIT3D (Sánchez et al. 2007). This plot is only intended to demonstrate the diversity of the DR2 sample.

3. Observing strategy and setup overview

For the sake of completeness, we provide here a brief summary of the instrument layout and observing strategy. All the details can be found in S12. The PPak fiber bundle of the PMAS instrument has a FoV of $74'' \times 64''$. There are 382 fibers in total, distributed in three different groups. The PPak Integral Field Unit (IFU) holds 331 “science” fibers in a hexagonal grid with a maximum diameter of $74''$ while each fiber projects to $2''.7$ in diameter on the sky. The fiber-to-fiber distance is $3''.2$, which yields a total filling factor of 0.6. An additional set of 36 fibers devoted to measuring the surrounding sky background are distributed in six bundles of 6 fibers each, located in a ring $72''$

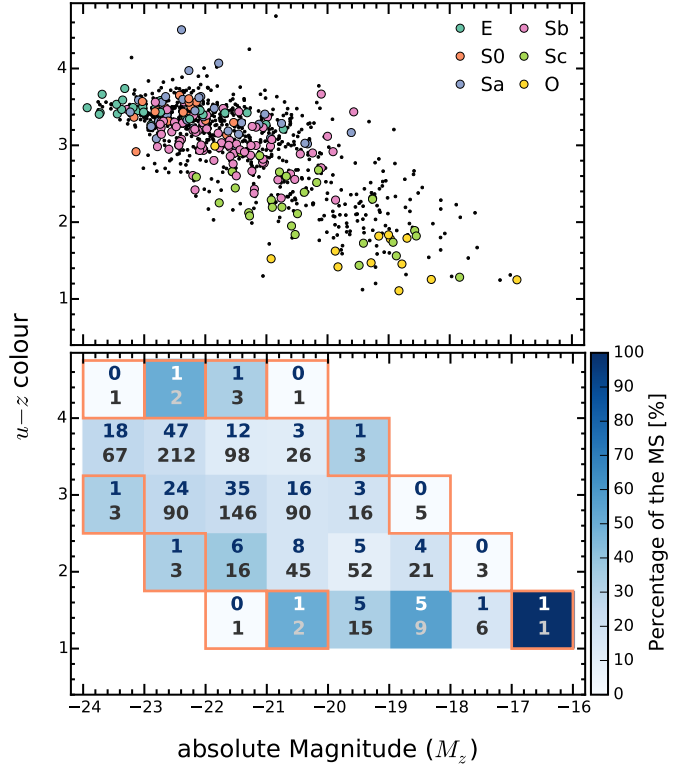


Fig. 2. *Upper panel:* distribution of CALIFA galaxies in the $u-z$ vs. M_z color-magnitude diagram. Black dots denote galaxies in the CALIFA mother sample (S12, W14) and colored symbols indicate CALIFA DR2 galaxies. Different colors account for the morphological classification, which range from ellipticals (E) to late-type spirals; group “O” includes Sd, Sdm, Sm, and I types. *Lower panel:* fraction of galaxies in the DR2 sample with respect to the CALIFA MS distribution (939 objects) in bins of 1 mag in M_z and 0.75 mag in $u-z$. The total number of galaxies per bin in the DR2 sample and the MS are shown in the upper and lower part of each bin, respectively. Bins for which the number of galaxies in the MS is less than 5 are prone to low-number statistics and enclosed by an orange square for better identification.

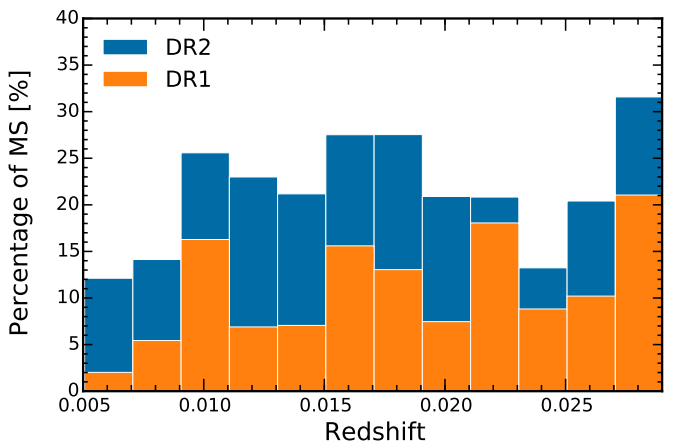


Fig. 3. Redshift distribution of the DR2 (blue) and DR1 (orange) as percentage of the CALIFA MS.

from the center. Finally, there are 15 extra fibers connected to the calibration unit.

Every galaxy in the CALIFA sample is observed in the optical range using two different overlapping setups. The V500 low-resolution mode ($R \sim 850$) covers the range $3745\text{--}7500 \text{\AA}$,

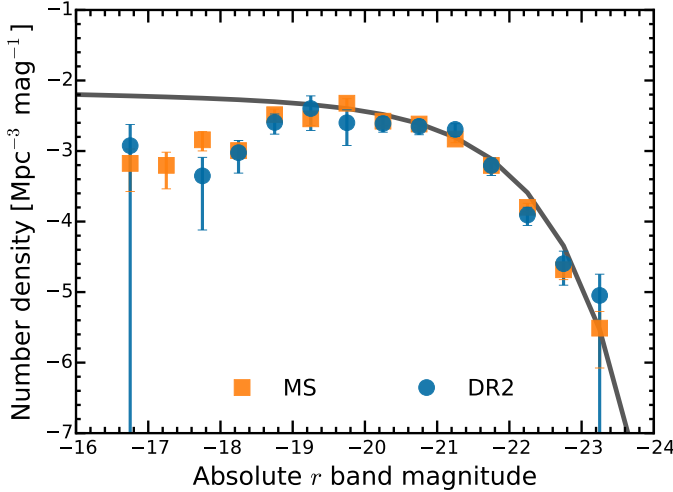


Fig. 4. Luminosity functions in the r band of the CALIFA mother sample (orange squares) and the DR2 sample (blue points). Error bars represent Poissonian uncertainties. The line shows the Schechter fit to the LF of Blanton et al. (2005).

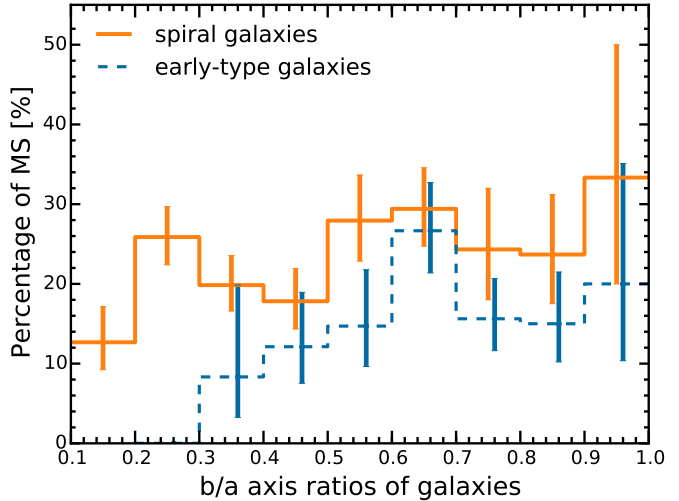


Fig. 6. Percentage of galaxies in the DR2 sample with respect to the CALIFA MS distribution, as a function of the light-weighted axis ratio (b/a). Galaxies were separated into early-type galaxies (E+S0) and spiral galaxies (Sa and later). The CALIFA mother sample does not include any elliptical galaxies with $b/a < 0.3$. Error bars are computed from the binomial errors of the associated DR2 number counts.

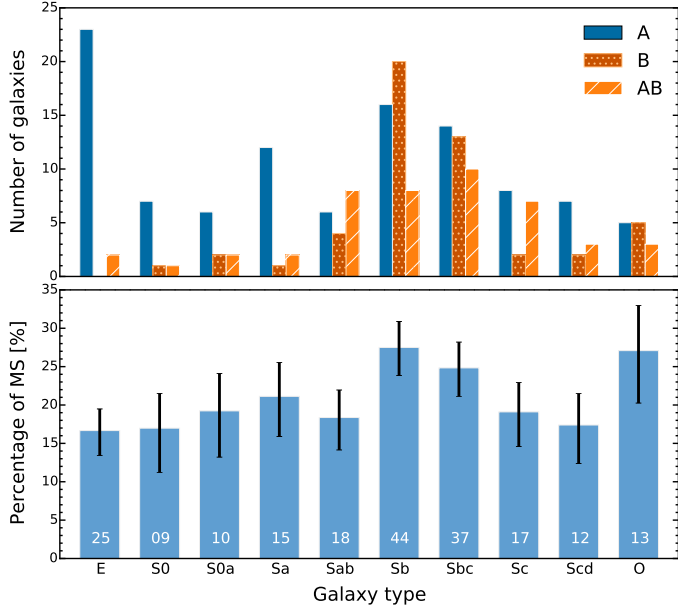


Fig. 5. Distribution of visually classified morphological types in the DR2 sample. We divide the galaxies into ellipticals (E), spirals (from S0 to Scd), and the “other” group “O”, which includes Sd, Sdm, Sm, and I (only one) types. *Upper panel:* bar strength histogram, where A stands for non-barred, B for barred and AB if unsure. *Lower panel:* the percentage of galaxies in the DR2 sample with respect to the CALIFA MS distribution. The total number of galaxies in the DR2 for each morphology type is written on each bar. Error bars are computed from the binomial errors of the associated DR2 number counts (Wilson 1927). The morphological distribution of the DR2 sample is similar to that of the mother sample.

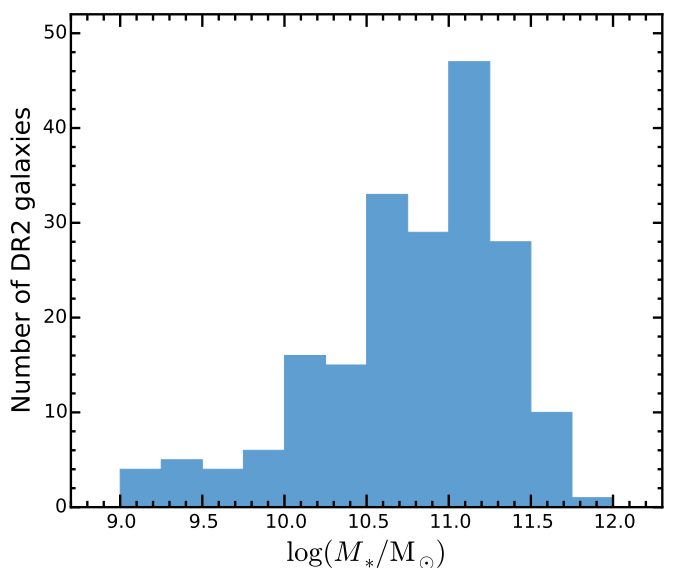


Fig. 7. Distribution of stellar masses in the DR2 sample. The stellar masses are determined from the CALIFA data using spectral fitting techniques (see text for details).

The exposure time per pointing is fixed. We carry out V1200 observations during dark nights with an exposure time of 1800 s per pointing (split in 2 or 3 individual exposures). We take V500 observations during gray nights with 900 s per pointing.

In the following section, we describe the improvements to the CALIFA data reduction pipeline used to produce the DR2 data.

4. Data processing and error propagation

4.1. Overview of the reduction scheme

As described in H13, since V1.3c the CALIFA pipeline has a Python-based architecture (Py3D package). Here we present a summary of the main steps of the reduction process. The

but it is affected by internal vignetting within the spectrograph giving an unvignetted range of 4240–7140 Å. The blue mid-resolution setup (V1200; $R \sim 1650$) covers the range 3400–4840 Å with an unvignetted range of 3650–4620 Å. The resolutions quoted are those at the overlapping wavelength range ($\lambda \sim 4500$ Å). To reach a filling factor of 100% across the FoV, a 3-pointing dithering scheme is used for each object.

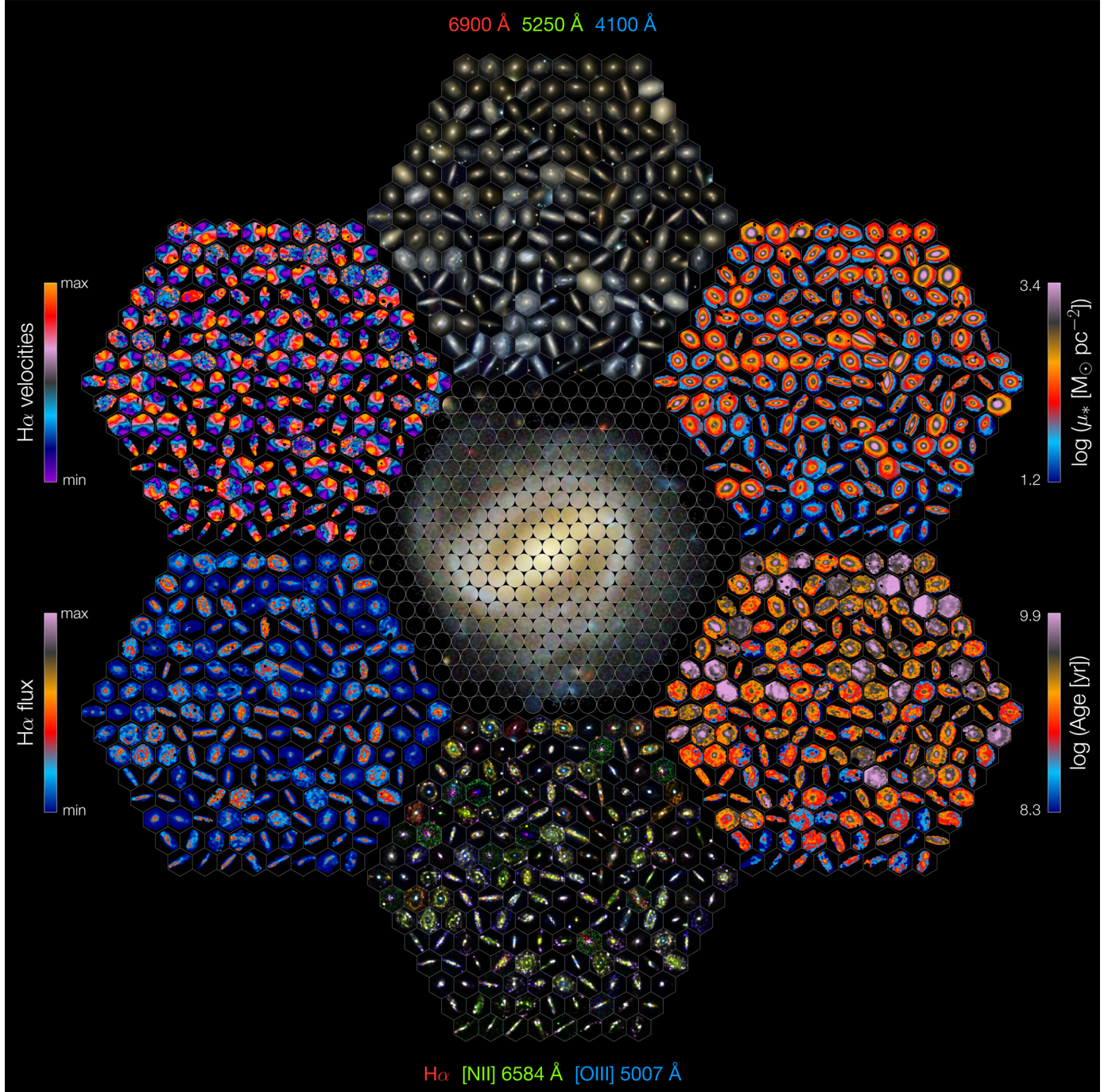


Fig. 8. CALIFA ‘panoramic view’ (also CALIFA’s ‘Mandala’) representation, consisting of the basic physical properties (all of them derived from the CALIFA datacubes) of a subsample of 169 galaxies extracted randomly from DR2. We show 1) 3-color broadband images (top center; central wavelength 6900 Å, 5250 Å, and 4100 Å); 2) stellar mass surface densities (upper right); 3) ages (lower right); 4) narrowband images (bottom center; emission lines: H α , [N II] 6584 Å, and [O III] 5007 Å); 5) H α emission (lower left), and 6) H α kinematics (upper left). The CALIFA logo is placed at the central hexagon.

particular improvements on the new CALIFA pipeline, V1.5, are described in Sect. 4.2.

Each raw frame is stored in four different FITS files, corresponding to each of the four amplifiers of the detector. As a first step, these four files are combined into a single frame and bias subtracted. We developed a new tool (Husemann et al. 2012) for the detection and clipping of cosmic rays, which uses a Laplacian edge detection scheme combined with a point spread function convolution approach. Relative flexure offsets are estimated with respect to the continuum and arc-lamp calibration

frames and the wavelength solution is corrected for each individual science frame. The stray-light map is reconstructed using the gaps between the fiber traces and subtracted from the calibration and science exposures. For spectral extraction, the widths of the fiber profiles are measured using the position of the fibers obtained from the continuum lamp. An optimal extraction algorithm (Horne 1986) is used to extract the spectra based on the previous measurements of the position and widths. The extracted flux, for each pixel in the dispersion direction, is stored in a row-stacked-spectrum file (RSS). The wavelength

solution is obtained from the HeHgCd calibration lamp exposure for each CALIFA data set. The spectra are resampled to a linear grid in wavelength and the spectral resolution is homogenized to a common value along the dispersion axis using a Gaussian convolution. Flexure offsets in the dispersion direction are included at this step. The Poisson plus read-out noise (and bad pixel masks) are propagated in the reduction process. For the wavelength solution, errors are analytically propagated during the Gaussian convolution and a Monte Carlo approach is used to estimate the noise vector after the spline resampling of the spectra. Fiber transmission throughput is corrected by comparing the RSS science frames with the corresponding sky exposures taken during twilight.

In the V1.3c pipeline, standard star observations were used to derive the sensitivity curve to perform the flux calibration of the science exposures. Aperture losses were empirically corrected by comparing the CALIFA spectra with SDSS images. In the V1.5 pipeline, we follow a completely new approach described in Sect. 4.2. After flux calibration, frames are corrected for telluric lines. The sky spectrum is obtained by taking the mean of the 30 faintest sky fibers out of the 36 sky fibers of PPak, and then subtracted from the science frames.

The science spectra corresponding to the three dithered exposures are combined into a single frame of 993 spectra. In V1.3c, these three pointings were rescaled to a common intensity, by comparing the integrated spectra within an aperture of $30''/\text{diameter}$. The new procedure followed in V1.5 is explained in Sect. 4.2. After correction for Galactic extinction, the RSS is ready for the spatial rearranging of the fibers and creation of the datacube. We use a flux-conserving inverse-distance weighting scheme to reconstruct a spatial image with a sampling of $1''$. The pipeline V1.5 uses a new set of parameters (see Sect. 4.2) that improves the spatial resolution of the datacube. First, we reconstruct the datacube and estimate the differential atmospheric refraction (DAR) effect. In a second step, we reconstruct the cube again where the position of the fiber against the regular grid is changed according to the DAR offset measured in the first reconstruction. This two-stage iteration avoids another resampling step, important for accurate error propagation. Finally, a new procedure is applied for the absolute flux recalibration and astronomical registration, explained in the following section.

4.2. Improvements to the CALIFA data reduction scheme

The main improvements to the current pipeline, V1.5, are: i) a new sensitivity curve for the V500 setup obtained from a dedicated calibration program for several CALIFA elliptical galaxies (Husemann et al., in prep.); ii) a new registering method, comparing individual CALIFA pointings with SDSS images; and iii) an improved image reconstruction method (cube interpolation). Step ii) also improves the absolute photometric matching of the three dithered pointings.

The new version starts with the RSS files of the three individual pointings after sky subtraction produced by pipeline V1.3c. The V500 RSS files are spectrophotometrically recalibrated with the new sensitivity curve. A new estimate for the sensitivity curve was necessary because it was based on standard star observations in V1.3c, which result in significant uncertainties. Although this is a common procedure for optical spectroscopy, it is an issue for CALIFA because of the finite size of the fibers of PPak. Aperture losses can be very significant, and come in two flavors for PPak: 1) a global aperture loss that depends on the relative position of star with respect to its nearest fibers; and 2) a wavelength-dependent aperture loss caused

by atmospheric dispersion, which leads to a smooth change in the apparent position of the star and the FWHM of the seeing as a function of wavelength. While the global aperture loss can be corrected for by renormalizing the spectra based upon photometry, the wavelength-dependent losses affect the shape of the sensitivity curve and are harder to correct.

The aperture losses of the stars are mainly introduced by their point-like nature. Wavelength dependent aperture losses are significantly reduced when an extended source with a smooth surface brightness distribution is observed. Bright nearby early-type galaxies, such as those observed by CALIFA, come close to a flat surface brightness distribution except for their very center. In addition, they are predominately composed of old stellar populations, so that the shape of their optical spectra only varies smoothly with radius.

For this reason, we decide to adopt smooth elliptical galaxies as secondary spectrophotometric calibrators from which the sensitivity curves for the CALIFA PMAS-PPak observations are derived. This, in turn, requires that we have this set of secondary calibrators calibrated against primary calibrators, i.e., standard spectrophotometric stars.

A dedicated calibration program was initiated to reobserve about two dozen elliptical CALIFA galaxies chosen as secondary calibrators and the standard stars with the PMAS Lens-Array (LArr) and the V300 grism. The LArr covers a continuous $16'' \times 16''$ FoV centered on the elliptical galaxies with a sampling of $1''$. A robust and accurate spectrophotometric calibration is achieved for these observations because almost the entire flux of the star is captured within the large continuous field, except the flux in the broad wings of the PSF (Sandin et al. 2008). We mainly targeted the primary HST spectroscopic standard stars, which are DA white dwarfs, for which high spectral resolution reference spectra and very accurate model spectra exist. Special care was taken in monitoring the atmospheric extinction curve during the different observing runs by targeting the same standard star twice a night with an airmass difference of about ~ 1 .

During the data reduction we homogenized LArr data taken with the V300 grism to a common spectral resolution of 9 \AA (FWHM) across the FoV and across the wavelength range. The sensitivity curve for the LArr data is the ratio of the observed counts in the standard star spectrum (corrected for atmospheric extinction at the given airmass) to the reference spectrum, smoothed to the adopted spectral resolution. Then we calibrate the early-type galaxy observations with the derived sensitivity curve and atmospheric extinction curve for each night comparing the photometry of the calibrated LArr data with aperture matched SDSS photometry in the g and r bands, we achieve an absolute spectrophotometric accuracy of <0.03 mag. Further details about the calibration program and its application to obtain a sensitivity curve for coarse fiber IFU spectrographs will be presented in a separate publication (Husemann et al., in prep.). Below we briefly outline how we processed the CALIFA data to determine the sensitivity curve based on the LArr observations of early-type galaxies.

We start with the reduced, but spectrophotometrically uncalibrated, RSS spectra for individual CALIFA pointings of the early-type galaxies. Again, we need to compare the count spectrum with the reference spectra in physical units to derive the sensitivity curve. Specifically, we smooth the RSS spectra to a spectral resolution of 9 \AA (FWHM, significantly coarser than the public CALIFA data) to match the LArr V300 grism characteristics. In addition, we resample the spectra to the heliocentric frame. All CALIFA fibers that overlap with the LArr FoV

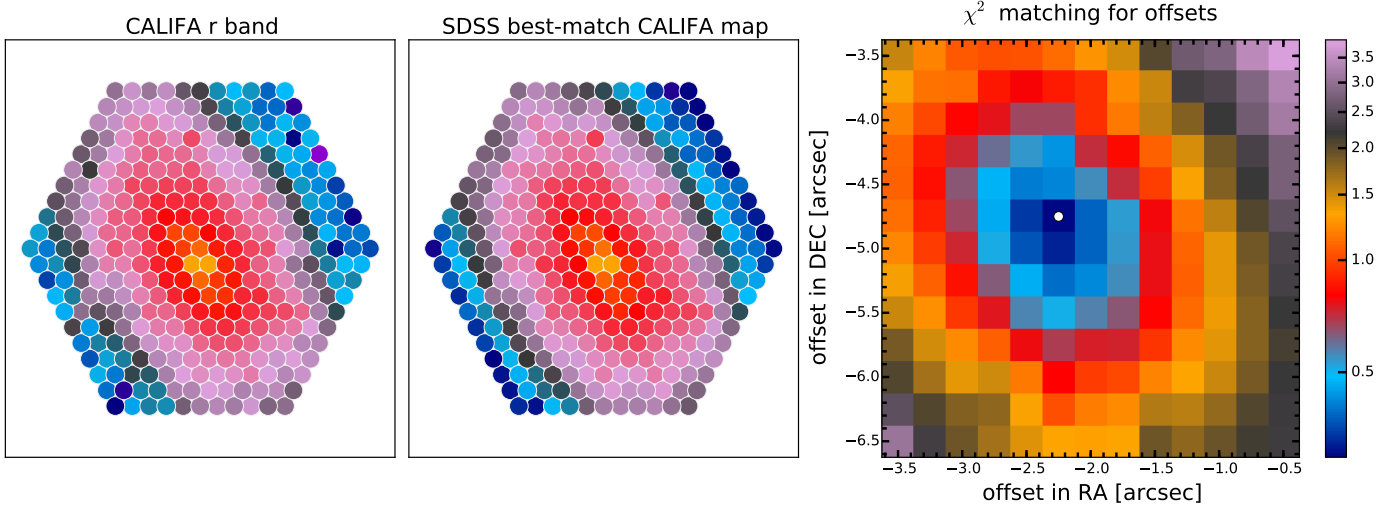


Fig. 9. Example of the registering method for pointing 1 of NGC 0496 (ID 45). *Left panel:* flux map in r -band for the PPak fibers. *Central panel:* predicted SDSS flux for each CALIFA fiber estimated using 2.7'' diameter apertures and adopting the PPak layout projected on the SDSS image for the best match according to the χ^2 map. Note that the PPak layout is not to scale, i.e., relative distances between adjacent fibers have been decreased for the sake of clarity. *Right panel:* χ^2 map of the offsets (best offset marked with a white dot).

and are more than 3'' away from the galaxy center are coadded. A corresponding reference spectrum is extracted from the LArr data based on the relative position and apertures of the CALIFA fibers considered. The ratio of the flux-calibrated LArr and uncalibrated CALIFA spectrum then corresponds to the instrumental sensitivity curve. In this case, we adopt the mean atmospheric extinction curve for Calar Alto presented by Sánchez et al. (2007) because the specific extinction curve for a given CALIFA observing night is not measured. Then we smooth the sensitivity curve by a high-order polynomial to obtain a noise-free representation, while masking out spectral regions suffering from telluric absorption. The final master sensitivity curve is computed as the average of all sensitivity curves independently derived from different reference early-type galaxies. We anticipate that most of the remaining systematic spectrophotometric uncertainty for CALIFA will be driven by the uncertainties in the wavelength-dependent atmospheric extinction at the time of each CALIFA observation.

The current pipeline also implements a new scheme for the registration of the images. First, sky-subtracted and calibrated images are created from SDSS DR7 (in the r -band for the V500 setup and the g -band for the V1200) based on the so-called “corrected frames” (fpC³). Then, the magnitude in the corresponding SDSS filter is computed for each RSS spectrum. The predicted SDSS flux for each CALIFA fiber is estimated using 2''.7 diameter apertures, adopting the PPak layout projected on the SDSS image. This layout is displaced in steps in RA and Dec across a search box in the SDSS image. Then a χ^2 map is computed to obtain the best offsets for each pointing, taking errors in the flux measurements into account (only fibers with $S/N > 3.0$ are considered) and allowing for a photometric scaling factor between the SDSS and the CALIFA observations as an additional parameter. The minimum value of the χ^2 map is used to obtain the best-fitting RA and Dec for the center of the PPak IFU with respect to the center of the CALIFA galaxy seen by SDSS. Figure 9 shows

an example of the described procedure. The photometric scale factor at the best matching position is used to rescale the absolute photometry of each particular RSS pointing to bring them onto the same flux scale.

The photometric anchoring to the SDSS images of the V1.5 data is more accurate than that of the previous version. However, there are a few datacubes where the new registering method does not return optimal results, particularly in low surface brightness edge-on galaxies or in the presence of bright foreground field stars⁴. This effect is more likely to occur in the V1200 setup, given its lower S/N on average compared to V500. In these cases, we apply the photometric SDSS matching of pipeline V1.3c described in H13 (to both setups, for the sake of consistency). We included a new “REGISTER” keyword in the header of the datacubes (see Sect. 5.4) and added a dagger symbol to the quality tables (Tables 6 and 7) to easily identify these galaxies.

The third step in the reduction sequence is the interpolation method used to convert from RSS to cube format, aimed at improving the spatial resolution. We use the position of each RSS pointing obtained in the previous step for the image reconstruction. In a series of tests, we found that an inverse-distance weighted image reconstruction scheme performs more favorably than, e.g., the drizzle method (Fruchter & Hook 2002). To increase the spatial resolution and reduce the correlation between nearby pixels, we have reduced the extent of the Gaussian kernel for the interpolation. We adopt 0.75'' for the dispersion of the Gaussian (instead of 1'' in V1.3c) and limit the kernel to a radius of 3.5'' (instead of 5''). This results in a much sharper image and a lower value for the correlated noise. In the previous pipeline V1.3c, a minimum number of 3 contributing fibers was imposed in the reconstruction of the image to achieve a homogeneous data quality across the field. With the new maximum radius in pipeline V1.5, this type of prescription results in the absence of data in the outer 2'' of the FoV, due to the wider fiber separation in the outer ring of the fiber bundle. Thus, we decided to lower this limit to 1 as the minimum number of fibers needed to fill

³ SDSS pipeline frames that have been flat-fielded and bias-subtracted; bad columns and cosmic rays have been interpolated over and sky has been subtracted.

⁴ Poor registration cases are confirmed by visual inspection of synthetic B and V broadband images and of the spectra.

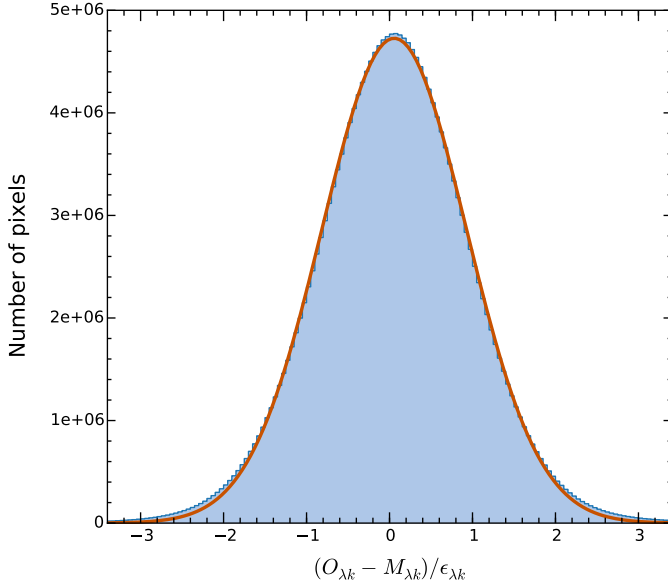


Fig. 10. Histogram of the reduced residuals $(O_{\lambda,k} - M_{\lambda,k})/\epsilon_{\lambda,k}$ for all λ 's, all bins (k) and all galaxies in DR2 (209151086 points in total). The orange line shows the best Gaussian fit to the sample.

a spaxel. We have added a new header data unit (see Sect. 5.3) that records the number of fibers used to compute the total flux per spaxel. This allows the user to control which spaxels to include if a particular science case requires a minimum number of fibers for the reconstruction of the flux. The final sampling of the produced datacube is $1'' \times 1''$ per pixel.

4.3. Characterization of spatially correlated noise

Because of the interpolation procedure used to obtain a regular grid, the output pixels in the final datacube are not independent of one another. The Gaussian interpolation method distributes the flux from a given fiber between several pixels, which are combined with neighboring pixels within a certain radius, as described in Sect. 4.2. This causes the noise in the adjacent pixels to be correlated (in the spatial dimension). The correlation implies that a measurement of the noise in a stacked spectrum of N pixels will be underestimated (noise is underestimated on scales larger than pixel units). Characterizing this effect is essential for estimating the statistical errors when spectra in datacubes are coadded.

First of all, it is important to check that the error spectra derived from the pipeline for individual spaxels are reliable. Spectral fitting analysis can provide an approximate assessment of the accuracy of the error spectra. In Fig. 10 we update Fig. 9 of H13 for DR2 data. The plot shows the histogram of reduced residuals, i.e., the difference between the observed (O_λ) and synthetic (M_λ) spectra obtained with ϵ_λ in units of the corresponding error ϵ_λ (details on the fitting procedures can be found in 6.5). The distribution is very well described by a Gaussian centered at 0.03 with $\sigma = 0.87$, only slightly less than expected if residuals are purely due to uncorrelated noise.

The correlated noise can be taken into account by providing the spatial covariance (Sharp et al. 2015). However, a more practical approach consists of using the datacubes to calculate the expected rms noise⁵, with the noise correlation ratio $\beta(N)$, as

⁵ The noise is obtained from the detrended standard deviation in certain defined wavelength windows (see Sect. 6.6).

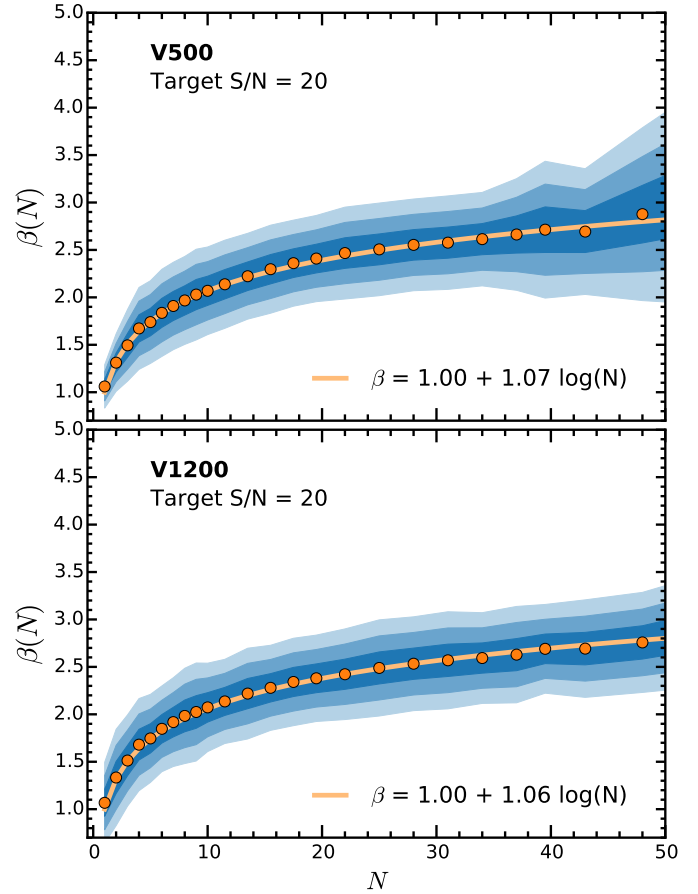


Fig. 11. Noise correlation ratio β (ratio of the real estimated error to the analytically propagated error) as a function of number of spaxels per bin for all the V500 (upper panel) and V1200 (lower panel) data of DR2 at a target S/N of 20. Shaded areas mark the 1σ , 2σ , and 3σ levels. The orange lines represent the best-fit logarithmic function with a slope $\alpha = 1.07$ and $\alpha = 1.06$, respectively.

a function of the number of pixels. To obtain a sample of coadded spaxels with different areas, we used the Voronoi adaptive binning method (implemented for optical IFS data by Cappellari & Copin 2003) with a target S/N of 20. We removed individual spaxels with $S/N < 5$ from the analysis, and coadded bins with areas larger than 60 spaxels. The β correlation ratio (or correction factor) is the ratio of the “real” or measured error to the analytically propagated error of the binned spectra as a function of bin size. The results obtained for all DR2 datacubes, shown in Fig. 11, can be well described by the logarithmic function

$$\beta(N) = 1 + \alpha \log N, \quad (1)$$

with N the number of spaxels per bin.

The values for the slope α are equal within the errors (0.01) in both setups, with a value of 1.06 for V1200 and 1.07 for V500. The slope is lower than the DR1 value (mean ~ 1.4), indicating that the noise in DR2 datacubes is less correlated than in DR1. This is expected since we changed the parameters in the interpolation (reducing the number of adjacent fibers contributing to a particular spaxel) and the registering method. In Appendix A we give some instructions on how to estimate the final coadded error spectrum and the limit of the application of Eq. (1).

Table 2. CALIFA FITS file structure.

HDU	Extension name	Format	Content
0	Primary	32-bit float	Flux density in units of $10^{-16} \text{ erg s}^{-1} \text{ cm}^{-2} \text{ \AA}^{-1}$
1	ERROR	32-bit float	1σ error on the flux density
2	ERRWEIGHT	32-bit float	Error weighting factor
3	BADPIX	8-bit integer	Bad pixel flags (1 = bad, 0 = good)
4	FIBCOVER	8-bit integer	Number of fibers used to fill each spaxel

Table 3. Dimension and sampling of CALIFA datacubes.

Setup	N_α^a	N_δ^a	N_λ^a	λ_{start}^b	λ_{end}^c	d_λ^d	δ_λ^e
V500	78	73	1877	3749 Å	7501 Å	2.0 Å	6.0 Å
V1200	78	73	1701	3650 Å	4840 Å	0.7 Å	2.3 Å

Notes. ^(a) Number of pixels in each dimension. ^(b) Wavelength of the first pixel on the wavelength direction. ^(c) Wavelength of the last pixel on the wavelength direction. ^(d) Wavelength sampling per pixel. ^(e) Homogenized spectral resolution (FWHM) over the entire wavelength range.

5. CALIFA data format and characteristics

The CALIFA data are stored and distributed as datacubes (three-dimensional data) in the standard binary FITS format and consist of several FITS Header Data Units (HDU). These datacubes contain, (1) the measured flux densities, corrected for Galactic extinction as described in S12, in units of $10^{-16} \text{ erg s}^{-1} \text{ cm}^{-2} \text{ \AA}^{-1}$ (primary datacube); (2) associated errors; (3) error weighting factors; (4) bad pixels flags; and (5) fiber coverage (Table 2). The last HDU is new added content absent in DR1, as explained in Sect. 4.2, but the others share the same properties as the previous data release. The first two axes of the cubes correspond to the spatial dimension along right ascension and declination with a $1'' \times 1''$ sampling. The third dimension represents the wavelength and is linearly sampled. Table 3 summarizes the dimensions of each datacube (N_α , N_δ , and N_λ), as well as the spectral sampling (d_λ) and constant resolution (δ_λ) along the entire wavelength range.

5.1. Error and weight datacubes

The 1σ noise level of each pixel as formally propagated by the pipeline can be found in the first FITS extension. Section 4.3 discusses the accuracy of the formal noise and the correlation, important when CALIFA data need to be spatially binned, and an empirical function is provided to account for the correlation effect. The second FITS extension (ERRWEIGHT) stores the error scaling factor for each pixel in the limiting case that all valid spaxels of the cube would be coadded (see also Appendix A). In the case of bad pixels, we assign an error value that is roughly ten orders of magnitude higher than the typical value.

5.2. Bad pixel datacubes

Bad pixel datacubes are stored in the third FITS extension (BADPIX). This information, in combination with the error vector, is essential to properly account for the potential problems in each spaxel. Pixels with flag =1 report the absence of sufficient information in the raw data due to cosmic rays, bad CCD

columns, or the effect of vignetting⁶. These bad pixels have been interpolated over and we strongly suggest not to use them for any science analysis.

Finally, the uncovered corners of the hexagonal PPak FoV are filled with zeros and flagged as bad pixels for consistency. The residuals of bright night-sky emission lines are not flagged as bad pixels.

5.3. Fiber coverage datacubes

Pipeline V1.5 adds a new FITS extension (FIBCOVER) to the datacubes, not available in previous DR1 datacubes. As explained in Sect. 4.2 we have reduced the maximum distance of fibers that can contribute to the flux of a given spaxel. The outer hexagonal-ring of fibers do not have the same coverage as any other fiber inside the hexagon. In pipeline V1.3c we imposed a minimum of 3 fibers for computing the flux of given spaxel. In V1.5, with the new radius limit this would yield an empty outer hexagonal-ring of $\sim 2''$ in the FoV. Thus, we relax to 1 the minimum number of fibers. In order to control which spaxels have enough flux “resolution”, we include a new HDU reporting the number of fibers used to account for the computed flux.

5.4. FITS header information

The FITS header contains the standard keywords that encode the information required to transform the pixel-space coordinates into sky and wavelength-space coordinates, following the World Coordinate System (WCS, Greisen & Calabretta 2002). Each CALIFA datacube contains the full FITS header information of all raw frames from which it was created. Information regarding observing and instrumental conditions such us sky brightness, flexure offsets, Galactic extinction or approximate limiting magnitude is also kept in the FITS header of each datacube. See Sect. 4.3 of H13 for nomenclature and their Table 4 for a summary of the main header keywords and meaning.

The most important new keyword added in DR2 datacubes is “REGISTER” and takes a boolean value. It indicates if a particular datacube has been successfully registered using the new method explained in Sect. 4.2 (*True*) or it has used the old V1.3c scheme (*False*). Datacubes with a *False* value are marked with a dagger in Tables 6 and 7.

6. Data quality

This second CALIFA data release (DR2) provides science-grade data for a sample of 200 galaxies, including the 100 galaxies released in the first data release (DR1), identified by an asterisk in Tables 6 and 7. As for DR1, we have run a careful quality control (QC) on the data products and selected only those

⁶ The vignetting effect imprints a characteristic inhomogeneous pattern across the FoV on the bad pixels vector. See Fig. 11 of H13 for more details.

Table 4. Definition of CALIFA DR2 quality control flags for the V500 data.

QC flag	QC parameters involved		condition(s)	condition(s)	Flag definition
— —	— —	—	>1.7	>2.0	Worst of the three parameters
			>2.0	>2.5	
			>0.15	...	
— —	— —	—	<20.5 mag _V arcsec ⁻²	<19.5	Worst of the two parameters
			>0.1	...	
			>0.30 mag	...	Worst of the three parameters
— —	— —	—	>0.35	...	
			>0.10	...	
			>30 counts	>50	Worst of the three parameters
— —	— —	—	>50	>100	
			>5	>10	
			>5.5 Å (FWHM)	...	Worst of the three parameters
— —	— —	—	>10.0	...	
			>0.5	>1.0	
			>3.0 pixels (FWHM)	...	Worst of the three parameters
— —	— —	—	≥4.0	...	
			>0.25	...	
			5577_	<-0.1 counts	Worst of the three parameters
— —	— —	—	>0.1	...	
			>1.0	...	
			<23.25 mag _V arcsec ⁻²	<22.50	
— —	— —	—	>0.06 dex	>0.097 dex	Worst of the three parameters
			<-0.06 dex	<-0.097 dex	combined with visual checks
			>0.06 dex	>0.097 dex	of the 30''-integrated spectrum:
			<-0.06 dex	<-0.097 dex	spectral shape and comparison
			>0.1	>0.2	with SDSS photometry
— —	—	—	>2.0 km s ⁻¹	>5.0	
			2	—	Combined parameter and visual inspection of registration and synthetic broadband image

galaxies that passed a series of QC checks in both setups (V500 and V1200), as we detail in this section. The QC checks are based on a set of measured parameters and/or visual inspection, resulting in a set of flags that allows one to quickly assess the quality of the data and their suitability for scientific use. Quantities and flags are organized into three distinct categories, related to: observing conditions (denoted by the `obs` prefix); instrumental performance and effectiveness of the data reduction (`inst`); accuracy and quality of the final data products (`prod`). The flags in each category are computed based on thresholds of measured quantities, possibly combined with flags given by human classifiers based on visual inspection, as detailed below and summarized in Tables 4 and 5. Thresholds are determined from the distribution of the parameters to exclude outliers and also to analyze the effects of anomalous parameters on the final quality of the data cubes. The tables of the relevant QC parameters, along with the QC flags, are available on the DR2 website.

Each flag can have one of the following values:

- 1 = undefined;
- 0 = good quality — ;
- 1 = minor issues that do not significantly affect the quality — ;
- 2 = significant issues affecting the quality — .

By selection, DR2 excludes galaxies with `obs` flags, with just a few minor exceptions affecting previously released DR1 galaxies: in these cases, the revised QC criteria adopted here would have prevented us from including these galaxies in the DR, but

given the incremental nature of our data releases we keep them in the current sample.

In naming the QC parameters, we adopt the following convention: the first part is the category prefix (`obs`, `inst` or `prod`), followed by a measured parameter, and sometimes a final suffix indicating the statistics applied to combine the parameter as measured in different observations/pointings/fibers (i.e., `_mean`, `_median`, `_rms`, `_std`).

In the following subsections, we describe the QCs in each of the above-mentioned categories.

6.1. Quality of the observing conditions (obs)

Three quantities are considered crucial in determining the quality of the observing conditions of the CALIFA data: the airmass, the brightness of the sky, and the atmospheric extinction. While seeing is in general an important parameter of the observing conditions, the imaging quality and spatial resolution of the CALIFA cubes is mostly limited by the sampling of the fibers on the plane of the sky and the resampling process (see Sect. 6.4.1 for more detail), rather than by the seeing. Moreover, the seeing measurement is only available for a small fraction of the objects (see Sect. 6.4.2), and therefore cannot be used as a reliable QC parameter.

For the airmass, we consider the average and the maximum airmass of the observations over all contributing pointings (`inst_mean` and `inst_max`) and its rms (`inst_rms`). For each of these quantities, we defined two thresholds (the same for V500 and V1200, see Tables 6

Table 5. Definition of CALIFA DR2 quality control flags for the V1200 data.

QC flag	QC parameters involved			condition(s)	condition(s)	Flag definition			
— —	— —			>1.7	>2.0	Worst of the three parameters			
	— —			>2.0	>2.5				
	— —			>0.15	...				
— —	— —			<21.5 mag _V arcsec ⁻²	<21.0	Worst of the two parameters			
	— —			>0.1	...				
— —	— —			>0.30 mag	...	Worst of the three parameters			
	— —			>0.35	...				
	— —			>0.10	...				
— —	— —			>15 counts	>30	Worst of the three parameters			
	— —			>20	>40				
	— —			>1.5	>2.0				
— —	— —			>2.0 Å (FWHM)	>2.5	Worst of the three parameters			
	— —			>10.0	...				
	— —			>0.15	...				
— —	— —			>3.0 pixels (FWHM)	...	Worst of the two parameters			
	— —			>0.66	...				
— —	— 4358_			<-0.1 counts	...	Worst of the three parameters			
	— 4358_			>0.1	...				
	— 4358_			>0.7	...				
— —				<22.50 mag _B arcsec ⁻²	<22.00				
— —									
Visual checks on 30''-aperture integrated spectrum for spectral shape and mismatch with V500 spectrophotometry									
— —				>1.0 km s ⁻¹	>2.0				
— —				>10	...	Combined parameter of visual inspection of registration and synthetic broadband image			

and 7), above which the flags are raised. The combined

or the flags, respectively, is the worst of the

brightness corresponding to a 3σ detection per spaxel and spectral resolution element measured on the final cube.

The so-called straylight is an additional source of illumination internal to the instrument, possibly as a distributed scattered light component. Straylight, if not subtracted properly, introduces systematic errors and thus limits the final sensitivity and accuracy of the data reduction⁸. High mean levels of straylight in a frame (), as well as high maximum values () and large rms (), are indications of poor performance. Levels above the thresholds provided in Tables 4 and 5 in at least one of the exposures (suffix) raise a or a flag.

The spectral dispersion and cross dispersion are measured on individual fiber spectra as the FWHM of skylines and the FWHM of the spectral trace⁹, respectively. Thresholds are set on the mean values to ensure that the typical parameters do not depart too much from the nominal target specifications, and on the maximum and rms to check for anomalies in the data. Any failure to comply with the thresholds reported in Tables 4 and 5 raises a or a .

⁸ For a detailed description on the straylight subtraction, see Appendix A.3 of H13.

⁹ The dispersed light from a fiber results in a trace with a finite extension in the spectral dispersion direction and in the spatial (cross-dispersion) direction, with a peaked, approximately Gaussian profile. We quantify the width of the trace in the spatial direction with its FWHM.

¹⁰ The values we check for these quantities are obtained from all the fibers along the whole wavelength coverage in an intermediate step of the reduction, before final bad pixel masks are produced. It is therefore

6.2. Quality of the instrumental/data reduction performance (red)

The quality of the instrumental and data reduction performance is assessed via a series of four quantities measured on the reduced data *before* combining them into the final datacube: , spectral , cross dispersion , and the residuals from the subtraction of bright skylines (namely, the 5577 Å O₂ line in the V500 setup and the 4358 Å Hg in the V1200 setup). In addition, we consider the limiting surface

⁷ See Appendix A.8 of H13.

To assess the performance of the sky subtraction, we consider the minimum and the maximum over all pointings of the average (over all fibers) flux residual of a bright skyline within an individual pointing ($-4358-$ and $-4358-$, and $-5577-$ and $-5577-$ for the V1200 and the V500 setup, respectively). We also consider the maximum over all pointings of the rms residuals (over all fibers in an individual pointing), $-4358-$ and $-5577-$. Average residuals that are too negative or too positive are indications of systematic bias in the sky subtraction. An rms that is too large can be regarded as a symptom of localized failures or noisy data. In these cases, the $- -$ is set.

Finally, the 3σ continuum flux density detection limit per interpolated 1 arcsec 2 -spaxel and spectral resolution element¹¹ for the faintest regions is used to identify cubes whose depth does not fulfill the survey requirements, which is reflected in the $- - -$ flag. More about the depth of the final datacubes is discussed in Sect. 6.6.

6.3. Quality of the calibrated data products (cal)

The quality of the calibrated data products is determined by checks on the global spectrophotometry, on the stability of the wavelength calibration across the spectral range, and on the quality of the resulting 2D flux distribution (synthetic image) and its ability to match the SDSS broadband imaging.

The quality of global spectrophotometric calibration is assessed by comparing the photometric fluxes derived from spectra integrated within 30'-radius apertures with the corresponding fluxes derived from SDSS imaging, as explained below in Sect. 6.5. For the V500 setup, in particular, it is possible to derive the flux ratio between SDSS and CALIFA in g and r -bands ($- -$ and $- -$, averaged over all pointings for a given galaxy): values of these ratios departing from 1 by more than the tolerances listed in Table 4 are flagged. Large rms variations of these values over the three V500 pointings ($- -$, which combines g and r bands) are also considered symptoms of poor quality. In addition to these quantitative parameters, we visually check that the spectral energy distribution (SED) measured via SDSS photometry matches the CALIFA integrated spectrum. For this check we also consider the u and the i band data points: although the CALIFA spectra do not cover the full extent of these pass-bands, they prove helpful in judging the matching of spectral shapes. Five members of the collaboration performed these checks independently and assigned flags $- - -$: the second-to-worst classification is retained. This flag is then combined with the flags based on the quantitative flux ratios to create the final $- -$ flag.

to be expected that there are lower quality regions that do not comply with the requirements (i.e., spectral resolution lower than the final homogenized resolution). These regions will be eventually flagged as bad pixels. However, by how much they exceed the minimum requirement provides an indication on the overall quality of the data. By looking at the distribution of $- - *^*$ quantities, we established a criterion to pinpoint bad cubes, where very large values of $- -$ (and $- -$, $- -$) occur: basically this criterion indicates when departures from nominal requirements are no longer emendable by just flagging bad pixels. Furthermore, we checked that in all the pixels that are not flagged as bad, and that the instrumental dispersion is lower than or equal to the homogenized value.

¹¹ See Sect. 6.6 for a definition of the wavelength range used to derive this quantity.

In order to check the stability of the wavelength calibration over the full spectral range we performed the same measurements presented in Sect. 5.3 of H13: for each galaxy and setup, the spectra within 5'' of the center of the galaxy are integrated and the systemic velocity is estimated first for the full spectrum and then for 3 (4) independent spectral ranges in V1200 (V500). The rms of these values with respect to the systemic velocity from the full spectrum ($- - -$) is an estimate of the stability of the wavelength calibration across the wavelength range and is used to set the corresponding quality flag $- - -$. In $>97.5\%$ of the cases, we obtain $- -$ well below 2 km s^{-1} for the V1200 and 3 km s^{-1} for the V500 grating.

Finally, the quality flag on the 2D flux distribution and plane-of-sky registration, $- - -$, is defined by combining the information on the goodness of matching between SDSS images and synthetic images from the CALIFA datacube with a series of visual checks. The former is provided by the chi-squared of the registration procedure (see Sect. 4.2). The visual checks include: a check on possible artefacts in the synthetic broadband image from the final CALIFA cubes (e.g., mismatched features, elongated PSF); a comparison of the CALIFA fiber footprints of each pointing with the registered SDSS image, looking for apparent mismatched and miscomputed spatial offsets; a check of the chi-squared surface plot displaying the dependence of the registration procedure (see below) on the x and y spatial offsets, whereby irregular chi-square surfaces and lack of clear minima imply the possibility of an inaccurate registration. Out of five independent classifiers we chose the median value of the attributed flags and combine it with the flag corresponding to the chi-squared measurements. We note that a small number of objects already released as part of DR1 do not reach the imaging quality standards using the registration procedure adopted in the pipeline V1.5 (see Sect. 4.2), which uses cross-correlation with SDSS images: in these cases we revert to the old registration scheme adopted for DR1 (pipeline V1.3c) and mark the objects with a dagger in Tables 6 and 7.

6.4. Astrometric accuracy and spatial resolution

6.4.1. Astrometric registration accuracy

Pipeline V1.5 implements a new method (see Sect. 4.2) to register the absolute astrometry of the datacube coordinate system to the International Coordinate Reference System (ICRS). The previous pipeline, V1.3c, used tabulated coordinates of the galaxy V band photometric center that were assigned to the barycenter measured in the reconstructed image from the datacubes (just one point, instead of the global match applied in V1.5).

To check the accuracy of the new astrometric registration for V500 and V1200 datacubes, we performed independent tests using SDSS r and g -band images (DR10) for each galaxy. Synthetic r and g -band PPAK images were computed using the V1.5 reduced data. The coordinates of the peak centroid PPAK images are used as an approximate galactic center, and the corresponding peak was measured in the SDSS images. The offsets between the SDSS and CALIFA are less than 3'' (rms $\sim 1''$) for the majority of the DR2 sample. Large offsets are mostly due either to edge-on galaxies, centers of the galaxies not well defined because of dust lanes, irregular morphologies or bright field star(s) near the center of the galaxy. Objects with offsets larger than 3'' measured in V500 setup are: IC1 652, NGC 0444, UGC 00809, UGC 00841, NGC 0477, IC 1683, NGC 0499, NGC 0496, NGC 0528, UGC 01938, NGC 1056, NGC 3991,

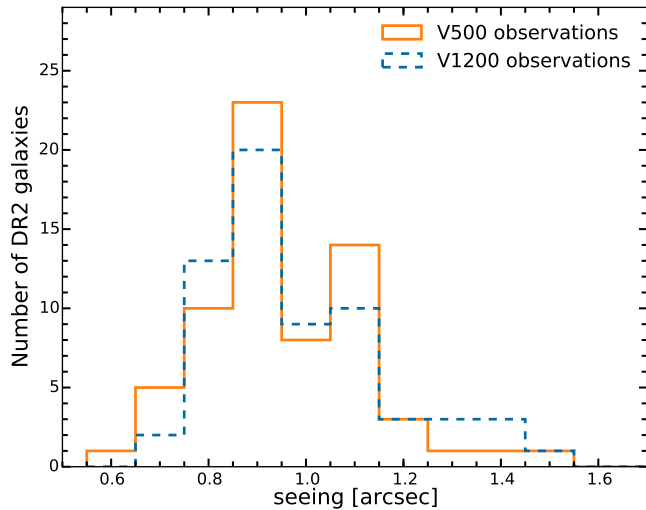


Fig. 12. Distribution of the seeing during the CALIFA observations as measured by the automatic Differential Image Motion Monitor (DIMM, Aceituno 2004).

MCG-01-01-012, and NGC 7800. For the V1200 setup: IC1 528, IC1 652, NGC 0444, UGC 00809, UGC 00841, NGC 0477, NGC 0499, NGC 0496, NGC 0528, UGC 02222, NGC 3991, UGC 11792, MCG-01-01-012, and NGC 7800.

6.4.2. Seeing and spatial resolution

To cover the complete FoV of the central bundle and to increase the final resolution of the CALIFA datacubes (PPak fibers have a diameter of $2.7''$), we adopt a dithering scheme with three pointings, as described in S12. For imaging, in addition to the telescope aperture, instrumental and atmospheric seeing determine the final spatial resolution. This has to be added to the particular IFU characteristics.

The average atmospheric seeing conditions throughout CALIFA observations were derived from the measurements acquired by the DIMM (DIMM, Aceituno 2004), which operates fully automatically at the Calar Alto observatory during the night. The DIMM has different operational constraints from the 3.5 m telescope (humidity lower than 80% and wind speed less than 12 m s^{-1}). Thus seeing information is not available for every CALIFA observation and these values are missing from Tables 6 and 7, but the overall seeing distribution is not expected to be very different¹². Figure 12 shows the DIMM seeing distribution for the DR2 sample, which has a median value of $0''.9$ FWHM (the distribution is very similar to the DR1 sample), and therefore atmospheric seeing is not a limiting factor in the spatial resolution of the CALIFA cubes. At any rate, the final spatial resolution of the CALIFA data is mainly set by fiber size and the dithering and interpolation scheme.

We use the following approach to measure the PSF in the datacubes. Since January 2012 standard stars were observed using the same dithering pattern adopted for the science observations for the V500 setup. We observed a total of 107 nights in

¹² Sánchez et al. (2008) have shown that the seeing distribution within the Dome under the standard observing conditions (i.e., with or without the DIMM monitor under operations) is very similar to the seeing distribution derived by the DIMM. In average the seeing is degraded by just 10% inside the Dome in comparison with the values provided by the DIMM.

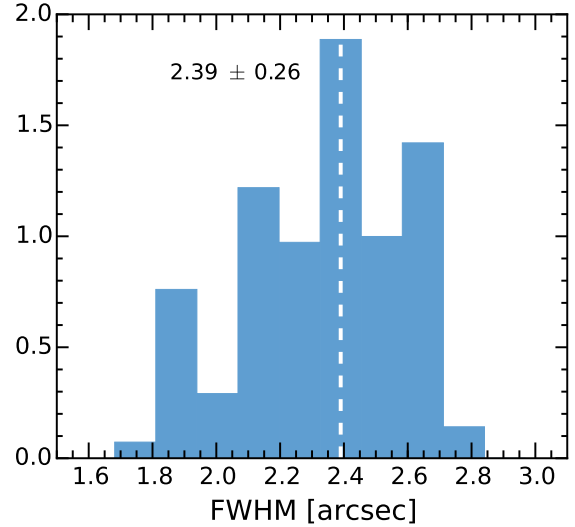


Fig. 13. Normalized distributions of PSF FWHM (top) and β_M (bottom) parameters of a 2D Moffat profile fitted to 45 calibration stars, weighted by the likelihood of the fit. The mean values of the distributions are marked with a white dashed line.

this period. Only 70% of the nights had weather conditions good enough to acquire a calibration star and 2/3 were observed adopting the dithering scheme, yielding a total of 45 datacubes. We reduced these data using the same procedure described before for the science objects. The PSF can be measured very precisely because the calibration stars have a very high S/N. We synthesize a SDSS g -band image simulated from the datacubes for each of these stars. For each of these images, we fit a 2D Moffat profile using the software [\(Erwin 2015\)](http://www.mpe.mpg.de/~erwin/code/imfit/)¹³. Figure 13 shows the normalized distributions of FWHM and β_M parameters of the Moffat profile, weighted by the likelihood of the fit. We obtain a mean value and 1σ scatter of the $FWHM = 2.39 \pm 0.26$ arcsec, with $\beta_M = 1.73 \pm 0.11$. The ellipticity ($1 - b/a$, with a and b being the semimajor and semiminor axes, respectively) is also measured, with mean value and 1σ scatter of 0.08 ± 0.06 . Given the uncertainties, this value means the PSF can be considered effectively axisymmetric. The uncertainties in these measurements correspond to 1σ of the distributions.

¹³ <http://www.mpe.mpg.de/~erwin/code/imfit/>

Table 6. CALIFA DR2 quality control parameters for the V500 data.

ID ^a	Airmass ^b	$\mu_{V,\text{sky}}^c$	A_V^d	Seeing ^e	Flags(O) ^f	δ_λ^g	$S/N(R_{50})^h$	$I_{3\sigma}^i$	Flags(R) ^j	$(\frac{g_{\text{CALIFA}}}{g_{\text{SDSS}}})^k$	$(\frac{r_{\text{CALIFA}}}{r_{\text{SDSS}}})^l$	Flags(C) ^m
001*	1.02 ± 0.01	21.4	0.18	...	000	4.68	24.8	24.0 ± 0.9	00000	1.04	1.03	000
002	1.41 ± 0.05	20.9	00-	4.63	28.9	23.7 ± 1.2	00000	0.96	0.98	000
003*	1.01 ± 0.01	20.8	0.23	0.8 ± 0.1	000	5.17	12.8	23.7 ± 1.2	00100	0.92	0.97	100
005	1.40 ± 0.01	21.0	00-	4.65	24.3	23.6 ± 1.3	00000	0.99	1.01	000
007*,†	1.34 ± 0.05	20.5	00-	5.21	27.6	23.5 ± 1.4	10100	1.03	1.05	000
008	1.34 ± 0.07	21.0	0.20	...	000	4.63	29.1	23.7 ± 1.1	00000	1.02	0.99	000
010*	1.31 ± 0.05	21.0	0.22	...	000	4.62	18.2	23.7 ± 1.2	00000	1.01	0.98	000
013	1.57 ± 0.10	20.8	0.19	...	000	4.63	31.5	23.6 ± 1.3	-00-0	0.96	1.01	001
014*	1.26 ± 0.04	21.0	0.21	...	000	4.62	22.0	23.8 ± 1.1	00000	1.03	1.01	000
017	1.23 ± 0.03	21.1	00-	4.61	9.2	23.6 ± 1.3	00000	1.00	1.00	000
022	1.18 ± 0.05	20.9	00-	4.76	24.8	23.6 ± 1.3	10000	0.94	0.94	100
023	1.86 ± 0.03	19.7	0.15	...	110	4.87	14.6	22.8 ± 2.7	10011	0.92	0.98	000
025	1.24 ± 0.04	21.0	0.17	...	000	4.63	17.9	23.6 ± 1.3	00000	0.98	1.02	001
026	1.26 ± 0.02	20.9	0.13	...	000	4.82	26.3	23.8 ± 1.1	00000	0.99	1.00	000
027	1.90 ± 0.01	20.1	0.20	...	110	4.71	30.3	23.5 ± 1.5	00010	1.00	1.04	001
030	1.34 ± 0.04	20.9	0.20	...	000	4.65	30.1	23.9 ± 1.0	00000	0.99	1.04	101
037	1.58 ± 0.11	20.8	0.17	...	000	4.68	34.7	24.0 ± 0.9	00000	1.20	1.25	101
039*	1.03 ± 0.01	20.8	0.23	0.9 ± 0.1	000	5.21	15.6	23.8 ± 1.1	01000	0.95	0.99	110
040	1.29 ± 0.06	21.1	0.17	...	000	4.69	24.4	24.0 ± 0.9	00000	0.99	1.00	010
041	1.09 ± 0.03	21.1	0.14	...	000	4.95	21.0	23.8 ± 1.1	00010	1.02	1.01	000
042*	1.10 ± 0.03	21.0	0.13	...	000	5.21	14.3	23.6 ± 1.3	10000	1.08	1.09	101
043*	1.01 ± 0.01	21.3	0.19	...	000	4.79	29.5	23.9 ± 1.0	-00-0	1.05	1.02	001
044	1.17 ± 0.04	21.0	00-	4.79	22.3	23.2 ± 1.8	00001	0.96	0.96	000
045	1.28 ± 0.06	20.8	0.14	...	000	5.22	12.6	23.3 ± 1.7	10000	0.98	1.03	001
050	1.43 ± 0.08	20.9	0.16	...	000	4.89	37.7	23.7 ± 1.2	00000	0.99	1.02	000
053*	1.19 ± 0.04	20.7	...	0.8 ± 0.1	00-	5.25	27.4	23.7 ± 1.2	00100	0.95	0.98	000
072	1.16 ± 0.03	21.1	0.15	...	000	4.84	27.3	23.8 ± 1.1	00000	1.00	1.02	000
073*	1.04 ± 0.01	21.1	0.20	...	000	4.73	18.6	23.3 ± 1.8	00000	1.01	1.01	000
076	1.15 ± 0.03	21.2	0.12	...	000	4.95	16.4	23.4 ± 1.6	10000	0.96	0.97	111
077	1.43 ± 0.07	20.9	0.19	...	000	4.64	37.1	23.9 ± 1.0	00000	1.05	1.11	101
088*	1.13 ± 0.03	20.8	...	1.0 ± 0.4	00-	5.43	23.7	23.4 ± 1.5	01100	0.97	0.99	101
100*	1.37 ± 0.26	20.7	0.14	...	100	5.24	23.5	23.1 ± 2.1	10001	0.99	1.00	001
103	1.42 ± 0.08	20.9	0.19	...	000	4.69	28.3	23.6 ± 1.3	00000	1.01	1.05	001
104	1.62 ± 0.10	20.8	00-	4.73	9.4	23.6 ± 1.3	00000	1.01	1.00	000
115	1.28 ± 0.02	20.6	00-	4.67	16.6	23.6 ± 1.3	00010	0.98	0.99	000
127*	1.22 ± 0.02	20.6	0.28	0.9 ± 0.1	000	5.12	11.1	23.0 ± 2.2	00001	0.93	0.98	000
131	1.20 ± 0.01	21.0	00-	4.72	22.2	23.3 ± 1.8	00000	0.98	0.97	000
133	1.17 ± 0.02	20.6	0.28	0.8 ± 0.1	000	5.13	13.8	23.1 ± 2.1	00001	0.88	0.95	100
134	1.47 ± 0.04	21.0	00-	5.26	20.9	23.2 ± 1.9	10101	0.88	0.93	101
141	1.42 ± 0.03	21.0	00-	4.72	11.3	23.8 ± 1.1	00000	1.01	0.97	111
146*,†	1.47 ± 0.00	20.7	0.12	...	000	5.79	15.4	23.0 ± 2.2	01101	1.03	1.02	001
147	1.15 ± 0.01	21.2	0.14	...	000	5.63	22.7	23.2 ± 1.8	01101	0.98	1.00	100
148	1.34 ± 0.04	20.9	0.11	...	000	5.01	17.0	23.6 ± 1.2	10000	1.04	0.93	101
149	1.14 ± 0.01	21.4	00-	5.78	24.8	22.9 ± 2.4	11101	0.86	0.91	101
150	1.01 ± 0.01	21.1	00-	4.76	24.0	23.8 ± 1.1	00000	1.00	0.98	010
151*	1.07 ± 0.02	21.0	0.15	...	000	5.85	18.7	23.0 ± 2.2	11001	0.88	0.91	101

Notes. We describe the meaning of each column, including the identifier of each column in the electronic table available on the DR2 web page.
 (a) IDs marked with an asterisk were already part of the DR1. A dagger indicates cubes that were registered with the old method of the pipeline V1.3c.
 (b) Mean airmass (OBS_AIR_MEAN) and rms (OBS_AIR_RMS) of the observations for the frames used to create the considered datacube.
 (c) Average night-sky surface brightness (OBS_SKY_MAG) in the V band during the observations in units of mag arcsec $^{-2}$.
 (d) Average night-sky attenuation (OBS_EXT_MEAN) in the V band during the observations in magnitudes.
 (e) Average natural seeing (OBS_SEEING_MEAN) in the V -band during the observations in arcsec (FWHM).
 (f) Observation quality flags, combining the three individual column flags (FLAG_OBS_AM, FLAG_OBS_SKYMAG, FLAG_OBS_EXT) as described in Sect. 6.
 (g) Average spectral resolution (RED_DISP_MEAN) in Å (FWHM), measured by fitting the night-sky emission lines with single Gaussian functions.
 (h) Average signal-to-noise ratio (CAL_SN1HLR) estimated for the full wavelength range at one half-light radius from the center.
 (i) Average flux at the 3σ continuum detection limit in units of V -band mag arcsec $^{-2}$ and in units of $10^{-18} \text{ erg s}^{-1} \text{ cm}^{-2} \text{ Å}^{-1} \text{ arcsec}^{-2}$.
 (j) Reduction/instrumental performance quality flags, combining the five individual column flags (FLAG_RED_STRaylight, FLAG_RED_DISP, FLAG_RED_CDISP, FLAG_RED_SKYLINES, FLAG_RED_LIMSB) as described in Sect. 6.
 (k) Ratio between the SDSS g band flux derived from the datacube and the derived from the SDSS images for a 30''-diameter aperture (CAL_QFLUX_G).
 (l) Ratio between the SDSS r band flux derived from the datacube and the derived from the SDSS images for a 30''-diameter aperture (CAL_QFLUX_R).
 (m) Quality control flags, combining the three individual column flags (FLAG_CAL_SPECPHOTO, FLAG_CAL_WL, FLAG_CAL_IMA) as described in Sect. 6.

Table 6. continued.

ID ^a	Airmass ^b	$\mu_{V,\text{sky}}^c$	A_V^d	Seeing ^e	Flags(O) ^f	δ_λ^g	$S/N(R_{50})^h$	$I_{3\sigma}^i$	Flags(R) ^j	$(\frac{g_{\text{CALIFA}}}{g_{\text{SDSS}}})^k$	$(\frac{r_{\text{CALIFA}}}{r_{\text{SDSS}}})^l$	Flags(C) ^m
153	1.19 ± 0.04	21.1	00-	4.90	25.6	23.7 ± 1.2	00000	0.98	0.99	000
155*	1.03 ± 0.01	21.1	0.16	...	000	5.61	14.8	23.1 ± 2.0	11001	0.94	0.94	001
156*	1.12 ± 0.04	21.0	0.16	...	000	5.54	19.4	23.3 ± 1.7	11000	0.99	1.00	001
165	1.03 ± 0.01	21.1	0.15	...	000	5.98	23.6	23.0 ± 2.2	11001	0.92	0.93	100
231	1.03 ± 0.01	21.2	00-	4.89	8.7	23.9 ± 1.0	00000	1.00	0.99	000
232	1.07 ± 0.00	21.1	00-	4.70	17.1	23.6 ± 1.3	00010	1.02	1.01	000
272	1.15 ± 0.01	21.1	00-	5.19	27.3	23.3 ± 1.7	10000	0.97	0.97	000
273*	1.06 ± 0.01	21.1	0.14	...	000	5.33	21.5	23.6 ± 1.3	00000	0.98	1.00	001
274*	1.18 ± 0.02	20.9	00-	4.92	30.1	23.7 ± 1.2	00000	1.02	1.03	001
275	1.14 ± 0.00	21.0	00-	4.93	35.7	23.7 ± 1.2	01000	0.99	1.01	000
277*	1.60 ± 0.12	20.3	0.33	...	011	5.65	15.9	22.8 ± 2.8	11101	0.95	1.01	101
278	1.32 ± 0.08	20.8	0.12	...	000	5.33	25.8	23.6 ± 1.3	00100	1.04	1.05	000
306*	1.28 ± 0.08	20.6	0.17	1.0 ± 0.1	000	4.59	6.5	23.6 ± 1.4	00010	1.01	0.96	101
307*	1.06 ± 0.01	21.2	0.16	...	000	5.64	14.3	23.5 ± 1.4	01000	0.97	0.97	001
309*	1.27 ± 0.05	21.0	0.15	...	000	5.97	12.8	23.1 ± 2.1	11001	0.99	0.99	001
311	1.03 ± 0.01	21.3	0.16	...	000	5.96	7.1	23.0 ± 2.2	11001	0.87	0.86	101
314	1.13 ± 0.05	21.1	0.15	1.1 ± 0.1	000	4.99	31.1	24.0 ± 0.9	00000	1.05	1.07	001
319*	1.11 ± 0.03	20.5	0.56	...	001	5.54	21.7	23.3 ± 1.8	01100	0.91	1.00	001
326*	1.05 ± 0.01	20.8	00-	4.66	24.8	23.9 ± 1.0	00000	1.00	1.02	000
340	1.27 ± 0.05	20.9	...	1.1 ± 0.2	00-	5.21	12.7	23.8 ± 1.1	01000	0.93	0.95	100
341*	1.17 ± 0.03	...	0.17	1.5 ± 0.2	0-0	5.06	17.0	23.7 ± 1.2	00000	1.01	1.03	000
353	1.03 ± 0.02	20.9	00-	4.74	20.8	23.3 ± 1.7	00000	0.98	1.00	001
364*	1.33 ± 0.07	20.8	0.12	...	000	5.39	34.0	23.8 ± 1.1	00100	1.01	1.05	000
381	1.01 ± 0.00	21.2	00-	4.77	32.5	23.9 ± 1.0	00000	1.04	1.03	001
388	1.02 ± 0.01	21.1	...	0.2 ± 0.2	00-	5.18	7.8	23.2 ± 1.9	00001	0.95	0.94	000
436	1.13 ± 0.03	21.1	0.19	...	000	...	21.7	23.1 ± 2.1	0-011	0.97	0.98	000
475*,†	1.35 ± 0.07	20.8	0.12	...	000	5.36	21.2	23.7 ± 1.2	00000	0.96	1.03	110
476	1.06 ± 0.02	20.8	00-	4.75	64.0	23.9 ± 1.0	00010	1.01	1.03	100
479*	1.14 ± 0.03	20.8	00-	4.67	28.4	23.9 ± 0.9	00010	1.02	1.03	000
486*	1.05 ± 0.03	...	0.16	1.2 ± 0.7	0-0	4.66	22.3	24.0 ± 0.9	00000	0.99	0.98	000
502	1.11 ± 0.01	21.3	00-	5.04	40.3	24.0 ± 0.9	00000	1.09	1.07	100
515*	1.01 ± 0.00	20.9	0.14	...	000	5.25	14.9	23.2 ± 1.9	00001	0.95	0.98	000
518*	1.16 ± 0.01	20.9	0.15	...	000	5.64	18.6	23.3 ± 1.7	01100	0.97	1.00	000
528*	1.14 ± 0.01	20.8	00-	4.71	7.5	23.7 ± 1.2	00000	1.01	1.02	001
548*	1.16 ± 0.01	20.8	0.19	1.2 ± 0.1	000	4.64	43.6	23.8 ± 1.1	00010	1.02	1.00	001
569	1.06 ± 0.01	21.2	00-	4.65	33.8	24.1 ± 0.8	10000	0.96	1.01	000
577*,†	1.02 ± 0.01	21.0	0.15	...	000	4.95	13.3	24.0 ± 0.9	01100	-0-
592	1.03 ± 0.01	20.9	00-	4.69	20.0	23.3 ± 1.7	00000	0.82	0.84	101
593	1.11 ± 0.02	21.0	00-	4.73	19.5	23.9 ± 1.0	00000	0.98	0.99	000
606	1.07 ± 0.01	21.4	00-	5.19	15.8	23.9 ± 1.0	00000	0.95	1.00	101
607*	1.22 ± 0.03	21.3	0.16	...	000	5.39	41.2	23.6 ± 1.3	10000	0.91	0.92	100
608*	1.31 ± 0.06	21.1	00-	5.87	11.3	23.3 ± 1.7	11000	0.91	0.91	101
609*	1.07 ± 0.02	21.3	0.14	...	000	5.55	17.3	23.8 ± 1.1	01000	0.99	0.97	100
610*	1.11 ± 0.03	21.2	00-	5.85	22.7	23.5 ± 1.5	11000	0.96	0.97	000
630	1.36 ± 0.04	20.0	01-	4.64	17.6	23.4 ± 1.6	00000	0.99	1.00	001
633	1.13 ± 0.01	21.0	00-	4.77	13.8	23.7 ± 1.2	00000	0.93	0.96	000
657*	1.02 ± 0.01	21.2	0.19	1.1 ± 0.1	000	4.69	10.4	23.9 ± 1.0	00000	1.01	1.00	000
663*	1.20 ± 0.04	20.9	00-	5.32	24.4	23.7 ± 1.2	01000	1.01	1.02	100
664*	1.04 ± 0.02	21.2	...	1.1 ± 0.1	00-	5.21	35.6	23.9 ± 0.9	00000	1.05	1.06	000
665*	1.06 ± 0.01	21.1	00-	5.21	18.8	23.7 ± 1.2	00000	1.02	1.03	100
676*	1.03 ± 0.03	21.0	0.15	...	000	5.52	12.5	23.2 ± 1.8	-10-1	0.96	0.97	100
680*	1.07 ± 0.02	21.0	00-	4.66	11.8	24.1 ± 0.8	00010	1.00	1.03	000
684*	1.05 ± 0.02	21.0	00-	4.66	25.1	23.5 ± 1.5	00000	0.97	0.99	000
708	1.18 ± 0.03	20.8	00-	4.76	18.8	23.0 ± 2.2	00011	0.93	0.95	000
714	1.09 ± 0.01	20.6	0.14	...	000	4.66	28.1	23.8 ± 1.0	00010	1.03	1.02	000
715	1.10 ± 0.06	21.1	0.21	...	000	4.74	35.9	24.0 ± 0.9	-00-0	1.02	1.04	101
740	1.12 ± 0.03	21.0	00-	4.66	30.0	23.3 ± 1.7	00000	0.96	0.99	001
749	1.08 ± 0.02	21.1	0.19	1.1 ± 0.1	000	4.90	28.9	24.0 ± 0.9	00000	1.03	1.04	100
758*	1.02 ± 0.00	21.1	0.24	1.1 ± 0.1	000	4.72	12.2	24.0 ± 0.9	00000	0.96	0.97	000
764*	1.29 ± 0.05	21.1	0.18	1.0 ± 0.1	000	4.62	20.0	24.0 ± 0.9	00000	1.07	1.02	000
769*	1.02 ± 0.01	21.2	00-	5.47	18.7	23.6 ± 1.3	01100	1.00	1.00	000
778	1.15 ± 0.04	21.2	...	0.9 ± 0.1	00-	4.77	25.3	23.6 ± 1.4	00000	0.99	1.00	000

Table 6. continued.

ID ^a	Airmass ^b	$\mu_{V,\text{sky}}^c$	A_V^d	Seeing ^e	Flags(O) ^f	δ_λ^g	$S/N(R_{50})^h$	$I_{3\sigma}^i$	Flags(R) ^j	$(\frac{g_{\text{CALIFA}}}{g_{\text{SDSS}}})^k$	$(\frac{r_{\text{CALIFA}}}{r_{\text{SDSS}}})^l$	Flags(C) ^m
783*	1.08 ± 0.02	21.3	0.16	...	000	5.46	29.3	23.6 ± 1.3	00010	0.98	0.98	000
789	1.15 ± 0.03	21.1	0.20	0.9 ± 0.1	000	4.64	27.3	24.0 ± 0.9	00010	0.99	0.99	000
791	1.16 ± 0.03	20.9	00-	4.78	35.6	23.5 ± 1.4	00000	0.99	1.01	001
795	1.01 ± 0.00	21.1	...	0.8 ± 0.1	00-	4.71	27.7	23.9 ± 1.0	00000	0.97	1.00	000
797*	1.05 ± 0.07	21.0	0.15	...	000	5.11	17.6	24.0 ± 0.9	01100	0.99	1.00	000
798*	1.05 ± 0.02	21.3	0.21	...	000	4.66	27.0	24.3 ± 0.7	00000	0.97	1.00	000
806*	1.00 ± 0.00	21.1	0.25	1.1 ± 0.1	000	4.70	59.9	23.6 ± 1.3	00000	0.85	0.86	101
807	1.16 ± 0.04	20.9	00-	4.67	18.3	23.4 ± 1.5	00010	0.99	1.00	100
809	1.35 ± 0.05	21.0	...	1.0 ± 0.5	00-	4.85	16.2	23.3 ± 1.8	00000	0.84	0.87	101
813	1.08 ± 0.01	20.9	0.22	1.4 ± 0.1	000	4.65	19.4	23.6 ± 1.4	00010	0.98	0.99	000
815	1.21 ± 0.05	21.1	0.18	0.8 ± 0.1	000	4.82	11.6	23.6 ± 1.3	00000	0.96	0.98	000
816	1.21 ± 0.04	20.7	...	0.8 ± 0.1	00-	4.67	34.2	23.8 ± 1.1	00010	1.02	1.02	001
820*	1.07 ± 0.02	21.2	0.17	...	000	5.61	7.2	22.9 ± 2.5	21001	1.03	1.03	101
822*	1.03 ± 0.01	21.2	00-	6.08	10.1	23.1 ± 2.1	11001	0.96	0.96	101
823*	1.15 ± 0.00	20.9	0.19	...	000	4.62	21.3	23.8 ± 1.1	10010	0.99	0.98	000
824* [†]	1.14 ± 0.01	20.9	00-	4.72	22.9	23.9 ± 1.0	00000	0.92	0.89	101
826*	1.18 ± 0.03	21.1	00-	5.32	26.4	23.7 ± 1.2	00100	1.03	1.04	000
828*	1.21 ± 0.03	21.3	0.26	0.9 ± 0.1	000	4.64	27.2	24.0 ± 0.9	00000	1.11	1.04	101
829*	1.09 ± 0.01	21.2	0.18	...	000	4.73	17.7	23.4 ± 1.6	10000	0.95	0.93	101
831	1.42 ± 0.07	20.2	01-	4.65	22.3	23.3 ± 1.7	00000	1.03	1.02	000
832*	1.01 ± 0.01	21.3	00-	5.49	23.4	23.5 ± 1.5	00100	0.98	0.99	100
833*	1.12 ± 0.03	21.2	0.18	0.9 ± 0.1	000	5.00	18.1	23.8 ± 1.1	00100	1.02	0.98	000
834	1.39 ± 0.07	20.5	0.29	...	010	4.70	28.0	23.9 ± 1.0	00000	1.17	1.23	101
835*	1.00 ± 0.00	21.1	...	1.1 ± 0.2	00-	5.28	38.2	24.0 ± 0.9	01000	0.98	1.01	000
837*	1.11 ± 0.00	21.1	0.17	0.9 ± 0.1	000	4.84	43.0	24.1 ± 0.8	01000	1.07	1.03	001
838	1.46 ± 0.09	20.3	01-	4.65	25.7	23.6 ± 1.4	00000	1.06	1.06	000
840*	1.18 ± 0.04	21.0	0.28	0.9 ± 0.1	000	4.65	3.0	23.5 ± 1.4	00000	1.02	0.96	100
841	1.16 ± 0.04	21.2	...	0.9 ± 0.1	00-	4.71	24.0	23.6 ± 1.3	00000	1.01	1.03	001
843*	1.45 ± 0.09	21.0	0.23	0.8 ± 0.1	000	4.60	9.3	23.8 ± 1.1	00000	1.08	1.05	011
845*	1.03 ± 0.02	21.4	0.19	...	000	4.64	16.0	23.8 ± 1.1	00000	0.93	0.95	100
846*	1.06 ± 0.02	21.0	0.39	0.8 ± 0.1	001	4.64	7.7	23.7 ± 1.2	00000	0.97	0.98	000
847*	1.31 ± 0.09	21.3	0.15	0.7 ± 0.1	010	4.66	20.4	24.0 ± 0.9	20000	1.16	1.25	101
848*	1.10 ± 0.00	21.0	0.38	0.9 ± 0.1	001	4.74	32.3	23.8 ± 1.1	00000	1.02	1.01	000
850*	1.05 ± 0.01	21.0	0.29	...	000	4.66	29.6	23.7 ± 1.2	00000	1.00	1.01	000
851*	1.32 ± 0.04	20.5	0.41	0.7 ± 0.1	001	4.66	9.5	23.3 ± 1.7	00010	0.93	0.93	100
852*	1.12 ± 0.01	21.0	0.36	0.9 ± 0.1	001	4.76	8.1	23.8 ± 1.1	00000	1.01	0.99	000
854*	1.18 ± 0.03	20.7	0.42	0.9 ± 0.1	001	4.68	20.3	23.6 ± 1.3	00010	1.00	1.01	001
856*	1.05 ± 0.02	21.2	0.17	...	000	4.61	24.1	23.9 ± 1.0	00000	0.99	0.99	000
857*	1.08 ± 0.00	21.5	0.16	0.9 ± 0.1	000	4.67	36.7	24.2 ± 0.8	00000	0.98	1.01	000
858*	1.10 ± 0.03	21.2	0.15	1.3 ± 0.2	000	4.67	15.8	23.7 ± 1.2	00000	1.01	0.98	000
859*	1.16 ± 0.02	21.2	0.15	0.7 ± 0.1	000	4.67	11.0	23.6 ± 1.4	00000	0.92	0.95	000
860*	1.04 ± 0.02	21.2	0.29	1.0 ± 0.1	000	4.60	41.5	23.6 ± 1.3	00000	1.10	1.06	101
861	1.08 ± 0.02	21.1	00-	4.62	22.4	23.5 ± 1.4	00000	1.04	1.06	001
862	1.13 ± 0.03	20.8	...	1.1 ± 0.2	00-	5.19	20.3	23.4 ± 1.6	00100	0.99	1.01	001
863*	1.09 ± 0.01	21.4	0.16	0.7 ± 0.1	000	4.67	29.4	24.1 ± 0.8	00000	1.02	1.05	001
864*	1.06 ± 0.01	20.9	0.28	...	000	4.70	12.2	23.5 ± 1.5	20010	0.99	0.98	100
865*	1.01 ± 0.01	21.2	0.25	...	000	4.71	32.4	23.9 ± 1.0	10000	1.01	1.02	001
866*	1.04 ± 0.02	21.3	0.21	1.1 ± 0.1	000	4.64	12.6	24.0 ± 0.9	20000	1.04	1.02	000
867*	1.13 ± 0.01	21.2	0.21	1.1 ± 0.1	000	4.69	39.2	24.0 ± 0.9	10000	1.08	1.09	001
868	1.65 ± 0.04	20.1	01-	4.84	25.3	23.3 ± 1.7	-00-0	0.96	0.99	001
869	1.41 ± 0.06	20.8	0.19	1.1 ± 0.1	000	4.66	16.4	23.5 ± 1.5	00000	1.04	1.02	101
871	1.38 ± 0.01	20.6	0.17	0.9 ± 0.1	000	4.70	21.3	23.4 ± 1.6	-00-0	0.99	1.02	100
872*	1.28 ± 0.01	20.9	0.15	0.6 ± 0.1	000	4.66	18.2	23.4 ± 1.5	00010	0.98	0.98	000
874*	1.10 ± 0.02	21.0	0.22	...	000	4.75	24.4	23.2 ± 1.9	00001	1.01	1.03	101
877* [†]	1.24 ± 0.05	21.0	0.22	...	000	4.72	16.8	23.6 ± 1.3	20000	1.23	1.23	101
878*	1.33 ± 0.01	20.9	0.22	0.9 ± 0.1	000	4.59	6.8	23.7 ± 1.1	00010	1.01	0.99	101
880	1.24 ± 0.03	20.7	0.29	0.9 ± 0.1	000	4.63	24.2	23.6 ± 1.3	00010	0.93	0.94	100
881*	1.10 ± 0.00	21.1	0.15	0.8 ± 0.1	000	4.67	18.2	23.8 ± 1.1	00010	0.94	0.94	000
883*	1.10 ± 0.01	21.2	0.17	1.0 ± 0.2	000	4.63	10.1	23.6 ± 1.3	00000	0.99	0.95	101
884	1.66 ± 0.10	20.4	01-	4.90	10.8	23.4 ± 1.5	00000	0.97	0.98	110
885	1.25 ± 0.04	20.9	0.20	0.7 ± 0.1	000	4.88	25.4	23.7 ± 1.2	00100	1.04	1.01	001
886	1.29 ± 0.04	21.0	0.17	0.9 ± 0.2	000	4.65	40.5	23.4 ± 1.5	00000	1.01	1.00	000

Table 6. continued.

ID ^a	Airmass ^b	$\mu_{V,\text{sky}}^c$	A_V^d	Seeing ^e	Flags(O) ^f	δ_λ^g	$S/N(R_{50})^h$	$I_{3\sigma}^i$	Flags(R) ^j	$(\frac{g_{\text{CALIFA}}}{g_{\text{SDSS}}})^k$	$(\frac{r_{\text{CALIFA}}}{r_{\text{SDSS}}})^l$	Flags(C) ^m
887*	1.08 ± 0.02	21.3	0.17	0.9 ± 0.1	000	4.67	31.9	$23.9 1.0$	00000	1.01	0.98	001
888*	1.01 ± 0.01	20.9	0.22	...	000	4.68	2.5	$23.5 1.5$	00010	0.93	0.94	000
890*	1.08 ± 0.02	21.0	0.22	...	000	4.71	29.9	$23.9 1.0$	00010	1.00	1.01	000
891	1.37 ± 0.06	20.3	0.21	1.2 ± 0.2	010	5.23	9.2	$23.1 2.0$	00101	0.91	0.98	000
893*	1.35 ± 0.07	20.5	0.20	1.0 ± 0.1	000	5.32	6.9	$22.9 2.6$	20111	0.89	0.92	111
894	1.31 ± 0.06	20.5	...	0.9 ± 0.1	00-	4.74	21.3	$23.6 1.3$	00010	1.06	1.11	101
895	1.15 ± 0.03	20.5	0.22	1.1 ± 0.1	000	5.15	10.3	$23.5 1.4$	00000	0.94	0.97	100
896*	1.36 ± 0.08	20.8	0.18	0.9 ± 0.1	000	5.01	21.8	$23.8 1.1$	00100	1.04	1.02	001
898	1.60 ± 0.11	20.4	...	0.9 ± 0.1	01-	4.66	12.4	$22.9 2.5$	00011	0.97	1.00	000
901*	1.10 ± 0.03	21.3	0.14	1.0 ± 0.1	000	4.63	29.9	$23.7 1.2$	20000	0.97	1.03	101
902*	1.10 ± 0.00	21.2	0.17	0.8 ± 0.1	000	4.71	39.3	$23.6 1.3$	00000	1.06	1.01	001
903	1.45 ± 0.08	20.9	00-	4.64	30.5	$23.3 1.8$	00000	0.97	0.97	001
904*	1.20 ± 0.04	21.0	0.17	0.9 ± 0.1	000	4.71	21.5	$23.6 1.4$	00000	1.01	0.98	000
909	1.09 ± 0.02	20.8	00-	5.05	29.5	$23.8 1.1$	00000	1.02	1.00	000
910	1.22 ± 0.03	21.1	00-	4.62	18.7	$23.4 1.6$	00000	0.99	1.01	101
913	1.47 ± 0.09	21.1	00-	4.63	38.8	$23.4 1.6$	00000	0.96	1.01	100
914	1.18 ± 0.02	21.0	0.13	...	000	4.79	31.4	$23.8 1.1$	00000	0.98	1.00	000
915	1.28 ± 0.05	21.1	00-	4.61	25.4	$23.4 1.6$	00000	1.06	1.03	000
916	1.55 ± 0.10	20.8	00-	4.65	25.0	$23.0 2.2$	00001	0.95	0.99	101
917	1.21 ± 0.03	20.9	00-	4.69	31.5	$23.5 1.4$	00010	1.03	1.00	100
922	1.15 ± 0.00	20.8	0.14	...	000	5.20	16.8	$23.5 1.5$	00100	1.06	1.08	101
924	1.43 ± 0.12	20.6	00-	4.79	12.8	$23.0 2.3$	-00-1	1.01	1.00	000
927	1.29 ± 0.03	21.0	00-	4.64	14.7	$23.8 1.1$	00000	1.01	1.02	000
930	1.29 ± 0.03	20.8	00-	4.62	7.3	$23.1 2.1$	00011	1.03	1.04	010
932	1.27 ± 0.02	21.0	00-	4.71	33.5	$23.7 1.2$	00000	1.00	1.00	100
935*	1.04 ± 0.02	21.0	...	1.1 ± 0.1	00-	5.09	11.1	$23.7 1.2$	00000	0.96	1.00	000
936	1.42 ± 0.05	20.8	0.15	...	000	4.84	30.7	$24.0 0.9$	00000	1.06	1.11	101
937	1.13 ± 0.02	21.0	00-	4.62	13.8	$23.7 1.2$	00010	0.99	0.97	000
938	1.01 ± 0.01	...	0.16	...	0-0	4.74	31.5	$24.0 0.9$	00000	0.98	1.00	100
939*	1.11 ± 0.04	20.8	0.15	...	000	4.99	8.7	$23.6 1.3$	01110	1.05	1.03	100

As a consequence of the improvements in the interpolation scheme, the PSF FWHM has substantially decreased with respect to DR1 (pipeline V1.3c). The improvement in spatial resolution is illustrated on the H α maps presented in Fig. 15. This figure shows H α maps obtained using FIT3D on the CALIFA datacubes for NGC 5406 (ID 684) for DR1, DR2, and one image taken with the *William Herschel Telescope* (WHT) using a narrowband filter. The last image has also been degraded to the DR2 nominal resolution for the sake of comparison. This improvement impacts directly, for example, on the detection rate of H α regions. Using (Sánchez et al. 2012b) on the V1.3c datacubes of the 200 galaxies, a total of 5878 are recovered, while this number rises to 7646 H α regions for the DR2 galaxies using pipeline V1.5, which represents an increase of $\sim 30\%$.

6.5. Spectrophotometric accuracy

As mentioned in Sect. 4.2, the new registration scheme of the pipeline uses r -band for the V500 setup and g -band for the V1200 of the SDSS DR7. Each V500 datacube is rescaled in the absolute flux level to match the SDSS DR7 broadband photometry using the photometric scale factor at the best matching position for each pointing. On the other hand, the V1200 data is matched to the V500 data (S12). This procedure, together with the new recalibrated sensitivity curve (see Sect. 4.2 and Husemann et al., in prep.), improves the spectrophotometric calibration over DR1. This is clearly shown in Fig. 14. As part of the CALIFA pipeline V1.5, a 30'' diameter photometric

aperture in r and g is measured both in the SDSS DR7 images and the equivalent synthetic CALIFA broadband images. The mean SDSS/CALIFA g and r band ratios in DR2 and their scatter are 1.00 ± 0.05 and 0.99 ± 0.06 , respectively. In the right panel of Fig. 14 the distribution in $\Delta(g - r)$ color difference between the SDSS and CALIFA data shows that the spectrophotometric accuracy across the wavelength range is better than 3%, with a median value of 0.01 ± 0.03 .

Spectral fitting methods can be used to perform useful tests of the data and their calibration, and this has been done before in CALIFA. H13 used fits to evaluate the accuracy of the error estimates in DR1 datacubes, while Cid Fernandes et al. (2014) used these fits to map systematic features in the spectral residuals that may indicate calibration issues.

We repeated the same experiments for the DR2 datacubes. Results are shown in Fig. 16. The top panel shows in blue the mean spectrum of 170670 Voronoi bins of the 200 galaxies in DR2¹⁴. The average is taken after normalizing each spectrum by its median flux in the 5635 ± 45 Å window. The mean synthetic spectrum (overplotted orange line) as well as the mean residual (at the bottom of the upper panel, purple line) are also plotted. The middle panel zooms in on the residual spectrum, which now excludes emission lines and bad pixels, which are masked in the fitting process. Finally, the bottom panel shows what fraction of all spectra was used in the statistics at each λ .

¹⁴ The spatial binning is used to guarantee a minimum S/N of 20 in the continuum at ~ 5635 Å. In practice, 88% of the Voronoi bins actually comprise a single spaxel.

Table 7. CALIFA DR2 quality control parameters for the V1200 data.

ID ^a	Airmass ^b	$\mu_{V,\text{sky}}^c$	A_V^d	Seeing ^e	Flags(O) ^f	δ_λ^g	$S/N(R_{50})^h$	$I_{3\sigma}^i$	Flags(R) ^j	Flags(C) ^k
001*	1.01 ± 0.02	...	0.26	...	0–0	1.90	9.0	$23.2 3.3$	00000	000
002	1.32 ± 0.04	21.8	0.13	...	000	1.94	12.4	$23.3 3.0$	00000	000
003*	1.08 ± 0.06	22.0	0.17	...	000	1.96	6.5	$23.3 2.9$	11000	000
005	1.44 ± 0.05	21.8	0.16	...	000	1.94	13.2	$23.4 2.8$	-00–0	100
007* [†]	1.18 ± 0.02	21.7	0.14	...	000	1.96	10.2	$22.8 4.9$	00000	001
008	1.04 ± 0.03	21.9	0.43	...	001	1.90	10.2	$23.2 3.3$	00010	000
010*	1.29 ± 0.09	22.2	00–	1.92	6.1	$23.0 4.1$	00000	001
013	1.53 ± 0.04	21.8	0.14	...	000	1.94	16.0	$23.4 2.9$	00010	100
014*	1.27 ± 0.08	22.2	0.19	...	000	1.90	11.4	$23.3 3.0$	00000	000
017	1.19 ± 0.03	21.9	00–	1.94	4.4	$23.5 2.5$	00000	001
022	1.12 ± 0.08	22.4	0.15	...	000	1.99	6.2	$22.7 5.3$	-00–0	001
023	1.89 ± 0.07	1–	1.96	8.7	$22.9 4.3$	10010	000
025	1.22 ± 0.06	22.0	0.15	...	000	1.94	8.5	$23.1 3.5$	00010	101
026	1.27 ± 0.03	21.8	00–	1.91	10.5	$23.4 2.7$	00010	000
027	1.93 ± 0.05	21.3	0.13	...	110	1.95	14.0	$23.2 3.2$	10000	101
030	1.28 ± 0.03	21.9	0.14	...	000	1.94	17.2	$23.7 2.1$	00000	001
037	1.02 ± 0.01	22.2	00–	1.93	15.7	$23.7 2.0$	00010	001
039*	1.07 ± 0.04	22.1	0.21	1.1 ± 0.2	000	1.96	9.3	$23.6 2.3$	01000	000
040	1.03 ± 0.03	22.2	0.21	...	000	1.93	11.0	$23.5 2.5$	00000	000
041	1.02 ± 0.02	22.3	00–	1.90	9.9	$23.5 2.6$	00000	000
042*	1.19 ± 0.09	22.3	0.15	0.9 ± 0.1	000	2.01	9.1	$23.6 2.3$	01000	101
043*	1.01 ± 0.01	22.3	0.27	...	000	1.90	11.1	$23.4 2.7$	00000	000
044	1.05 ± 0.04	22.4	0.11	...	000	1.97	7.4	$22.7 5.3$	00110	000
045	1.01 ± 0.01	22.4	0.14	1.2 ± 0.2	000	1.99	9.2	$23.5 2.4$	00000	001
050	1.14 ± 0.07	22.3	0.14	...	000	2.06	16.2	$23.2 3.3$	01000	101
053*	1.33 ± 0.17	21.9	0.16	...	100	2.13	10.3	$23.1 3.5$	01110	000
072	1.13 ± 0.04	21.9	0.12	...	000	1.94	11.4	$23.4 2.8$	00000	000
073*	1.08 ± 0.04	22.2	0.26	...	000	1.91	7.2	$22.9 4.3$	00000	001
076	1.23 ± 0.08	22.2	0.11	...	000	2.09	4.6	$22.6 5.6$	01100	001
077	1.17 ± 0.01	21.8	00–	1.94	17.3	$23.6 2.3$	00010	001
088*	1.31 ± 0.13	21.4	0.21	...	010	1.99	9.1	$22.7 5.1$	01100	011
100*	1.36 ± 0.14	21.8	0.15	1.1 ± 0.1	000	2.00	13.2	$23.1 3.7$	01000	001
103	1.09 ± 0.09	22.2	00–	2.01	11.3	$22.8 4.8$	01100	001
104	1.26 ± 0.03	21.9	0.14	...	000	1.94	5.0	$23.5 2.6$	00000	001
115	1.34 ± 0.09	22.1	0.15	...	000	2.01	5.3	$22.7 5.2$	01100	101
127*	1.37 ± 0.27	21.7	0.15	...	100	1.99	4.2	$22.5 6.4$	-00–1	000
131	1.19 ± 0.00	22.3	0.14	...	000	1.99	7.0	$22.3 7.7$	-00–1	000
133	1.13 ± 0.01	21.9	0.16	...	000	2.00	5.5	$22.5 6.4$	-10–1	101
134	1.37 ± 0.01	22.0	00–	2.00	10.0	$23.1 3.5$	01000	000
141	1.37 ± 0.02	22.0	0.15	...	000	1.98	5.1	$23.0 4.1$	00100	001
146*, [†]	1.48 ± 0.01	22.2	0.14	1.3 ± 0.2	000	2.00	10.7	$23.3 2.9$	01000	001
147	1.16 ± 0.02	22.3	0.14	1.1 ± 0.1	000	1.95	16.3	$23.6 2.3$	00010	001
148	1.29 ± 0.06	22.1	0.12	...	000	1.93	8.2	$23.4 2.7$	00000	001
149	1.27 ± 0.06	22.2	0.11	...	000	1.92	13.2	$23.0 4.1$	10000	001
150	1.06 ± 0.04	22.2	0.15	...	000	1.93	12.4	$23.3 3.0$	10000	000
151*	1.52 ± 0.19	21.4	11–	2.04	9.7	$22.9 4.4$	01100	001
153	1.09 ± 0.03	21.6	00–	1.97	10.7	$23.1 3.4$	-00–0	001
155*	1.09 ± 0.05	22.1	0.13	0.9 ± 0.1	000	2.33	4.8	$22.5 6.2$	21110	001
156*	1.08 ± 0.05	22.3	0.14	...	000	2.36	8.1	$22.6 5.6$	01100	001
165	1.25 ± 0.11	21.7	00–	1.94	15.7	$23.1 3.5$	00100	000

Notes. We describe the meaning of each column including the identifier of each column in the electronic table available on the DR2 web page.

(^a) IDs marked with an asterisk were already part of the DR1. A dagger indicates cubes that were registered with the old method of the pipeline V1.3c. (^b) Mean airmass (OBS_AIR_MEAN) and rms (OBS_AIR_RMS) of the observations for the frames used to create the considered datacube.

(^c) Average night-sky surface brightness (OBS_SKY_MAG) in the V band during the observations in units of mag arcsec⁻². (^d) Average night-sky attenuation (OBS_EXT_MEAN) in the V band during the observations in magnitudes. (^e) Average natural seeing (OBS_SEEING_MEAN) in the V-band during the observations in arcsec (FWHM). (^f) Observation quality flags, combining the three individual column flags (FLAG_OBS_AM,

FLAG_OBS_SKYMAG, FLAG_OBS_EXT) as described in Sect. 6. (^g) Average spectral resolution (RED_DISP_MEAN) in Å (FWHM), measured by fitting the night-sky emission lines with single Gaussian functions. (^h) Average signal-to-noise ratio (CAL_SNR1HLR) estimated for the full wavelength range at one half-light radius from the center. (ⁱ) Average flux at the 3 σ continuum detection limit in units of B-band mag arcsec⁻² and in units of 10^{-18} erg s⁻¹ cm⁻² Å⁻¹ arcsec⁻². (^j) Reduction/instrumental performance quality flags, combining the five individual column flags (FLAG_RED_STRaylight, FLAG_RED_DISP, FLAG_RED_CDISP, FLAG_RED_SKYLINES, FLAG_RED_LIMSB) as described in Sect. 6.

(^k) Quality control flags, combining the three individual column flags (FLAG_CAL_SPECPHOTO, FLAG_CAL_WL, FLAG_CAL_IMA) as described in Sect. 6.

Table 7. continued.

ID ^a	Airmass ^b	$\mu_{V,\text{sky}}^c$	A_V^d	Seeing ^e	Flags(O) ^f	δ_A^g	$S/N(R_{50})^h$	$I_{3\sigma}^i$	Flags(R) ^j	Flags(C) ^k
231	1.06 ± 0.03	22.3	00-	1.92	5.4	$23.5 2.5$	10000	001
232	1.31 ± 0.12	21.9	0.11	...	000	1.96	9.8	$23.5 2.4$	00010	101
272	1.13 ± 0.03	22.1	00-	2.09	9.2	$22.8 5.0$	01010	000
273*	1.06 ± 0.01	22.2	0.14	1.1 ± 0.1	000	2.01	12.6	$23.6 2.3$	01000	000
274*	1.30 ± 0.09	22.0	00-	2.05	10.7	$23.0 4.0$	01100	000
275	1.16 ± 0.02	22.4	0.15	...	000	1.99	9.2	$22.4 6.7$	-00-1	000
277*	1.08 ± 0.04	21.7	0.15	...	000	2.13	12.0	$23.0 4.0$	01010	001
278	1.09 ± 0.05	22.5	0.11	...	000	2.24	7.4	$22.8 4.8$	01100	100
306*	1.14 ± 0.03	21.3	01-	2.02	3.5	$23.2 3.4$	21100	001
307*	1.20 ± 0.08	22.2	0.15	0.8 ± 0.1	000	2.33	4.8	$22.7 5.2$	11100	001
309*	1.25 ± 0.08	22.1	0.14	...	000	2.38	6.3	$22.8 4.8$	01100	000
311	1.03 ± 0.03	22.4	00-	2.02	4.2	$22.9 4.3$	01100	000
314	1.05 ± 0.01	22.4	0.12	...	000	1.92	11.5	$23.2 3.3$	-00-0	001
319*	1.07 ± 0.06	22.2	0.15	1.1 ± 0.1	000	1.99	12.5	$23.6 2.3$	-01-0	000
326*	1.29 ± 0.05	21.9	00-	2.02	5.4	$22.7 5.0$	01100	001
340	1.08 ± 0.02	22.5	00-	2.01	4.0	$23.0 3.9$	01100	001
341*	1.21 ± 0.08	22.0	0.16	1.2 ± 0.1	000	1.91	7.9	$23.4 2.7$	00100	001
353	1.04 ± 0.03	22.5	0.10	...	000	2.07	9.4	$23.3 2.9$	01010	001
364*	1.02 ± 0.02	22.1	...	0.9 ± 0.1	00-	2.03	15.8	$23.3 2.9$	11000	001
381	1.01 ± 0.01	22.2	00-	1.96	12.4	$23.6 2.4$	-00-0	000
388	1.33 ± 0.11	22.1	00-	2.15	2.3	$22.4 6.7$	01111	101
436	1.10 ± 0.03	21.4	01-	1.96	11.1	$23.0 3.9$	-00-0	001
475*,†	1.13 ± 0.07	22.1	00-	2.03	11.6	$23.3 2.9$	21010	101
476	1.40 ± 0.28	21.8	10-	2.02	25.5	$22.9 4.5$	01100	001
479*	1.16 ± 0.03	22.3	00-	2.05	7.2	$22.7 5.3$	01100	001
486*	1.21 ± 0.10	22.1	0.15	0.8 ± 0.1	000	1.99	8.6	$23.5 2.5$	10100	100
502	1.23 ± 0.08	21.9	00-	1.93	11.6	$22.5 6.1$	00000	001
515*	1.20 ± 0.09	22.3	0.15	0.9 ± 0.1	000	2.30	4.2	$22.6 5.5$	11110	000
518*	1.18 ± 0.03	22.6	0.13	...	000	2.03	12.6	$23.3 2.9$	01100	000
528*	1.48 ± 0.08	22.0	00-	2.10	2.0	$22.7 5.5$	01100	110
548*	1.21 ± 0.05	21.9	0.18	0.8 ± 0.1	000	2.00	14.6	$23.2 3.3$	10000	100
569	1.16 ± 0.05	22.0	0.15	...	000	1.95	15.0	$23.5 2.4$	00000	001
577*,†	1.06 ± 0.04	22.2	0.22	...	000	1.89	6.5	$23.6 2.3$	00100	00-
592	1.03 ± 0.02	22.3	00-	2.25	4.9	$22.6 5.5$	01100	000
593	1.15 ± 0.05	21.9	00-	1.95	8.3	$23.5 2.6$	00000	010
606	1.33 ± 0.09	22.1	0.17	...	000	1.94	10.4	$23.6 2.3$	00000	001
607*	1.25 ± 0.07	22.3	0.14	...	000	2.25	16.7	$23.1 3.7$	01000	000
608*	1.20 ± 0.10	21.9	0.16	...	000	1.92	6.3	$23.2 3.3$	00000	000
609*	1.08 ± 0.05	22.4	0.15	0.8 ± 0.1	000	2.28	6.8	$23.0 3.9$	11100	011
610*	1.17 ± 0.07	22.5	00-	2.14	8.9	$23.0 4.1$	11100	100
630	1.26 ± 0.06	22.4	00-	1.92	10.7	$23.3 2.9$	00000	000
633	1.55 ± 0.12	22.0	00-	1.92	4.3	$23.2 3.3$	00010	000
657*	1.09 ± 0.05	22.4	0.19	1.5 ± 0.2	000	1.90	5.3	$23.7 2.1$	00000	000
663*	1.10 ± 0.02	22.0	00-	1.98	11.8	$23.3 2.9$	01000	001
664*	1.07 ± 0.04	22.0	0.26	1.2 ± 0.1	000	1.96	16.2	$23.4 2.7$	00000	001
665*	1.17 ± 0.10	22.1	0.10	...	000	1.95	5.1	$22.8 4.6$	00000	001
676*	1.01 ± 0.02	22.5	0.17	0.8 ± 0.1	000	2.26	4.6	$22.9 4.2$	01100	001
680*	1.07 ± 0.05	22.4	0.10	...	000	1.95	5.4	$23.7 2.0$	00000	000
684*	1.06 ± 0.04	22.3	0.13	0.9 ± 0.1	000	1.96	13.0	$23.4 2.8$	00000	001
708	1.12 ± 0.04	22.2	00-	1.91	7.7	$23.0 4.0$	00010	000
714	1.43 ± 0.12	21.9	00-	1.93	12.6	$23.4 2.7$	-00-0	001
715	1.18 ± 0.06	21.9	0.22	...	000	2.00	18.7	$23.6 2.3$	00000	001
740	1.05 ± 0.04	22.8	00-	2.24	4.4	$22.2 8.3$	01011	001
749	1.07 ± 0.04	22.3	00-	2.06	13.2	$23.4 2.7$	11010	001
758*	1.18 ± 0.05	22.2	0.26	1.0 ± 0.1	001	1.89	5.5	$23.4 2.7$	-00-0	100
764*	1.11 ± 0.04	...	0.16	...	0-0	2.02	7.7	$23.6 2.4$	01100	001
769*	1.03 ± 0.02	22.2	00-	2.00	9.6	$23.3 3.1$	01000	000
778	1.02 ± 0.01	22.5	00-	2.13	8.8	$23.2 3.3$	01000	000
783*	1.20 ± 0.07	22.3	0.17	...	000	2.29	11.3	$22.9 4.2$	01000	000
789	1.10 ± 0.05	22.1	00-	1.95	12.4	$23.5 2.6$	00000	000
791	1.08 ± 0.02	22.6	00-	2.28	9.0	$22.7 5.1$	01110	001
795	1.23 ± 0.09	22.3	00-	1.92	12.3	$23.5 2.6$	00000	000
797*	1.06 ± 0.04	22.5	0.17	1.3 ± 0.2	000	1.89	8.4	$23.6 2.4$	00000	000
798*	1.13 ± 0.07	22.2	0.30	0.8 ± 0.1	001	1.93	8.1	$23.4 2.8$	00000	001

Table 7. continued.

ID ^a	Airmass ^b	$\mu_{V,\text{sky}}^c$	A_V^d	Seeing ^e	Flags(O) ^f	δ_A^g	$S/N(R_{50})^h$	$I_{3\sigma}^i$	Flags(R) ^j	Flags(C) ^k
806*	1.06 ± 0.05	22.2	0.21	1.1 ± 0.1	000	1.90	29.0	23.5 ± 2.4	00010	000
807	1.30 ± 0.19	22.0	10-	1.96	9.8	23.5 ± 2.5	-00-0	001
809	1.30 ± 0.08	21.7	00-	1.95	8.2	23.2 ± 3.2	00010	001
813	1.07 ± 0.02	22.3	00-	2.05	8.7	23.1 ± 3.7	01010	000
815	1.15 ± 0.10	22.2	00-	2.05	3.8	23.1 ± 3.7	-10-0	001
816	1.15 ± 0.06	22.2	00-	2.08	12.1	23.3 ± 3.0	11010	001
820*	1.15 ± 0.10	22.3	0.15	0.7 ± 0.1	000	2.35	4.3	22.7 ± 5.4	-11-0	101
822*	1.09 ± 0.05	22.1	0.16	0.8 ± 0.1	000	1.91	7.4	23.4 ± 2.9	00000	000
823*	1.17 ± 0.03	22.0	0.26	0.9 ± 0.1	000	1.91	10.3	23.3 ± 3.1	00000	001
824*,†	1.18 ± 0.04	21.6	0.24	1.1 ± 0.2	000	1.98	6.4	22.6 ± 5.7	00000	001
826*	1.16 ± 0.04	22.0	00-	2.10	10.9	22.9 ± 4.5	-11-0	001
828*	1.17 ± 0.04	22.6	0.16	1.0 ± 0.1	000	1.89	12.4	23.6 ± 2.2	10000	000
829*	1.24 ± 0.07	22.0	0.17	1.4 ± 0.2	000	1.95	7.1	23.3 ± 2.9	01110	000
831	1.18 ± 0.05	21.3	0.17	...	010	1.95	12.5	23.1 ± 3.6	10000	000
832*	1.02 ± 0.02	22.1	00-	2.00	10.4	23.4 ± 2.9	-10-0	001
833*	1.07 ± 0.03	22.2	0.10	...	000	1.95	4.6	22.9 ± 4.4	00000	001
834	1.27 ± 0.10	22.3	0.23	...	000	2.04	10.5	23.5 ± 2.5	01010	001
835*	1.04 ± 0.03	22.3	0.16	1.0 ± 0.1	000	1.95	16.8	23.6 ± 2.2	00000	000
837*	1.15 ± 0.04	22.2	0.14	0.8 ± 0.1	000	1.98	22.1	23.6 ± 2.3	00100	001
838	1.32 ± 0.12	21.9	00-	2.03	14.6	23.4 ± 2.7	01010	001
840*	1.24 ± 0.09	22.1	0.10	...	000	1.95	1.8	23.2 ± 3.2	00000	000
841	1.40 ± 0.09	21.8	0.15	...	000	1.94	9.5	23.1 ± 3.6	-00-0	000
843*	1.11 ± 0.05	22.4	0.26	...	000	1.92	5.6	23.5 ± 2.6	00000	001
845*	1.19 ± 0.15	21.7	0.28	0.8 ± 0.1	100	1.93	4.5	23.2 ± 3.3	-00-0	000
846*	1.17 ± 0.07	22.0	0.25	...	000	1.95	3.3	23.3 ± 2.9	00000	000
847*	1.03 ± 0.03	21.9	0.32	0.8 ± 0.1	001	1.93	7.9	23.1 ± 3.5	00010	001
848*	1.24 ± 0.12	...	0.28	1.0 ± 0.1	0-1	1.88	13.9	23.2 ± 3.3	-00-0	001
850*	1.05 ± 0.02	22.0	0.19	0.8 ± 0.1	000	1.93	12.3	23.3 ± 3.0	00000	000
851*	1.12 ± 0.04	22.1	0.28	0.9 ± 0.1	000	1.89	5.0	23.2 ± 3.4	00000	000
852*	1.38 ± 0.09	21.6	0.19	1.4 ± 0.2	000	1.99	3.6	23.4 ± 2.7	01100	001
854*	1.20 ± 0.06	22.0	0.37	0.9 ± 0.1	001	1.88	9.0	23.2 ± 3.3	20000	001
856*	1.05 ± 0.03	22.7	0.24	0.9 ± 0.1	001	1.91	7.0	22.8 ± 4.7	-00-0	001
857*	1.10 ± 0.02	22.4	0.21	0.9 ± 0.1	000	1.95	14.8	23.5 ± 2.6	00000	000
858*	1.25 ± 0.14	22.1	0.23	0.9 ± 0.1	000	1.98	5.5	23.1 ± 3.7	-00-0	001
859*	1.18 ± 0.05	22.2	0.32	0.7 ± 0.1	001	1.93	3.7	23.0 ± 3.9	00010	000
860*	1.04 ± 0.02	22.3	0.27	0.9 ± 0.3	001	1.91	20.4	23.1 ± 3.4	00010	001
861	1.32 ± 0.13	22.2	00-	1.96	8.7	23.0 ± 3.8	10010	001
862	1.09 ± 0.04	22.2	...	1.1 ± 0.1	00-	1.95	14.3	23.4 ± 2.6	00000	001
863*	1.20 ± 0.06	22.3	0.19	0.9 ± 0.1	000	1.95	10.7	23.3 ± 3.0	00010	001
864*	1.05 ± 0.02	22.4	0.20	...	000	1.96	6.7	23.5 ± 2.6	00010	000
865*	1.02 ± 0.02	22.3	0.27	0.9 ± 0.1	000	1.93	13.0	23.4 ± 2.8	00010	001
866*	1.08 ± 0.05	22.1	0.34	...	001	1.96	4.7	23.5 ± 2.5	00000	101
867*	1.13 ± 0.01	22.1	0.39	...	001	1.96	16.4	23.2 ± 3.3	00000	001
868	1.74 ± 0.13	21.5	0.15	...	110	2.01	12.2	23.0 ± 4.1	01100	001
869	1.35 ± 0.01	22.0	0.22	...	000	1.92	5.8	22.9 ± 4.4	00000	001
871	1.40 ± 0.04	21.7	00-	1.95	11.0	23.0 ± 3.8	00110	000
872*	1.37 ± 0.05	21.7	0.22	1.0 ± 0.1	000	1.94	6.5	23.0 ± 4.1	-00-0	001
874*	1.14 ± 0.05	21.8	0.31	0.8 ± 0.1	001	1.95	9.7	23.1 ± 3.6	00010	001
877*,†	1.10 ± 0.05	...	0.22	1.0 ± 0.1	0-0	1.94	5.1	22.9 ± 4.3	10010	001
878*	1.37 ± 0.07	22.1	0.18	1.1 ± 0.1	000	1.91	4.1	23.5 ± 2.5	00000	001
880	1.25 ± 0.07	22.0	...	0.9 ± 0.1	00-	1.91	8.7	22.8 ± 4.9	00000	001
881*	1.17 ± 0.11	22.0	0.30	0.9 ± 0.2	000	1.96	5.3	23.2 ± 3.4	-00-0	000
883*	1.13 ± 0.04	22.1	0.31	0.9 ± 0.1	001	1.90	2.6	22.7 ± 5.1	00000	001
884	1.49 ± 0.13	21.8	00-	2.01	5.8	23.0 ± 3.9	01000	101
885	1.15 ± 0.00	22.1	00-	1.93	12.4	23.3 ± 3.1	-00-0	000
886	1.32 ± 0.09	22.0	0.19	0.9 ± 0.1	000	1.99	13.8	22.3 ± 7.3	00011	001
887*	1.05 ± 0.01	22.2	0.29	0.8 ± 0.1	000	1.89	10.4	23.1 ± 3.8	-00-0	001
888*	1.08 ± 0.05	21.9	0.41	...	001	2.01	1.3	23.1 ± 3.8	01000	000
890*	1.02 ± 0.01	21.8	0.23	0.9 ± 0.1	000	1.94	10.8	23.4 ± 2.9	-00-0	000
891	1.20 ± 0.03	22.1	00-	1.94	4.1	23.0 ± 4.1	10110	000
893*	1.40 ± 0.21	21.8	0.15	1.0 ± 0.1	100	1.95	3.2	22.8 ± 4.6	-00-0	001
894	1.03 ± 0.01	22.5	00-	1.98	8.0	23.1 ± 3.7	10100	101
895	1.12 ± 0.03	21.9	00-	1.99	5.2	23.2 ± 3.4	-00-0	001
896*	1.03 ± 0.02	22.3	0.14	1.4 ± 0.3	000	2.13	8.3	23.2 ± 3.3	01100	000

Table 7. continued.

ID ^a	Airmass ^b	$\mu_{V,\text{sky}}^c$	A_V^d	Seeing ^e	Flags(O) ^f	δ_λ^g	$S/N(R_{50})^h$	$I_{3\sigma}^i$	Flags(R) ^j	Flags(C) ^k
898	1.20 ± 0.09	22.2	0.24	...	000	1.97	6.1	22.6 5.9	00100	000
901*	1.20 ± 0.10	22.1	0.25	1.0 ± 0.2	000	2.02	10.7	22.9 4.5	01010	000
902*	1.38 ± 0.14	21.7	0.21	1.1 ± 0.1	000	1.97	17.0	23.2 3.3	00010	001
903	1.26 ± 0.07	21.9	0.12	...	000	1.95	12.6	22.8 4.6	00010	000
904*	1.27 ± 0.08	21.7	0.22	1.3 ± 0.3	000	1.99	9.2	23.0 3.9	00000	101
909	1.29 ± 0.11	21.9	0.12	...	000	1.95	7.6	22.5 6.1	00000	001
910	1.28 ± 0.06	21.8	00-	2.05	6.8	23.0 4.0	-10-0	000
913	1.24 ± 0.10	22.1	01-	2.24	13.4	22.9 4.3	01100	001
914	1.16 ± 0.02	22.0	00-	1.92	12.4	23.2 3.4	00010	101
915	1.30 ± 0.11	22.0	00-	1.90	12.2	23.3 3.1	00010	001
916	1.21 ± 0.07	22.2	0.13	...	000	2.00	12.0	22.9 4.4	01010	000
917	1.12 ± 0.01	22.4	0.20	...	000	1.93	11.6	23.0 3.9	00010	001
922	1.23 ± 0.06	22.0	0.14	...	000	1.94	11.0	23.4 2.7	00000	100
924	1.32 ± 0.06	21.9	00-	1.94	10.4	23.3 3.1	00000	101
927	1.29 ± 0.05	22.0	0.11	...	000	1.98	3.9	22.7 5.1	00000	001
930	1.27 ± 0.05	21.9	00-	1.90	7.8	23.5 2.4	00000	000
932	1.29 ± 0.05	21.8	0.12	...	000	1.95	10.6	23.3 3.0	00000	001
935*	1.09 ± 0.06	22.3	0.18	...	000	2.13	4.5	23.4 2.8	01100	000
936	1.45 ± 0.13	21.6	00-	1.94	7.0	23.0 3.9	-00-0	001
937	1.16 ± 0.04	22.1	0.19	...	000	1.98	7.1	23.2 3.2	-01-0	101
938	1.13 ± 0.07	...	0.23	1.0 ± 0.1	0-0	1.94	12.6	23.4 2.8	00000	000
939*	1.32 ± 0.08	21.9	0.28	0.9 ± 0.1	001	1.89	5.2	23.3 3.0	-00-0	000

The layout of Fig. 16 is identical to Fig. 13 of Cid Fernandes et al. (2014), to which it should be compared¹⁵. Focusing on the middle panel, one sees that from ~ 5000 Å to the red the residuals are very similar, including the humps around 5800 Å associated with the imperfect removal of telluric features. Toward the blue however, the new reduction pipeline leads to smaller residuals. For instance, the broad feature around H β seen with V1.3c spectra is essentially eliminated by the new reduction. A systematic excess blueness persists for $\lambda < 3900$ Å, but overall the improvement is clear.

Residuals for the 200 DR2 nuclear spectra are shown in Fig. 17, where galaxies are sorted by redshift and stacked. This visualization facilitates the identification of telluric features, which appear as slanted lines in the image. Comparison with an identical plot in H13 (their Fig. 16) shows the improvements achieved with the new pipeline.

6.6. Limiting sensitivity and signal-to-noise

To assess the depth of the data, we estimated the 3σ continuum flux density detection limit per interpolated 1 arcsec 2 -spaxel and spectral resolution element for the faintest regions. Figure 18 shows the limiting continuum sensitivity of the spectrophotometrically recalibrated CALIFA spectra. The depth is plotted against the average S/N per 1 arcsec 2 and spectral resolution element within an elliptical annulus of $\pm 1''$ around the galaxies' r -band half-light semimajor axis (HLR), with PA and radius values taken from W14. A narrow wavelength window at 4480–4520 Å for the V1200 and at 5590–5680 Å for the V500 was used to estimate both values¹⁶. These small windows

are nearly free of stellar absorption features or emission lines. The 3σ continuum flux density detection limit per spaxel and spectral resolution element¹⁷ for the V1200 data ($I_{3\sigma} = 3.2 \times 10^{-18}$ erg s $^{-1}$ cm $^{-2}$ Å $^{-1}$ arcsec $^{-2}$ in the median at 4500 Å) is a factor of ~ 2 –3 brighter than for the V500 data ($I_{3\sigma} = 1.2 \times 10^{-18}$ erg s $^{-1}$ cm $^{-2}$ Å $^{-1}$ arcsec $^{-2}$ in the median at 5635 Å) mainly because of the difference in spectral resolution. These continuum sensitivities can be transformed into equivalent limiting broadband surface brightnesses of 23.0 mag arcsec $^{-2}$ in the g -band for the V1200 data and 23.4 mag arcsec $^{-2}$ in the r -band for the V500. The variance of the sky brightness of each night might be one of the main factors causing the dispersion in the limiting continuum sensitivity. Dust attenuation, transparency of the night, and other atmospheric conditions might also affect the depth achievable at fixed exposure times.

The limiting sensitivity is a measure of the noise and thus it correlates mildly with the S/N. The mean S/N in the continuum per 1 arcsec 2 and spectral resolution element at the half-light semimajor axis (HLR) of all objects is ~ 9.5 for the V1200 setup, while it is ~ 22.2 for the V500 data. Thus, we achieve a $S/N \gtrsim 10$ for a significant number of the objects even for the V1200 setup.

7. Access to the CALIFA DR2 data

7.1. The CALIFA DR2 search and retrieval tool

The public data are distributed through the CALIFA DR2 web page¹⁸. A simple web form interface, already in use for the first data release, allows the user to select data of a particular target galaxy, or a subsample of objects within some constraints on observing conditions or galaxy properties. Among the selection parameters, we include the instrument setup, galaxy coordinates, redshift, g -band magnitudes, observing date, Hubble type, bar strength, inclination estimated from axis ratio, V band atmospheric attenuation, airmass, and relative accuracy of the SDSS/CALIFA photometric calibration.

¹⁵ Fig. 13 in Cid Fernandes et al. (2014) is in fact busier than our Fig. 16, as it shows results obtained with three different spectral bases.

Here we adopt the same base described in González Delgado et al. (2014b), which is very similar to base GM in Cid Fernandes et al. (2014).

¹⁶ The signal (also used for the surface brightness limit) is computed as the median value in the defined wavelength intervals, while the noise is the detrended standard deviation in the same windows.

¹⁷ Note that this is a continuum flux density. See Note 5 of H13.

¹⁸ <http://califa.caha.es/DR2>

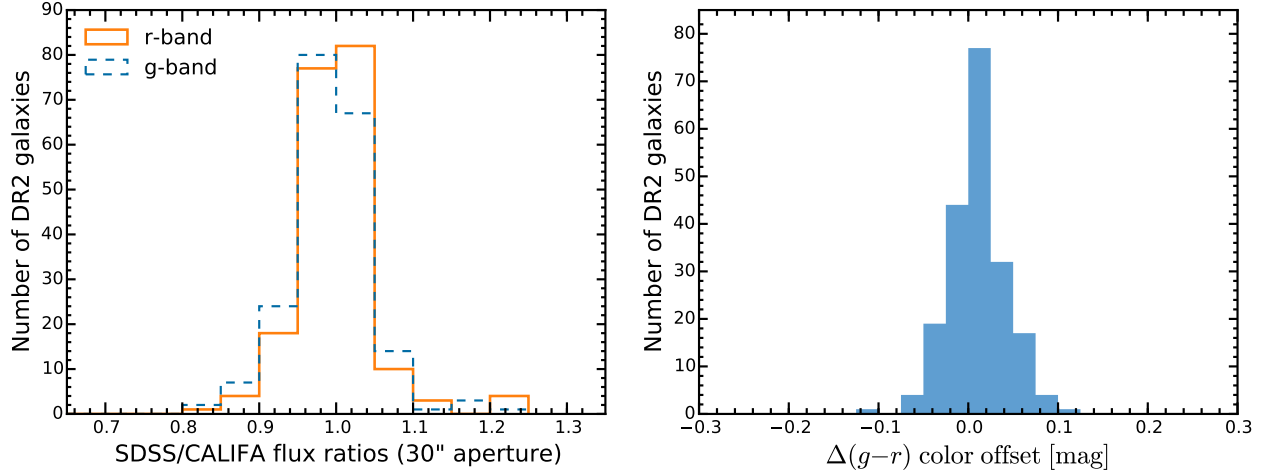


Fig. 14. *Left panel:* distribution of the $30''$ aperture photometry scale factor between the SDSS DR7 images and recalibrated CALIFA data. We compare the photometry only for the g and r bands, which are both entirely covered by the V500 wavelength range. *Right panel:* distribution of the corresponding color offset between the SDSS DR7 images and the synthetic CALIFA broadband images.

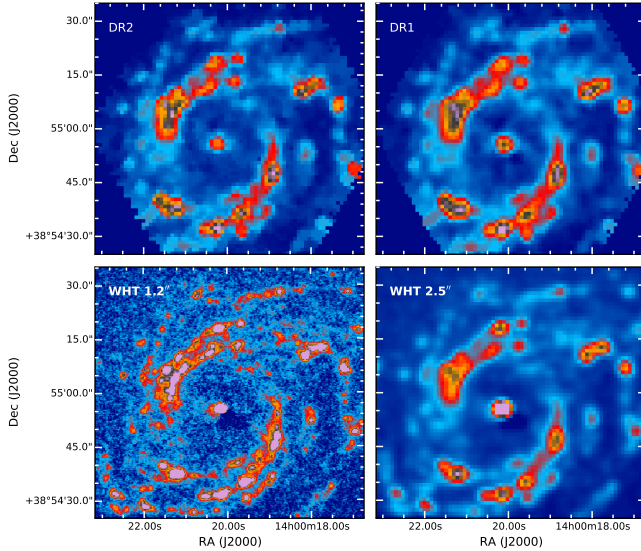


Fig. 15. DR2 spatial resolution comparison for NGC 5406 (ID 684). The upper left panel shows the DR2 image of the H α map and the upper right the DR1 image. The lower row are H α images taken with the 4.2 m William Herschel Telescope (Roque de los Muchachos Observatory, La Palma, Spain), using the AUXCAM detector (Sánchez-Menguiano et al., in prep.). The image, with an original resolution of $1.2''$ (bottom left), has been degraded to a resolution of $2.5''$ with the same pixel scale (bottom right) and the FoV has been reduced to match exactly the same WCS coordinates as CALIFA.

If any CALIFA data sets are available given the search parameters, they are listed in the following web page and can be selected to be downloaded. The download process requests a target directory on the local machine to store the data, after the downloading option is selected. The CALIFA data are delivered as fully reduced datacubes in FITS format separately for each of the two CALIFA spectral settings, i.e., the V500 and V1200 setup. Each DR2 data set is uniquely identified by their file name, `GALNAME.V1200.rscube.fits.gz` and `GALNAME.V500.rscube.fits.gz` for the V1200 and V500 setup respectively, where `GALNAME` is the name of the CALIFA galaxy listed in Table 1.

All the QC tables discussed throughout this article are also distributed in CSV and FITS-table formats in the same webpage. In addition, we distribute the more relevant tables discussed in W14 regarding the characterization of the MS, using similar formats. These tables could be useful in further science explorations of the cubes.

7.2. Virtual observatory services

CALIFA data is also available through several Virtual Observatory (VO) facilities:

1. The FITS files of the full cubes are accessible through GAVO's ObsCore (Louys et al. 2011) service, which is part of the TAP (Dowler et al. 2011) service¹⁹. ObsCore provides a homogeneous description of observational data products of all kinds and thus allows for a global data set discovery. The system already supports the upcoming IVOA DataLink standard for performing cutouts and similar server-side operations.
2. At the same TAP endpoint, the `califadr2.cubes` and `califadr2.objects` tables enable queries versus CALIFA-specific metadata, and in particular, the quality control parameters given in Tables 6 and 7.
3. Individual, cutout spectra can be located and retrieved from the CALIFA SSA service²⁰; advanced SSAP clients like Splat (Draper 2014) also support server-side spectral cutouts on this service via a DataLink prototype.
4. The spaxels can also be queried in database tables via GAVO's TAP service mentioned above (the tables are called `califadr2.fluxv500` and `califadr2.fluxv1200`).

An overview of VO-accessible resources generated from CALIFA, possibly updated from what is reported here, is available at <http://dc.g-vo.org/browse/califa/q2>. This page also gives some usage scenarios for CALIFA VO resources.

8. Summary

In this article we have presented the main characteristics of the second public data release of the Calar Alto Legacy Integral

¹⁹ <http://dc.g-vo.org/tap>

²⁰ SSA access URL <http://victor:8080/califa/q2/s/info>

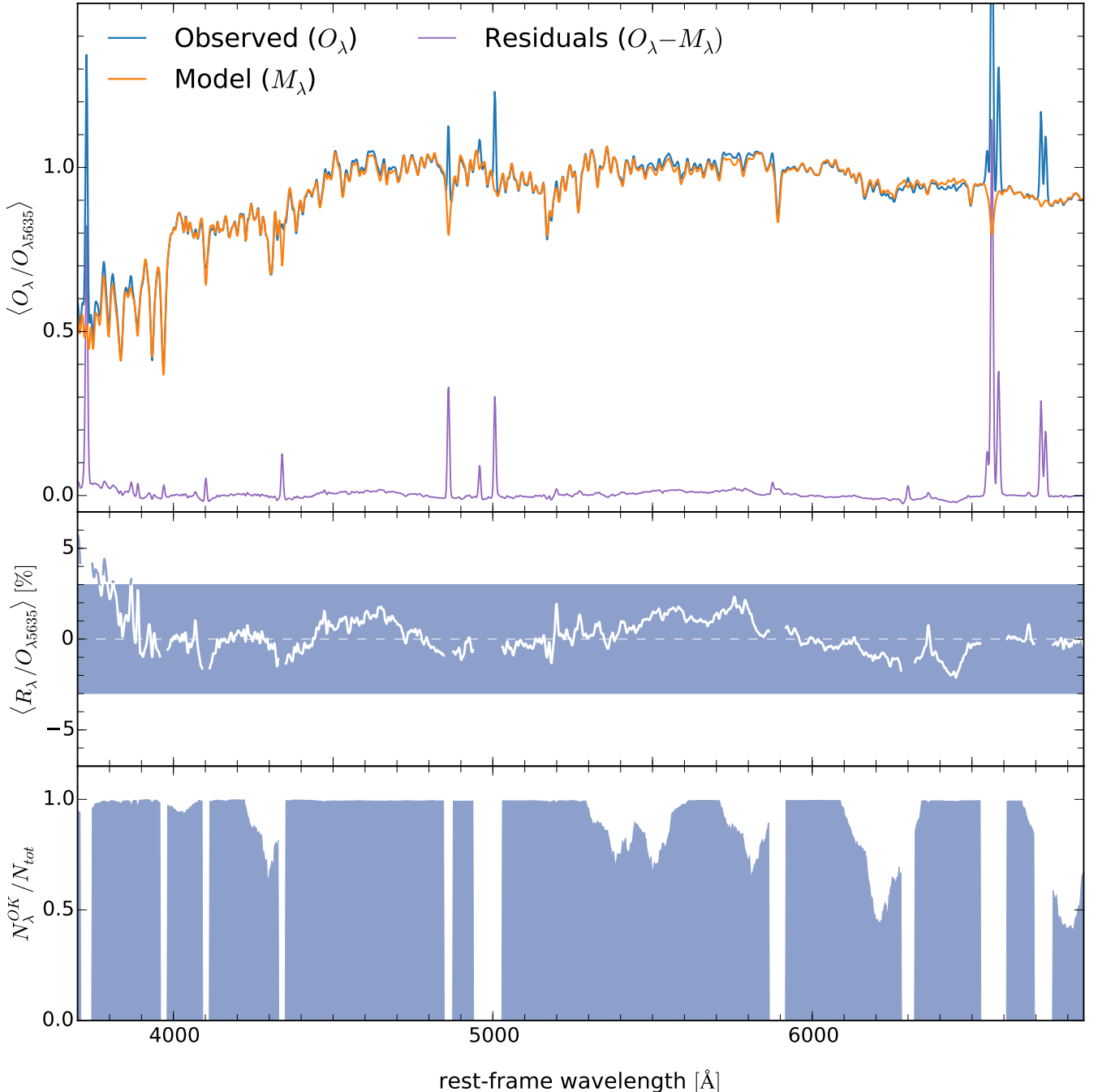


Fig. 16. Statistics of the spectral residuals (compare to Fig. 13 of Cid Fernandes et al. 2014). *Top:* the mean normalized spectrum of 170670 bins from 200 galaxies. The mean fit is overplotted in orange, while the mean residual is plotted at the bottom of the panel (purple). *Middle:* zoom of the residual spectrum, with emission lines removed for clarity. The shaded rectangle encompasses the $\pm 3\%$ area. *Bottom:* fraction of the bins contributing to the statistics at each λ .

Field Area (CALIFA) survey. This data release comprises 200 galaxies (400 datacubes) containing more than 1.5 million spectra²¹, covering a wide range of masses, morphological types, colors, etc. This subset of randomly selected objects comprises a statistically representative sample of the galaxies in the Local Universe. The CALIFA DR2 provides science-grade and quality-checked, integral-field spectroscopy publicly distributed to the community²².

We described in detail the main quality parameters analyzed in the validation process, which are provided to the users with complete tables to select the objects for their science cases. We reduced the data using a new version of the pipeline (V1.5), which considerably improves the quality of the data in terms of: (i) the spatial resolution; (ii) the covariance between the adjacent spectra; and (iii) the spectrophotometric calibration.

Compared with other ongoing major surveys, CALIFA offers a similar spatial resolution. The PSF of the datacubes has been improved considerably, with a mean value of $\sim 2.5''$ (Sect. 6.4.2), similar to SAMI (Sharp et al. 2015). In the case of MaNGA, the

²¹ Obtained from $\sim 400\,000$ independent spectra from the RSS files.

²² <http://califa.caha.es/DR2>

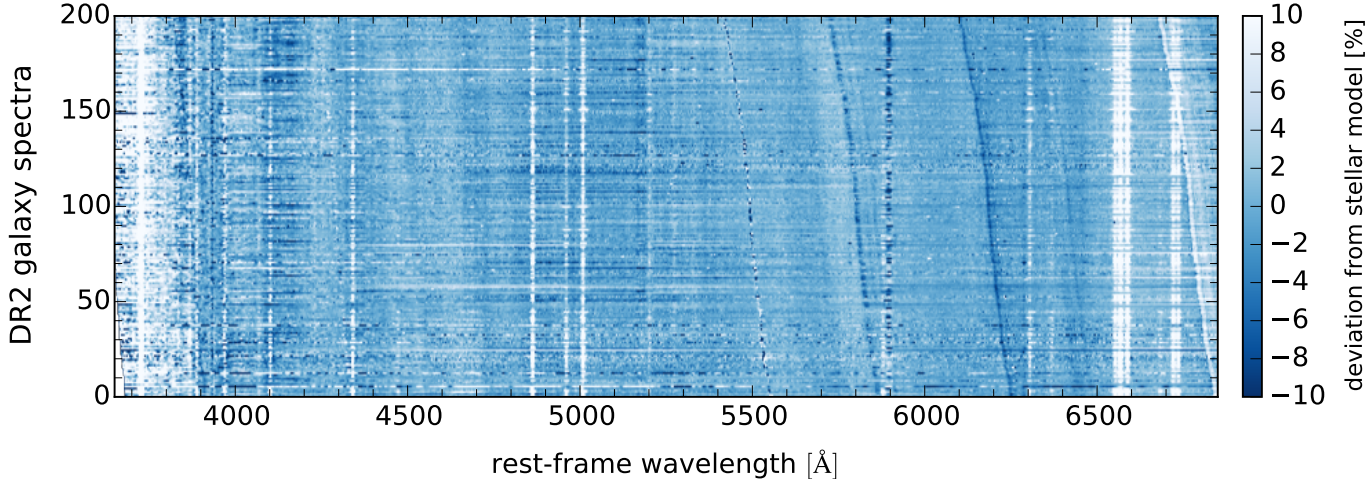


Fig. 17. Relative spectral deviations, $(O_\lambda - M_\lambda)/O_\lambda$, where O and M denote the observed and the model spectra, for the nuclear regions of all DR2 galaxies, vertically sorted by redshift. Unlike in Fig. 16, emission lines and bad pixels are not masked in this plot. Systematic deviations from the model appear as vertical stripes (rest-frame mismatches, e.g., imperfect stellar model or emission lines), while slanted stripes trace observed-frame mismatches (e.g., imperfect sky model). Compare to Fig. 16 of H13.

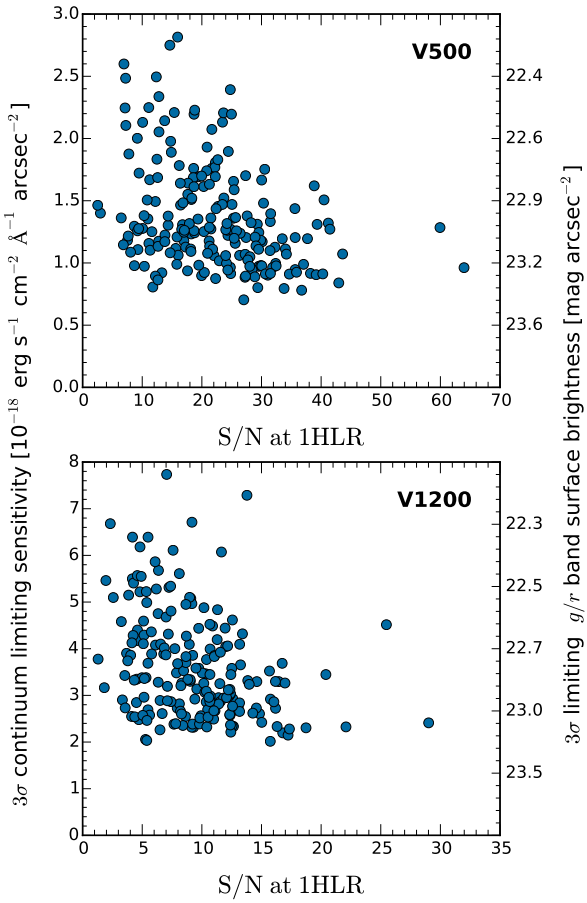


Fig. 18. Limiting 3σ continuum sensitivity per spaxel and spectral resolution element as a function of the average continuum S/N at the half-light radius (HLR). The corresponding broadband surface brightness limits in r (V500) and g (V1200) are indicated on the right y -axis. The limiting continuum sensitivity and the S/N were computed from the median signal and noise in the wavelength region 4480–4520 Å and 5590–5680 Å for the V1200 and V500 data, respectively.

combination of an average seeing at the Sloan Telescope ($\sim 1.5''$) and the fiber size ($2''$), would produce a PSF with a very similar

FWHM. The redshift range of SAMI and MaNGA surveys is considerably larger than CALIFA, reaching up to $z \sim 0.1$. This means that only galaxies at the lowest redshift range in SAMI and MaNGA will offer a similar physical resolution. On the other hand, the spatial coverage of CALIFA is larger than any of those surveys, both in physical and in projected terms (five times larger than SAMI and two times larger than MaNGA). In summary, CALIFA is the survey that samples the galaxies with the largest number of spatial elements for the largest FoV. The penalty for this wider coverage is the lower number of galaxies observed (6 times lower than SAMI and 15 times lower than MaNGA), and a lower spectral resolution of CALIFA over the full wavelength range.

The dataset analysed so far have produced significant advances in our knowledge of the stellar and gas composition in galaxies, their kinematical structure, and the overall star formation history and chemical enrichment (as reviewed in the introduction). We have uncovered new local relations within galaxies, tightly connected to the global relations described using classical spectroscopic surveys. With this new DR, we open to the astronomical community the possibility to further analyze the spatially resolved properties of galaxies, presenting a panoramic view of the galaxy properties.

Acknowledgements. CALIFA is the first legacy survey being performed at Calar Alto. The CALIFA collaboration would like to thank the IAA-CSIC and MPIA-MPG as major partners of the observatory, and CAHA itself, for the unique access to telescope time and support in manpower and infrastructures. The CALIFA collaboration thanks also the CAHA staff for the dedication to this project. R.G.B., R.G.D., and E.P. are supported by the Spanish *Ministerio de Ciencia e Innovación* under grant AYA2010-15081. S.Z. is supported by the EU Marie Curie Integration Grant “SteMaGE” Nr. PCIG12-GA-2012-326466 (Call Identifier: FP7-PEOPLE-2012 CIG). J.F.B. acknowledges support from grants AYA2010-21322-C03-02 and AIB-2010-DE-00227 from the Spanish Ministry of Economy and Competitiveness (MINECO), as well as from the FP7 Marie Curie Actions of the European Commission, via the Initial Training Network DAGAL under REA grant agreement number 289313. Support for L.G. is provided by the Ministry of Economy, Development, and Tourism’s Millennium Science Initiative through grant IC12009, awarded to The Millennium Institute of Astrophysics. M.A.S. L.G. also acknowledges support by CONICYT through FONDECYT grant 3140566. A.G. acknowledges support from the FP7/2007–2013 under grant agreement n. 267251 (AstroFit). J.M.G. acknowledges support from the Fundação para a Ciência e a Tecnologia (FCT) through the Fellowship SFRH/BPD/66958/2009 from FCT (Portugal) and research grant PTDC/FIS-AST/3214/2012. RAM was funded by the Spanish programme of International Campus of Excellence Moncloa (CEI). J.M.A. acknowledges support from the

European Research Council Starting Grant (SEDmorph; P.I. V. Wild). I.M., J.M. and A.d.O. acknowledge the support by the projects AYA2010-15196 from the Spanish Ministerio de Ciencia e Innovación and TIC 114 and PO08-TIC-3531 from Junta de Andalucía. AMI acknowledges support from Agence Nationale de la Recherche through the STILISM project (ANR-12-BS05-0016-02). M.M. acknowledges financial support from AYA2010-21887-C04-02 from the Ministerio de Economía y Competitividad. P.P. is supported by an FCT Investigador 2013 Contract, funded by FCT/MCTES (Portugal) and POPH/FSE (EC). P.P. acknowledges support by FCT under project FCOMP-01-0124-FEDER-029170 (Reference FCT PTDC/FIS-AST/3214/2012), funded by FCT-MEC (PIDAAC) and FEDER (COMPETE). T.R.L. thanks the support of the Spanish Ministerio de Educación, Cultura y Deporte by means of the FPU fellowship. PSB acknowledges support from the Ramón y Cajal program, grant ATA2010-21322-C03-02 from the Spanish Ministry of Economy and Competitiveness (MINECO). C.J.W. acknowledges support through the Marie Curie Career Integration Grant 303912. V.W. acknowledges support from the European Research Council Starting Grant (SEDmorph P.I. V. Wild) and European Career Re-integration Grant (Phiz-Ev P.I. V. Wild). Y.A. acknowledges financial support from the *Ramón y Cajal* programme (RyC-2011-09461) and project AYA2013-47742-C4-3-P, both managed by the *Ministerio de Economía y Competitividad*, as well as the “Study of Emission-Line Galaxies with Integral-Field Spectroscopy” (SELGIFS) programme, funded by the EU (FP7-PEOPLE-2013-IRSES-612701) within the Marie-Sklodowska-Curie Actions scheme. We thank the referee David Wilman for very useful comments that improved the presentation of the paper.

Appendix A: Computing the error spectrum for co-added spectra

Some science cases require a minimum S/N in the spectra, especially in the outer parts of the galaxies. This is achieved by spatially coadding spaxels in the datacubes, often by means of an adaptive binning method, such as the Voronoi-binning scheme, implemented for optical IFS data by Cappellari & Copin (2003). However, the final error spectrum of the coadded spectra cannot be simply quadratically summed since the spectra are not independent of each other. As described in Sect. 4.2, we adopt an inverse-distance weighted image reconstruction which, like many other image resampling schemes, introduces a correlation between spaxels in the final datacube. In Sect. 4.3, we provide an equation that relates the analytically propagated error recorded in the datacubes with the final “real” error of the coadded spectrum²³.

Let B be a bin of size N spectra, i.e., we want to coadd N spectra and compute the corresponding error spectrum for that bin. Since we are adding the flux to obtain an integrated spectrum, first we need to add the errors of each individual spectra in quadrature,

$$\epsilon_B^2 = \sum_{k=1}^N \epsilon_k^2.$$

This would be the error spectrum of the bin B if the spaxels were completely independent. To account for the correlated noise, we simply need to multiply by the corresponding “correlation factor” (Eq. (1)) for a given number of spectra in a particular bin,

$$\epsilon_{\text{real},B}^2 = \beta(N)^2 \times \epsilon_B^2,$$

when the bin B contains a large number of spaxels ($N \gtrsim 80$), the use of Eq. (1) is not recommended. In this case, the ERRWEIGHT HDU extension of the CALIFA FITS file datacube should be used (see Table 2) as a correction factor for each spaxel,

$$\epsilon_B^2 = \sum_{k=1}^N w_k^2 \times \epsilon_k^2,$$

²³ See also Sects. 3.2 and 3.3 of Cid Fernandes et al. (2013) for a detailed disquisition on error propagation and correlated noise for IFS.

where w_k is the error weight of each individual spaxel. The error weighting factor is estimated for each pixel such that the formal error of the coadded spectrum of the entire cube is identical at the obtained by coadding the individual 993 fibers of the RSS.

References

- Abazajian, K. N., Adelman-McCarthy, J. K., Agüeros, M. A., et al. 2009, *ApJS*, **182**, 543
 Aceituno, J. 2004, Calar Alto Newsletter No. 8, <http://www.caha.es/newsletter/news04b/Aceituno/Newsletter.html>
 Aguerri, J. A. L., Méndez-Abreu, J., Falcón-Barroso, J., et al. 2015, 576, A102
 Alonso-Herrero, A., Rosales-Ortega, F. F., Sánchez, S. F., et al. 2012, *MNRAS*, **425**, L46
 Barrera-Ballesteros, J. K., Falcón-Barroso, J., García-Lorenzo, B., et al. 2014, *A&A*, **568**, A70
 Bershadsky, M. A., Verheijen, M. A. W., Swaters, R. A., et al. 2010, *ApJ*, **716**, 198
 Blanton, M. R., Schlegel, D. J., Strauss, M. A., et al. 2005, *AJ*, **129**, 2562
 Bryant, J. J., Owers, M. S., Robotham, A. S. G., et al. 2015, *MNRAS*, **447**, 2857
 Cappellari, M., & Copin, Y. 2003, *MNRAS*, **342**, 345
 Cappellari, M., Emsellem, E., Krajnović, D., et al. 2011, *MNRAS*, **413**, 813
 Cid Fernandes, R., Mateus, A., Sodré, L., Stasińska, G., & Gomes, J. M. 2005, *MNRAS*, **358**, 363
 Cid Fernandes, R., Pérez, E., García Benito, R., et al. 2013, *A&A*, **557**, A86
 Cid Fernandes, R., González Delgado, R. M., García Benito, R., et al. 2014, *A&A*, **561**, A130
 Croom, S. M., Lawrence, J. S., Bland-Hawthorn, J., et al. 2012, *MNRAS*, **421**, 872
 Davies, R. L., Kewley, L. J., Ho, I.-T., & Dopita, M. A. 2014, *MNRAS*, **444**, 3961
 De Geyter, G., Baes, M., Camps, P., et al. 2014, *MNRAS*, **441**, 869
 Dowler, P., Rixon, G., & Tody, D. 2011, ArXiv e-prints [[arXiv:1110.0497](https://arxiv.org/abs/1110.0497)]
 Draper, P. W. 2014, Astrophysics Source Code Library, [record ascl: 1402.007]
 Erwin, P. 2015, *ApJ*, **799**, 226
 Fruchter, A. S. & Hook, R. N. 2002, *PASP*, **114**, 144
 Galbany, L., Stanishev, V., Mourão, A. M., et al. 2014, *A&A*, **572**, A38
 García-Lorenzo, B., Márquez, I., Barrera-Ballesteros, J. K., et al. 2015, *A&A*, **573**, A59
 González Delgado, R. M., Cerviño, M., Martins, L. P., Leitherer, C., & Hauschildt, P. H. 2005, *MNRAS*, **357**, 945
 González Delgado, R. M., Cid Fernandes, R., García Benito, R., et al. 2014a, *ApJ*, **791**, L16
 González Delgado, R. M., Pérez, E., Cid Fernandes, R., et al. 2014b, *A&A*, **562**, A47
 Greisen, E. W., & Calabretta, M. R. 2002, *A&A*, **395**, 1061
 Holwerda, B. W., & Keel, W. C. 2013, *A&A*, **556**, A42
 Horne, K. 1986, *PASP*, **98**, 609
 Husemann, B., Kamann, S., Sandin, C., et al. 2012, *A&A*, **545**, A137
 Husemann, B., Jahnke, K., Sánchez, S. F., et al. 2013, *A&A*, **549**, A87 (H13)
 Iglesias-Páramo, J., Vilchez, J. M., Galbany, L., et al. 2013, *A&A*, **553**, L7
 Kehrig, C., Monreal-Ibero, A., Papaderos, P., et al. 2012, *A&A*, **540**, A11
 Kelz, A., Verheijen, M. A. W., Roth, M. M., et al. 2006, *PASP*, **118**, 129
 Law, D. R., & MaNGA Team 2014, Am. Astron. Soc. Meet. Abstr., 223, 254.31
 Louys, M., Bonnarel, F., Schade, D., et al. 2011, ArXiv e-prints [[arXiv:1111.1758](https://arxiv.org/abs/1111.1758)]
 Marino, R. A., Rosales-Ortega, F. F., Sánchez, S. F., et al. 2013, *A&A*, **559**, A114
 Mármlor-Queraltó, E., Sánchez, S. F., Marino, R. A., et al. 2011, *A&A*, **534**, A8
 Martínez-García, E. E., Puerari, I., Rosales-Ortega, F. F., et al. 2014, *ApJ*, **793**, L19
 Mast, D., Rosales-Ortega, F. F., Sánchez, S. F., et al. 2014, *A&A*, **561**, A129
 Papaderos, P., Gomes, J. M., Vilchez, J. M., et al. 2013, *A&A*, **555**, L1
 Pérez, E., Cid Fernandes, R., González Delgado, R. M., et al. 2013, *ApJ*, **764**, L1
 Rosales-Ortega, F. F., Kennicutt, R. C., Sánchez, S. F., et al. 2010, *MNRAS*, **405**, 735
 Rosales-Ortega, F. F., Díaz, A. I., Kennicutt, R. C., & Sánchez, S. F. 2011, *MNRAS*, **415**, 2439
 Rosales-Ortega, F. F., Sánchez, S. F., Iglesias-Páramo, J., et al. 2012, *ApJ*, **756**, L31
 Roth, M. M., Kelz, A., Fechner, T., et al. 2005, *PASP*, **117**, 620
 Sánchez, S. F., Cardiel, N., Verheijen, M. A. W., Pedraz, S., & Covone, G. 2007, *MNRAS*, **376**, 125
 Sánchez, S. F., Thiele, U., Aceituno, J., et al. 2008, *PASP*, **120**, 1244

- Sánchez, S. F., Rosales-Ortega, F. F., Kennicutt, R. C., et al. 2011, [MNRAS](#), **410**, 313
- Sánchez, S. F., Kennicutt, R. C., Gil de Paz, A., et al. 2012a, [A&A](#), **538**, A8 (S12)
- Sánchez, S. F., Rosales-Ortega, F. F., Marino, R. A., et al. 2012b, [A&A](#), **546**, A2
- Sánchez, S. F., Rosales-Ortega, F. F., Jungwiert, B., et al. 2013, [A&A](#), **554**, A58
- Sánchez, S. F., Rosales-Ortega, F. F., Iglesias-Páramo, J., et al. 2014, [A&A](#), **563**, A49
- Sánchez-Blázquez, P., Rosales-Ortega, F. F., Méndez-Abreu, J., et al. 2014, [A&A](#), **570**, A6
- Sandin, C., Schönberner, D., Roth, M. M., et al. 2008, [A&A](#), **486**, 545
- Sharp, R., Allen, J. T., Fogarty, L. M. R., et al. 2015, [MNRAS](#), **446**, 1551
- Singh, R., van de Ven, G., Jahnke, K., et al. 2013, [A&A](#), **558**, A43
- Vazdekis, A., Sánchez-Blázquez, P., Falcón-Barroso, J., et al. 2010, [MNRAS](#), **404**, 1639
- Verheijen, M. A. W., Bershady, M. A., Andersen, D. R., et al. 2004, [Astron. Nachr.](#), **325**, 151
- Viironen, K., Sánchez, S. F., Marmol-Queraltó, E., et al. 2012, [A&A](#), **538**, A144
- Walcher, C. J., Wisotzki, L., Bekeraïté, S., et al. 2014, [A&A](#), **569**, A1 (W14)
- Wild, V., Rosales-Ortega, F., Falcón-Barroso, J., et al. 2014, [A&A](#), **567**, A132
- Wilson, E. B. 1927, [J. Am. Statis. Assoc.](#), **22**, 209
-
- ¹ Instituto de Astrofísica de Andalucía (IAA/CSIC), Glorieta de la Astronomía s/n Aptdo. 3004, 18080 Granada, Spain,
e-mail: rgb@iaa.es
- ² INAF–Osservatorio Astrofisico di Arcetri, Largo Enrico Fermi 5, 50125 Firenze, Italy
- ³ Instituto de Astronomía, Universidad Nacional Autónoma de México, A.P. 70-264, 04510 México, D.F., Mexico
- ⁴ European Southern Observatory, Karl-Schwarzschild-Str. 2, 85748 Garching b. München, Germany
- ⁵ Departamento de Física, Universidade Federal de Santa Catarina, PO Box 476, 88040-900 Florianópolis, SC, Brazil
- ⁶ Departamento de Astrofísica y CC. de la Atmósfera, Universidad Complutense de Madrid, 28040 Madrid, Spain
- ⁷ Australian Astronomical Observatory, PO Box 915, North Ryde, NSW 1670, Australia
- ⁸ Instituto de Astrofísica de Canarias, vía Láctea s/n, 38205 La Laguna, Tenerife, Spain
- ⁹ Departamento de Astrofísica, Universidad de La Laguna, 38205 La Laguna, Tenerife, Spain
- ¹⁰ Millennium Institute of Astrophysics, Universidad de Chile, Santiago, Chile
- ¹¹ Departamento de Astronomía, Universidad de Chile, Casilla 36-D, Santiago, Chile
- ¹² School of Physics and Astronomy, University of St Andrews, SUPA, North Haugh, KY16 9SS, St Andrews, UK
- ¹³ Kapteyn Astronomical Institute, University of Groningen, Postbus 800, 9700 AV Groningen, The Netherlands
- ¹⁴ Max-Planck-Institut für Astronomie, Königstuhl 17, 69117 Heidelberg, Germany
- ¹⁵ CEI Campus Moncloa, UCM-UPM, Departamento de Astrofísica y CC. de la Atmósfera, Facultad de CC. Físicas, Universidad Complutense de Madrid, Avda. Complutense s/n, 28040 Madrid, Spain
- ¹⁶ Instituto de Cosmología, Relatividade e Astrofísica – ICRA, Centro Brasileiro de Pesquisas Físicas, Rua Dr. Xavier Sigaud 150, CEP 22290-180, Rio de Janeiro, RJ, Brazil
- ¹⁷ Departamento de Física Teórica, Facultad de Ciencias, Universidad Autónoma de Madrid, 28049 Madrid, Spain
- ¹⁸ Leibniz-Institut für Astrophysik Potsdam (AIP), An der Sternwarte 16, 14482 Potsdam, Germany
- ¹⁹ Sydney Institute for Astronomy, School of Physics, University of Sydney, NSW 2006, Australia
- ²⁰ Astronomisches Institut, Ruhr-Universität Bochum, Universitätsstr. 150, 44801 Bochum, Germany
- ²¹ RUB Research Department Plasmas with Complex Interactions, Germany
- ²² Universität Heidelberg, Zentrum für Astronomie, Astronomisches Rechen-Institut, Mönchhofstraße 12-14, 69120 Heidelberg, Germany
- ²³ Departamento de Física Teórica y del Cosmos, University of Granada, Facultad de Ciencias (Edificio Mecenas), 18071 Granada, Spain
- ²⁴ Dark Cosmology Center, University of Copenhagen, Niels Bohr Institute, Juliane Maries Vej 30, 2100 Copenhagen, Denmark
- ²⁵ Instituto de Astrofísica e Ciências do Espaço, Universidade do Porto, CAUP, Rua das Estrelas, 4150-762 Porto, Portugal
- ²⁶ Department of Physics, Royal Military College of Canada, PO box 17000, Station Forces, Kingston, Ontario, K7K 7B4, Canada
- ²⁷ Centro Astronómico Hispano Alemán de Calar Alto (CSIC-MPG), C/ Jesús Durbán Remón 2-2, 4004 Almería, Spain
- ²⁸ Department of Physics 4-181 CCIS, University of Alberta, Edmonton AB T6G 2E1, Canada
- ²⁹ Institute of Astronomy, University of Cambridge, Madingley Road, Cambridge CB3 0HA, UK
- ³⁰ Department of Physics and Astronomy, Macquarie University, NSW 2109, Australia
- ³¹ CIEMAT, Avda. Complutense 40, 28040 Madrid, Spain
- ³² GEPI, Observatoire de Paris, CNRS, Université Paris Diderot, Place Jules Janssen, 92190 Meudon, France
- ³³ Instituto Universitario Carlos I de Física Teórica y Computacional, Universidad de Granada, 18071 Granada, Spain
- ³⁴ Landessternwarte, Zentrum für Astronomie der Universität Heidelberg, Königstuhl 12, 69117 Heidelberg, Germany
- ³⁵ Instituto Nacional de Astrofísica, Óptica y Electrónica, Luis E. Erro 1, 72840 Tonantzintla, Puebla, Mexico
- ³⁶ CENTRA – Centro Multidisciplinar de Astrofísica, Instituto Superior Técnico, Av. Rovisco Pais 1, 1049-001 Lisbon, Portugal
- ³⁷ Department of Physics, Chemistry and Biology, IFM, Linköping University, 581 83 Linköping, Sweden
- ³⁸ Departamento de Astronomía, Universidad de Guanajuato, Apartado Postal 144, 36000 Guanajuato, Mexico
- ³⁹ University of Vienna, Department of Astrophysics, Türkenschanzstr. 17, 1180 Vienna, Austria
- ⁴⁰ Centro de Astrobiología (CSIC-INTA), Depto. Astrofísica, ESAC Campus, 28691 Villanueva de la Cañada, Madrid, Spain

A.2 Insights on the stellar mass-metallicity relation from the CALIFA Survey

Artigo por González Delgado et al. (2014a) ([doi:10.1088/2041-8205/791/1/L16](https://doi.org/10.1088/2041-8205/791/1/L16)).
Também disponível em *pre-print* ([arXiv:1407.1315](https://arxiv.org/abs/1407.1315)).

INSIGHTS ON THE STELLAR MASS–METALLICITY RELATION FROM THE CALIFA SURVEY

R. M. GONZÁLEZ DELGADO¹, R. CID FERNANDES², R. GARCÍA-BENITO¹, E. PÉREZ¹, A. L. DE AMORIM², C. CORTIJO-FERRERO¹, E. A. D. LACERDA², R. LÓPEZ FERNÁNDEZ¹, S. F. SÁNCHEZ^{1,3,4}, N. VALE ASARI², J. ALVES⁵, J. BLAND-HAWTHORN⁶, L. GALBANY⁷, A. GALLAZZI^{8,9}, B. HUSEMANN^{10,11}, S. BEKERAITE¹¹, B. JUNGWIERT¹², A. R. LÓPEZ-SÁNCHEZ¹³, A. DE LORENZO-CÁCERES¹⁴, R. A. MARINO¹⁵, D. MAST¹⁶, M. MOLLÁ¹⁷, A. DEL OLMO¹, P. SÁNCHEZ-BLÁZQUEZ¹⁸, G. VAN DE VEN¹⁹, J. M. VÍLCHEZ¹, C. J. WALCHER¹¹, L. WISOTZKI¹¹, B. ZIEGLER⁵, AND CALIFA COLLABORATION^{9,20}

¹ Instituto de Astrofísica de Andalucía (CSIC), Glorieta de la Astronomía s/n, E-18008 Granada, Spain

² Departamento de Física, Universidade Federal de Santa Catarina, P.O. Box 476, 88040-900 Florianópolis, SC, Brazil

³ Centro Astronómico Hispano Alemán, Calar Alto (CSIC-MPG), Jesús Durbán Remón 2-2, E-04004 Almería, Spain

⁴ Instituto de Astronomía, Universidad Nacional Autónoma de México, A.P. 70-264, 04510 Distrito Federal, Mexico

⁵ University of Vienna, Türkenschanzstrasse 17, A-1180 Vienna, Austria

⁶ Sydney Institute for Astronomy, The University of Sydney, NSW 2006, Australia

⁷ Millennium Institute of Astrophysics and Departamento de Astronomía, Universidad de Chile, Casilla 36-D, Santiago, Chile

⁸ INAF—Osservatorio Astrofisico di Arcetri, Largo Enrico Fermi 5, I-50125 Firenze, Italy

⁹ Dark Cosmology Center, University of Copenhagen, Niels Bohr Institute, Juliane Maries Vej 30, DK-2100 Copenhagen, Denmark

¹⁰ European Southern Observatory, Karl-Schwarzschild-Strasse 2, D-85748 Garching b. München, Germany

¹¹ Leibniz-Institut für Astrophysik Potsdam, An der Sternwarte 16, D-14482 Potsdam, Germany

¹² Astronomical Institute of the Academy of Sciences of the Czech Republic, v.v.i., Boční II 1401, 14131 Prague, Czech Republic

¹³ Australian Astronomical Observatory, P.O. Box 915, North Ryde, NSW 1670, Australia

¹⁴ School of Physics and Astronomy, University of St. Andrews, North Haugh, St. Andrews, KY16 9SS, UK

¹⁵ CEI Campus Moncloa, UCM-UPM, Departamento de Astrofísica y CC. de la Atmósfera, Facultad de CC. Físicas, Universidad Complutense de Madrid, Avda. Complutense s/n, E-28040 Madrid, Spain

¹⁶ Instituto de Cosmología, Relatividade e Astrofísica ICRA, Centro Brasileiro de Pesquisas Físicas, Rua Dr. Xavier Sigaud 150, CEP 22290-180, Rio de Janeiro, RJ, Brazil

¹⁷ Departamento de Investigación Básica, CIEMAT, Avda. Complutense 40, E-28040 Madrid, Spain

¹⁸ Depto. de Física Teórica, Universidad Autónoma de Madrid, E-28049 Madrid, Spain

¹⁹ Max-Planck-Institut für Astronomie, Königstuhl 17, D-69117 Heidelberg, Germany

²⁰ CALIFA International Collaboration <http://califa.caha.es>

Received 2014 June 18; accepted 2014 July 3; published 2014 July 28

ABSTRACT

We use spatially and temporally resolved maps of stellar population properties of 300 galaxies from the CALIFA integral field survey to investigate how the stellar metallicity (Z_*) relates to the total stellar mass (M_*) and the local mass surface density (μ_*) in both spheroidal- and disk-dominated galaxies. The galaxies are shown to follow a clear stellar mass–metallicity relation (MZR) over the whole 10^9 – $10^{12} M_\odot$ range. This relation is steeper than the one derived from nebular abundances, which is similar to the flatter stellar MZR derived when we consider only young stars. We also find a strong relation between the local values of μ_* and Z_* (the μ ZR), betraying the influence of local factors in determining Z_* . This shows that both local (μ_* -driven) and global (M_* -driven) processes are important in determining metallicity in galaxies. We find that the overall balance between local and global effects varies with the location within a galaxy. In disks, μ_* regulates Z_* , producing a strong μ ZR whose amplitude is modulated by M_* . In spheroids it is M_* that dominates the physics of star formation and chemical enrichment, with μ_* playing a minor, secondary role. These findings agree with our previous analysis of the star formation histories of CALIFA galaxies, which showed that mean stellar ages are mainly governed by surface density in galaxy disks and by total mass in spheroids.

Key words: galaxies: evolution – galaxies: fundamental parameters – galaxies: stellar content – galaxies: structure

Online-only material: color figures

1. INTRODUCTION

The quest for understanding the physical association between mass and metallicity in galaxies has a long history in astrophysics. In its currently most common form, mass is represented by the stellar mass (M_*), while the nebular oxygen abundance is taken as the metallicity tracer. Perhaps the best known contemporary example of this mass–metallicity relation (MZR) is that derived for star-forming galaxies in the Sloan Digital Sky Survey (SDSS) by Tremonti et al. (2004).

An independent way to explore the metal content of galaxies is through their stars, whose combined spectra encode a fossil record of galaxy evolution. This approach has been widely explored in relation to elliptical galaxies, which also follow a

MZR (the Mg– σ_* relation; Faber & Jackson 1976). The historical limitation to early-type systems comes about because of their predominantly old and relatively simple stellar populations (SSPs, often approximated as a single burst), in contrast with the more complex star formation histories (SFHs) of spirals, which complicates the translation of their spectroscopic features into tracers of the characteristic stellar metallicity (Z_*). Recent work has started to lift this restriction. In particular, spectral synthesis techniques have shown that useful estimates of Z_* can be derived for galaxies of all types (Cid Fernandes et al. 2005, 2007; Gallazzi et al. 2005; Panter et al. 2007), especially when used comparatively and for large samples. These studies obtain a purely stellar version of the MZR, as well as a broad correlation between O/H and Z_* , and a Z_* evolutionary pattern

characteristic of chemical enrichment, all derived on the basis of an archeological spectral analysis of local SDSS galaxies.

A common problem in both approaches is that they are most often based on integrated data, where one gathers all or part of the light of a galaxy in a single spectrum. The exact meaning of the global O/H, Z_* , and other properties derived from such data is rendered somewhat ambiguous (and aperture-dependent; e.g., Iglesias-Páramo et al. 2013; Mast et al. 2014) by the existence of spatial gradients in both nebular and stellar population properties within galaxies. More critically, the lack of spatial resolution limits our ability to map the influence of local factors on the local metallicity which, if present, propagate to the global MZR.

Integral field spectroscopy surveys like CALIFA (Sánchez et al. 2012) best tackle these issues. Rosales-Ortega et al. (2012) and Sánchez et al. (2013) applied nebular diagnostics to thousands of H II regions in these data cubes, finding that O/H is strongly correlated with the local stellar mass *surface density* (μ_*), and that this relation shapes the global MZR. The notion that M_* plays a less fundamental role than μ_* in the evolution of galactic disks (homes of the H II regions whose O/H represent the metallicity in the nebular MZR) has been raised previously. Bell & de Jong (2000), for instance, analyzed optical and near-IR imaging of spirals, finding that the surface density of a galaxy drives its SFH, and that M_* is a less important parameter. In the context of integral field studies, González Delgado et al. (2014, hereafter GD14) carried out a spectral synthesis analysis of 107 CALIFA galaxies, also finding that mean stellar ages correlate more strongly with μ_* in galaxy disks. Conversely, they find that in spheroids (elliptical galaxies and bulges), it is M_* that controls the SFH.

Here we explore global and local estimates of the Z_* obtained from the spatially resolved spectral synthesis of CALIFA galaxies. The focus on stars complements the work based on H II regions, bringing in new perspectives. First, stellar metallicities reflect the whole history of a galaxy, while O/H measures a present-day snapshot of its evolution. Second, our analysis ignores H II regions, and so can be applied to disks and spheroids, increasing statistics and broadening the scope of the study.

2. DATA AND STELLAR POPULATION ANALYSIS

Our sample comprises 300 galaxies ranging from ellipticals to late-type spirals, representative of the full CALIFA mother sample (Walcher et al. 2014). Technical details are described in Sánchez et al. (2012), Husemann et al. (2013), and the forthcoming Data Release 2 paper by R. García-Benito et al. (in preparation).

Our method to extract stellar population properties from data cubes has been explained in Pérez et al. (2013) and Cid Fernandes et al. (2013, 2014). In short, we use STARLIGHT (Cid Fernandes et al. 2005) to fit each spectrum as a combination of SSPs spanning different ages and metallicities. The SSP spectra used in this work consist of Granada (González Delgado et al. 2005) and MILES (Vazdekis et al. 2010) models, similar to those used in Cid Fernandes et al. (2013) but extended to cover the full metallicity range of the MILES models. The 235 elements base covers ages from 0.001 to 14 Gyr, and $\log Z_*/Z_\odot$ from -2.3 to +0.33. A Salpeter initial mass function is adopted.

This whole analysis transforms the data cubes to two-dimensional maps of a series of stellar population properties. The main ones for the purposes of this Letter are the stellar mass surface density, and the mass-weighted mean stellar metallicity,

defined as

$$\langle \log Z_* \rangle_{M,xy} = \frac{\sum_{tZ} M_{\star,tZ,xy} \times \log Z}{\sum_{tZ} M_{\star,tZ,xy}}, \quad (1)$$

where $M_{\star,tZ,xy}$ denotes the mass in stars of age t and metallicity Z in spaxel xy .

3. RESULTS

3.1. The Global Mass–Metallicity Relation

The MZR is a relation between *global* galaxy properties, which requires us to compress our xy maps to single numbers. The total stellar mass is obtained from $M_* = \sum_{xy} M_{\star,xy}$, i.e., adding up the masses derived for individual spaxels (thus accounting for spatial variations in the mass-to-light ratio and extinction). For the metallicity, we use a galaxy-wide averaging scheme, such that

$$\langle \log Z_* \rangle_M^{\text{galaxy}} = \frac{\sum_{xy} M_{\star,xy} \langle \log Z_* \rangle_{M,xy}}{\sum_{xy} M_{\star,xy}}, \quad (2)$$

as done for light and mass-weighted mean stellar ages by GD14, who showed that these averages match very well the value obtained from the synthesis of the integrated spectrum, as well as that at radial distances of $R = 1$ half light radius (HLR).

Our mass versus stellar metallicity relation for CALIFA galaxies is shown in Figure 1(a). A clear correlation is seen, with metallicities rising by roughly an order of magnitude for M_* between $\sim 10^9$ and $10^{12} M_\odot$. The thick black curve, obtained by smoothing the mass-binned relation, offers as better visualization of the general trend. In order to get a sense of the SFHs in this plane, we color-code the points by the value of the galaxy-wide mean stellar age (see Equation (1) of GD14). One sees that galaxies become progressively older as one moves up the MZR.

Figure 1 also compares our stellar MZR with those obtained for SDSS galaxies by Gallazzi et al. (2005; brown line) and Panter et al. (2008; magenta), both shifted by +0.25 dex in mass to match our initial mass function. Given the significant differences in data, samples, and methodology, one should not take this comparison too literally. The overall agreement, however, is remarkable.

3.2. Stellar Versus Nebular MZRs and Chemical Evolution

The flattening of our MZR at $\sim 10^{11} M_\odot$ is reminiscent of the behavior observed in the nebular MZR (e.g., Tremonti et al. 2004). A quantitative comparison of nebular and stellar metallicities is not warranted given the huge differences in the underlying physics, not to mention inherent uncertainties affecting both estimates. A qualitative comparison, however, is instructive. Figure 1(b) overplots the Sánchez et al. (2013; cyan line) relation between M_* and O/H obtained from H II regions in CALIFA data cubes. The two (black and cyan lines) occupy the same zone at high M_* , but diverge at low M_* , with the nebular MZR being visibly flatter than the stellar one.

Besides the caveats noted above, this comparison is skewed by the fact that O/H portrays the current state of the warm gas, while Z_* reflects the whole history of a galaxy. To mitigate this mismatch in timescales, we compute Z_* considering only stars younger than 2 Gyr, and derive the corresponding galaxy-wide average. The resulting MZR is shown as blue stars in Figure 1(b), with a thick blue line representing its smoothed version.

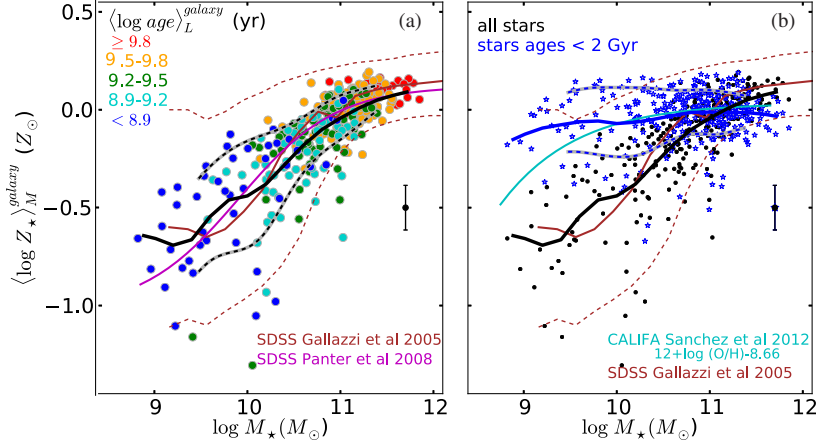


Figure 1. (a) Global stellar MZR for 300 CALIFA galaxies is shown as circles, color-coded by the mean stellar age. A mass-binned smooth mean relation is shown as a black solid line (the dashed black indicates the 16th and 84th percentiles, and the error bar represents the typical dispersion). The MZRs obtained for SDSS galaxies by Gallazzi et al. (2005) and Panter et al. (2008) are plotted as brown and magenta lines, respectively, with a dashed brown line indicating the 16th and 84th percentiles of Gallazzi et al. (b) Comparison of our global stellar MZR (black circles and line) with the one obtained considering only stars younger than 2 Gyr in the computation of the stellar metallicity (blue stars and line); blue dashed lines indicate the 16th and 84th percentiles; error bar represents the typical dispersion. The CALIFA-based nebular MZR (Sánchez et al. 2013) is shown as a cyan line.

(A color version of this figure is available in the online journal.)

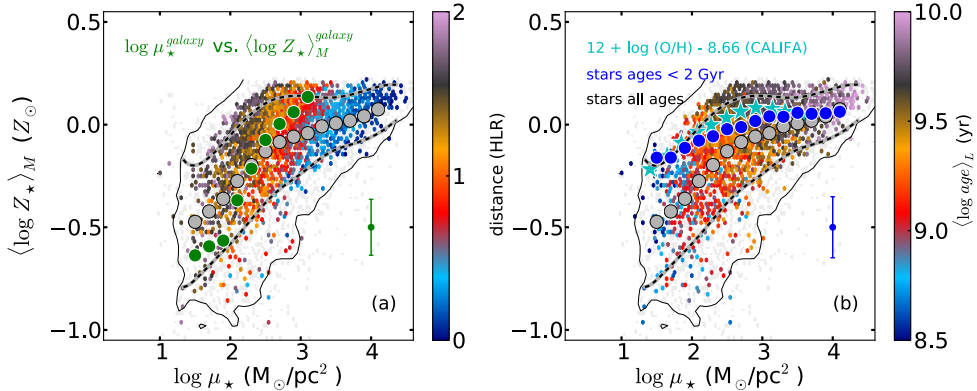


Figure 2. Local stellar metallicity vs. the local stellar mass surface density. Small dots show values for 6000 radial bins of 300 galaxies. The solid line traces the contour of point number density larger than 1 per 0.075×0.035 dex box. (a) Gray circles track the μ_{\star} -binned average $Z_{\star}(\mu_{\star})$ relation (black dashed lines indicate the 16th and 84th percentiles). Green circles trace the (μ_{\star} -binned) global relation, obtained from the $\langle \log Z_{\star} \rangle_M^{galaxy}$ and μ_{\star}^{galaxy} galaxy-wide averages; the error bar represents the typical dispersion in this relation. The individual points are color-coded by the distance from the center in HLR. (b) Dots as in panel (a), but colored to display the (luminosity-weighted) mean stellar age. Large blue circles show the μ_{\star} -binned global relation obtained considering only stars younger than 2 Gyr in the computation of Z_{\star} (error bar represents the typical dispersion). Cyan stars show the CALIFA-based nebular μ ZR of Sánchez et al. (2013), assuming $12 + \log(O/H)_{\odot} = 8.66$.

(A color version of this figure is available in the online journal.)

The plot reveals a clear signature of chemical evolution, with young stars being more enriched than older stars. The MZR for young stars is flatter than the global one, in line with the nebular relation.

The overall picture portrayed by Figure 1 is the same as that drawn by Cid Fernandes et al. (2007) in their analysis of SDSS galaxies: most of the chemical evolution of massive galaxies has occurred many gigayears ago, while low- M_{\star} systems grow their metallicities over a longer cosmic time span. This “chemical downsizing” is, of course, not coincidental, since star formation and chemical evolution work in tandem.

3.3. The Local and Global μ_{\star} Versus Z_{\star} Relations

Our data are ideally suited to investigate the relative roles of global and local properties in controlling the metallicity. To explore the information encoded in our spatially resolved maps of stellar population properties, we first compress them

to one-dimensional radial profiles computed as explained in GD14. Besides allowing for clearer visualization of the results, this compression (1) reduces statistical uncertainties (see Cid Fernandes et al. 2013), and (2) balances the role of each galaxy in our statistics, which would otherwise be biased toward galaxies filling up more spaxels in the integral field unit.

Radial profiles of μ_{\star} and $\langle \log Z_{\star} \rangle_M$ were computed in elliptical annuli in steps of 0.1 HLR. The profiles typically cover out to $R = 2$ HLR reliably, so we restrict our analysis to this limit.

Figure 2(a) shows the resulting μ_{\star} - Z_{\star} relation (μ ZR). Note that this plot is ultimately a collection of 300 metallicity profiles, where the radial coordinate is replaced by $\mu_{\star}(R)$, such that R increases to the left. The ~ 6000 dots (20 per galaxy) are color-coded according to their distance from the nucleus, in units of the corresponding HLR. Points in the upper right correspond to the inner regions of massive, early-type spheroids, while in the bottom left the outer zones of late-type spirals dominate.

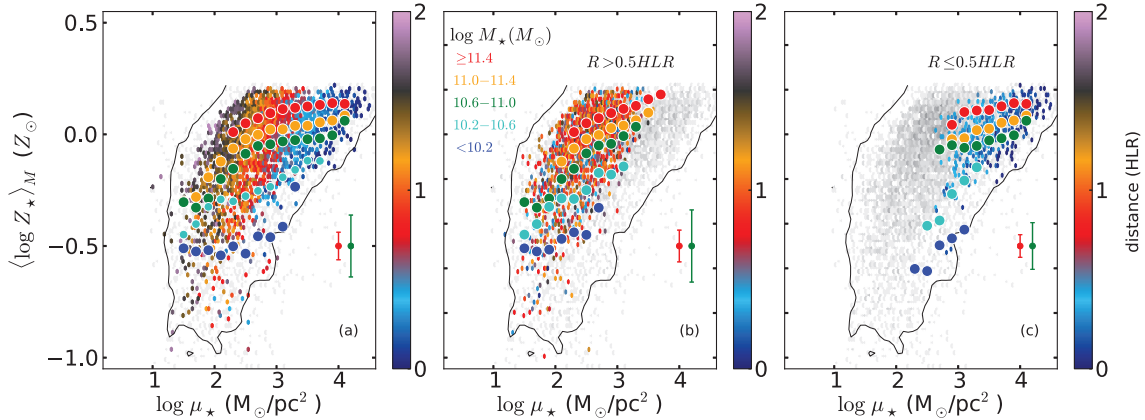


Figure 3. (a) Local μ ZR, color-coded by R ; circles show the (μ_* -binned) mean relations obtained by breaking up the sample into five M_* intervals. (b) Same as panel (a), but restricting the analysis to spatial regions outward of $R = 0.5$ HLR. (c) As in the middle panel, but for the inner $R < 0.5$ HLR regions. Error bars represent the typical dispersion in metallicity in the local MZR in two of the five M_* intervals.

(A color version of this figure is available in the online journal.)

Clearly, despite the scatter, local stellar mass surface density and metallicity are strongly correlated, and in a radially dependent fashion. The general trend is depicted as gray circles, which averages over metallicities in 0.2 dex wide bins in μ_* .

The average μ ZR traced by the gray circles in Figure 2(a) should not be confused with the global one, since R bins do not contribute equally to the galaxy-wide averages of either μ_* or $\langle \log Z_* \rangle_M$. The (μ_* -binned) global version of the μ ZR is shown by the large green circles. Note that they follow closely the underlying orange/red points ($R \sim 1$ HLR in our color scheme), as expected from the fact that galaxy-wide averages essentially reflect properties at 1 HLR (GD14).

The global μ ZR is visibly steeper than the local one, particularly in the high-density regime of the inner regions of galaxies (blueish points in Figure 2(a)), where the local μ ZR (gray circles) flattens. This flattening is not picked up by the global relation, as there are no galaxies globally as dense as these central regions of spheroids.

Overall, we conclude that the μ ZR shows the local stellar surface density to be an important driver of the stellar metallicity, except for their innermost densest regions, where some other property must take over the dominant role. Even in the outer regions, however, the vertical scatter in the μ ZR is such that μ_* cannot be the sole parameter regulating Z_* .

3.4. Stellar versus Nebular μ ZRs and Chemical Evolution

Before furthering our investigation of global and local effects, we repeat in Figure 2(b) the exercise carried out in Figure 1(b) for the global MZR, but now for the μ ZR. The large gray circles are as in panel (a), but the blue ones track the relation obtained considering only young stars. Again, one obtains a flatter relation, indicative of chemical evolution. Also, as in Figure 1(b), the shape of the μ ZR for young stellar populations approaches that obtained from H II regions (cyan-colored stars; Sánchez et al. 2013).

Figure 2(b) also summarizes how local SFHs vary across the μ Z plane. This is revealed by the colors of the dots, which now indicate the radially averaged mean stellar age. As for the global MZR, one finds younger systems (i.e., those with more significant recent star formation) toward the low- μ_* , metal-poor corner of the μ ZR. Large ages, on the other hand, occur at the densest, more metal-rich regions typical of small R . These inner

zones essentially completed their star formation and chemical evolution long ago. Note that this is also the regime where the local μ ZR (gray circles) flattens.

4. LOCAL + GLOBAL EFFECTS AND THE DISTINCT ROLES OF μ_* AND M_* IN DISKS AND SPHEROIDS

The results reported above send mixed messages as to what the main driver of stellar metallicities might be: while Figure 1 indicates that M_* is involved in establishing global Z_* values, Figure 2 points to μ_* playing a major role in defining the local Z_* . It thus seems that both local and global effects play relevant roles in determining the metallicity.

Figure 3 shows that this is indeed the case. The dots in all panels repeat the local μ ZR, but now breaking the mean (i.e., μ_* -binned) relation (large circles) into five approximately equally populated M_* intervals. Panel (a) shows results considering all 6000 radial bins, while panels (b) and (c) take into account only points outside and inside $R = 0.5$ HLR, respectively. The figure thus explores the whole M_* - $\mu_*(R)$ - $Z_*(R)$ - R landscape.

Comparing Figure 3(a) with the mean μ ZR traced by gray circles in Figure 2, one immediately realizes that a pure μ ZR analysis overlooks the important role of M_* in defining the metallicity scale. Mass is a major source of scatter in the μ ZR, with massive galaxies being locally (and globally) more chemically enriched than low-mass ones for the same $\mu_*(R)$. Still, the rise of $Z_*(R)$ with $\mu_*(R)$ for constant M_* shows the relevance of local effects, particularly for low- and intermediate- M_* systems.

Though revealing, the M_* -dependent mean μ ZRs in Figure 3(a) do not distinguish the whereabouts within a galaxy, as disk and bulge/spheroid locations are treated on equal footing. A coarse way to discriminate between these morphological components is to define them by a $R >$ or < 0.5 HLR criterion. Panel (b) in Figure 3 shows the μ ZR(M_*) for $R > 0.5$ HLR. Except for the 41 ellipticals, this plot should be read as a μ ZR(M_*) for galactic disks. In stark contrast to Figure 3(a), no downward flattening is seen. Stellar metallicities increase steadily with μ_* , modulated by a M_* -related amplitude.

The panorama changes in Figure 3(c), where only the inner zones are considered. For the three largest M_* ranges ($> 10^{10.6} M_\odot$), one sees a very weak dependence of Z_* on μ_* . Local effects thus seem of secondary importance in the

dense regime of the inner regions of massive galaxies. The $M_{\star} < 10^{10.6} M_{\odot}$ bins, however, still follow a strong (M_{\star} -modulated) μ ZR. Galaxies in these low- M_{\star} bins are predominantly (87%) late-type spirals (Sc–Sd), with small or non-existent bulges (possibly resulting from secular disk evolution; Fisher & Drory 2011), which explains their disk-like μ ZR.

5. DISCUSSION

The general picture one draws from these results is that both global (M_{\star} -driven) and local (μ_{\star} -driven) effects are important in determining the stellar (and, by extension, also the nebular) metallicities in galaxies, and that the overall balance between these two varies with the location within a galaxy. Two clearly distinct regimes are identified: (1) one related to disks, where μ_{\star} (hence local physics) regulates metallicity, modulated by an M_{\star} -related amplitude, and (2) the other pertaining to the bulge/spheroid component, where M_{\star} dominates the physics of star formation and chemical enrichment.

These results tie in nicely with the recent analysis of GD14. We have shown there that mean stellar ages (a first moment descriptor of the SFH) relate strongly to μ_{\star} in galactic disks, indicating that local properties dictate the pace of star formation. The slower growth (hence younger ages) found at low μ_{\star} should lead to less metal enrichment, in agreement with our μ ZR. Within bulges/spheroids, M_{\star} is a much more relevant driver of the SFH. Most of the star formation in these regions was finished long ago, leading to fast metal enrichment and little or no chemical evolution since those early days, as found in this Letter.

Despite the overall consistency and physical appeal of our results, there are some caveats. Aside from limitations of the method (e.g., Cid Fernandes et al. 2014), and the choice of $R = 0.5$ to segregate bulges from disks, a more philosophical kind of caveat holds the promise of interesting future work. The goal of this Letter was to evaluate the role of global and local effects in determining stellar metallicities in and within galaxies. To this end, we have chosen M_{\star} and μ_{\star} as the representatives of global and local effects, respectively, but was this a wise choice of variables?

Our answer at this stage is a “yes” for M_{\star} , but only a “perhaps” for μ_{\star} . Both the SFH of a galaxy and its chemical evolution are thought to be affected by its mass, including its dark + gaseous + stellar components. In practice, M_{\star} is the most readily available proxy for total mass, and thus a relevant variable.

The status of μ_{\star} as a tracer of local effects is less clear. The choice of μ_{\star} as an independent variable is inspired by Schmidt (1959), who postulated a density-controlled star formation rate law, and by the fact that our analysis provides robust estimates of μ_{\star} . Clearly, μ_{\star} is but a proxy for complex star formation

physics. The fact that we find Z_{\star} to correlate strongly with μ_{\star} in disks suggests it to be a reasonable empirical proxy for local effects. Yet, the fact that the disk μ ZR has its amplitude modulated by M_{\star} raises doubts as to how fundamental μ_{\star} really is.

While one can think of ways to relate local Z_{\star} values to the global M_{\star} , there are other ways of formulating the problem. The Z_{\star} -scaling role of M_{\star} in the disk μ ZR may be reflecting the works of a different M_{\star} -related property, like morphological type, gas fraction, in/outflow rates, or others. Future work should explore these possibilities.

This Letter is based on data obtained by the CALIFA survey (<http://califa.caha.es>), funded by the Spanish MINECO grants ICTS-2009-10, AYA2010-15081, and the CAHA operated jointly by the Max-Planck IfA and the IAA (CSIC). The CALIFA Collaboration thanks the CAHA staff for the dedication to this project. Support from CNPq (Brazil) through Programa Ciéncia sem Fronteiras (401452/2012-3) is duly acknowledged.

REFERENCES

- Bell, E. F., & de Jong, R. S. 2000, *MNRAS*, **312**, 497
- Cid Fernandes, R., Asari, N. V., Sodré, L., et al. 2007, *MNRAS*, **375**, L16
- Cid Fernandes, R., González Delgado, R. M., Pérez, E., et al. 2014, *A&A*, **561**, 130
- Cid Fernandes, R., Mateus, A., Sodré, L., Stasińska, G., & Gomes, J. M. 2005, *MNRAS*, **358**, 363
- Cid Fernandes, R., Pérez, E., García Benito, R., et al. 2013, *A&A*, **557**, 86
- Faber, S. M., & Jackson, R. E. 1976, *ApJ*, **204**, 668
- Fisher, D. B., & Drory, N. 2011, *ApJL*, **733**, L47
- Gallazzi, A., Charlot, S., Brinchmann, J., White, S. D. M., & Tremonti, C. A. 2005, *MNRAS*, **362**, 41
- González Delgado, R. M., Cerviño, M., Martins, L. P., Leitherer, C., & Hauchlildt, P. H. 2005, *MNRAS*, **357**, 945
- González Delgado, R. M., Pérez, E., Cid Fernandes, R., et al. 2014, *A&A*, **562**, 47
- Husemann, B., Jahnke, K., Sánchez, S. F., et al. 2013, *A&A*, **549**, A87
- Iglesias-Páramo, J., Vilchez, J. M., Galbany, L., et al. 2013, *A&A*, **553**, L7
- Mast, D., Rosales-Ortega, F. F., Sánchez, S. F., et al. 2014, *A&A*, **561**, 129
- Panter, B., Jimenez, R., Heavens, A. F., & Charlot, S. 2007, *MNRAS*, **378**, 1550
- Panter, B., Jimenez, R., Heavens, A. F., & Charlot, S. 2008, *MNRAS*, **391**, 1117
- Pérez, E., Cid Fernandes, R., González Delgado, R. M., et al. 2013, *ApJL*, **764**, L1
- Rosales-Ortega, F. F., Sánchez, S. F., Iglesias-Páramo, J., et al. 2012, *ApJL*, **756**, L31
- Sánchez, S. F., Kennicutt, R. C., Gil de Paz, A., et al. 2012, *A&A*, **538**, A8
- Sánchez, S. F., Rosales-Ortega, F. F., Jungwiert, B., et al. 2013, *A&A*, **554**, 58
- Schmidt, M. 1959, *ApJ*, **129**, 243
- Tremonti, C. A., Heckman, T. M., Kauffmann, G., et al. 2004, *ApJ*, **613**, 898
- Vazdekis, A., Sánchez-Blázquez, P., Falcón-Barroso, J., et al. 2010, *MNRAS*, **404**, 1639
- Walcher, C. J., Wisotzki, L., Bekaraité, S., et al. 2014, *A&A*, in press (arXiv:1407.2939)

A.3 The CALIFA survey across the Hubble sequence. Spatially resolved stellar population properties in galaxies

Artigo por González Delgado et al. (2015) (doi:10.1051/0004-6361/201525938). Também disponível em *pre-print* (arXiv:1506.04157).

The CALIFA survey across the Hubble sequence

Spatially resolved stellar population properties in galaxies*

R. M. González Delgado¹, R. García-Benito¹, E. Pérez¹, R. Cid Fernandes², A. L. de Amorim², C. Cortijo-Ferrero¹, E. A. D. Lacerda^{1,2}, R. López Fernández¹, N. Vale-Asari², S. F. Sánchez³, M. Mollá⁴, T. Ruiz-Lara⁵, P. Sánchez-Blázquez⁶, C. J. Walcher⁷, J. Alves⁸, J. A. L. Aguerri⁹, S. Bekeraite⁷, J. Bland-Hawthorn¹⁰, L. Galbany^{11,12}, A. Gallazzi¹³, B. Husemann¹⁴, J. Iglesias-Páramo^{1,15}, V. Kalinova¹⁶, A. R. López-Sánchez¹⁷, R. A. Marino¹⁸, I. Márquez¹, J. Masegosa¹, D. Mast¹⁹, J. Méndez-Abreu²⁰, A. Mendoza¹, A. del Olmo¹, I. Pérez⁵, A. Quirrenbach²¹, S. Zibetti¹², and CALIFA collaboration**

(Affiliations can be found after the references)

Received 21 February 2015 / Accepted 11 June 2015

ABSTRACT

Various different physical processes contribute to the star formation and stellar mass assembly histories of galaxies. One important approach to understanding the significance of these different processes on galaxy evolution is the study of the stellar population content of today's galaxies in a spatially resolved manner. The aim of this paper is to characterize in detail the radial structure of stellar population properties of galaxies in the nearby universe, based on a uniquely large galaxy sample, considering the quality and coverage of the data. The sample under study was drawn from the CALIFA survey and contains 300 galaxies observed with integral field spectroscopy. These cover a wide range of Hubble types, from spheroids to spiral galaxies, while stellar masses range from $M_\star \sim 10^9$ to $7 \times 10^{11} M_\odot$. We apply the fossil record method based on spectral synthesis techniques to recover the following physical properties for each spatial resolution element in our target galaxies: the stellar mass surface density (μ_\star), stellar extinction (A_V), light-weighted and mass-weighted ages ($\langle \log \text{age} \rangle_L$, $\langle \log \text{age} \rangle_M$), and mass-weighted metallicity ($\langle \log Z_\star \rangle_M$). To study mean trends with overall galaxy properties, the individual radial profiles are stacked in seven bins of galaxy morphology (E, S0, Sa, Sb, Sbc, Sc, and Sd). We confirm that more massive galaxies are more compact, older, more metal rich, and less reddened by dust. Additionally, we find that these trends are preserved spatially with the radial distance to the nucleus. Deviations from these relations appear correlated with Hubble type: earlier types are more compact, older, and more metal rich for a given M_\star , which is evidence that quenching is related to morphology, but not driven by mass. Negative gradients of $\langle \log \text{age} \rangle_L$ are consistent with an inside-out growth of galaxies, with the largest $\langle \log \text{age} \rangle_L$ gradients in Sb–Sbc galaxies. Further, the mean stellar ages of disks and bulges are correlated and with disks covering a wider range of ages, and late-type spirals hosting younger disks. However, age gradients are only mildly negative or flat beyond $R \sim 2$ HLR (half light radius), indicating that star formation is more uniformly distributed or that stellar migration is important at these distances. The gradients in stellar mass surface density depend mostly on stellar mass, in the sense that more massive galaxies are more centrally concentrated. Whatever sets the concentration indices of galaxies obviously depends less on quenching/morphology than on the depth of the potential well. There is a secondary correlation in the sense that at the same M_\star early-type galaxies have steeper gradients. The μ_\star gradients outside 1 HLR show no dependence on Hubble type. We find mildly negative $\langle \log Z_\star \rangle_M$ gradients, which are shallower than predicted from models of galaxy evolution in isolation. In general, metallicity gradients depend on stellar mass, and less on morphology, hinting that metallicity is affected by both – the depth of the potential well and morphology/quenching. Thus, the largest $\langle \log Z_\star \rangle_M$ gradients occur in Milky Way-like Sb–Sbc galaxies, and are similar to those measured above the Galactic disk. Sc spirals show flatter $\langle \log Z_\star \rangle_M$ gradients, possibly indicating a larger contribution from secular evolution in disks. The galaxies from the sample have decreasing-outward stellar extinction; all spirals show similar radial profiles, independent from the stellar mass, but redder than E and S0. Overall, we conclude that quenching processes act in manners that are independent of mass, while metallicity and galaxy structure are influenced by mass-dependent processes.

Key words. techniques: spectroscopic – Galaxy: evolution – Galaxy: stellar content – galaxies: structure – Galaxy: fundamental parameters – galaxies: spiral

1. Introduction

Galaxies are a complex mix of stars, gas, dust, and dark matter distributed in different components (bulge, disk, and halo) whose present day structure and dynamics are intimately linked to their assembly and evolution over the history of the Universe. Different observational and theoretical approaches can be followed to learn how galaxies form and evolve.

Theoretically, the formation of large-scale structures arise through the evolution of cold dark matter. In this picture, small-scale density perturbations in the dark matter collapse and form the first generation of dark matter halos, which subsequently merge to form larger structures such as clusters and superclusters (Springel et al. 2005; De Lucia et al. 2006). This basic hierarchical picture explains the global evolution of the star formation rate density of the universe, with galaxy peak formation epoch at redshift 2–3 (e.g. Madau & Dickinson 2014, and references therein). The stellar components formed at earlier epochs likely evolved into elliptical galaxies and bulges through mergers of the primordial star-forming disks (Elmegreen et al. 2007; Bournaud et al. 2007). However, this framework fails to

* Appendices are available in electronic form at
<http://www.aanda.org>

** <http://califa.caha.es>

explain how the galaxy population emerges at $z \sim 1$, and how the present day Hubble sequence of galaxies was assembled.

The growth of galaxies is not related in a simple way to the build up of dark matter; the interplay of energy and matter exchange (between the process of gas accretion and cooling and star formation) is essential for the growth the gaseous and stellar components in galaxies. Feedback mechanisms resulting from stellar winds, supernova explosions, and AGN are relevant to stop the gas collapse and cooling, quenching the star formation and hence galaxy growth (Silk & Rees 1998; Hopkins et al. 2011). Although these processes are difficult to implement in theoretical models, they are essential to explain the masses, structures, morphologies, stellar populations, and chemical compositions of galaxies, and the evolution of these properties with cosmic time.

Recently, a new set of cosmological hydrodynamic simulations have started to predict how the spatially resolved information of the properties of stellar populations in galaxies can constrain the complex interplay between gas infall, outflows, stellar migration, radial gas flows, and star formation efficiency, in driving the inside-out growth of galactic disks (Brook et al. 2012; Gibson et al. 2013; Few et al. 2012; Pilkington et al. 2012a; Minchev et al. 2014). Radiative cooling, star formation, feedback from supernovae, and chemical enrichment are also included in simulations to predict radial metallicity gradients as a function of merging history. Shallow metallicity gradients are expected if elliptical galaxies result from major mergers (e.g. Kobayashi 2004), but a minor merger picture for the formation of ellipticals can successfully explain the strong size evolution of massive galaxies (Oser et al. 2012). This late-time accretion of low-mass and metal poor galaxies (dry mergers) into the already formed massive galaxy can produce a variation of the age and metallicity radial structure of the galaxy as it increases in size. Galactic stellar winds and metal cooling also have an important effect on these ex situ star formation models, predicting different behavior of the mass and metallicity assembly in massive early-type galaxies, and in the radial gradient of present stellar populations properties of galaxies (Hirschmann et al. 2013, 2015).

In summary, these theoretical works show that observational data with spatial information of the mass and metallicity assembly and their cosmic evolution, and the present radial structure of stellar population properties (stellar mass surface density, age, metallicity) contain relevant information to constrain the formation history of galaxies and the physics of feedback mechanisms involved.

Observationally, a first step is to study what kinds of galaxies are there in the Universe, and which are their physical properties. Attending to their form and structure, galaxies can be grouped into a few categories. Results show that most of the massive nearby galaxies are ellipticals, S0's, or spirals (Blanton & Moustakas 2009) following the Hubble tuning-fork diagram. In this scheme, S0's are a transition between spirals and ellipticals (Cappellari et al. 2013), and the bulge/disk ratio increases from late to early-type spirals. At the same time, galaxy properties such as color, mass, surface brightness, luminosity, and gas fraction are correlated with Hubble type (Roberts & Haynes 1994), suggesting that the Hubble sequence somehow reflects possible paths for galaxy formation and evolution. However, the processes structuring galaxies along the Hubble sequence are still poorly understood.

Integral field spectroscopy (IFS) enables a leap forward, providing 3D information (2D spatial + 1D spectral) on galaxies. These datacubes allow one to recover two-dimensional maps of stellar mass surface density, stellar ages, metallicities,

extinction and kinematics, as well as a suit of nebular properties, such as gas kinematics, metallicity, excitation, etc. Until a few years ago, IFS was used to target small samples of galaxies. Detailed programs, such as SAURON (Bacon et al. 2001), VENGA (Blanc et al. 2013), (U)LIRs at $z \leq 0.26$ (Arribas et al. 2010), PINGS (Rosales-Ortega et al. 2010), or DiskMass Survey (Bershady et al. 2010), have been limited to less than a hundred galaxies, but it is more than fair to recognize that to get these amounts of IFU data was a challenge at the time. ATLAS3D (Cappellari et al. 2011) represented a step forward, with the observation of a volume-limited sample of 260 galaxies, but with three important limitations: the sample only includes early-type galaxies, the field of view is limited to 1 effective radius, and the spectral range is restricted from $\text{H}\beta$ to $[\text{NI}]\lambda 5200$.

CALIFA (Calar Alto Legacy Integral Field Area) is our ongoing survey of 600 nearby galaxies at the 3.5 m at Calar Alto (Sánchez et al. 2012)¹. The data set provided by the survey (see Husemann et al. 2013, for DR1; García-Benito et al. 2015 for DR2) is unique to advance in these issues not only because of its ability to provide spectral and spatial information, but also because of the following: a) It includes a large homogeneous sample of galaxies across the color-magnitude diagram, covering a large range of masses (10^9 to $10^{12} M_\odot$, González Delgado et al. 2014c), and morphologies from Ellipticals (E0-E7), Lenticulars (S0-S0a), to spirals (Sa to Sm; see Walcher et al. 2014 for a general description of the sample). b) It has a large field of view ($74'' \times 65''$) with a final spatial sampling of 1 arcsec, and a resolution of ~ 2.5 arcsec, allowing it to spatially resolve the stellar population properties well, and to obtain the total integrated properties, such as galaxy stellar mass, and stellar metallicity. c) It covers the whole rest-frame optical wavelength at intermediate spectral resolution, including the most relevant absorption diagnostics for deriving the stellar population properties.

Previous papers in this series used the first ~ 100 datacubes of the survey to derive spatially resolved stellar population properties by means of full spectral fitting techniques. We obtained the following: 1) massive galaxies grow their stellar mass inside-out. The signal of downsizing is shown to be spatially preserved, with both inner and outer regions growing faster for more massive galaxies. The relative growth rate of the spheroidal component (nucleus and inner galaxy), which peaked 5–7 Gyr ago, shows a maximum at a critical stellar mass $M_* \sim 7 \times 10^{10} M_\odot$ (Pérez et al. 2013). 2) The inside-out scenario is also supported by the negative radial gradients of the stellar population ages (González Delgado et al. 2014c). 3) Global and local relations between stellar mass, stellar mass surface density, and stellar metallicity relation were investigated, along with their evolution (as derived from our fossil record analysis). In disks, the stellar mass surface density regulates the ages and the metallicity. In spheroids, the galaxy stellar mass dominates the physics of star formation and chemical enrichment (González Delgado et al. 2014c,a). 4) In terms of integrated versus spatially resolved properties, the stellar population properties are well represented by their values at 1 HLR (González Delgado et al. 2014c,a). The CALIFA collaboration has also compared the age and metallicity gradients in a subsample of 62 face-on spirals and it was found that there is no difference between the stellar population properties in barred and unbarred galaxies (Sánchez-Blázquez et al. 2014).

In this paper, we extend our study of the spatially resolved star formation history (SFH) of CALIFA galaxies to derive the radial structure of the stellar population properties as a function

¹ <http://califa.caha.es>

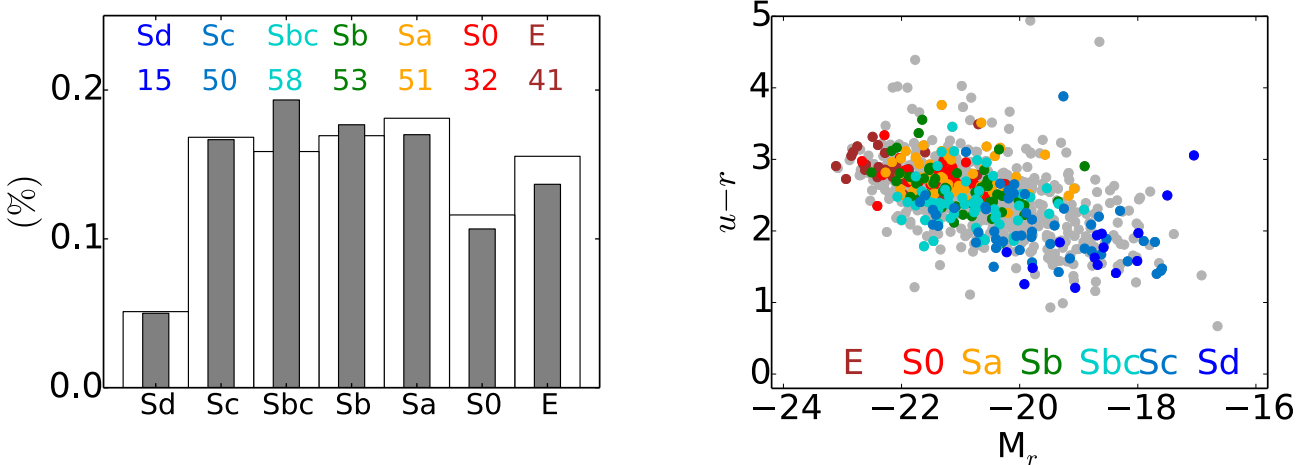


Fig. 1. *Left:* comparison of the distribution of Hubble types in the CALIFA mother sample (empty bars) and the galaxies analyzed here (filled bars). The number of galaxies in our sample are labeled in colors. The histograms are normalized to form a probability density, i.e., each bar scales with the ratio of the number of galaxies in each bin and the total number of galaxies, such that the two distributions are directly comparable. *Right:* color-magnitude diagram. Mother sample galaxies are plotted in grey, while the 300 galaxies analyzed in this work are marked as colored points.

of Hubble type, and galaxy stellar mass, M_{\star} . The goals are: 1) to characterize in detail the radial structure of stellar population properties of galaxies in the local universe; 2) to find out how these properties are correlated with Hubble type, and if the Hubble sequence is a scheme to organize galaxies by mass and age, and/or mass and metallicity; 3) to establish observational constraints to galaxy formation models via the radial distributions and gradients of stellar populations for disk and bulge dominated galaxies.

This paper is organized as follows: Sect. 2 describes the observations and summarizes the properties of the CALIFA galaxies analyzed here. In Sect. 3 we summarize our method for extracting the SFH, based on the fossil record method, and we explain the main differences between the analysis presented here and that in previous works. Section 4 presents results on the galaxy stellar mass, half-light, and half-mass radii (HLR, HMR, respectively), and galaxy averaged stellar metallicity. Section 5 deals with the spatially resolved properties of the stellar population: stellar mass surface density, μ_{\star} ; luminosity weighted mean age, $\langle \log \text{age} \rangle_L$; mass weighted mean metallicity, $\langle \log Z_{\star} \rangle_M$; and stellar extinction, A_V . We discuss the results in Sect. 6; and Sect. 7 presents the conclusions.

2. Sample, observations, and data reduction

2.1. Sample and morphological classification

The CALIFA mother sample consists of 939 galaxies selected from SDSS survey in the redshift range $z = 0.005\text{--}0.03$, and with r -band angular isophotal diameter of $45\text{--}80''$. These criteria guarantee that the objects fill the $74'' \times 64''$ FoV well. The sample includes a significant number of galaxies in different bins in the color-magnitude diagram (CMD), ensuring that CALIFA spans a wide and representative range of galaxy types.

The galaxies were morphologically classified as Ellipticals (E0–7), Spirals (S0, S0a, Sab, Sb, Sbc, Sc, Scd, Sd, Sm), and Irregulars (I). The classification was carried out through visual inspection of the r -band images averaging the results (after clipping outliers) from five members of the collaboration. Galaxies are also classified as B for barred, otherwise A , or AB if it is unsure, and as M if it shows “merger” or “interaction features” (Walcher et al. 2014).

The sample for this paper comprises the 312 CALIFA galaxies observed in both V1200 and V500 setups as of January 2014. The 12 galaxies showing “merger or interacting features” are not discussed here, leaving a main sample of 300 objects with a well defined morphology. For this work we have grouped galaxies into seven morphology bins: E, S0 (including S0 and S0a), Sa (Sa and Sab), Sb, Sbc, Sc (Sc and Scd), and Sd (13 Sd, 1 Sm and 1 Irr).

Figure 1 shows that these 300 galaxies provide a fair representation of the CALIFA survey as a whole. The left panel shows scaled histograms of the Hubble type in the mother sample (empty bars) and in our sample (filled bars). The number of objects in each morphology bin for our sample is indicated at the top, with a brown to blue color palette that represents Hubble types from ellipticals to late spirals. This same color scheme is used throughout this paper. The similarity of the distributions reflects the random sampling strategy of CALIFA, with targets picked from the mother sample on the basis of visibility criteria alone. The right panel in Fig. 1 shows the $u - r$ versus M_r CMD, with grey points representing the mother sample and colored points the 300 galaxies. As for the Hubble type distribution, a simple visual inspection shows that our subsample is representative of the full CALIFA sample in terms of CMD coverage.

2.2. Observations and data reduction

The observations were carried out with the Potsdam Multi-Aperture Spectrometer (Roth et al. 2005, PMAS) in the PPaK mode (Verheijen et al. 2004) at the 3.5 m telescope of Calar Alto observatory. PPaK contains 382 fibers of $2.7''$ diameter each, and a $74'' \times 64''$ FoV (Kelz et al. 2006). Each galaxy is observed with two spectral settings, V500 and V1200, with spectral resolutions $\sim 6 \text{ \AA}$ (FWHM) and 2.3 \AA , respectively. The V500 grating covers from 3745 to 7300 \AA , while the V1200 covers $3650\text{--}4840 \text{ \AA}$. Detailed descriptions of the observational strategy and of the data can be found in Sánchez et al. (2012), and Husemann et al. (2013).

The datacubes analyzed here have been calibrated with version 1.5 of the reduction pipeline. The main issues addressed by this new version are: (i) correction of the sensitivity curve for the V500 grating; (ii) new registering method to determine,

for each galaxy, the relative positioning of the three pointings of the dithering pattern, and absolute WCS registration; (iii) a new cube interpolation method. CALIFA pipeline v1.5 improves the flux calibration to an accuracy of 2–3% and is the current official data release. A detailed account of this new pipeline is presented in the Data Release 2 article (García-Benito et al. 2015).

To reduce the effects of vignetting on the data, we combine the observations in the V1200 and V500 setups. The combined datacubes were processed as described in Cid Fernandes et al. (2013). Our analysis requires that spectra have signal-to-noise ratio $S/N \geq 20$ in a 90 Å window centered at 5635 Å (rest-frame). When individual spaxels do not meet this S/N threshold, they are coadded into Voronoi zones (Cappellari & Copin 2003). Further pre processing steps include spatial masking of foreground and background sources, rest-framing, and spectral resampling. The resulting 253 418 spectra were then processed through y (the Python CALIFA

Synthesis Organizer), producing the stellar population properties discussed here as described in detail in the next section.

3. Stellar population analysis: differences with respect to previous work

Our method to extract stellar population properties from datacubes has been explained and applied to CALIFA in Pérez et al. (2013), Cid Fernandes et al. (2013, 2014), and González Delgado et al. (2014c,a). In short, we analyze the data with the

code (Cid Fernandes et al. 2005), which fits an observed spectrum (O_λ) in terms of a model (M_λ) built by a non-parametric linear combination of N_\star simple stellar populations (SSP) from a base spanning different ages (t) and metallicities (Z). Dust effects are modeled as a foreground screen with a Cardelli et al. (1989) reddening law with $R_V = 3.1$. Windows around the main optical emission lines and the NaID absorption doublet (because of its interstellar component) are masked in all spectral fits². Bad pixels (identified by the reduction pipeline) are also masked. Results for each spectrum are then packed and organized with the y pipeline.

This working scheme is preserved here, but with three new developments:

1. The datacubes come from the version 1.5 of the reduction pipeline (García-Benito et al. 2015).
2. Larger and more complete SSP bases are employed.
3. A somewhat different definition of mean stellar metallicity is adopted (see González Delgado et al. 2014a).

This section describes the novelties related to the stellar population synthesis. Improvements resulting from the new reduction pipeline are described in Appendix A.

3.1. SSP spectral bases

SSP models are a central ingredient in our analysis, linking the results of the spectral decomposition to physical properties of the stellar populations. Our previous applications of to CALIFA explored spectral bases built from three sets of

SSP models, labeled as GM , CB , and BC in Cid Fernandes et al. (2014). The first two are used again here, but extended to a wider range of metallicities, producing what we denote as bases GMe and CBe .

Base GMe is a combination of the SSP spectra provided by Vazdekis et al. (2010) for populations older than $t = 63$ Myr and the González Delgado et al. (2005) models for younger ages. The evolutionary tracks are those of Girardi et al. (2000), except for the youngest ages (1 and 3 Myr), which are based on the Geneva tracks (Schaller et al. 1992; Schaerer et al. 1993; Charbonnel et al. 1993). The Initial Mass Function (IMF) is Salpeter. In our previous studies of the first 100 CALIFA galaxies, we defined base GM as a regular (t, Z) grid of these models, with 39 ages spanning $t = 0.001\text{--}14$ Gyr and four metallicities from 0.2 to $1.5 Z_\odot$. We now extend the Z range to use of all seven metallicites provided by Vazdekis et al. (2010) models: $\log Z/Z_\odot = -2.3, -1.7, -1.3, -0.7, -0.4, 0$, and $+0.22$. Because these models lack ages below 63 Myr, these young ages are only covered by the four largest metallicities, such that our extended GM base is no longer regular in t and Z . Base GMe contains $N_\star = 235$ elements.

Base CBe is built from an update of the Bruzual & Charlot (2003) models (Charlot & Bruzual 2007, private communication), replacing STELIB (Le Borgne et al. 2003) with a combination of the MILES (Sánchez-Blázquez et al. 2006; Falcón-Barroso et al. 2011) and (Martins et al. 2005) spectral libraries (the same ones used in base GMe). The evolutionary tracks are those collectively known as Padova 1994 (Alongi et al. 1993; Bressan et al. 1993; Fagotto et al. 1994a,b; Girardi et al. 1996). The IMF is that of Chabrier (2003). Whereas in previous works we limited the Z range to ≥ 0.2 solar, we now extend this base to six metallicities: $\log Z/Z_\odot = -2.3, -1.7, -0.7, -0.4, 0$, and $+0.4$. Base CBe contains $N_\star = 246$ elements (41 ages from 0.001 to 14 Gyr and the six metallicities above).

The main similarities and differences between bases GMe and CBe are the same as between the original GM and CB bases, which are thoroughly discussed in Cid Fernandes et al. (2014). Throughout the main body of this paper we focus on results obtained with base GMe , but we anticipate that our overall qualitative findings remain valid for base CBe . The role of base CBe is to enable a rough assessment of the uncertainties associated with the model choice.

A minor technical difference with respect to our previous analysis is that we now smooth the spectral bases to 6 Å FWHM effective resolution prior to the fits. This is because the kinematical filter implemented in operates in velocity-space, whereas both CALIFA and the SSP model spectra have a constant spectral resolution in λ -space, so that effects of the instrumental broadening can only be mimicked approximately by . We have verified that this modification does not affect the stellar population properties used in this paper.

Appendix B presents some comparisons of the results obtained with these two bases. Experiments were also performed with bases which extend the age range to 18 Gyr and configure to allow negative values of A_V . These tests are also discussed in Appendix B, which adds to the collection of “sanity checks” on the results of our analysis.

4. Galaxy mass, metric, and stellar metallicity

This section addresses three relatively unrelated aspects, which are all important to better understand the results presented in the next section, where we examine how the spatial distribution of stellar population properties relates to a galaxy’s stellar

² To test the effect of this process in age estimation, we have compared with the Sánchez-Blázquez et al. (2014) results for the 60 galaxies in common. This work uses Steckmap (Ocvirk et al. 2006) and the H β line (previously corrected for the emission contribution). Statistically, we find that there is no difference in age (mean = −0.04, std = 0.15 dex) if the same SSP models are used in the two methods.

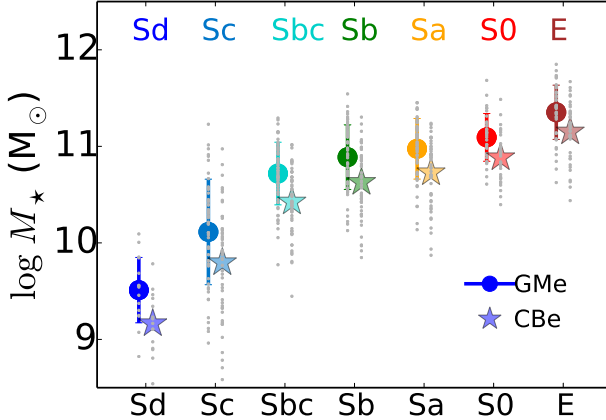


Fig. 2. Distribution of the stellar masses obtained from the spatially resolved spectral fits of each galaxy for each Hubble type (grey small points). The colored dots (stars) are the mean galaxy stellar mass in each Hubble type obtained with the *GMe* (*CBe*) SSP models. The bars show the dispersion in mass.

Table 1. Number of galaxies for each Hubble type and M_{\star} interval (*GMe*).

$\log M_{\star} (M_{\odot})$ bin	E	S0	Sa	Sb	Sbc	Sc	Sd
≤ 9.1	–	–	–	–	–	2	2
9.1–9.6	–	–	–	–	–	9	8
9.6–10.1	–	–	–	–	2	10	5
10.1–10.6	–	–	7	11	16	21	–
10.6–10.9	3	8	9	14	21	4	–
10.9–11.2	8	14	22	17	16	3	–
11.2–11.5	17	8	13	10	3	1	–
11.5–11.8	12	2	–	1	–	–	–
≥ 11.8	1	–	–	–	–	–	–
total	40	32	51	53	58	50	15

mass and morphology. First, Sect. 4.1 reviews the relation between stellar mass and morphological type for our sample. This strong relation is imprinted on virtually all results discussed in Sect. 5. Second, Sect. 4.2 compares our measurements of the HMR and HLR. As discussed by González Delgado et al. (2014c), these two natural metrics for distances are not identical because of the inside-out growth of galaxies. Here we inspect how the HMR/HLR ratio varies as a function of Hubble type and stellar mass in our sample. Finally, Sect. 4.3 presents our definition of mean stellar metallicity. González Delgado et al. (2014c) showed that stellar mass surface densities, mean ages, and extinction values defined from the integrated spectrum, from galaxy-wide spatial averages, and measured at $R = 1$ HLR all agree very well with each other. Here we extend this test to stellar metallicities. Throughout this section, results for the two SSP models discussed in Sect. 3.1 are presented.

4.1. Stellar masses

To obtain the total stellar mass of a galaxy, we add the mass in each zone, thus taking spatial variations of the stellar extinction and M/L ratio into account. Masked spaxels (e.g., foreground stars) are accounted for using the μ_{\star} radial profile as explained in González Delgado et al. (2014c).

Figure 2 shows the distribution of M_{\star} as a function of Hubble type. Table 1 shows the distribution of galaxies by Hubble type in several bins of M_{\star} . The masses range from 7×10^8 to $7 \times 10^{11} M_{\odot}$ for fits with *GMe* (Salpeter IMF).

CBe-based masses (Chabrier IMF) are on average smaller by a factor 1.84. As for the general galaxy population, mass is well correlated with Hubble type, decreasing from early to late types. High bulge-to-disk ratios (E, S0, Sa) are the most massive ones ($\geq 10^{11} M_{\odot}$), while galaxies with small bulges (Sc–Sd) have $M_{\star} \leq 10^{10} M_{\odot}$. The average $\log M_{\star}(M_{\odot})$ is 11.4, 11.1, 11.0, 10.9, 10.7, 10.1, and 9.5 for E, S0, Sa, Sb, Sbc, Sc, and Sd, respectively. The dispersion is typically 0.3 dex, except for Sc galaxies, which have a dispersion of ~ 0.5 dex.

Because CALIFA is not complete for $M_r \geq -19.5$, this distribution in mass is not completely representative of the local Universe. In particular, it is important to remember that dwarf ellipticals are not included, so M_{\star} or any other property discussed here for E's are restricted to massive ellipticals.

4.2. The HMR/HLR

As explained in Cid Fernandes et al. (2013), we define the HLR as the semi-major axis length of the elliptical aperture which contains half of the total light of the galaxy at the rest-frame wavelength 5635 Å. Similarly, the HMR is derived from the 2D distribution of the stellar mass, as the elliptical aperture at which the mass curve of growth reaches 50% of its asymptote. The ratio between the HMR and the HLR (a_{50}^M/a_{50}^L) reflects the spatial variation of the SFH in a galaxy. This ratio is lower than 1 in almost all cases (González Delgado et al. 2014c), a signpost of the inside-out growth found by Pérez et al. (2013).

Figure 3 shows the relation between a_{50}^M/a_{50}^L and Hubble type (left panel), and galaxy stellar mass (right panel). These plots confirm our earlier finding that galaxies are more compact in mass than in light. If the gradient in stellar extinction is taken into account, the average $a_{50}^M/a_{50}^{L_{\text{intrinsic}}} = 0.82 (0.80) \pm 0.10 (0.13)$ for base *GMe* (*CBe*). Figure 3 shows that the ratio decreases from late to early-type spirals; while lenticulars and ellipticals have similar a_{50}^M/a_{50}^L .

These results are also in agreement with our previous result, which a_{50}^M/a_{50}^L shows a dual dependence with galaxy stellar mass: it decreases with increasing mass for disk galaxies, but is almost constant in spheroidal galaxies, as confirmed in the right panel of Fig. 3. Sb–Sbc galaxies are those with the lowest a_{50}^M/a_{50}^L .

4.3. Stellar metallicity

Metallicity is one of the most difficult stellar population properties to estimate. Reasons for this include: (i) the coarse metallicity grid of the SSP bases; (ii) the limitation of the stellar libraries to the solar neighborhood; and (iii) inherent degeneracies like the dependence of the continuum shape on extinction, age, and metallicity, whose effects are hard to disentangle. Notwithstanding these difficulties, meaningful estimates of Z_{\star} can be extracted from observed spectra, particularly by means of full spectral synthesis methods (Sánchez-Blázquez et al. 2011).

-based estimates of Z_{\star} for the same CALIFA sample used in this paper were previously used by González Delgado et al. (2014a) to study global and local relations of Z_{\star} with the stellar mass and stellar mass surface density. We have shown there that: (i) our sample follows a well defined stellar mass-metallicity relation (MZR); (ii) this relation is steeper than one obtained from O/H measurements in HII regions, but that considering only young stellar populations the two MZR's are similar; and (iii) Z_{\star} is strongly related to μ_{\star} in galaxy disks

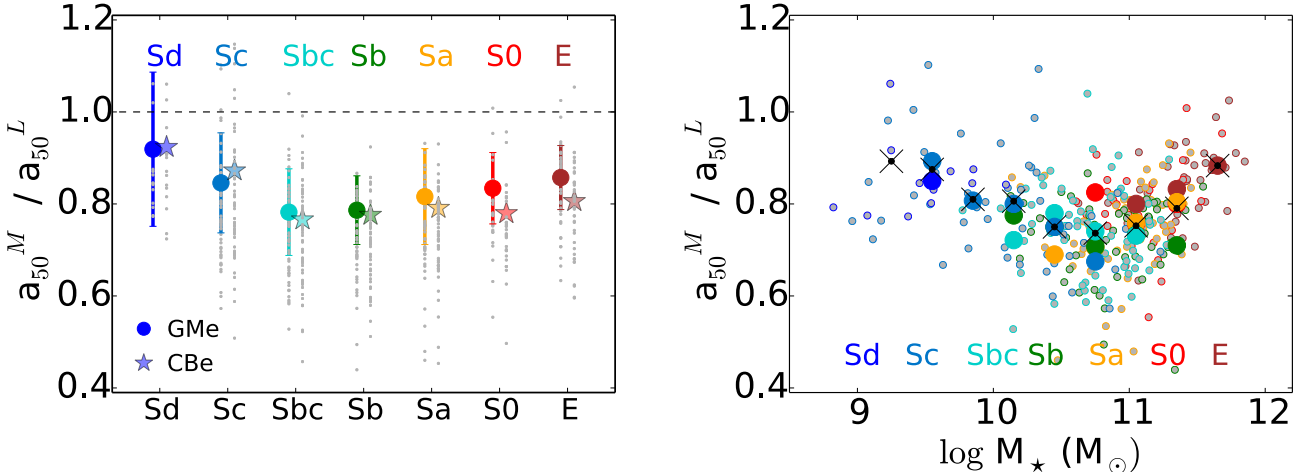


Fig. 3. Left: the ratio between half mass and half light radius (a_{50}^M / a_{50}^L) with the Hubble type (left). Big colored dots represent the averaged a_{50}^M / a_{50}^L in each Hubble type bin, and the lines the dispersion. Stars and big circles show the results obtained with the *GMe* and *CBe* bases, respectively. Right: a_{50}^M / a_{50}^L as a function of the galaxy stellar mass. The black crosses show the averaged correlation independent of the morphological type. Large circles represent the averaged relation in mass intervals of 0.25 dex for each color-coded morphological type.

and to M_\star in spheroids. All these results lend confidence to our Z_\star estimates.

Here we review our definition of the mean stellar metallicity, and test whether its value at 1 HLR matches the galaxy wide average value as well as at obtained from the spatially collapsed data cube.

4.3.1. Mean stellar metallicity

The main properties analyzed in this paper are the stellar mass surface density (μ_*), stellar extinction (A_V), mean age ($\langle \log \text{age} \rangle_L$), and metallicity of the stellar population, whose spatial distributions are studied as a function of Hubble type and total stellar mass (M_\star). These properties were defined in previous articles in this series. For instance, the mean light weighted log stellar age is defined as

$$\langle \log \text{age} \rangle_L = \sum_{t,Z} x_{tZ} \times \log t \quad (1)$$

(Eq. (9) of Cid Fernandes et al. 2013), where x_{tZ} is the fraction of flux at the normalization wavelength (5635 Å) attributed to the base element with age t and metallicity Z . The mass-weighted version of this index, $\langle \log \text{age} \rangle_M$, is obtained by replacing x_{tZ} by its corresponding mass fraction m_{tZ} .

While Cid Fernandes et al. (2013) average the base metallicities linearly (their Eq. (10)), as in González Delgado et al. (2014a), we employ a logarithmic average:

$$\langle \log Z_\star \rangle_M = \sum_{t,Z} m_{tZ} \times \log Z \quad (2)$$

for the mass-weighted mean $\log Z_\star$ and

$$\langle \log Z_\star \rangle_L = \sum_{t,Z} x_{tZ} \times \log Z \quad (3)$$

for the luminosity-weighted mean $\log Z_\star$. The motivation to use this definition is that the extended SSP bases used in this study span a much wider dynamical range in Z_\star (nearly three orders of magnitude, compared to barely one in our previous papers), which is better handled with a geometric mean (implicit in the

use of the logarithm). This is the same reasoning behind the use of $\langle \log \text{age} \rangle$ instead of $\log(\text{age})$.

To some degree, the definition of mean Z is largely a matter of taste (albeit one with mathematical consequences because of the inequality of the arithmetic and geometric means, $\langle \log Z \rangle \leq \log \langle Z \rangle$), so much so that one finds both types of averaging in the literature. For instance, in Gallazzi et al. (2005) metallicities are averaged logarithmically, whereas Asari et al. (2007) work with arithmetic averages.

As shown in González Delgado et al. (2014a; see also Fig. 4), our metallicities span about 1 dex for galaxy masses ranging from 10^9 to $10^{12} M_\odot$, with an MZR which matches well the stellar metallicities of both Milky Way and LMC-like galaxies.

4.3.2. Galaxy averaged stellar metallicity

González Delgado et al. (2014c) obtained the important result that galaxy-averaged stellar ages, mass surface density, and extinction are well matched by the corresponding values of these properties at $R = 1$ HLR and also with the values obtained from the analysis of the integrated spectrum (i.e., the one obtained by collapsing the datacube to a single spectrum). The general pattern, therefore, is that galaxy averaged properties match both the values at 1 HLR and those obtained from integrated spectra. Do our stellar metallicities comply with this rule?

To answer this question, we first define the galaxy-wide average stellar metallicity following Eq. (2) in González Delgado et al. (2014a), which gives the mass-weighted mean value of $\langle \log Z_{\star,xy} \rangle_M$ as

$$\langle \log Z_\star \rangle_M^{\text{galaxy}} = \frac{\sum_{xy} M_{\star,xy} \langle \log Z_\star \rangle_{M,xy}}{\sum_{xy} M_{\star,xy}}, \quad (4)$$

where $M_{\star,xy}$ is the stellar mass in spaxel xy .

Figure 4 compares our results for $\langle \log Z_\star \rangle_M^{\text{galaxy}}$ with the mass-weighted mean $\langle \log Z_\star \rangle_M$ values obtained at $R = 1$ HLR ($\langle \log Z_\star \rangle_M^{\text{HLR}}$, bottom panels) and those derived from the integrated spectrum ($\langle \log Z_\star \rangle_M^{\text{integrated}}$, top panels), analyzed in the exact same way as the individual zone spectra. Results are shown for both base *GMe* (left panels) and *CBe* (right).

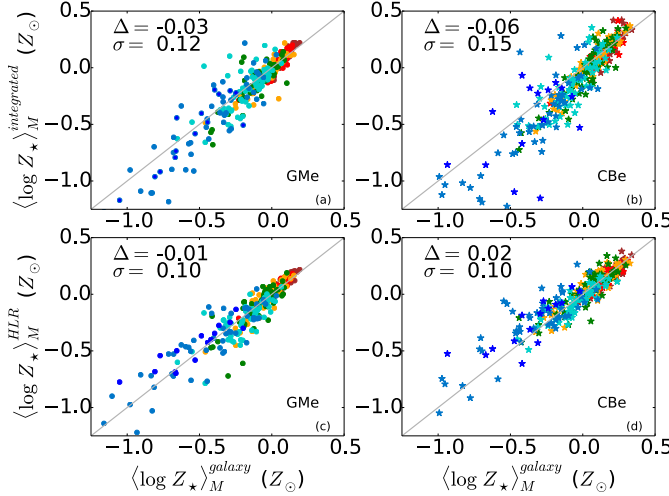


Fig. 4. Upper panels: comparison of the galaxy-wide average stellar metallicity (weighted in mass) derived from the spatially resolved spectral analysis ($\langle \log Z_{\star} \rangle_M^{\text{galaxy}}$) and the integrated metallicity derived from fitting the total (integrated) galaxy spectrum ($\langle \log Z_{\star} \rangle_M^{\text{integrated}}$). Lower panel: comparison of $\langle \log Z_{\star} \rangle_M^{\text{galaxy}}$ with the value measured at $R = 1$ HLR ($\langle \log Z_{\star} \rangle_M^{\text{HLR}}$). Left and right panels show results obtained with base GMe and CBe SSPs, respectively. All panels include 300 galaxies. The difference between the y -axis and x -axis is labeled in each panel as Δ , and the dispersion as σ .

The agreement is remarkable. The galaxy averaged metallicity and at 1 HLR are the same to within a dispersion of 0.1 dex. The integrated metallicity also matches the galaxy averaged value with only slightly larger dispersions. The largest deviations occur for low-metallicity systems. Similar conclusions are reached if the comparison in Fig. 4 is done using the light weighted version of Eq. (4),

$$\langle \log Z_{\star} \rangle_L^{\text{galaxy}} = \frac{\sum_{xy} L_{\star,xy} \langle \log Z_{\star} \rangle_{L,xy}}{\sum_{xy} L_{\star,xy}}, \quad (5)$$

where $L_{\star,xy}$ is the luminosity (corrected by stellar extinction) in each spaxel evaluated at a reference wavelength (5635 Å in our case).

The stellar metallicities behave as expected, in the sense that like other properties, their galaxy-wide averages match the values at $R = 1$ HLR, and also the values derived from integrated spatially unresolved spectroscopy (González Delgado et al. 2014c). We thus conclude that galaxy-wide spatially averaged stellar population properties (stellar mass, mass surface density, age, metallicity, and extinction) match those obtained from the integrated spectrum, and that these spatially averaged properties match those at $R = 1$ HLR, proving that effective radii are really effective (González Delgado et al. 2014b).

5. Spatially resolved stellar population properties as a function of morphology and mass

This section presents a series of results derived from our spatially resolved spectral synthesis analysis of CALIFA galaxies. We focus on the following four stellar populations properties: mass surface density (μ_{\star} , Sect. 5.1), mean ages ($\langle \log \text{age} \rangle_L$, Sect. 5.2), metallicities ($\langle \log Z_{\star} \rangle_M$, Sect. 5.3), and extinction (A_V , Sect. 5.4). Each of these properties is studied by means of (i) 2D maps of the individual galaxies; (ii) radial profiles; and (iii) radial gradients. Throughout the section, the emphasis is on

evaluating and comparing the roles of morphology and total stellar mass in shaping the observed behavior of these four properties. Before discussing the results, we briefly explain how these quantities are obtained and how they are presented.

2D maps in the CMD: using y we obtain, for each galaxy, 2D maps of each of the four properties. The results for all the galaxies are presented in the framework of the color-magnitude diagram, where each map is placed at the galaxy's coordinates in the $u - r$ vs. M_r CMD. Because absolute magnitude is related to M_{\star} and redder galaxies are (usually) older and more metal rich, these plots show the correlations M_{\star} - μ_{\star} , M_{\star} -age, and M_{\star} -metallicity in a 2D fashion. Because in our sample the galaxy Hubble type is correlated with color and luminosity, these plots not only show how the galaxy averaged properties and their radial structure change with the galaxy stellar mass, but also with the morphological type. These maps are shown in the Appendix C (Figs. C.1–C.4).

Radial profiles: each 2D map is azimuthally averaged to study the radial variations of each of the four stellar population properties. Elliptical apertures 0.1 HLR in width are used to extract the radial profiles, with ellipticity and position angle obtained from the moments of the 5635 Å flux image. Expressing radial distances in units of HLR allows the profiles of individual galaxies to be compared on a common metric, as well as averaging (“stacking”) them as a function of Hubble type or stellar mass. Radial profiles expressed in units of the HMR were also analyzed and lead to similar shapes, so all profiles presented below use HLR as the unit for radius.

Radial gradients: inner and outer gradients are defined as differences between the values at $R = 1$ and 0 (∇_{in}), and $R = 2$ and 1 (∇_{out}), respectively. For instance,

$$\nabla_{\text{in}} \log \mu_{\star} = \log \mu_{\star}(1 \text{ HLR}) - \log \mu_{\star}(0), \quad (6)$$

$$\nabla_{\text{out}} \log \mu_{\star} = \log \mu_{\star}(2 \text{ HLR}) - \log \mu_{\star}(1 \text{ HLR}), \quad (7)$$

for $\log \mu_{\star}$, and similarly for $\langle \log \text{age} \rangle_L$, $\langle \log Z_{\star} \rangle_M$ and A_V . Defined in this way, the gradients have units of dex/HLR (mag/HLR for ∇A_V). Since the stellar population properties of galaxies at 1 HLR represent very well the galaxy-wide average, ∇_{in} (∇_{out}) effectively measures how the bulge (disk) properties change with respect to those of the galaxy as a whole³.

Unless otherwise noted, all results reported below are for the GMe base, although the whole analysis was carried out with properties derived with both sets of SSP models discussed in 3.1. Differences between GMe and CBe SSPs are as: (a) The stellar mass surface density is lower with CBe than with GMe by 0.27 dex on average, mostly due to the different IMFs (Salpeter in GMe versus Chabrier in CBe). (b) Variations in stellar extinction are negligible. (c) CBe yields somewhat younger ages and higher metallicities than GMe, by an average of 0.14 dex in $\langle \log \text{age} \rangle_L$ and 0.12 dex in $\langle \log Z_{\star} \rangle_M$. These shifts reflect the age-metallicity degeneracy, and are mainly a consequence of the different sets of metallicities available in these bases. However,

³ Based on the exponential fit analysis developed by Sánchez et al. (2013) and Sánchez-Blázquez et al. (2014), we conclude that the regions between 1 and 2 HLR are dominated by the disk component; thus, ∇_{out} measures the disk gradient. However, ∇_{in} is not measuring the bulge gradient. The reason is that the effective radius (R_e) of the spheroidal component can be smaller than 1 HLR, and it shows a dependence with the morphological type. Thus, $R_e \sim 1$ HLR for E, but is significantly smaller in late-type spirals.

radial gradients are not affected by this degeneracy. A detailed comparison of properties derived with the two bases is given in Appendix B.

5.1. Stellar mass surface density

2D maps of the stellar mass surface density for the 300 individual galaxies of our sample are presented in the Appendix C (Fig. C.1). Here we discuss the radial structure of $\log \mu_*$ as a function of Hubble type and M_* .

5.1.1. μ_* -morphology and μ_* -mass relations

Figure 5 shows how μ_* measured at 1 HLR changes with Hubble type (left panel), and with the galaxy stellar mass (right). Recall from González Delgado et al. (2014c) that properties measured at 1 HLR match the corresponding galaxy-wide average value very well, so these plots ultimately show how the global μ_* depends on the morphology and on M_* .

The plot shows $\langle \log \mu_*^{\text{HLR}} \rangle$ increasing from late spirals to spheroids, with average and dispersion values of 3.1 ± 0.2 , 3.10 ± 0.18 , 3.05 ± 0.25 , 2.70 ± 0.17 , 2.65 ± 0.24 , 2.40 ± 0.28 , 2.04 ± 0.27 , for E, S0, Sa, Sb, Sbc, Sc, and Sd, respectively. Note that E and S0 are remarkably similar.

Surface densities also increase with M_* , as seen in the right panel of Fig. 5. The overall $\mu_*^{\text{HLR}} - M_*$ relation is relatively smooth, with no evidence of an abrupt change of behavior as that discussed by Kauffmann et al. (2003) for SDSS galaxies. Figure 5, however, reveals that morphology is also behind the dispersion in the $\mu_* - M_*$ relation. The black line shows the relation for the full sample, obtained by averaging $\log \mu_*$ in 0.4 dex-wide bins in mass, while the big circles break this general relation into different (color-coded) morphological types for the same mass bins. Despite the reduced statistics, it is evident that: (a) for the same stellar mass, early-type galaxies are denser than late-type galaxies; and (b) Sa and earlier type galaxies exhibit a much flatter $\mu_* - M_*$ relation than later types. The overall impression from these results is that morphology, and not only stellar mass, plays a fundamental role in defining stellar surface densities, and it is responsible for the change of slope in the SDSS $\mu_* - M_*$ relation.

5.1.2. Radial profiles

Azimuthally averaged radial profiles of $\log \mu_*$ are shown in Fig. 6. Results are stacked by Hubble type (left panel) and mass (right). In the left panel galaxies are grouped in our seven morphological classes. The typical dispersion within these bins is illustrated by the error bar, which shows the standard deviation in $\log \mu_*$ ($R = 1 \text{ HLR}$) for galaxies of the Sa class.

A clear trend with Hubble type is seen: the $\mu_*(R)$ profiles scale with Hubble type from late to early spirals, and this modulation with morphology is preserved at any given distance. E and S0 have remarkably similar profiles, with core and extended envelope equally dense at any given distance, suggesting that the disk of S0 galaxies and the extended envelope of ellipticals have grown their mass by similar processes.

The right panel of Fig. 6 shows the radial profiles grouped in seven bins of stellar mass spanning the $\log M_*(M_\odot) = 9.1 - 11.8$ range. These also show that the average of $\log \mu_*(R)$ is modulated by M_* . However, this $\mu_*(R) - M_*$ modulation breaks for early-type galaxies (concentration index C ($r_{90}/r_{50} \geq 2.8$; see also Fig. 13 in González Delgado et al. 2014c), which

in our sample are populated mainly by E and S0, and some Sa. On the other hand, these early types are all massive, with $M_* \geq 10^{11} M_\odot$.

5.1.3. Radial gradients

Inner (0–1 HLR) and outer (1–2 HLR) gradients in $\log \mu_*$, as defined by Eqs. (6) and (7), are plotted as a function of morphology and stellar mass in Fig. 7. $\nabla_{\text{in}} \log \mu_*$ values (corresponding to the core region) are plotted in grey-red, while $\nabla_{\text{out}} \log \mu_*$ (which trace the disks of spirals and S0 and the extended envelope of ellipticals) are plotted in grey-blue. Circles and stars show results for bases GMe and CBe, respectively, illustrating that the resulting gradients are nearly identical even though these bases yield different absolute values of μ_* .

A clear correlation exists between $\nabla_{\text{in}} \log \mu_*$ and Hubble type. The gradient in the inner HLR increases (in absolute values) significantly from late to early spirals, converging to a constant value for E and S0. This relation reflects the variation of the bulge to disk ratio in spirals, and the dominance of the bulge component in spheroids (S0 and E). The outer gradient is weaker (smaller in absolute value) than the inner gradient, as expected if a disk component dominates the mass outward of 1 HLR.

The right panel of Fig. 7 shows the relation between the inner gradient and stellar mass. There is a clear increase (in absolute values) of $\nabla_{\text{in}} \log \mu_*$ with M_* , with the more massive galaxies having a steeper increase of the central density. The dispersion with respect to the average values (black crosses) within M_* -bins is significant. To check the effect of morphology on this dispersion we have averaged $\nabla_{\text{in}} \log \mu_*$ in mass intervals for each Hubble type and plotted the resulting averages (large colored circles). The general trend that emerges is that, for galaxies of the same mass, early type galaxies tend to be overall centrally denser than later types, in agreement with Fig. 5; although, there are a few intervals of stellar mass (e.g. $\log M_* = 11.4 M_\odot$), in which the variations in $\nabla_{\text{in}} \log \mu_*$ with Hubble type are not significant.

It is also worth mentioning that $\nabla_{\text{in}} \log \mu_*$ in Sa and Sb is very close to that in S0 and E, and in this sense it would be easy to fade early-type spirals into S0's.

5.2. Ages of the stellar populations

2D maps of the luminosity-weighted mean log stellar ages (Eq. (1)) for the 300 galaxies are presented in Fig. C.2. Here we discuss the radial structure of $\langle \log \text{age} \rangle_L$ and its relation to Hubble type and M_* . The presentation follows the same script used in the presentation of μ_* -related results in Sect. 5.1.

5.2.1. Age-morphology and age-mass relations

Figure 8 shows how the mean age of the stellar populations at 1 HLR changes along the Hubble sequence (left panel), and with the galaxy stellar mass (right). Similar to $\log \mu_*^{\text{HLR}}$, $\langle \log \text{age} \rangle_L^{\text{HLR}}$ represents well the galaxy-wide averaged stellar population age ($\langle \log \text{age} \rangle_{L \text{ galaxy}}$, González Delgado et al. 2014c).

Clearly, $\langle \log \text{age} \rangle_L^{\text{HLR}}$ scales with Hubble type, increasing steadily from Sd to Sa. S0 and ellipticals have stellar populations of similar mean age, and they are older than spirals. The average and dispersion values of $\langle \log \text{age} \rangle_L^{\text{HLR}}$ (yr) are 8.62 ± 0.22 , 8.89 ± 0.22 , 9.07 ± 0.19 , 9.33 ± 0.21 , 9.55 ± 0.19 , 9.71 ± 0.11 , and 9.74 ± 0.11 , for Sd, Sc, Sbc, Sb, Sa, S0, and E, respectively.

Mean ages also increase with the galaxy mass (right panel of Fig. 8), a “downsizing” behavior that has been confirmed with

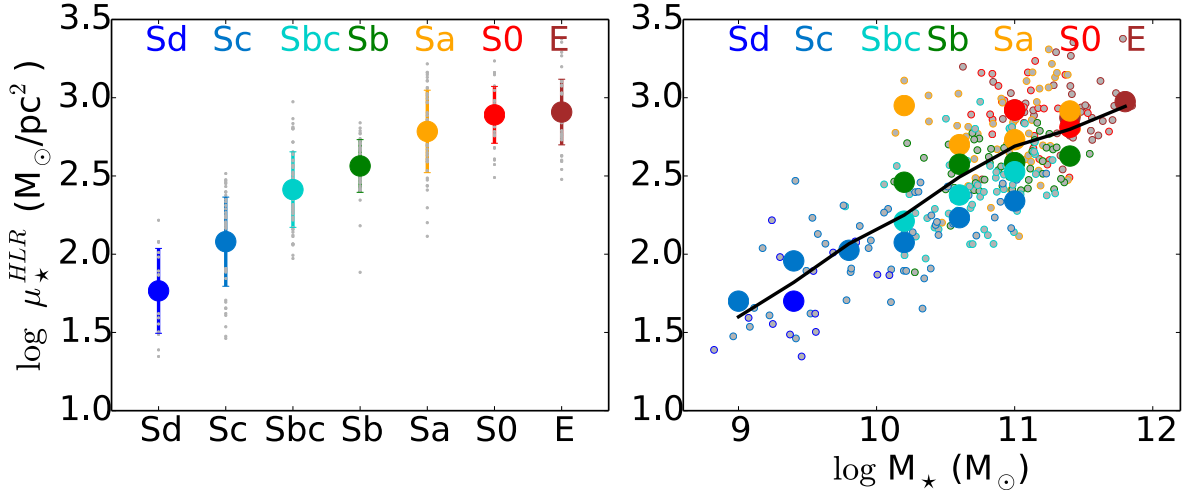


Fig. 5. Left panel: stellar mass surface density measured at 1 HLR as a function of Hubble type. Small dots represent $\log \mu_*$ for each galaxy; the colored circles are the average $\log \mu_*$ for each Hubble type, and the error bars are the dispersion in $\log \mu_*$ for each morphological type. Right panel: $\log \mu_*$ – $\log M_*$ relation. Individual galaxies are represented by small dots colored by their morphological type. The black line is the average $\log \mu_*$ in galaxy stellar mass bins of 0.4 dex. Large colored circles are the average $\log \mu_*$ in each bin of mass for each Hubble type.

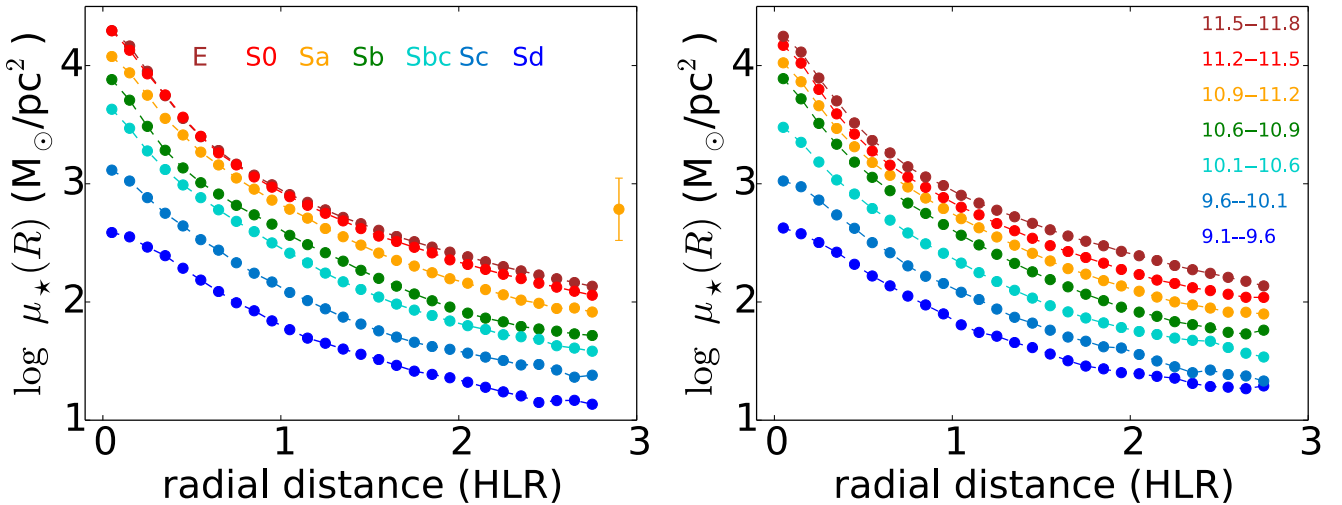


Fig. 6. Left: radial profiles (in units of HLR) of the stellar mass surface density obtained with base GMe . The results are stacked in seven morphology bins. The error bar in the panel indicates the dispersion at one HLR distance in the galaxies of the Sa bin. It is similar for other Hubble types and radial distances. Right: radial profiles stacked in seven bins of galaxy stellar mass, $\log M_*(M_\odot)$: 9.1–9.6, 9.6–10.1, 10.1–10.6, 10.6–10.9, 10.9–11.2, 11.2–11.5, 11.5–11.8.

widely different samples and methods. For instance, our age–mass relation is similar to that derived for SDSS galaxies by Gallazzi et al. (2005, their Fig. 8.). They found that there is a transition at $M_* \sim 3 \times 10^{10} M_\odot$ ⁴, below which galaxies are typically young and above which they are old. This is the same mass at which Kauffmann et al. (2003) find the μ_* – M_* relation to flatten.

Unlike in these SDSS-based works, we do not see sharp transitions as a function of M_* in either μ_* nor $\langle \log \text{age} \rangle_L$, although differences in sample selection and statistics prevent a proper comparison. We do, however, note a common behavior in the right panels of Figs. 5 and 8, in the sense that the dispersion above $\sim 10^{10} M_\odot$ is strongly related to morphology.

Like in Fig. 5 (right panel), the black line in the right panel of Fig. 8 shows the age–mass relation for the whole sample, obtained by averaging $\langle \log \text{age} \rangle_L^{\text{HLR}}$ values in M_* bins. Small dots show individual galaxies, while the large colored

circles represent the mass-binned average $\langle \log \text{age} \rangle_L^{\text{HLR}}$ for each Hubble type. As with the μ_* – M_* relation, breaking the age–mass relation into morphological types reveals clean trends. In this case, we see that, for a fixed M_* , earlier type galaxies are older than later types. The corollary is that mass is not the sole property controlling the SFH of a galaxy. In fact, given the ~flat age–mass relations for Sa, S0, and E, morphology seems to be a more relevant factor, at least in these cases.

5.2.2. Radial profiles

Figure 9 shows the age radial profiles obtained by stacking galaxies as a function of Hubble type and mass. The $\langle \log \text{age} \rangle_L(R)$ profiles scale with Hubble type, but by different amounts at the center than at 1 HLR. At any radial distance, however, the early-type galaxies are older than later-type galaxies. E and S0 are again very similar at all radii. This suggests that E and S0 have similar histories not only on average, but also spatially resolved, at least in the inner 2 HLR. Negative age gradients are detected in all galaxies (except perhaps in Sd, whose

⁴ Equivalent to $\sim 5.5 \times 10^{10} M_\odot$ for our IMF.

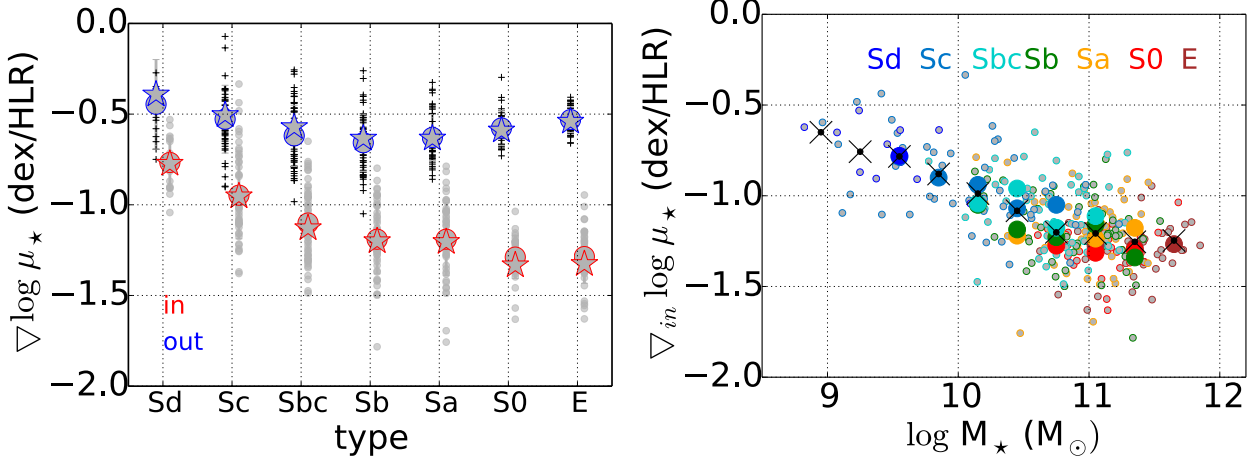


Fig. 7. Left panel: correlation between the inner (grey-red) and outer (grey-blue) gradient of $\log \mu_*$ and the morphological type. The results are shown for the *GMe* (stars) and *CBe* (circles) SSP models. The inner gradient is calculated between the galaxy nucleus and 1 HLR, and the outer gradient between 1 HLR and 2 HLR. Right panel: correlation between the inner gradient of $\log \mu_*$ and the galaxy stellar mass. Small dots represent the results for each galaxy, and black crosses the average for each 0.3 dex mass bin. Large circles represent the averaged inner gradient in mass intervals of 0.3 dex for each color-coded morphological type. Black crosses show the average correlation between the inner gradient of $\log \mu_*$ and galaxy mass independent of the morphological type.

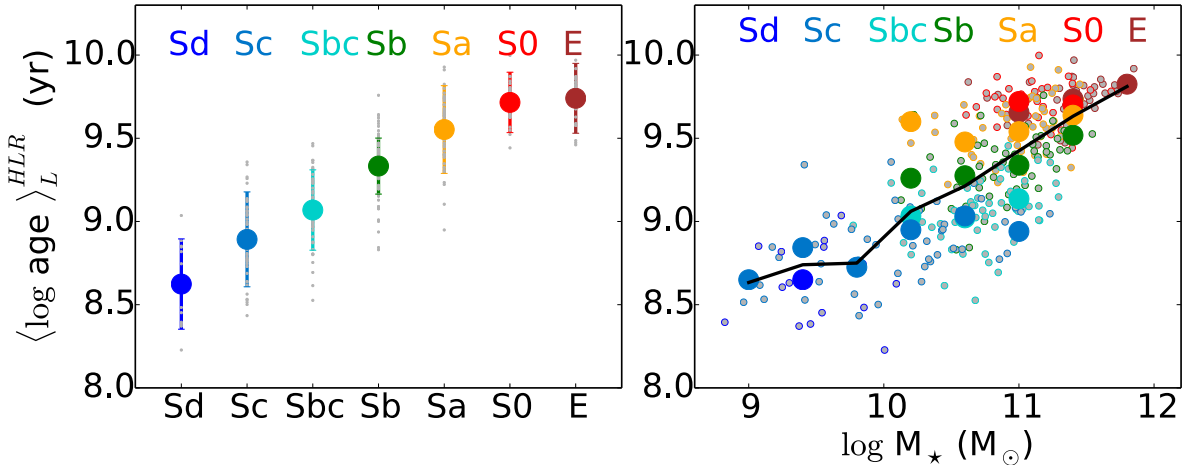


Fig. 8. $\langle \log \text{age} \rangle_L$ measured at 1 HLR as a function of Hubble type (left) or galaxy stellar mass (right). Symbols and colors are the same as in Fig. 5. The black line is the average $\langle \log \text{age} \rangle_L$ in galaxy stellar mass bins of 0.4 dex.

ages profiles are flatter than in the other spirals⁵). These negative gradients reflect the inside-out growth of galaxies. Furthermore, the decrease of $\langle \log \text{age} \rangle_L$ with R indicates that quenching happens earlier at the galaxy center; and also earlier in early-type galaxies (spheroids and Sa) than in later-type spirals (Sbc–Sc).

The radial profiles also show a clear trend with M_* (Fig. 9, right), with the more massive galaxies being older everywhere, hence preserving the downsizing pattern at all radial distances. Comparing the left and right panels in Fig. 9, one sees that grouping galaxies by their stellar mass leads to a reduced vertical stretch in their $\langle \log \text{age} \rangle_L(R)$ profiles than when the averaging is done by morphology. But the profiles expand to a similar vertical scale if galaxies earlier than Sd and more massive than $10^{9.6} M_\odot$ are considered indicating that the effect of morphology and stellar mass are not easily disentangled here. However, in Sect. 6.3, Fig. 20 shows that the dispersion in the $\langle \log \text{age} \rangle_L(R)$

profiles between galaxies of the same M_* and different Hubble type is significant, and larger than between the $\langle \log \text{age} \rangle_L(R)$ profiles of galaxies of different M_* but the same Hubble type. These results, in agreement with Fig. 8, indicate that the age profiles are more related to morphology than to M_* . Since $\langle \log \text{age} \rangle_L(R)$ is essentially a first moment of the spatially resolved SFH, we can conclude that the SFH and its radial variation are modulated primarily by the galaxy morphology, with mass playing a secondary role.

5.2.3. Radial gradients

Gradients in $\langle \log \text{age} \rangle_L$, computed as indicated in Eqs. (6) and (7), are plotted in Fig. 10 against Hubble type (left panel) and stellar mass (right). The figure layout is exactly as in Fig. 7. Whilst in that plot results obtained with bases *GMe* and *CBe* (circles and stars in the left panel, respectively) could hardly be distinguished, here the results for these two sets of SSPs do not overlap so precisely, although the differences in $\nabla \langle \log \text{age} \rangle_L$ are clearly very small (see Sect. B.2).

A clear relation exists between $\nabla_{in} \langle \log \text{age} \rangle_L$ and morphology: the inner age gradient increases from early-type galaxies to

⁵ The small drop of $\langle \log \text{age} \rangle_L$ toward the center of Sd galaxies is caused by a couple of galaxies with young nuclear regions. Given that this group is the least populated in our analysis (only 15 galaxies), better statistics is needed to evaluate the reality of this feature.

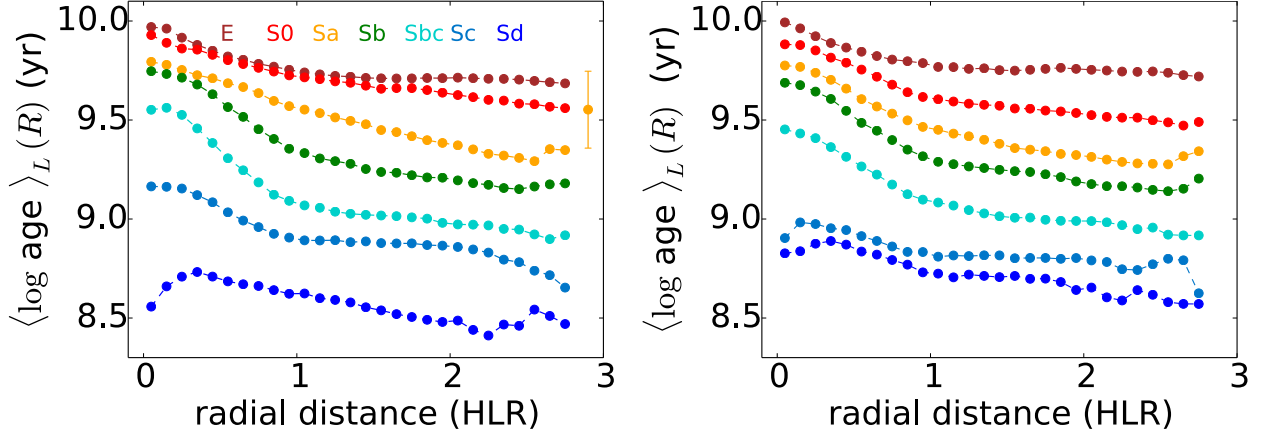


Fig. 9. Radial profiles of $\langle \log \text{age} \rangle_L$ as a function of Hubble type (left) and in seven bins of galaxy stellar mass (right). These bins are $\log M_\star(M_\odot) = 9.1\text{--}9.6, 9.6\text{--}10.1, 10.1\text{--}10.6, 10.6\text{--}10.9, 10.9\text{--}11.2, 11.2\text{--}11.5, 11.5\text{--}11.8$. Symbols and colors are the same as in Fig. 6. These results are obtained with base GMe .

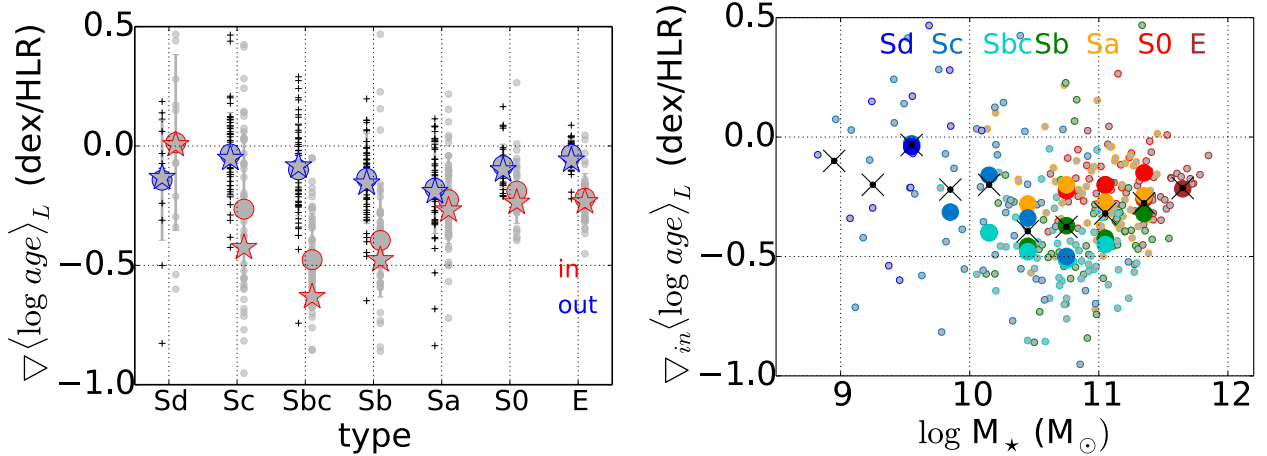


Fig. 10. Left panel: as Fig. 7 except for $\langle \log \text{age} \rangle_L$. The inner gradient shows a clear dependence with Hubble type, that seems to be stronger than with the galaxy mass. Sb–Sbc–Sc galaxies have larger inner gradients with CBe than with GMe , but both sets of models show a similar dependence with Hubble type. Right panel: the inner gradient of $\langle \log \text{age} \rangle_L$ as a function of galaxy mass. Colors and symbols are the same as in Fig. 7.

Sb–Sbc spirals, which are the galaxies with the largest variation between the age of the stellar population at the bulge and the disk. Spirals of later type (Sc and Sd) have flatter radial profiles than Sb–Sbc. The outer (between 1 and 2 HLR) age gradient shows a similar bimodal behavior as $\nabla_{in} \langle \log \text{age} \rangle_L$, but with a smaller amplitude.

The right panel of Fig. 10 shows the behavior of $\nabla_{in} \langle \log \text{age} \rangle_L$ with M_\star . The gradient tends to increase (become more negative) from low-mass galaxies (which have roughly flat profiles) up to about $10^{11} M_\odot$, at which point the trend reverses and $\nabla_{in} \langle \log \text{age} \rangle_L$ decreases with increasing M_\star . This is best seen following the black crosses, which trace the mass-binned mean relation. The dispersion with respect to this relation is significant and is related to the morphology, as seen through the large colored circles. The tendency is that, at a given mass, S0 and early-type spirals have weaker $\nabla_{in} \langle \log \text{age} \rangle_L$ than Sb–Sbc. This dependence of age gradients with the Hubble type at a fixed M_\star indicates again that the spatial variation of the SFH is mainly driven by morphology and not by stellar mass.

However, the morphology (understood as the B/D ratio Graham & Worley 2008) cannot be the only driver of the spatial variation of the SFH along all the Hubble sequence. Figure 10 shows that there is not a monotonic relation between the B/D ratio and $\nabla_{in} \langle \log \text{age} \rangle_L$, with galaxies with the smaller B/D ratio

having the largest variations in $\langle \log \text{age} \rangle_L$ between the central core and the disk. This bimodal behavior seen in Fig. 10 suggests that other physical properties are also important in establishing the spatial variation of the SFH, which on the other hand is reflecting the different bulge formation processes along the Hubble sequence.

5.3. Stellar metallicity

Figure C.3 presents the images of the mass-weighted mean (logarithmic) stellar metallicity (cf. Eq. (2)). Here we discuss the radial structure of $\langle \log Z_\star \rangle_M$ as a function of Hubble type and M_\star .

5.3.1. Metallicity-morphology and mass-metallicity relations

Figure 11 shows how the stellar metallicity measured at 1 HLR changes with the Hubble type (left panel) and with the galaxy stellar mass (right).

Stellar metallicities grow systematically from late to early-type galaxies. The statistics within each Hubble type are $\langle \log Z_\star \rangle_M^{\text{HLR}}(Z_\odot) = -0.05 \pm 0.13, -0.05 \pm 0.33, -0.21 \pm 0.16, -0.10 \pm 0.18, -0.05 \pm 0.15, +0.06 \pm 0.08$, and $+0.10 \pm 0.08$ for Sd, Sc, Sbc, Sb, Sa, S0, and E, respectively.

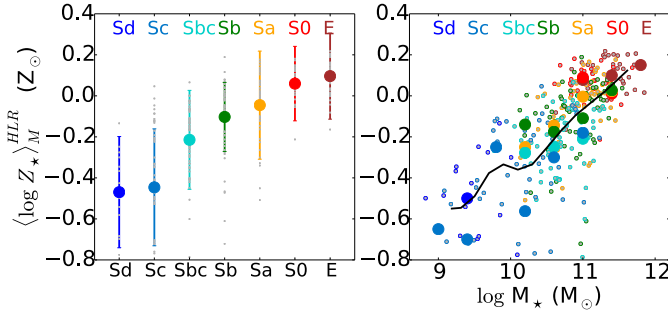


Fig. 11. $\langle \log Z_\star \rangle_M$ measured at 1HLR as function of Hubble type (left) and galaxy stellar mass (right). Symbols and colors are the same as in Fig. 5. The black line is the average $\langle \log Z_\star \rangle_M$ obtained in 0.4 dex bins of $\log M_\star$.

Not surprisingly, metallicities also grow with M_\star , as shown in the right panel of Fig. 11. Since we have shown in Sect. 4.3.2 that the galaxy-wide average stellar metallicity is well represented by the metallicity at 1 HLR, this plot is in fact equivalent to the global mass-stellar metallicity relation (MZR). We have previously found that this relation is steeper than that derived from HII regions, which is similar to the flatter stellar MZR obtained when we consider only young stars (González Delgado et al. 2014a). As in Fig. 5, the smoothed black curve is obtained by averaging $\langle \log Z_\star \rangle_M^{\text{HLR}}$ in 0.4 dex bins of $\log M_\star$. The dispersion in the MZR is significant, and larger than the dispersion produced by the galaxy morphology as shown by the distribution of large colored circles. These circles are the average $\langle \log Z_\star \rangle_M^{\text{HLR}}$ in each mass bin for each Hubble type, and show the tendency of earlier type galaxies to be more metal rich than late-type galaxies of the same stellar mass.

5.3.2. Radial profiles

Figure 12 shows the results of stacking the radial profiles of $\langle \log Z_\star \rangle_M$ as a function of Hubble type and M_\star . Outwards decreasing $\langle \log Z_\star \rangle_M$ is detected for most morphological classes, but flat profiles are found for Sc–Sd galaxies. Intermediate type spirals (Sb–Sbc) stand out as those with the largest variations in stellar metallicity.

The behavior of the radial variation of the stellar metallicity with M_\star (right panel in Fig. 12) is similar to the behavior with morphology. Most galaxies have $\langle \log Z_\star \rangle_M$ that decreases with R , except for the two lowest mass bins, which show flat profiles. The largest spatial variations are also found in galaxies in the intermediate mass bins ($10 \leq \log M_\star(M_\odot) \leq 11$).

These negative radial gradients of the metallicity are also an indicator of the inside-out formation processes in galaxies. The inversion of the gradient in late-type spirals and in low-mass spirals may be an indicator of the secular processes or the outside-in formation scenario in these galaxies (Pérez et al. 2013).

5.3.3. Radial gradients

Figure 13 clones Figs. 7 and 10 for $\langle \log Z_\star \rangle_M$ gradients. On the left panel, one sees that, as for stellar densities and ages, results for bases *GMe* and *CBe* are very similar. On average, galaxies have $\langle \log Z_\star \rangle_M$ gradients ~ -0.1 dex/HLR similar to the value obtained from nebular oxygen abundances (Sánchez et al. 2013). Outer and inner gradients are not significantly different. Despite the large scatter, there is a hint of a bimodal distribution as that found for stellar ages, also with intermediate-type spirals in a

pivotal position and late-type spirals with the flattest gradients, at least in a statistical sense.

The right panel of Fig. 13 shows $\nabla_{\text{in}} \langle \log Z_\star \rangle_M$ as a function of M_\star . The dispersion is significant, but on average there is a tendency to turn flat profiles into negative gradient profiles as M_\star increases from 10^9 to $10^{10} M_\odot$. The largest gradients are found between 10^{10} and $10^{11} M_\odot$. More massive galaxies tend to have weaker stellar metallicity gradients. The dispersion is significant throughout this relation. A trend with morphology is seen in the sense that, for a given mass, early types are those with weaker gradients.

5.4. Stellar extinction

models the stellar extinction as a foreground screen, parametrized by A_V and following the Galactic reddening law. Images showing the spatial distribution of A_V for our 300 galaxies are presented in Fig. C.4. Here we present A_V related results as a function of Hubble type and M_\star , following the same script adopted in the discussion of μ_\star , $\langle \log \text{age} \rangle_L$, and $\langle \log Z_\star \rangle_M$ in the previous subsections, thus completing the list of stellar population properties studied in this work. Unlike masses, ages, and metallicities, extinction is more easily affected by inclination effects, so the results reported below should be interpreted with caution. Section 5.5 explores this issue in depth.

5.4.1. Extinction-morphology and extinction-mass relations

Figure 14 shows how the stellar extinction at 1 HLR changes with Hubble type (left panel) and with stellar mass (right panel). As with other properties, A_V^{HLR} represents well the mean extinction of the galaxy⁶ as well as the A_V value derived from spectral fits of the integrated spectra⁷. The left panel in Fig. 14 shows A_V^{HLR} as a function of morphology. Ellipticals and S0s have almost no extinction, with mean $A_V^{\text{HLR}} = 0.01 \pm 0.01$, and 0.06 ± 0.07 mag, respectively. Sa, Sb, and Sc galaxies have A_V^{HLR} around 0.25 mag, and somewhat smaller (0.19 ± 0.08 mag) in Sd's.

There is no clear behavior of stellar extinction with galaxy stellar mass. In general, galaxies with $M_\star \leq 10^{11} M_\odot$ have $A_V^{\text{HLR}} = 0.2\text{--}0.3$ mag. More massive galaxies are less extinguished, and for fixed mass early types tend to have smaller A_V^{HLR} , but the dispersion is large.

5.4.2. Radial profiles

Figure 15 shows $A_V(R)$ profiles stacked by Hubble type (left panel), and mass (right). Spirals have $A_V \sim 0.2$ mag in the disk and up to 0.6 mag in the center. Their A_V profiles are similar for all Hubble types except for Sd's, where A_V does not change much from disk to center. Ellipticals and S0's also show negative A_V gradients, although at distances larger than 1 HLR they are almost dust-free. The radial profiles in different bins of M_\star (right panel) show a similar behavior to that with morphology. Except for the most massive bins, shifted to lower extinction values, all other mass-binned $A_V(R)$ profiles are similar.

⁶ The galaxy average extinction for each galaxy is calculated as the mean of all the 20 radial values obtained for each galaxy between the center and 2 HLR.

⁷ The difference between A_V^{HLR} and $\langle A_V \rangle^{\text{galaxy}}$ is -0.03 ± 0.06 , while between A_V^{HLR} and $A_V^{\text{integrated}}$ is -0.0 ± 0.1 .

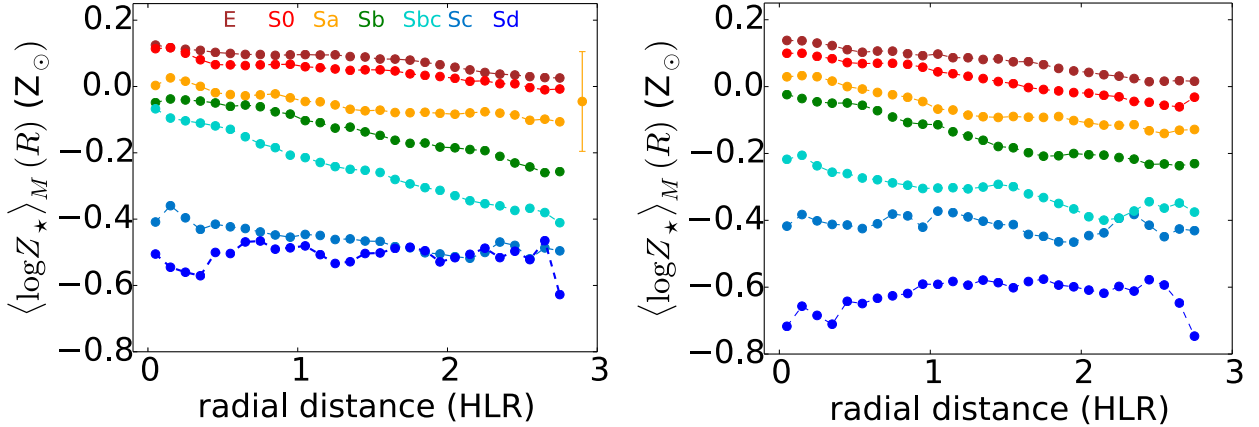


Fig. 12. Radial profiles of $\langle \log Z_* \rangle_M$ as a function of Hubble type (left) and of galaxy stellar mass (right). Mass bins are $\log M_*(M_\odot) = 9.1\text{--}9.6$, $9.6\text{--}10.1$, $10.1\text{--}10.6$, $10.6\text{--}10.9$, $10.9\text{--}11.2$, $11.2\text{--}11.5$, $11.5\text{--}11.8$. Symbols and colors are the same as Fig. 6. These results are obtained with base GMe .

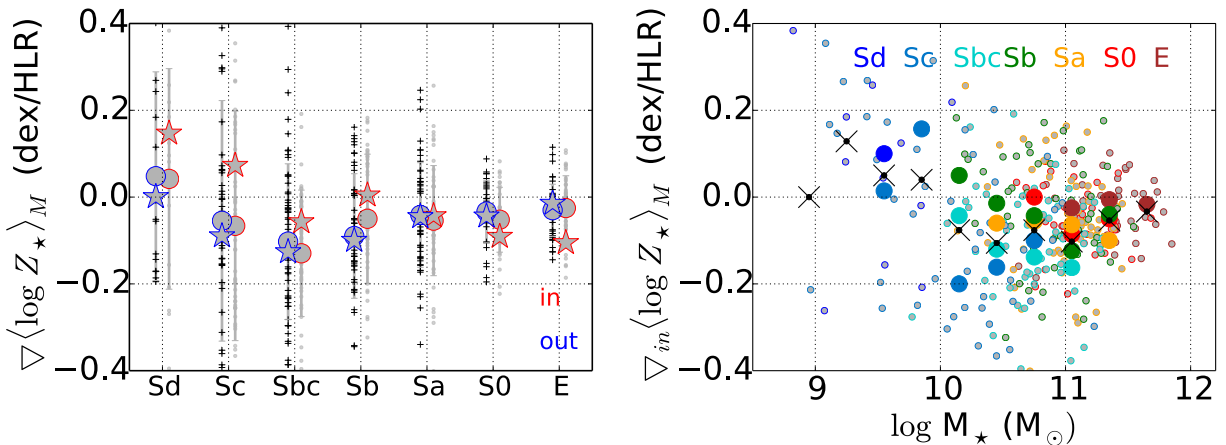


Fig. 13. Left: as Fig. 7 except for $\langle \log Z_* \rangle_M$. Right: the inner gradient as a function of the galaxy stellar mass. Symbols and colors are the same as in Fig. 7.

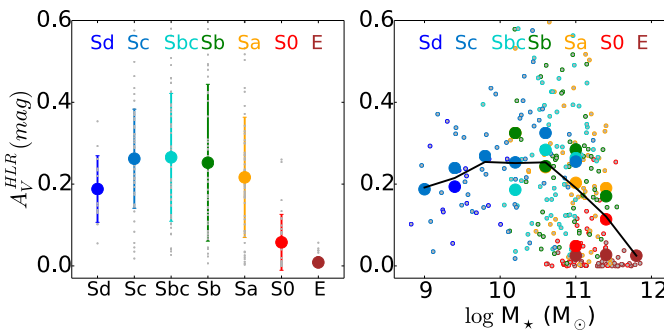


Fig. 14. A_V measured at 1HLR as function of Hubble type (left) and galaxy stellar mass (right). Symbols and colors are the same as in Fig. 5. The black line is the average $\langle \log Z_* \rangle_M$ obtained in 0.4 dex bins of $\log M_*$.

5.4.3. Radial gradients

A_V gradients are shown in Fig. 16, which is formatted as Figs. 7, 10 and 13. As for the previous properties, results for bases GMe and CBe are nearly indistinguishable, as illustrated by the overlap of circles and stars in the left panel. $\nabla_{in} A_V$ and $\nabla_{out} A_V$ show similar behavior with morphology, although the inner gradient is always higher than the outer gradient. In Ellipticals the gradient of A_V only exists in the central

region. With the exception of Sd galaxies, spirals have $\nabla_{in} A_V \sim -0.25$ mag/HLR.

On average, $\nabla_{in} A_V$ gets stronger with increasing M_* up to $10^{11} M_\odot$ (Fig. 16, right) and weakens toward higher mass, spheroid dominated systems. The dispersion with respect to the mass-binned relation (traced by the black crosses) is large, and not clearly related to morphology (coded by the colored circles).

As a whole, and despite the general trends summarized above, of the four properties analyzed in this section, A_V is the one for which tendencies with Hubble type and stellar mass are less clear. A major reason for this is that, unlike for μ_* , $\langle \log age \rangle_L$, and $\langle \log Z_* \rangle_M$, A_V estimates are sensitive to inclination effects, as explained next.

5.5. Effect of inclination on the radial profiles

An implicit hypothesis throughout the analysis presented so far is that galaxy inclination does not affect our estimates of the stellar population properties and their radial distributions. One expects this assumption to break down in the case of A_V , which should increase from face on to edge on galaxies, although it is not unreasonable to conceive that inclination effects propagate to the spectral synthesis-based estimates of stellar mass surface densities, mean ages, and metallicities. It is therefore relevant to evaluate if and how inclination affects our results.

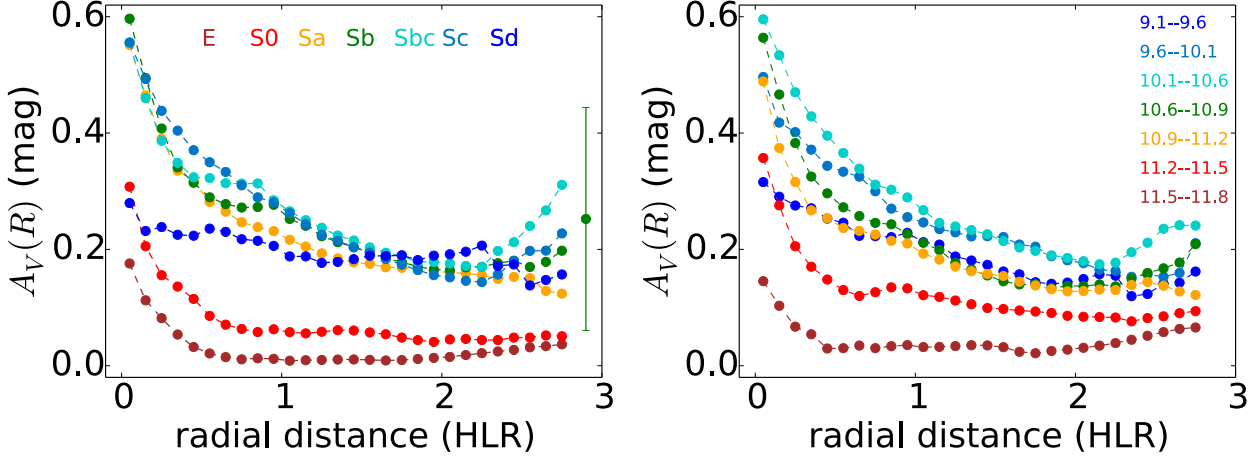


Fig. 15. Radial profiles of A_V as a function of Hubble type (*left*), and in seven bins of galaxy stellar mass (*right*). These bins are $\log M_\star(M_\odot) = 9.1$ –\$9.6\$, \$9.6\$–\$10.1\$, \$10.1\$–\$10.6\$, \$10.6\$–\$10.9\$, \$10.9\$–\$11.2\$, \$11.2\$–\$11.5\$, \$11.5\$–\$11.8\$. Symbols and colors are the same as Fig. 6. These results are obtained with base GMe .

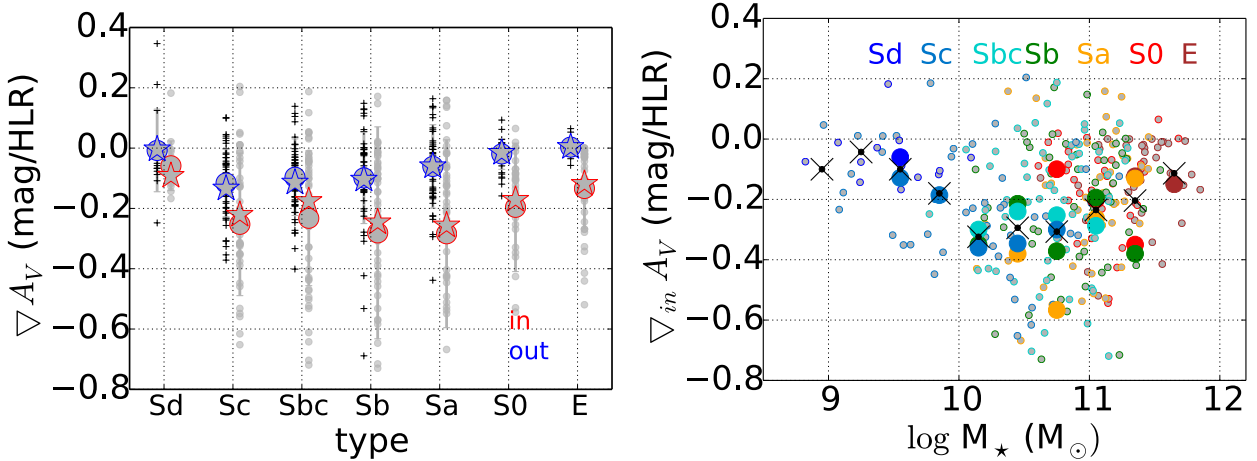


Fig. 16. *Left:* as Fig. 7 except for A_V . *Right:* the inner gradient as a function of galaxy stellar mass. Symbols and colors are the same as in Fig. 7.

In order to do so, we have divided the 300 galaxies in three subsamples on the basis of the b/a ratio (minor to major isophotal axes), as measured in SDSS R -band images. The three subsamples, each containing 100 galaxies, cover (i) $b/a \leq 0.39$, edge on; (ii) $0.39 < b/a \leq 0.63$; and (iii) $b/a > 0.63$, face on. Galaxies in each subsample were grouped by Hubble type, and their radial profiles of $\log \mu_\star$, $\langle \log \text{age} \rangle_L$, $\langle \log Z_\star \rangle_M$, and A_V averaged as previously done for the whole sample in the left panels of Figs. 6, 9, 12, and 15.

Figure 17 shows the resulting stacked profiles of $\log \mu_\star$, $\langle \log \text{age} \rangle_L$, $\langle \log Z_\star \rangle_M$, and A_V . Solid, dashed and dotted lines show profiles for the “face-on” ($b/a > 0.63$), intermediate inclination ($0.39 < b/a \leq 0.63$), and “edge-on” ($b/a \leq 0.39$) samples, respectively, and each column is for one of the seven Hubble types used throughout the paper. Average profiles were only computed for morphology-inclination bins containing at least four galaxies.

Stellar mass surface density, age, and metallicity profiles show a negligible variation among the b/a -based subsamples. This result indicates that inclination does not affect the estimates of these properties in any systematic way. Any difference is at a level not significant insofar as this paper is concerned. The exception is the $\langle \log Z_\star \rangle_M$ profiles for “edge-on” Sc’s, which differ substantially from the profiles of less inclined Sc’s. It so

happens, however, that the sub-group of $b/a \leq 0.39$ Sc’s has a mean stellar mass 0.4 dex lower than other Sc’s, which could explain their lower metallicities without implying inclination effects.

The one property that does vary systematically with b/a is A_V , and it does so in the expected sense: spirals with lower b/a have larger extinction. This is particularly evident in Sb’s. This dependence hinders the interpretation of the stacking results presented in Sect. 5.4, and explains why no clean tendencies of the A_V values and profiles with morphology and stellar mass were identified.

6. Discussion

This section is divided into four main parts. First we summarize our results in the context of related studies. We then discuss our findings in the context of the growth of galaxies – theoretical expectations, high-redshift observations, and previous results of inside-out growth for CALIFA galaxies. In the third part, we explore what the results tell us about the quenching of star formation in galaxies. Finally, we discuss the theoretical predictions for the radial variations of age and metallicity in early types and in spirals from different simulations of galaxy formation. We compare our results for variations of the radial structure in the

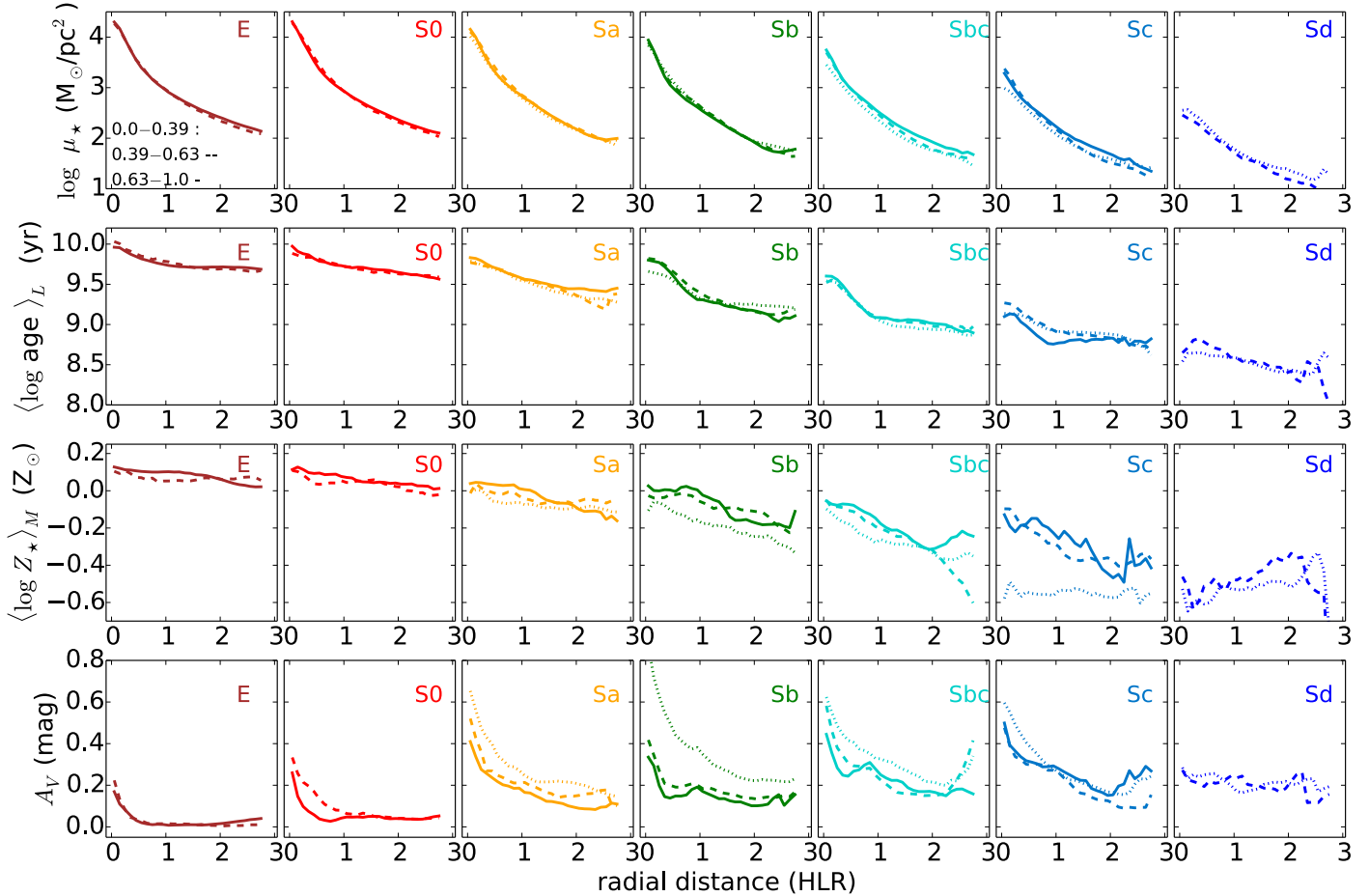


Fig. 17. Radial profiles of $\log \mu_*$, $\langle \log \text{age} \rangle_L$, $\langle \log Z_* \rangle_M$, and A_V (from the upper to the bottom panels) for the different Hubble types (from E to Sd from left to right panel) and three different bins of the ratio of minor to major photometric radius of the galaxy: solid line ($0.63 < b/a < 1.0$, face on), dashed line ($0.39 \leq b/a \leq 0.63$), and dotted line ($b/a < 0.39$, edge on).

inner ($R \leq 1$ HLR) and outer ($1 \leq R \leq 3$ HLR) parts with other observational results in the literature.

6.1. Age and metallicity of bulges and disks

The analysis of SDSS data has generated a general knowledge of how the age and metallicity of galaxies change with M_* , color, or concentration index (e.g. Kauffmann et al. 2003; Gallazzi et al. 2005; Mateus et al. 2006). These studies have confirmed that, in general, early-type galaxies are old and metal rich, while late-type galaxies are younger and more metal poor. Numerous (single spectra or longslit) studies have reported also that ellipticals are metal rich, and have a range of ages, 2–10 Gyr, which depend on stellar velocity dispersion (e.g. Trager et al. 2000; Thomas et al. 2005; Sánchez-Blázquez et al. 2006; Graves et al. 2009; Johansson et al. 2012).

Our spatially resolved analysis introduces a significant improvement in the study of the structure of galaxies. For example, we compute ages and metallicities of bulges in disk galaxies and compare them with elliptical galaxies in a systematic way, avoiding problems derived from the lack of spatial resolution prevalent in some of the previous studies.

We compute the luminosity-weighted and the mass-weighted age and metallicity: (i) in the central part of galaxies (values averaged within 0.25 HLR) as representative of the stellar population properties of bulges and central core of ellipticals;

and (ii) in the outer part of galaxies, values averaged in a ring at 1.5 ± 0.1 HLR, as representative of disks. Figure 18 plots the individual results as small dots; large dots represent the average values for each (color-coded) Hubble type, and the error bars show the dispersion. While $\langle \log \text{age} \rangle_L$ gives information about the globally “averaged” SFH, $\langle \log \text{age} \rangle_M$ informs when most of the stellar mass was formed.

Figure 18 shows that the bulges of Sa–Sb and the cores of E–S0 formed at a similar epoch; they are very old (~ 10 Gyr) and metal rich ($\gtrsim 1 Z_\odot$). Thus, they probably formed through common processes, that occurred rapidly and early on. However, the bulges in Sc–Sd galaxies (shown as the two darkest shade of blue) are younger and have a more extended SFH (both $\langle \log \text{age} \rangle_M$ and $\langle \log \text{age} \rangle_L$ are smaller), and have lower stellar metallicities. Thus, Sc–Sd galaxies formed in later times and/or with different processes.

Many bulges in late-type spirals are in fact pseudo–bulges. Unlike true bulges, pseudo–bulges are thought to grow by secular processes, where material from the disk (by the loss of angular momentum) is the main source of star formation in the central parts of these galaxies (e.g. Kormendy & Kennicutt 2004). We may see this effect at work in Figs. 9 and 12, as a flattening of the radial profiles of $\langle \log \text{age} \rangle_L$ and $\langle \log Z_* \rangle_M$, and the positive $\langle \log \text{age} \rangle_L$ gradient in the core of Sc galaxies. Some effects of the secular processes due to the disk may also be present in the bulges of Sa–Sb. For example, Fig. 18 shows that bulges of

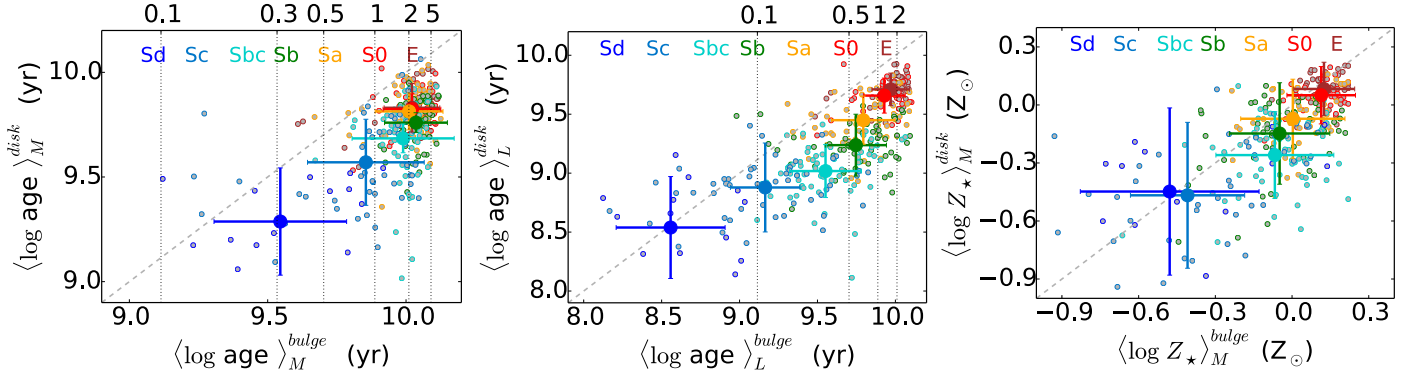


Fig. 18. Left panel: mass-weighted age at the galaxy center ($\langle \log \text{age} \rangle_M^{\text{bulge}}$) and at 1.5 HLR ($\langle \log \text{age} \rangle_M^{\text{disk}}$) for the different Hubble types. Small dots are the individual radial points, while big colored dots represent mean values for each Hubble type, with the error bars indicating the dispersion in the mean. Middle panel: as in the left panel but for the light-weighted age ($\langle \log \text{age} \rangle_L$). Right panel: as in the left panel for $\langle \log Z_* \rangle_M$. The top horizontal axes in the left and middle panels show the redshift scale. The diagonal line in the three panels is the bisector.

Sa–Sb have $\langle \log \text{age} \rangle_L \sim 6$ Gyr, younger than the 10 Gyr epoch of formation derived from $\langle \log \text{age} \rangle_M$; and this may be understood if some disk stars are rearranged into the bulges or if dissipation processes bring gas triggering new star formation in the center.

Figure 18 also shows that disks are younger and more metal poor than bulges. Both $\langle \log \text{age} \rangle_L$ and $\langle \log \text{age} \rangle_M$ are lower in disks than in their respective bulges, indicating that disks formed later than bulges, and that star formation continues for a longer time in disks than in bulges, probably as a consequence of a continuing availability of gas in disks (Roberts & Haynes 1994). This indicates a general scenario of inside-out formation.

6.2. Inside-out growth of spheroids and spirals

6.2.1. Theoretical expectations and recent results from high redshift galaxies

Models of galaxy formation predict a common inside-out view for the mass assembly in galaxies (e.g. Kauffmann et al. 1993; Aumer & White 2013). First, the bulge formed at high redshift; then, the disk was built around the bulge in the case of spirals. In the case of ellipticals, the central core formed at $z \geq 2$, and the envelope grew later through minor mergers (e.g. Oser et al. 2010; Hilz et al. 2013). Observational evidence come from the significant size evolution in early-type galaxies (ETG), which grow in size $\propto M_\star^2$ (van Dokkum et al. 2010; Patel et al. 2013).

More recently, van Dokkum et al. (2014) find evidence against the inside-out formation scenario for spirals. For a sample of MW-like spirals at redshift $z = 2.5$, they estimate the dependence of the radius with M_\star , and find that their size- M_\star relation is similar to the size- M_\star of similar galaxies at $z = 0$. They conclude that the mass growth took place in a fairly uniform way, with the galaxies increasing their mass at all radii, thus, their R_{eff} barely grows. These results seem to be supported by numerical simulation by Elmegreen et al. (2008), which find that bulges can be formed by migration of unstable disks. Other observational evidence come from the detection of clumpy star-forming disks in galaxies at $z \sim 2$ (Genzel et al. 2008; Förster Schreiber et al. 2011), which may indicate an early build up of bulges by secular evolution. Thus, studies at high redshift are providing new results that draw a complex landscape of galaxy build up. For example, Wuyts et al. (2011) also find clumpy disk star formation, but at the same time conclude that there is a Hubble sequence in place at least since $z \sim 2.5$. On the other hand, there is

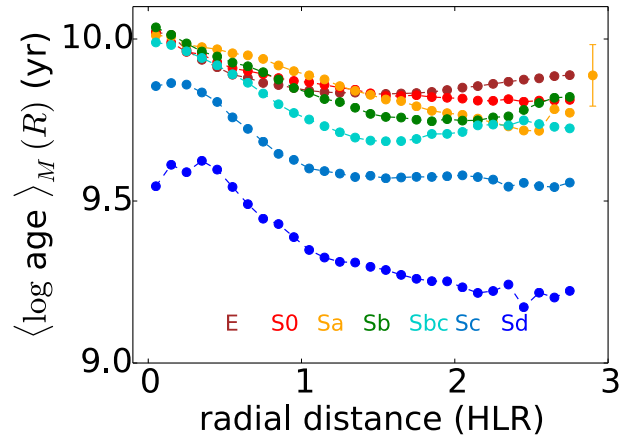


Fig. 19. Radial profiles (in units of HLR) of the mass-weighted age, $\langle \log \text{age} \rangle_M$, obtained with *GMe* base. The results are stacked by morphological type as in Fig. 7.

other evidence that galaxies rapidly assemble inside-out at $z = 1$ (Nelson et al. 2012; Szomoru et al. 2010, 2012); while Hammer et al. (2005) find evidence that MW-like galaxies have rebuilt their disk at $z \leq 1$ in a major merger epoch that drastically reshapes their bulges and disks, and is consistent with earlier cumply evolution.

In summary, there is mounting evidence of the major processes responsible for the assembly and shaping of galaxies at different epochs, and these are complemented with a variety of processes that modify the inside-out formation scenario: stellar migration, bar induced gas inflows, gas-rich minor merger, angular momentum loss due to reorientation of the disk, infall of gas with misaligned angular momentum, etc. (Aumer et al. 2014).

6.2.2. CALIFA view of the inside-out growth of galaxies

Our results favor an inside-out growth of spirals. Pérez et al. (2013) studied the stellar mass growth as a function of the radius and cosmic time in galaxies with $10^{10} \lesssim M_\star \lesssim 5 \times 10^{11} M_\odot$, and showed that the nuclei grow faster than the inner 0.5 HLR, which, in turn, grow faster than the outer 1 HLR. This conclusion is supported by the stellar age radial profiles presented in González Delgado et al. (2014c), and confirmed here in Fig. 10 for most spirals and spheroidals. Further support comes from the ratio HMR/HLR (Fig. 3), a good probe of the spatial variation of

the SFH in galaxies (González Delgado et al. 2014c). This ratio is lower than 1 (Fig. 3), a fingerprint of the inside-out growth found by Pérez et al. (2013).

Figure 19 shows how the radial profiles of $\langle \log \text{age} \rangle_M$ decrease outward for all the Hubble types. Most of the stellar mass in the center was formed 10 Gyr ago or earlier ($z \geq 2$). However, at 1.5 HLR, $\langle \log \text{age} \rangle_M$ ranges from 7 Gyr ($z \sim 1$) in E–S0 to 4.5 Gyr ($z \sim 0.4$) in Sbc, suggesting that, both early type and MW-like, galaxies have continued accreting or forming *in situ* stars in their disks until more recent times, thus supporting the inside-out scenario in these galaxies.

This trend, however, changes beyond 1.5–2 HLR, where $\langle \log \text{age} \rangle_M$ and $\langle \log \text{age} \rangle_L$ flatten. This may be interpreted as indicating that the mass was formed in a more uniformly distributed manner across the outer disk, or that stellar migration shuffles inner born stars to the outer disk, washing out the inside-out formation signs so clearly seen in the inner 1.5 HLR. In the case of E–S0, this may be understood if beyond 2 HLR most of the stellar mass in the galaxies was already accreted at $z = 1$.

6.3. Quenching

Several mechanisms have been proposed to explain the shutdown of star formation in galaxies. Halo mass quenching is one of the most popular explanations of the bimodal distribution of the properties of galaxies, and it is required to explain the green valley as a pathway towards quenching of star formation in early and late type galaxies (e.g. Schawinski et al. 2014). In this scheme, galaxies with a halo mass below a critical value (a few $\times 10^{12} M_\odot$) accrete cold gas conducive to star formation. Above this critical mass, the infalling gas reaches the sound speed and cannot form new stars (e.g. Cattaneo et al. 2006; Dekel & Birnboim 2006). The dependence with environment and clustering strongly supports this quenching mechanism (e.g. Weinmann et al. 2006; Peng et al. 2010).

The differential dependence of the stellar mass surface density (Figs. 5 and 6) with the galaxy stellar mass (a proxy of the halo mass) provides further evidence of the halo quenching (e.g. Behroozi et al. 2010). Estimating of the properties of the stellar populations in SDSS galaxies, Kauffmann et al. (2003) found that there is a critical mass ($M_\star = 3 \times 10^{10} M_\odot$, equivalent to $\sim 6 \times 10^{10} M_\odot$ for our Salpeter IMF) below which $\log \mu_\star$ scales with M_\star , and above which $\log \mu_\star$ is independent of the galaxy stellar mass. The right panels of Figs. 5 and 6 support this scenario because the radial profiles of $\log \mu_\star$ scale with $\log M_\star$, and furthermore they do so all along their extent. Our results also show that $\log \mu_\star$ saturates at high M_\star because the high-mass end of the distribution is dominated by early type galaxies (Sa–S0–E); this suggests that the spheroidal component plays a significant role in the quenching of star formation in high-mass galaxies.

The importance of morphology in the quenching of galaxies has also been reported in the literature (e.g. Bell 2008; Bell et al. 2012; Barro et al. 2013; Pan et al. 2014; Woo et al. 2015). Martig et al. (2009) found that the dependence of quenching with morphology is a consequence of the bulge-building mechanism. The steep potential well induced by the formation of a large spheroid component results in the stabilization of the disk, which cuts the supply of the gas, preventing its fragmentation into bound, star-forming clumps. Our results support this scenario, as it is explained below, because the dependence of the SFH of galaxies with the morphology.

If the halo mass is the main property responsible for quenching, we should expect that the radial structure of $\langle \log \text{age} \rangle_L$ (both,

the age values and the gradients) to change more with M_\star than with Hubble type. On the contrary, if quenching is driven by morphology, galaxies of similar stellar mass would have very different $\langle \log \text{age} \rangle_L$ structure depending on Hubble type. We explore the relevance of morphology versus M_\star in Fig. 20: age radial profiles are shown as a function of M_\star and of morphology, in four mass bins ($\log M_\star = 11.5\text{--}11.2, 11.2\text{--}10.9, 10.9\text{--}10.6, 10.6\text{--}10.1$). Clearly, morphology is the main driver: it can account for up to 0.75 dex change in age at a given mass (top panels); conversely, at a fixed morphology, mass accounts for less than 0.25 dex (bottom panels). Further, morphology accounts not only for changes in absolute values, but also for changes in the gradients at a given galaxy mass.

This confirms the similar result obtained above with $\log \mu_\star$, and it implies that galaxies of similar M_\star (equivalent to have similar M_{halo}) and with a large spheroid have shut down their star formation (outside their central core) earlier than galaxies of later morphology. These results indicate that the SFH and their radial variations are modulated primarily by galaxy morphology, and only secondarily by the galaxy mass, suggesting that the bulge formation has a relevant role in quenching the star formation in galaxies.

6.4. Radial structure of the stellar population properties in ETG and their relation with galaxy formation models

6.4.1. Theoretical predictions from cosmological simulations

Classical chemical evolution models of the formation of early-type galaxies (ETG) are based on two possible scenarios: 1) dissipative formation, the well-known monolithic collapse; and 2) the non-dissipative collapse. These scenarios produce very different radial gradients of ages and abundances, being very steep in the first case, with values of $\nabla[\text{Fe/H}] \sim -0.5$ to -1.0 [dex/dex] (Larson 1974, 1975; Carlberg 1984)⁸, but (almost) flat when there are pure stellar mergers. This second case may even erase a previously existing radial gradient.

The most recent cosmological simulations propose a two-phase formation scenario for ETG's in which the central core formed at $z \geq 2$, and the envelope grows after this through minor mergers (e.g. Naab et al. 2009; Oser et al. 2012; Hilz et al. 2012; Navarro-González et al. 2013). As follows: 1) galaxies assemble their mass through dissipative processes and star formation occurs *in situ*. Starbursts formed at the center as a consequence, for example, of large major mergers or monolithic collapse. The star formation is induced by cold flow of accretion or by gas-rich mergers. 2) Galaxies grow in size by mass assembly through the external accretion of satellites; ex situ star formation formed by dry mergers of galaxies toward the central most massive galaxies.

Observationally, there is evidence of a significant size evolution in ETG. The growth of the galaxy size with M_\star^2 supports this proposal. A transition region is expected between the *in situ* central core of ETG and *ex situ* outer regions. Since the central core of these ETG is enriched very quickly due to major mergers at high redshift ($z \geq 2$), and the satellites that are accreted are less metal rich than the central massive galaxies, a negative radial gradient of the metallicity is expected, even with a change of the slope in the transition region. Thus, values as $\nabla[\text{Fe/H}] = -0.5$ [dex/dex] (Pipino et al. 2010) or $\nabla[\text{Fe/H}] = -0.3$ [dex/dex] (Kawata & Gibson 2003) are predicted.

⁸ The metallicity gradient measured in spheroids is traditionally calculated as $\Delta[\text{Fe/H}]/\Delta \log r$ and expressed in [dex/dex] units.

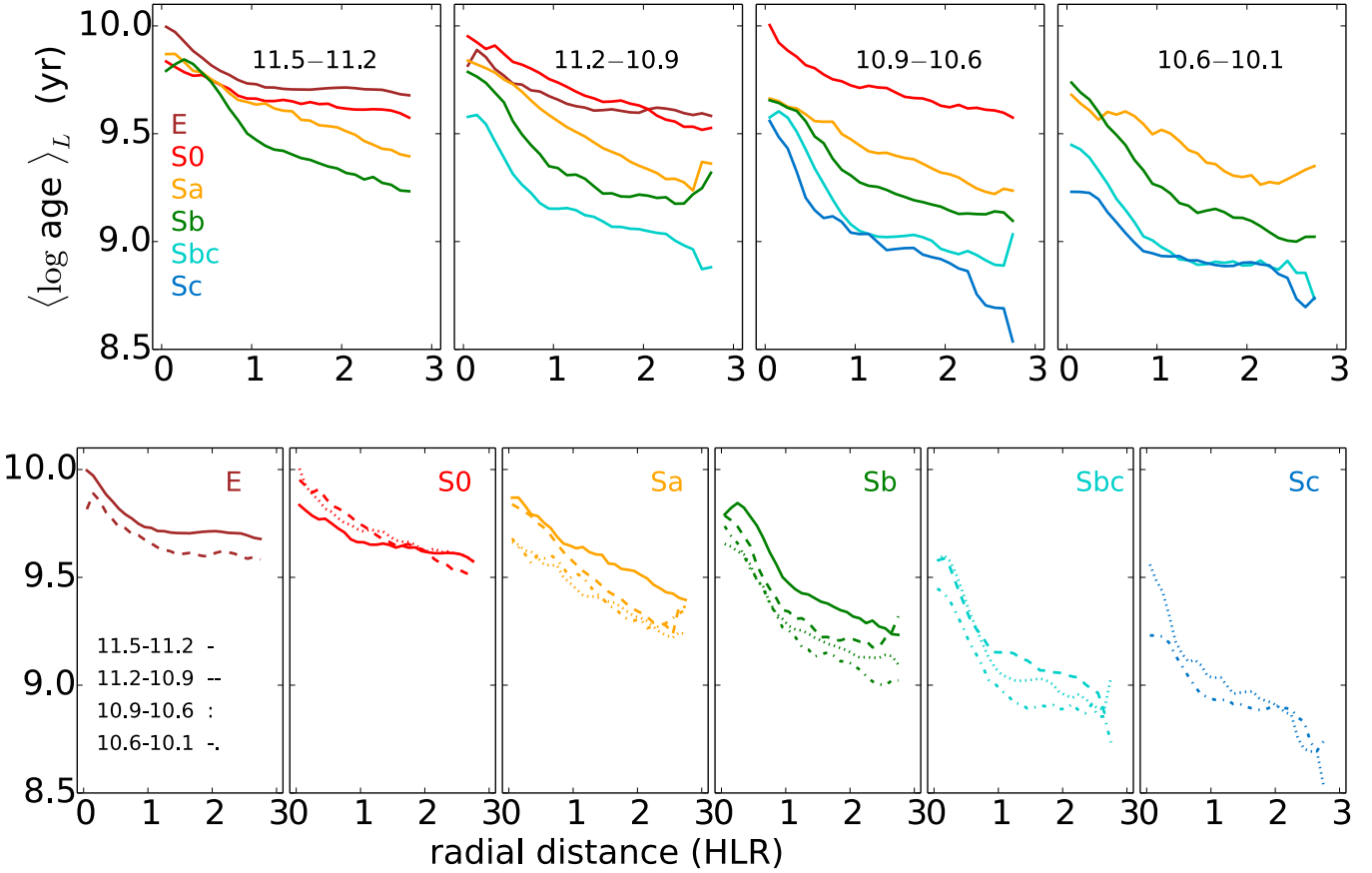


Fig. 20. Radial profiles of $\langle \log \text{age} \rangle_L$ (upper panel) in four galaxy stellar mass bins. From left to right: $\log M_\star(M_\odot) = 11.2 - 11.5$ (continuum line), $10.9 - 11.2$ (dashed line), $10.6 - 10.9$ (dashed-point line), $10.1 - 10.6$ (dotted line). In each panel, the average profile for each Hubble type is plotted if more than four galaxies have galaxy stellar mass in the $\log M_\star$ bin. Bottom: each panel shows the radial profile of each Hubble type averaged in each of the four $\log M_\star(M_\odot)$ bins.

However, the merger history may change an existing radial gradient: while dry major mergers can flatten the pre-existing gradient (Kobayashi 2004; Di Matteo et al. 2009; Hopkins et al. 2009), dry minor mergers can steepen the metallicity gradient. Thus, Kobayashi (2004) SPH chemodynamical simulations of elliptical galaxies which include radiative cooling, star formation and feedback from SNII-Ia, and chemical enrichment (but do not include kinematic feedback), found that the steep negative radial metallicity gradient, established during the initial starburst at $z \geq 2$, can flatten significantly by later major-mergers in the galaxy. Following these simulations, the average gradient at the present time is $\nabla[\text{Fe}/\text{H}] = -0.3$ [dex/dex], but it may decrease to a value of -0.2 [dex/dex] when major mergers appear.

Beside the merger history, feedback can change the inner and outer metallicity gradients. Thus, a strong AGN feedback can stop the star formation in the central core of massive galaxies, flattening the inner gradients. Feedback from in situ star formation can alter the outer metallicity gradient. Also, the existence of galactic winds may modify the composition of the ISM in a galaxy. Hirschmann et al. (2015) performed cosmological simulations, which include an empirical model for the momentum driven galactic winds, to investigate the dependence of the age and metallicity outer gradients with metal cooling and galactic winds; in principle, required to explain the mass-metallicity relation, MZR. These simulations including winds predict $\nabla[\text{Fe}/\text{H}] = -0.33$ [dex/dex], steeper than the simulations without winds that predict $\nabla[\text{Fe}/\text{H}] = -0.11$ [dex/dex]. The main explanation is that in wind models the stars accreted

are of lower metallicity than in the simulations with no winds. In both cases, however, they predict a positive *age* gradient of $\sim 0.03 - 0.04$ [dex/dex].

6.4.2. Implications from this work and comparison with other results from the literature

Following our own results, E and S0 have formed their central core at similar cosmic time since they have similar central ages (see Fig. 18). Further they must have formed through similar processes since their radial profiles of $\log \mu_\star$, $\langle \log \text{age} \rangle_L$, and $\langle \log Z_\star \rangle_M$ are remarkably similar. They both show small but negative $\langle \log \text{age} \rangle_L$, and $\langle \log Z_\star \rangle_M$ gradients in the central core. In the central 1 HLR, E and S0 in our sample have $\nabla \langle \log Z_\star \rangle_M \sim -0.1$ [dex/dex] (std = 0.15)⁹. Slightly steeper, $\nabla \langle \log Z_\star \rangle_M = -0.2$ [dex/dex], when CBe models are used. These are within the range of values found in other studies based on long-slit or IFS data up to one effective radius (e.g. Mehrt et al. 2003; Sánchez-Blázquez et al. 2007; Annibali et al. 2007; Rawle et al. 2008; Spolaor et al. 2010; Kuntschner et al. 2010). However, they are shallow compared with theoretical expectations if minor mergers are relevant in growing up the central core of E and S0 galaxies. This may indicate that major mergers are more likely the main process building the central regions (up to 1 HLR) of ETGs.

⁹ Our gradients, which are measured in a linear scale, are converted here to a logarithmic scale to be compared with predictions from simulations and other works in the literature.

Between 1 and 3 HLR, the radial profile of $\langle \log Z_\star \rangle_M$ is of similar slope or slightly shallower than in the inner 1 HLR. We do not find any evidence of a transition region where the metallicity radial profile steepens to metallicities below solar. If the 1 to 3 HLR envelope of ETG had grown through the accretion of low-mass satellites a steepening of metallicity would be expected, as explained before, because the mass-metallicity relation implies that low-mass satellites would be of low metallicity. In our results there is no evidence either of an inversion of the age radial profile toward older ages beyond 1–2 HLR, as expected if these satellites were formed very early on like the core of E and S0 (see Figs. 9 and 18). These results are in contrast with recent results by Greene et al. (2012, 2013): for a sample of ~ 30 early type galaxies they find at $2 R_{\text{eff}}$ an old (10 Gyr) stellar population with $[\text{Fe}/\text{H}] \sim -0.5$, and interpret this as the stellar outskirts of these galaxies being built up through minor mergers. Coccato et al. (2010), La Barbera et al. (2012), Montes et al. (2014) observing a few massive ellipticals reported a decline of the metallicity to under solar in an old stellar population in their outskirts ($\geq 10 R_{\text{eff}}$) suggesting that these galaxies are formed in two phases, the central core through major mergers, and through minor mergers farther out. However, other recent works show examples of ETG with an old and metal-rich stellar population and a very shallow metallicity gradient up to $3 R_{\text{eff}}$ (Trujillo et al. 2014) in contrast with the results by Greene et al. (2012, 2013).

Our results do not support the minor merger scenario for the size growth of ETG. Thus, the ages $\langle \log \text{age} \rangle_L \sim 9.7$ (yr) and metallicity $\langle \log Z_\star \rangle_M \sim Z_\odot$ at 1–3 HLR, and the shallow metallicity gradient, $\nabla \langle \log Z_\star \rangle_M \sim -0.1$ [dex/dex], that we obtain are more consistent with the growth of the 1–3 HLR envelope of ETGs through major mergers.

Another interesting result reported in the literature that can be compared with ours is the correlation between the metallicity gradient and the galaxy mass (or stellar velocity dispersion, σ_\star) found for E and S0. Spolaor et al. (2010) have found that the relation between σ_\star and the metallicity gradient shows two regimes of behavior: (i) for galaxies with $\log \sigma_\star \leq 2.2 \text{ km s}^{-1}$, the metallicity gradient steepens with σ_\star ; (ii) galaxies with $\log \sigma_\star > 2.2 \text{ km s}^{-1}$ (the most massive ellipticals), have a metallicity gradient that does not correlate with σ_\star (or galaxy mass), with a mean value ~ -0.15 [dex/dex]. On the other hand, Pastorello et al. (2014) derive the $[\text{Z}/\text{H}]$ gradient in the outer 1–2.5 R_{eff} of a sample of ellipticals, and they find that the gradient covers a wide range of values, from negative very steep (~ -2) to flat or even positive; these values correlate with the galaxy stellar mass and stellar velocity dispersion, with galaxies of lower M_\star (or σ_\star) having the steeper metallicity gradient. However, the most massive galaxies exhibit the flattest gradients and an average value of $\nabla \langle \log Z_\star \rangle_M \sim -0.2$ [dex/dex] (std = 0.38) for galaxies with $M_\star \geq 10^{11} M_\odot$. Both works show a significant scatter in the $\nabla \langle \log Z_\star \rangle_M - M_\star$ relation for $M_\star \geq 10^{11} M_\odot$, and reasonable doubts of the existence of the correlation for high-mass ellipticals.

Our results (Fig. 13) indicate that there is no correlation between the metallicity gradient and M_\star for the CALIFA early-type galaxies (E and S0). Even so, our results are compatible with Spolaor et al. (2010) and Pastorello et al. (2014) because E and S0 in our sample are all above $10^{11} M_\odot$ (and $\sigma_\star > 100 \text{ km s}^{-1}$), for which no correlation is found between the metallicity gradient and M_\star in Spolaor et al. (2010) or Pastorello et al. (2014). We find that CALIFA ellipticals have a shallow gradient. This behavior is also in agreement with Hirschmann et al. (2013) simulations and their interpretation of the lack of correlation between the metallicity gradient and M_\star in massive

ellipticals. Following these authors, massive galaxies accrete higher mass satellites, and because of their deeper potential well they retain their own gas against stellar winds, producing a shallower metallicity gradient in the outer regions of massive ellipticals.

Because the metallicity at 2–3 HLR in E and S0 are similar to the metallicity in the bulge of early spirals, and the stars at these distances are as old as the bulges of Sa–Sb galaxies (see Fig. 9), the 1–3 HLR envelope of early-type galaxies might have built from the centers of early-type spirals. In summary, the negative but shallow gradients of the metallicity and ages suggest that massive ($M_\star \geq 10^{11} M_\odot$) early-type galaxies built their inner 3 HLR through mergers with massive and metal-rich spirals.

6.5. Radial structure of the stellar population properties in spirals and their relation with galaxy formation models

New insights into the structure of the Milky Way disk, in particular through the measurements of chemical abundances of large sample of stars, are provided by the spectroscopic surveys undertaken in recent times (e.g., SEGUE, RAVE, Gaia-ESO survey, HERMES, APOGEE, LAMOST, etc.; Yanny et al. 2009; Steinmetz et al. 2006; Gilmore et al. 2012; Zucker et al. 2012; Majewski et al. 2010; Zhao et al. 2012). Radial Velocity Experiment (Steinmetz et al. 2006; Boeche et al. 2014, RAVE;) is studying the radial and vertical chemical gradients using a very large sample of dwarf stars. Close to the Galactic plane, RAVE shows a negative radial gradient of Fe abundance, $-0.054 \text{ dex/kpc}^{10}$, which becomes flatter or even positive when measured above the disk. So, the $[\text{Fe}/\text{H}]$ gradient ranges from -0.039 to $+0.047 \text{ dex/kpc}$ when measured at heights 0.4–0.8 kpc, or 1.2–2 kpc above the Galactic plane, respectively.

The radial gradient of abundances in the different regions of a spiral galaxy are important because they are directly related to the formation process. Obviously, not all scenarios of disk/spiral formation are valid, since it is necessary that they produce a radial gradient of abundances in the disk but not in the halo, as observed in the MW and in M 31. Thus, the formation of the halo from different fragments or minor mergers with very short free fall times does not create a radial gradient but a dispersion of abundances, and therefore it was concluded early on that the MW halo may be formed from mergers or from the accretion of low-mass galaxies (or part of them). However, disks are more likely formed from a single cloud falling on and from inside out.

6.5.1. Theoretical predictions from “classical” chemical evolution models

Most classical chemical evolution models claim that the infall of gas with a radial dependence, implying an inside-out scenario for the disk formation, is essential to reproduce the observed radial gradient of abundances. The key ingredient is the dependence of the disk infall time scale with the radial distance, which makes the gas to accumulate faster in the inner disk. Since the star formation rate depends on the gas density, these assumptions produce a radial dependence of the star formation rate and a negative radial metallicity gradient (Ferrini et al. 1994; Molla et al. 1996; Chiappini et al. 2001; Mollá & Díaz 2005). Thus Molla et al. (1996) give a value -0.08 for a MW-like galaxy, reproducing the value found by Shaver et al. (1983) and other H regions studies. Chiappini et al. (2001) models predict a gradient

¹⁰ The metallicity gradient in disks is traditionally calculated as $\Delta [\text{Fe}/\text{H}] / \Delta r$, and expressed in dex/kpc.

of -0.04 dex/kpc for a MW-like galaxy. In fact, as theoretical equations show (Goetz & Koeppen 1992), the radial gradient of abundances appears in the disk when there is an adequate ratio between star formation rate to infall rate. It also implies, therefore, that a dependence of the radial gradient on the morphological type of galaxies may exist. Molla et al. (1996) models already predicted radial gradients for galaxies of different morphological types, with values in the range -0.025 (for a M 31-like galaxy) to -0.183 dex kpc $^{-1}$ (for a late type galaxy like NGC 300). More recent works (Mollá & Díaz 2005) calculate models in which the infall rate was a function of the mass distribution (or rotation curve) of the galaxy, assuming a stronger radial dependence of the infall timescales than in Chiappini et al. (2001). Moreover Mollá & Díaz (2005) models also depend on an efficiency factor to condense the molecular gas, and to convert the gas reservoir into stars. The metallicity gradients range -0.02 to -0.15 dex kpc $^{-1}$ with flat gradients for galaxies with the largest efficiency factor, or the most massive galaxies, although in the extreme end the low-mass and lowest efficiencies models also show flat radial distributions. Thus, the steepest gradients appear in the intermediate-mass or intermediate-type galaxies. However, there is no dependence on the morphological type when the gradient is normalized to a characteristic value, such as the effective radius, as recent results by CALIFA have found based on HII regions abundances (Sánchez et al. 2013).

6.5.2. Theoretical predictions from cosmological simulations

Recently, hydrodynamical cosmological simulations have provided evidence in support of the imposed inside-out disk growth scenario adopted within the “classical” chemical evolution models. Like spheroidals, spirals are formed in two phases. In the first phase, the bulge formed in a similar way as the core of E-S0. In the second phase, the disk grows by star formation in situ from the infalling gas (Kauffmann et al. 1993; Aumer & White 2013). Metal poor gas with higher angular momentum at lower redshifts is turned into stars at larger radii. Negative radial metallicity gradients are expected, as the classical models predict. This assumption is a natural outcome of the mass, momentum, and energy conservation laws imposed in the simulations of disks in a cosmological context (Brook et al. 2011, 2012; Few et al. 2012; Pilkington et al. 2012a,b; Gibson et al. 2013).

Pilkington et al. (2012a) examined a set of 25 simulations, from several groups, using different codes and initial conditions (Stinson et al. 2010; Rahimi et al. 2011; Kobayashi & Nakasato 2011; Few et al. 2012) to predict the present-day metallicity gradient in MW-like galaxies and its evolution. Although the evolution of the simulated metallicity gradients depends strongly on the choice of the subgrid physics employed, most of the simulated galaxies tend to a similar present-day gradient of ~ -0.05 dex kpc $^{-1}$, in agreement with the Chiappini et al. (2001) and Mollá & Díaz (2005) models for normal galaxies as the MW.

6.5.3. Implications from this work

Our findings show that spiral galaxies (excluding Sd) have negative radial gradients as indicative of the inside-out growth of the disk (see Fig. 12). The average $\nabla_{\text{out}} \langle \log Z_{\star} \rangle_M$ for spirals (excluding Sd and later type) is -0.08 dex/HLR or -0.02 dex/kpc. These values are compatible with the results obtained by Sánchez-Blázquez et al. (2014), which have already derived the metallicity gradients for 62 CALIFA face-on spiral galaxies to study the effect of bars on the properties of the stellar

populations. For these galaxies, they find a metallicity gradient of -0.025 dex/kpc (std = 0.05), equal (-0.027 dex/kpc) to the gradient that we derive for the same group of galaxies.

To compare the RaDES simulated galaxies (Few et al. 2012) with our results, 19 galaxies of the Pilkington et al. (2012a) sample, have been analyzed, measuring the HLR and the gradients in a similar way as we have done with the CALIFA galaxies (Ruiz-Lara, in prep.; Ruiz-Lara et al., priv. comm.). However, these 19 simulated galaxies analyzed cover a narrow range of morphologies, mainly Sbc–Sc, in comparison with CALIFA. Therefore, these results cannot be extrapolated to the full work presented here, but they are representative of the state-of-art of cosmological simulations of disk galaxies, and can be used to compare them to similar disks from our observations. Mock B-band images are used to derive the HLR and to perform a bulge-disk decomposition used as a proxy for the morphology. Metallicities are calculated for disk particles using Eq. (2) and the gradient is derived between 0–1 HLR and also between 1 and 2 HLR. The stellar metallicity and age gradients of the simulated galaxies are compatible with the results presented here. Keeping in mind that the morphological range covered by these simulations is rather narrow and that they use B/D as a proxy for a morphological classification, the results show a slight dependence of $\nabla_{\text{out}} \langle \log Z_{\star} \rangle_M$ with B/D ratio, with a steeper slope for B/D = 1 (Sbc galaxies) for which $\nabla_{\text{out}} \langle \log Z_{\star} \rangle_M \sim -0.1$ dex/HLR. Later type spirals have a flatter gradient of $\nabla_{\text{out}} \langle \log Z_{\star} \rangle_M \sim -0.046$ dex/HLR. These results go in line with those found here, namely, that the metallicity radial gradient of spirals shows a dependence on morphology, with the steepest gradient found in the intermediate Sb–Sbc spirals (see Figs. 12 and 13). However, a larger set of cosmological simulations is required covering from early Sa to late Sd, and a large range of galaxy masses (from 10^9 to $10^{11} M_{\odot}$), to confirm the general trend found here. On the other hand, these results indicate that the feedback recipes used in these simulations are able to recover realistic galaxies with small bulges and are fully in agreement with the work presented here.

Furthermore, our results are also compatible with classical chemical models, and certainly, the CALIFA Sb–Sbc galaxies have stellar metallicity gradients (-0.025 dex/kpc) in the range observed in the MW disk, but somewhat shallower than the [Fe/H] gradient measured in the Galactic disk. However, it is necessary to take into account that the gradient usually given in the literature is obtained for young stars or HII regions, while here it is an average value obtained for all stellar populations existing in the studied galaxy or region. Besides that, the number of objects has increased compared with the old studies and, more importantly, all of them have been self-consistently analyzed using the same reduction technique and spectral models.

In any case our results favor an inside-out growth of spirals. This conclusion is supported by the stellar age radial profiles presented here: the age decreases outwards for all Hubble types studied¹¹. Beyond 1.5–2 HLR the radial distribution of ages flattens, suggesting that the mass forms more uniformly in those regions, or that the stellar mixing brings stars born in the inner disk to the outskirts. This last possibility has been recently investigated by Minchev et al. (2013, 2014), who have performed N-body hydrodynamical models with the chemical evolution implementation (Minchev et al. 2013, 2014). They simulated MW-like galaxies with the aim to investigate whether the Galactic disk can be understood as a single structure with kinematic and chemical features that are continuously distributed,

¹¹ Sd galaxies, however, show a much flatter age gradient.

being the thin and thick disks two extreme cases of these structures. Furthermore, they investigate the effect of stellar migration and kinematic heating in the scatter of the age-metallicity relation, and how it changes with the Galactic radius. In fact, an increase of the scatter in the age-metallicity relation and a flattening of the stellar metallicity gradient is produced by the stellar radial migration, which causes a radial mixing in the older stellar population and creating the appearance of a flatter gradient in early times, leading to a decoupling of the stellar population from their birth interstellar medium (Roškar et al. 2008). These results also indicate that even though radial mixing has a significant effect in flattening the metallicity gradient, it can not destroy the negative gradient.

7. Summary and conclusions

We analyzed the stellar population properties of 300 galaxies, observed by CALIFA with the V500 and V1200 gratings and IFU PPak at the 3.5 m telescope of Calar Alto, to investigate the trends in the stellar populations properties with radial distance as a function of Hubble type and galaxy stellar mass. The sample includes ellipticals, S0, and spirals from early (Sa–Sb) to late types (Sc–Sd). They cover a stellar mass range from 0.7×10^9 to $7 \times 10^{11} M_\odot$ if Salpeter IMF is assumed, and a factor 1.78 (0.25 dex) lower for a Chabrier IMF. A full spectral fitting analysis was performed using the `y` code and a combination of SSP spectra from González Delgado et al. (2005), Vazdekis et al. (2010), or Charlot & Bruzual (2007, priv. comm.). Our pipeline `y` is used to process the spectral fitting results to produce present day maps of the spatial distribution of the stellar population properties. For each galaxy, these maps are azimuthally averaged to produce radial profiles (in units of the half light radius, HLR: a_{50}^L) of the stellar mass surface density ($\log \mu_*$), stellar ages (light-weighted, $\langle \log \text{age} \rangle_L$, and mass-weighted, $\langle \log \text{age} \rangle_M$), metallicity ($\langle \log Z_* \rangle_M$), and extinction (A_V). The radial profiles are stacked as a function of Hubble type and of galaxy mass. Radial gradients of these properties measured within the inner 1 HLR and between 1 and 2 HLR are also obtained.

Our main results are:

1. *Spatially averaged vs. integrated galaxy properties:* the metallicity, $\langle \log Z_* \rangle_M$, galaxy-wide spatially averaged matches the metallicity obtained from the integrated spectrum, and the metallicity at $R = 1$ HLR. This result is equivalent to that obtained for the other stellar population properties, $\log \mu_*$, $\langle \log \text{age} \rangle_L$, and A_V , as reported by González Delgado et al. (2014c,b), proving that effective radii are indeed effective.
2. *Mass-weighted size:* we confirm our earlier finding (González Delgado et al. 2014c) that galaxies are more compact in mass than in light by $\sim 20\%$. The HMR/HLR ratio shows a dual distribution with Hubble type, that breaks the galaxies with the smaller HMR/HLR in the Sb–Sbc. This ratio also shows a dual dependence with M_* : it decreases with increasing mass for disk galaxies, and becomes almost constant in spheroidal galaxies. These results are a signpost of the inside-out growth previously found by Pérez et al. (2013).
3. *Stellar mass surface density:* $\log \mu_*(R)$ shows declining profiles that scale with morphology and with M_* ; this behavior

is preserved at any given distance. At constant M_* , $\log \mu_*(R)$ is higher in early-type than in late-type spirals. E and S0 show equal $\log \mu_*(R)$ profiles, independently of M_* . The inner gradient, $\nabla_{\text{in}} \log \mu_*$, correlates with Hubble type. The negative gradients steepen from late type spirals to spheroids, as well as with galaxy total mass in galaxies with $M_* \leq 10^{11} M_\odot$. At a constant M_* , $\nabla_{\text{in}} \log \mu_*$ steepens with morphology, with E and S0 having the steepest gradients. These results indicate that morphology, and not only M_* , plays a relevant role in defining μ_* , and the $\mu_* - M_*$ relation.

4. *Stellar ages:* $\langle \log \text{age} \rangle_L(R)$ shows declining profiles that scale with morphology; this behavior is preserved at any given distance. Early-type spirals are always older than late spirals. E and S0, although older than spirals, both have similar $\langle \log \text{age} \rangle_L(R)$ profiles, indicating that these galaxies have similar SFH. The more massive are also the older galaxies; this “downsizing” behavior is always preserved at any given distance. The negative $\nabla_{\text{in}} \langle \log \text{age} \rangle_L$ depends on Hubble type in different ways: steeper from E and S0 to Sbc, and shallower from Sbc to Sd. Thus, Milky Way-like galaxies have the steepest age gradient. A $\nabla_{\text{in}} \langle \log \text{age} \rangle_L - M_*$ relation exists, increasing the gradient from the low mass galaxies (which have roughly flat profiles) up to about $10^{11} M_\odot$, at this point the trend reverses and $\nabla_{\text{in}} \langle \log \text{age} \rangle_L$ decreases with increasing M_* . However, the dispersion in the $\nabla_{\text{in}} \langle \log \text{age} \rangle_L - M_*$ relation and $\langle \log \text{age} \rangle_L^{\text{HLR}} - M_*$ is significant and it is strongly related to the morphology. Even more, the dispersion of the $\langle \log \text{age} \rangle_L(R)$ profiles of galaxies of equal mass is significant and larger than between the $\langle \log \text{age} \rangle_L(R)$ profiles of galaxies of different M_* but the same Hubble type. Thus, the SFHs and their radial variations are modulated primarily by the Hubble type, with mass playing a secondary role.
5. *Stellar metallicity:* $\langle \log Z_* \rangle_M(R)$ shows mildly decreasing profiles for most Hubble types, except Sd that show little, if any, radial dependence. Milky Way-like galaxies (Sbc) stand out as those with the steepest radial profiles. $\langle \log Z_* \rangle_M(R)$ scales with M_* similar to the way as it scales with the morphology. This can be understood as a consequence of the global mass metallicity relation, which is a primary dependence of the metallicity with M_* . The metallicity gradients are negative but shallow on average, with $\nabla_{\text{in}} \langle \log Z_* \rangle_M \sim -0.1$ dex/HLR, and show a small dependence with M_* up to $M_* \sim 10^{11} M_\odot$, steepening with increasing mass. Above $10^{11} M_\odot$ (Sa’s, S0’s and E’s) they have similar metallicity gradient. The dispersion in the $\nabla_{\text{in}} \langle \log Z_* \rangle_M - M_*$ relation is significant and a trend with morphology is seen, in the sense that, for a given mass, intermediate-type spirals are those with steeper gradients.
6. *Stellar extinction:* all the galaxies show $A_V(R)$ declining profiles, but do not have a clear trend with morphology or with galaxy mass. Most spirals show similar radial variations, and similar average extinction, $A_V \sim 0.2$ mag at the disk and up to 0.6 mag in the center, with the inner gradient $\nabla_{\text{in}} A_V \sim -0.25$ mag/HLR. However, Sd galaxies show a shallow central gradient. E and S0 also show a negative gradient in the inner 1 HLR (shallower than in early-type spirals), but they are almost dust free out of the core. On average, $\nabla_{\text{in}} A_V$ gets stronger with increasing M_* up to $10^{11} M_\odot$, and weakens toward higher mass. However, the dispersion with respect to

the binned mass relation is not related to Hubble type. A major reason for this is that $A_V(R)$ profiles are sensitive to inclination effects, unlike μ_* , $\langle \log \text{age} \rangle_L$, or $\langle \log Z_* \rangle_M$. Thus, spirals with larger inclination have larger extinction. This is particularly evident in Sb that have the largest A_V^{HLR} and the steepest central gradient.

From these results, we conclude that:

- Evidence in favor of the inside-out growth of galaxies is found in the negative radial stellar age gradients. Metallicity gradients and the fact that galaxies are more compact in mass than in light also support this scenario. On the other hand, the flattening of the $\langle \log \text{age} \rangle_L(R)$ profiles beyond 1.5–2 HLR may be interpreted as indicative that the mass was formed in a more uniformly distributed manner across the outer disk of spirals. In the case of E and S0 this may be understood if beyond 2 HLR most of the stellar mass was accreted at $z = 1$.
- The mean stellar ages of disks and bulges are correlated with disks covering a large range of ages, and late-type spirals hosting the younger disks. The bulges of S0 and early type spirals are old and metal rich as the core of E. They formed with similar processes, through mergers. Later-type spirals, however, have younger bulges, and larger contributions from secular evolution are expected. Disks are younger and more metal poor than bulges, as an indicative of the inside-out formation scenario of these galaxies.
- S0 in this sample (all are massive galaxies) act as a transition class between E and spirals, with $\mu_*(R)$, $\langle \log \text{age} \rangle_L(R)$, and $A_V(R)$ between massive E and Sa. The gradient in μ_* and $\langle \log \text{age} \rangle_L$ of S0 is so similar to Sa galaxies that they can result from the same formation process.
- The Hubble type rather M_* drives differences in the galaxy averaged ages, and radial age gradients. These results indicate that the SFH and their radial variations are modulated primarily by galaxy morphology, and only secondarily by the galaxy mass. This suggests that galaxies are morphologically quenched and that the shutdown of star formation occurs outward and earlier in galaxies with a large spheroid than in galaxies of later Hubble type.

From the comparison of the results with the theoretical predictions from cosmological simulations, we conclude:

- Major mergers are likely the main process in building the central regions of ETGs. The metallicity gradient within 1 HLR is shallow compared with the theoretical expectation of whether minor mergers are relevant in the growth of the central core of E's and S0's. In our results there is no evidence either of an inversion of $\langle \log \text{age} \rangle_L$ toward older ages beyond 1–2 HLR, or of a steepening of the metallicity if these galaxies were growing in size through minor dry mergers. Massive galaxies probably accreted massive satellites that were able to retain their metal rich gas against winds, producing flatter metallicity gradients (Hirschmann et al. 2015). Alternatively, the flattening of the metallicity radial profile can result from the quenching of star formation. When this happens, the metal cycle stops and only stars of that last star formation event remain.

– Through the negative metallicity gradients, spirals show evidence of growing inside-out. These gradients are flatter than the predictions by the classical chemical evolution models (e.g. Chiappini et al. 2001; Mollá & Díaz 2005), but are similar to those measured above the Galactic disk. The largest gradient happens in intermediate types and intermediate galaxy mass, as predicted by the Mollá & Díaz (2005) models. However, Sbc galaxies have a $\langle \log Z_* \rangle_M$ gradient similar to the predictions by RaDES simulations (Few et al. 2012; Pilkington et al. 2012a). This indicates that the feedback recipes used in these simulations are able to recover realistic galaxies with small bulges. However, a larger set of cosmological simulations is required, covering from early-type Sa to late Sd, and a large range of galaxy mass (from 10^9 to $10^{11} M_\odot$), to confirm the general trend with the Hubble type found in this work.

Thanks to the uniqueness of the CALIFA data in terms of spatial coverage and resolution, large sample spanning all morphological types, and homogeneity and quality of the spectral analysis, we are able to characterize the radial structure of the stellar population properties of galaxies in the local universe. The results show that the Hubble sequence is a useful scheme to organize galaxies by their spatially resolved stellar density, ages, and metallicity; however, stellar extinction cannot discriminate between the different Hubble types so well. Stellar mass, although responsible for setting the average stellar population properties in galaxies, is less responsible for the quenching processes. Morphology is, however, more strongly connected with the shut down of the star formation activity in the bulges and disks of galaxies.

Acknowledgements. CALIFA is the first legacy survey carried out at Calar Alto. The CALIFA collaboration would like to thank the IAA-CSIC and MPIA-MPG as major partners of the observatory, and CAHA itself, for the unique access to telescope time and support in manpower and infrastructures. We also thank the CAHA staff for the dedication to this project. Support from the Spanish Ministerio de Economía y Competitividad, through projects AYA2010-15081 (PI R.G.D.), and Junta de Andalucía FQ1580 (PI R.G.D.), AYA2010-22111-C03-03, and AYA2010-10904E (S.F.S.). We also thank the Viabilidad, Diseño, Acceso y Mejora funding program, ICTS-2009-10, for funding the data acquisition of this project. R.C.F. thanks the hospitality of the IAA and the support of CAPES and CNPq. R.G.D. acknowledges the support of CNPq (Brazil) through Programa Ciencia sem Fronteiras (401452/2012-3). A.G. acknowledges support from EU FP7/2007-2013 under grant agreement n.267251 (AstroFit) and from the EU Marie Curie Integration Grant “SteMaGE” Nr. PCIG12-GA-2012-326466. C.J.W. acknowledges support through the Marie Curie Career Integration Grant 303912. E.P. acknowledges support from the Guillermo Haro program at INAOE. Support for L.G. is provided by the Ministry of Economy, Development, and Tourism’s Millennium Science Initiative through grant IC120009, awarded to The Millennium Institute of Astrophysics, MAS. L.G. acknowledges support by CONICYT through FONDECYT grant 3140566. J.I.P. acknowledges financial support from the Spanish MINECO under grant AYA2010-21887-C04-01 and from Junta de Andalucía Excellence Project PEX2011-FQM7058. I.M., J.M. and A.d.O. acknowledge support from the project AYA2013-42227-P. RAM is funded by the Spanish program of International Campus of Excellence Moncloa (CEI). J.M.A. acknowledges support from the European Research Council Starting Grant (SEDmorph; P.I. V. Wild).

References

- Alongi, M., Bertelli, G., Bressan, A., et al. 1993, *A&AS*, **97**, 851
 Annibali, F., Bressan, A., Rampazzo, R., Zeilinger, W. W., & Danese, L. 2007, *A&A*, **463**, 455
 Arribas, S., Colina, L., Monreal-Ibero, A., et al. 2010, in Galaxy Wars: Stellar Populations and Star Formation in Interacting Galaxies, eds. B. Smith, J. Higdon, S. Higdon, & N. Bastian, *ASP Conf. Ser.*, **423**, 317
 Asari, N. V., Cid Fernandes, R., Stasińska, G., et al. 2007, *MNRAS*, **381**, 263
 Aumer, M., & White, S. D. M. 2013, *MNRAS*, **428**, 1055
 Aumer, M., White, S. D. M., & Naab, T. 2014, *MNRAS*, **441**, 3679

- Bacon, R., Copin, Y., Monnet, G., et al. 2001, *MNRAS*, **326**, 23
- Barro, G., Faber, S. M., Pérez-González, P. G., et al. 2013, *ApJ*, **765**, 104
- Behroozi, P. S., Conroy, C., & Wechsler, R. H. 2010, *ApJ*, **717**, 379
- Bell, E. F. 2008, *ApJ*, **682**, 355
- Bell, E. F., van der Wel, A., Papovich, C., et al. 2012, *ApJ*, **753**, 167
- Bershady, M. A., Verheijen, M. A. W., Swaters, R. A., et al. 2010, *ApJ*, **716**, 198
- Blanc, G. A., Weinzierl, T., Song, M., et al. 2013, *AJ*, **145**, 138
- Blanton, M. R., & Moustakas, J. 2009, *ARA&A*, **47**, 159
- Boeche, C., Siebert, A., Piffl, T., et al. 2014, *A&A*, **568**, A71
- Bournaud, F., Jog, C. J., & Combes, F. 2007, *A&A*, **476**, 1179
- Bressan, A., Fagotto, F., Bertelli, G., & Chiosi, C. 1993, *A&AS*, **100**, 647
- Brook, C. B., Governato, F., Roškar, R., et al. 2011, *MNRAS*, **415**, 1051
- Brook, C. B., Stinson, G. S., Gibson, B. K., et al. 2012, *MNRAS*, **426**, 690
- Bruzual, G., & Charlot, S. 2003, *MNRAS*, **344**, 1000
- Cappellari, M., & Copin, Y. 2003, *MNRAS*, **342**, 345
- Cappellari, M., Emsellem, E., Krajnović, D., et al. 2011, *MNRAS*, **413**, 813
- Cappellari, M., McDermid, R. M., Alatalo, K., et al. 2013, *MNRAS*, **432**, 1862
- Cardelli, J. A., Clayton, G. C., & Mathis, J. S. 1989, *ApJ*, **345**, 245
- Carlberg, R. G. 1984, *ApJ*, **286**, 416
- Cattaneo, A., Dekel, A., Devriendt, J., Guiderdoni, B., & Blaizot, J. 2006, *MNRAS*, **370**, 1651
- Chabrier, G. 2003, *PASP*, **115**, 763
- Charbonnel, C., Meynet, G., Maeder, A., Schaller, G., & Schaerer, D. 1993, *A&AS*, **101**, 415
- Chiappini, C., Matteucci, F., & Romano, D. 2001, *ApJ*, **554**, 1044
- Cid Fernandes, R., Mateus, A., Sodré, L., Stasińska, G., & Gomes, J. M. 2005, *MNRAS*, **358**, 363
- Cid Fernandes, R., Pérez, E., García Benito, R., et al. 2013, *A&A*, **557**, A86
- Cid Fernandes, R., González Delgado, R. M., García Benito, R., et al. 2014, *A&A*, **561**, A130
- Coccato, L., Gerhard, O., & Arnaboldi, M. 2010, *MNRAS*, **407**, L26
- De Lucia, G., Springel, V., White, S. D. M., Croton, D., & Kauffmann, G. 2006, *MNRAS*, **366**, 499
- Dekel, A., & Birnboim, Y. 2006, *MNRAS*, **368**, 2
- Di Matteo, P., Pipino, A., Lehnert, M. D., Combes, F., & Semelin, B. 2009, *A&A*, **499**, 427
- Elmegreen, D. M., Elmegreen, B. G., Ravindranath, S., & Coe, D. A. 2007, *ApJ*, **658**, 763
- Elmegreen, B. G., Bournaud, F., & Elmegreen, D. M. 2008, *ApJ*, **688**, 67
- Fagotto, F., Bressan, A., Bertelli, G., & Chiosi, C. 1994a, *A&AS*, **104**, 365
- Fagotto, F., Bressan, A., Bertelli, G., & Chiosi, C. 1994b, *A&AS*, **105**, 29
- Falcón-Barroso, J., Sánchez-Blázquez, P., Vazdekis, A., et al. 2011, *A&A*, **532**, A95
- Ferrini, F., Molla, M., Pardi, M. C., & Diaz, A. I. 1994, *ApJ*, **427**, 745
- Few, C. G., Gibson, B. K., Courty, S., et al. 2012, *A&A*, **547**, A63
- Förster Schreiber, N. M., Shapley, A. E., Erb, D. K., et al. 2011, *ApJ*, **731**, 65
- Gallazzi, A., Charlot, S., Brinchmann, J., White, S. D. M., & Tremonti, C. A. 2005, *MNRAS*, **362**, 41
- García-Benito, R., Zibetti, S., Sánchez, S. F., et al. 2015, *A&A*, **576**, A135
- Genzel, R., Burkert, A., Bouché, N., et al. 2008, *ApJ*, **687**, 59
- Gibson, B. K., Pilkington, K., Brook, C. B., Stinson, G. S., & Bailin, J. 2013, *A&A*, **554**, A47
- Gilmore, G., Randich, S., Asplund, M., et al. 2012, *The Messenger*, **147**, 25
- Girardi, L., Bressan, A., Chiosi, C., Bertelli, G., & Nasi, E. 1996, *A&AS*, **117**, 113
- Girardi, L., Bressan, A., Bertelli, G., & Chiosi, C. 2000, *A&AS*, **141**, 371
- Goetz, M., & Koeppen, J. 1992, *A&A*, **262**, 455
- González Delgado, R. M., Cerviño, M., Martins, L. P., Leitherer, C., & Hauschildt, P. H. 2005, *MNRAS*, **357**, 945
- González Delgado, R. M., Cid Fernandes, R., García-Benito, R., et al. 2014a, *ApJ*, **791**, L16
- González Delgado, R. M., García-Benito, R., Pérez, E., et al. 2014b, Highlights of Spanish Astrophysics VIII, Proc. XI Scientific Meeting of the Spanish Astronomical Society held on September 8–12, in Teruel, Spain, eds. A. J. Cenarro, F. Figueras, C. Hernández-Monteagudo, J. Trujillo Bueno, & L. Valdvielso, 220
- González Delgado, R. M., Pérez, E., Cid Fernandes, R., et al. 2014c, *A&A*, **562**, A47
- Graham, A. W., & Worley, C. C. 2008, *MNRAS*, **388**, 1708
- Graves, G. J., Faber, S. M., & Schiavon, R. P. 2009, *ApJ*, **698**, 1590
- Greene, J. E., Murphy, J. D., Comerford, J. M., Gebhardt, K., & Adams, J. J. 2012, *ApJ*, **750**, 32
- Greene, J. E., Murphy, J. D., Graves, G. J., et al. 2013, *ApJ*, **776**, 64
- Hammer, F., Flores, H., Elbaz, D., et al. 2005, *A&A*, **430**, 115
- Hilz, M., Naab, T., Ostriker, J. P., et al. 2012, *MNRAS*, **425**, 3119
- Hilz, M., Naab, T., & Ostriker, J. P. 2013, *MNRAS*, **429**, 2924
- Hirschmann, M., Naab, T., Davé, R., et al. 2013, *MNRAS*, **436**, 2929
- Hirschmann, M., Naab, T., Ostriker, J. P., et al. 2015, *MNRAS*, **449**, 528
- Hopkins, P. F., Cox, T. J., Younger, J. D., & Hernquist, L. 2009, *ApJ*, **691**, 1168
- Hopkins, P. F., Quataert, E., & Murray, N. 2011, *MNRAS*, **417**, 950
- Husemann, B., Jahnke, K., Sánchez, S. F., et al. 2013, *A&A*, **549**, A87
- Johansson, J., Thomas, D., & Maraston, C. 2012, *MNRAS*, **421**, 1908
- Kauffmann, G., White, S. D. M., & Guiderdoni, B. 1993, *MNRAS*, **264**, 201
- Kauffmann, G., Heckman, T. M., White, S. D. M., et al. 2003, *MNRAS*, **341**, 54
- Kawata, D., & Gibson, B. K. 2003, *MNRAS*, **340**, 908
- Kelz, A., Verheijen, M. A. W., Roth, M. M., et al. 2006, *PASP*, **118**, 129
- Kobayashi, C. 2004, *MNRAS*, **347**, 740
- Kobayashi, C., & Nakasato, N. 2011, *ApJ*, **729**, 16
- Kormendy, J., & Kennicutt, Jr., R. C. 2004, *ARA&A*, **42**, 603
- Kuntschner, H., Emsellem, E., Bacon, R., et al. 2010, *MNRAS*, **408**, 97
- La Barbera, F., Ferreras, I., de Carvalho, R. R., et al. 2012, *MNRAS*, **426**, 2300
- Larson, R. B. 1974, *MNRAS*, **166**, 585
- Larson, R. B. 1975, *MNRAS*, **173**, 671
- Le Borgne, J.-F., Bruzual, G., Pelló, R., et al. 2003, *A&A*, **402**, 433
- Madau, P., & Dickinson, M. 2014, *ARA&A*, **52**, 415
- Majewski, S. R., Wilson, J. C., Hearty, F., Schiavon, R. R., & Skrutskie, M. F. 2010, in IAU Symp. 265, eds. K. Cunha, M. Spite, & B. Barbuy, 480
- Martig, M., Bournaud, F., Teyssier, R., & Dekel, A. 2009, *ApJ*, **707**, 250
- Martins, L. P., González Delgado, R. M., Leitherer, C., Cerviño, M., & Hauschildt, P. 2005, *MNRAS*, **358**, 49
- Mateus, A., Sodré, L., Cid Fernandes, R., et al. 2006, *MNRAS*, **370**, 721
- Mehlert, D., Thomas, D., Saglia, R. P., Bender, R., & Wegner, G. 2003, *A&A*, **407**, 423
- Minchev, I., Chiappini, C., & Martig, M. 2013, *A&A*, **558**, A9
- Minchev, I., Chiappini, C., Martig, M., et al. 2014, *ApJ*, **781**, L20
- Mollá, M., & Díaz, A. I. 2005, *MNRAS*, **358**, 521
- Molla, M., Ferrini, F., & Diaz, A. I. 1996, *ApJ*, **466**, 668
- Montes, M., Trujillo, I., Prieto, M. A., & Acosta-Pulido, J. A. 2014, *MNRAS*, **439**, 990
- Naab, T., Johansson, P. H., & Ostriker, J. P. 2009, *ApJ*, **699**, L178
- Navarro-González, J., Ricciardelli, E., Quilis, V., & Vazdekis, A. 2013, *MNRAS*, **436**, 3507
- Nelson, E. J., van Dokkum, P. G., Brammer, G., et al. 2012, *ApJ*, **747**, L28
- Ocvirk, P., Pichon, C., Lançon, A., & Thiébaut, E. 2006, *MNRAS*, **365**, 74
- Oser, L., Ostriker, J. P., Naab, T., Johansson, P. H., & Burkert, A. 2010, *ApJ*, **725**, 2312
- Oser, L., Naab, T., Ostriker, J. P., & Johansson, P. H. 2012, *ApJ*, **744**, 63
- Pan, Z., Li, J., Lin, W., Wang, J., & Kong, X. 2014, *ApJ*, **792**, L4
- Panter, B., Jimenez, R., Heavens, A. F., & Charlot, S. 2008, *MNRAS*, **391**, 1117
- Pastorello, N., Forbes, D. A., Foster, C., et al. 2014, *MNRAS*, **442**, 1003
- Patel, S. G., van Dokkum, P. G., Franx, M., et al. 2013, *ApJ*, **766**, 15
- Peng, Y.-j., Lilly, S. J., Kovač, K., et al. 2010, *ApJ*, **721**, 193
- Pérez, E., Cid Fernandes, R., González Delgado, R. M., et al. 2013, *ApJ*, **764**, L1
- Pilkington, K., Few, C. G., Gibson, B. K., et al. 2012a, *A&A*, **540**, A56
- Pilkington, K., Gibson, B. K., Brook, C. B., et al. 2012b, *MNRAS*, **425**, 969
- Pipino, A., D’Ercole, A., Chiappini, C., & Matteucci, F. 2010, *MNRAS*, **407**, 1347
- Rahimi, A., Kawata, D., Allende Prieto, C., et al. 2011, *MNRAS*, **415**, 1469
- Rawle, T. D., Smith, R. J., Lucey, J. R., & Swinbank, A. M. 2008, *MNRAS*, **389**, 113
- Roberts, M. S., & Haynes, M. P. 1994, *ARA&A*, **32**, 115
- Rosales-Ortega, F. F., Kennicutt, R. C., Sánchez, S. F., et al. 2010, *MNRAS*, **405**, 735
- Roth, M. M., Kelz, A., Fechner, T., et al. 2005, *PASP*, **117**, 620
- Roškar, R., Debattista, V. P., Quinn, T. R., Stinson, G. S., & Wadsley, J. 2008, *ApJ*, **684**, L79
- Sánchez, S. F., Kennicutt, R. C., Gil de Paz, A., et al. 2012, *A&A*, **538**, A8
- Sánchez, S. F., Rosales-Ortega, F. F., Jungwiert, B., et al. 2013, *A&A*, **554**, A58
- Sánchez-Blázquez, P., Peletier, R. F., Jiménez-Vicente, J., et al. 2006, *MNRAS*, **371**, 703
- Sánchez-Blázquez, P., Forbes, D. A., Strader, J., Brodie, J., & Proctor, R. 2007, *MNRAS*, **377**, 759
- Sánchez-Blázquez, P., Ocvirk, P., Ocvirk, P., Gibson, B. K., Pérez, I., & Peletier, R. F. 2011, *MNRAS*, **415**, 709
- Sánchez-Blázquez, P., Rosales-Ortega, F. F., Méndez-Abreu, J., et al. 2014, *A&A*, **570**, A6
- Schaerer, D., Charbonnel, C., Meynet, G., Maeder, A., & Schaller, G. 1993, *A&AS*, **102**, 339
- Schaller, G., Schaerer, D., Meynet, G., & Maeder, A. 1992, *A&AS*, **96**, 269
- Schawinski, K., Urry, C. M., Simmons, B. D., et al. 2014, *MNRAS*, **440**, 889
- Shaver, P. A., McGee, R. X., Newton, L. M., Danks, A. C., & Pottasch, S. R. 1983, *MNRAS*, **204**, 53
- Silk, J., & Rees, M. J. 1998, *A&A*, **331**, L1

- Spolaor, M., Kobayashi, C., Forbes, D. A., Couch, W. J., & Hau, G. K. T. 2010, *MNRAS*, **408**, 272
- Springel, V., White, S. D. M., Jenkins, A., et al. 2005, *Nature*, **435**, 629
- Steinmetz, M., Zwitter, T., Siebert, A., et al. 2006, *AJ*, **132**, 1645
- Stinson, G. S., Bailin, J., Couchman, H., et al. 2010, *MNRAS*, **408**, 812
- Szomoru, D., Franx, M., van Dokkum, P. G., et al. 2010, *ApJ*, **714**, L244
- Szomoru, D., Franx, M., & van Dokkum, P. G. 2012, *ApJ*, **749**, 121
- Thomas, D., Maraston, C., Bender, R., & Mendes de Oliveira, C. 2005, *ApJ*, **621**, 673
- Trager, S. C., Faber, S. M., Worthey, G., & González, J. J. 2000, *AJ*, **120**, 165
- Trujillo, I., Ferré-Mateu, A., Balcells, M., Vazdekis, A., & Sánchez-Blázquez, P. 2014, *ApJ*, **780**, L20
- van Dokkum, P. G., Whitaker, K. E., Brammer, G., et al. 2010, *ApJ*, **709**, 1018
- van Dokkum, P. G., Bezanson, R., van der Wel, A., et al. 2014, *ApJ*, **791**, 45
- Vazdekis, A., Sánchez-Blázquez, P., Falcón-Barroso, J., et al. 2010, *MNRAS*, **404**, 1639
- Verheijen, M. A. W., Bershady, M. A., Andersen, D. R., et al. 2004, *Astron. Nachr.*, **325**, 151
- Walcher, C. J., Wisotzki, L., Bekeraïtē, S., et al. 2014, *A&A*, **569**, A1
- Weinmann, S. M., van den Bosch, F. C., Yang, X., & Mo, H. J. 2006, *MNRAS*, **366**, 2
- Woo, J., Dekel, A., Faber, S. M., & Koo, D. C. 2015, *MNRAS*, **448**, 237
- Wuyts, S., Förster Schreiber, N. M., van der Wel, A., et al. 2011, *ApJ*, **742**, 96
- Yanny, B., Rockosi, C., Newberg, H. J., et al. 2009, *AJ*, **137**, 4377
- Zhao, G., Zhao, Y.-H., Chu, Y.-Q., Jing, Y.-P., & Deng, L.-C. 2012, *RA&A*, **12**, 723
- Zucker, D. B., de Silva, G., Freeman, K., Bland-Hawthorn, J., & Hermes Team 2012, in Galactic Archaeology: Near-Field Cosmology and the Formation of the Milky Way, eds. W. Aoki, M. Ishigaki, T. Suda, T. Tsujimoto, & N. Arimoto, *ASP Conf. Ser.*, **458**, 421
-
- ¹ Instituto de Astrofísica de Andalucía (CSIC), PO Box 3004, 18080 Granada, Spain
e-mail: rosa@iaa.es
- ² Departamento de Física, Universidade Federal de Santa Catarina, PO Box 476, 88040-900 Florianópolis, SC, Brazil
- ³ Instituto de Astronomía, Universidad Nacional Autónoma de México, A.P. 70-264, 04510 México, Mexico
- ⁴ Departamento de Investigación Básica, CIEMAT, Avda. Complutense 40, 28040 Madrid, Spain
- ⁵ Departamento de Física Teórica y del Cosmos, University of Granada, Facultad de Ciencias (Edificio Mecenas), 18071 Granada, Spain
- ⁶ Depto. de Física Teórica, Universidad Autónoma de Madrid, 28049 Madrid, Spain
- ⁷ Leibniz-Institut für Astrophysik Potsdam (AIP), An der Sternwarte 16, 14482 Potsdam, Germany
- ⁸ University of Vienna, Türkenschanzstrasse 17, 1180 Vienna, Austria
- ⁹ Instituto de Astrofísica de Canarias (IAC), 38205 La Laguna, Tenerife, Spain
- ¹⁰ Sydney Institute for Astronomy, The University of Sydney, NSW 2006, Australia
- ¹¹ Millennium Institute of Astrophysics and Departamento de Astronomía, Universidad de Chile, Casilla 36-D, 1058 Santiago, Chile
- ¹² Departamento de Astronomía, Universidad de Chile, Casilla 36-D, 1058 Santiago, Chile
- ¹³ INAF–Osservatorio Astrofisico di Arcetri, Largo Enrico Fermi 5, 50125 Firenze, Italy
- ¹⁴ European Southern Observatory, Karl-Schwarzschild-Str. 2, 85748 Garching b. München, Germany
- ¹⁵ Estación Experimental de Zonas Aridas (CSIC), Ctra. de Sacramento s/n, La Cañada, 04120 Almería, Spain
- ¹⁶ Department of Physics 4-181 CCIS, University of Alberta, Edmonton AB T6G 2E1, Canada
- ¹⁷ Australian Astronomical Observatory, PO BOX 296, Epping, 1710 NSW, Australia
- ¹⁸ CEI Campus Moncloa, UCM-UPM, Departamento de Astrofísica y CC. de la Atmósfera, Facultad de CC. Físicas, Universidad Complutense de Madrid, Avda. Complutense s/n, 28040 Madrid, Spain
- ¹⁹ Instituto de Cosmología, Relatividade e Astrofísica – ICRA, Centro Brasileiro de Pesquisas Físicas, Rua Dr. Xavier Sigaud 150, CEP 22290-180 Rio de Janeiro, RJ, Brazil
- ²⁰ School of Physics and Astronomy, University of St. Andrews, North Haugh, St. Andrews, KY169SS, UK
- ²¹ Landessternwarte, Zentrum fur Astronomie der Universität Heidelberg, Königstuhl 12, 69117 Heidelberg, Germany

Pages 25 to 44 are available in the electronic edition of the journal at <http://www.aanda.org>

Appendix A: Improvements resulting from the new reduction pipeline

The quality of the fits to CALIFA version 1.3c spectra was assessed in Cid Fernandes et al. (2014) by averaging $R_\lambda = O_\lambda - M_\lambda$ residual spectra of 107 galaxies ($\sim 10^5$ spectra). Inspection of these residuals revealed low amplitude (a few %) but systematic features related to unmasked weak emission lines, SSP deficiencies, and data calibration imperfections. This exercise needs updating now that the reduction pipeline has changed to version 1.5.

Figure A.1 summarizes the results of this re-evaluation. The plots show stacked $R_\lambda = O_\lambda - M_\lambda$ residual spectra, in units of the median flux in the 5635 ± 45 Å window. The top panel shows results for the nuclear extractions, while the middle and bottom panels are built using spectra from zones within radial distances $R = 0\text{--}1$ and $1\text{--}2$ half light radius (HLR, computed in the same wavelength range), respectively. Residuals are colored according with the Hubble type of the galaxies. When all galaxies are stacked, the residuals are colored according with the spatial zone extracted. These subdivisions are presented to get a sense of how the residuals relate to position within a galaxy and its Hubble type, which are two central aspects of this paper.

No matter which panel one looks at, the improvement with respect to version 1.3c is evident to the eye when compared

to figure 13 of Cid Fernandes et al. (2014). The broad trough around $H\beta$ present in the 1.3c spectra, for instance, is much shallower now. In fact, it is confined to late types (compare blue and red lines in the lower panel in Fig. A.1), indicating that its origin is related to calibration, and also to the SSP spectra of young stellar populations (as previously reported by Cid Fernandes et al. 2005 for SDSS data). Residuals are also visibly smaller towards the blue, including the CaII K line, which is now well fitted whereas in version 1.3c a small systematic residual subsisted¹². The humps around 5800 Å, on the other hand, are still present in version 1.5, particularly noticeable for outer regions, indicating that further refinement of the sky subtraction are warranted.

In short, the spectral fits have improved substantially with the new reduction pipeline. We attribute this to the updated sensitivity curve used in version 1.5. A more extended discussion of these and other aspects of the data reduction are presented in García-Benito et al. (2015).

Despite these changes, the stellar population properties derived from the spectral fits did not change much in comparison to those obtained for version 1.3c data. The most noticeable changes were in mean ages, which become 0.1 dex older, and extinction, which is now 0.2 mag smaller on a global average.

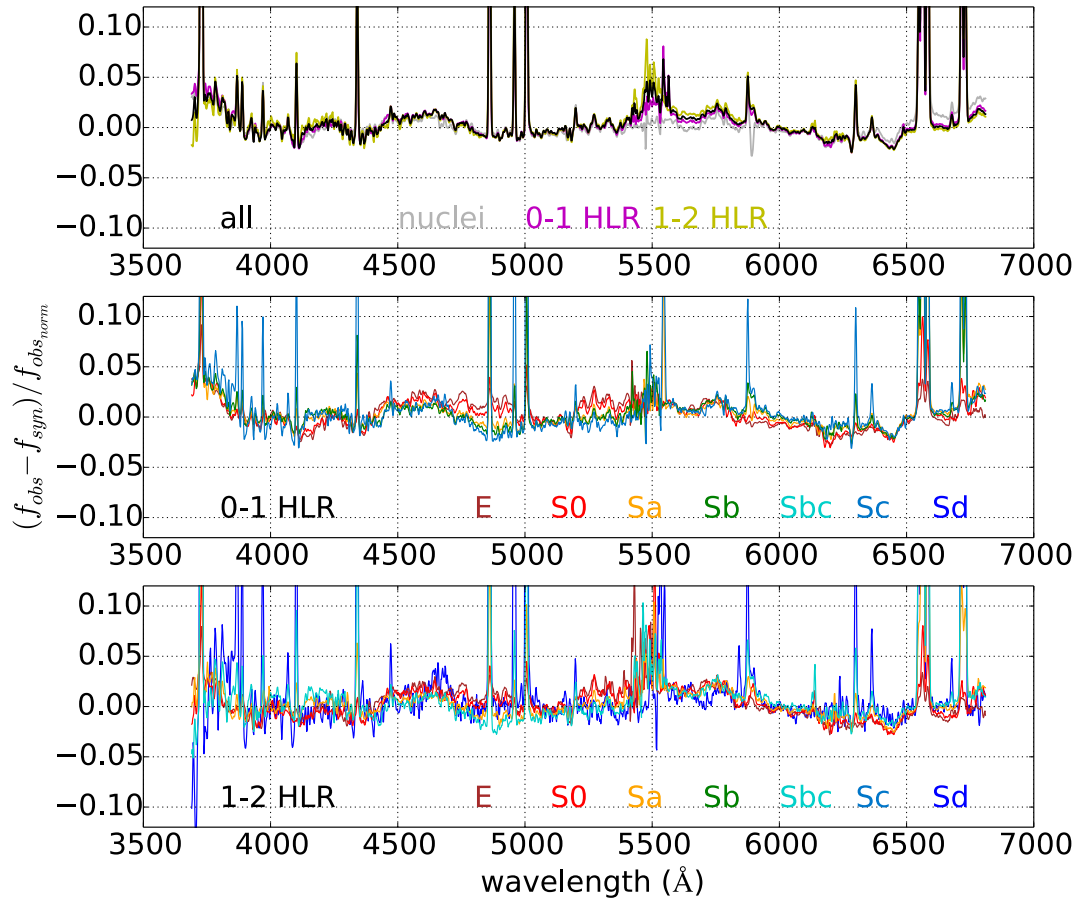


Fig. A.1. *Upper panel:* residual spectra averaged for all the spectra (black line), nuclei (grey line) and spectra belonging to zones that are between 0–1 HLR (pink line) and between 1–2 HLR (yellow line). *Middle panel:* residual spectra averaged for zones inner to 1 HLR and for Hubble type. *Bottom panel:* as in the *middle panel* except for spectra of zones located between 1 and 2 HLR.

¹² Because of this improvement, our fits now start at 3700 Å, whereas in previous articles in this series only the $\lambda > 3800$ Å range was considered.

Appendix B: Base experiments and uncertainties due to SSP templates

To derive the stellar population properties of these 300 CALIFA galaxies we have fitted ~ 253000 spectra with the *GMe* and *CBe* using the cluster Grid-CSIC at the Instituto de Astrofísica de Andalucía and the cluster Alphacrucis at IAG-USP São Paulo. Examples of the quality of the spectral fits as a function of the Hubble type and radial distance are presented in Fig. A.1.

B.1. Mass-metallicity relation

Here we want to find out how well our metallicity definitions follow a MZR which guarantees that galaxies like the MW or Andromeda ($\log M_\star(M_\odot) \sim 11$) have solar metallicity at the disk, while LMC-SMC-like galaxies ($\log M_\star(M_\odot) \sim 9$) have $\sim 1/4 Z_\odot$. We do this with mass-weighted and luminosity-weighted definitions of Eqs. (2) and (3), and with the two sets of SSP models (*GMe* or *CBe*).

Similarly, the correlation between the galaxy averaged stellar metallicities and the metallicity measured at 1 HLR, and the MZR, guarantee that the metallicity radial profiles scale with the galaxy stellar mass. However, the MZR in González Delgado et al. (2014a) was derived using the galaxy averaged stellar metallicity instead of the metallicity measured at 1 HLR, and using the mass-weighted definition of the metallicity and only the results with the base *GMe*. For these reasons, we derive the MZR that results from using the mass-weighted and the light-weighted definition of the metallicity, and the *GMe* and *CBe* bases.

Figure B.1 shows the correlation of M_\star and $\langle \log Z_\star \rangle_M^{\text{HLR}}$ (upper panels), and $\langle \log Z_\star \rangle_L^{\text{HLR}}$ (lower panels) for the *GMe* (left panels) and *CBe* (right panels) SSP models. The mass-metallicity relation found by Panter et al. (2008) and Gallazzi et al. (2005) are the magenta and brown lines, respectively¹³. Note that in the four cases, the metallicities are well in the range of the dispersion given by Gallazzi et al. (2005); brown dashed line represent the 16th and 84th percentiles of their distribution. To compare the general trend of these values, we derived a smoothed mass-binned relation, represented by a solid black or grey-black line. As expected from the global MZR derived in González Delgado et al. (2014a), base *GMe* and $\langle \log Z_\star \rangle_M$ predict stellar metallicities for MW and LMC-SMC with the expected values. But $\langle \log Z_\star \rangle_L$ gives a MZR that predict higher metallicities. The opposite happens for the MZR using the base *CBe*, which gives mass-weighted metallicities higher on average than the SDSS metallicities. But the MZR with $\langle \log Z_\star \rangle_L$ goes close to the Gallazzi et al. (2005) relation, and also predicts stellar metallicities for MW-Andromeda-like and LMC-SMC galaxies with the expected values.

In summary, $\langle \log Z_\star \rangle_M$ with *GMe* and $\langle \log Z_\star \rangle_L$ with *CBe* provide a mass-metallicity relation similar to the SDSS MZR, and predict metallicities between -0.7 and -0.4 dex for galaxies with mass between $\sim 10^9$ and $10^{10} M_\odot$, the expected values for LMC and SMC-like galaxies, and solar for MW-like galaxies.

B.2. Variations over bases *GMe* and *CBe*

Although the two sets of models are built with the same stellar libraries (*MILES* and), base *GMe* stops at $1.5 Z_\odot$,

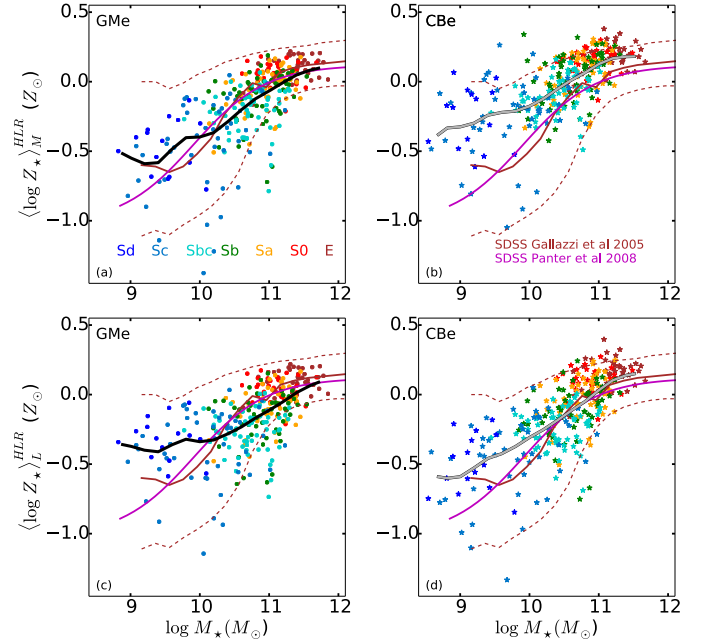


Fig. B.1. The global stellar MZR for 300 CALIFA galaxies is shown as dots, color coded by the morphological type. The metallicity is derived using $\langle \log Z_\star \rangle_M^{\text{HLR}}$ (upper panels) and $\langle \log Z_\star \rangle_L^{\text{HLR}}$ (lower panels), and the total stellar mass, M_\star , obtained with the *GMe* SSP models (left panels) and *CBe* (right panels). A mass-binned smooth mean relation is shown as a solid black or grey-black line. The MZRs obtained for SDSS galaxies by Gallazzi et al. (2005) and Panter et al. (2008) are plotted as brown and magenta lines, respectively, with dashed brown indicating the 16 and 84 percentiles of Gallazzi et al. (2005).

while *CBe* goes up to $2.5 Z_\odot$. Because *MILES* is built with stars in the solar neighborhood, it does not contain stars as metal rich as $2.5 Z_\odot$, so *CBe* results in over solar metallicity should be interpreted with care. On the other hand, the central parts of galaxies can be as metal rich as $2\text{--}3 Z_\odot$, and the base *GMe* may be too low to fit spectra of these regions, leading to saturation effects. To avoid these problems, we also fitted the spectra with another two sets of SSP, are identical to *GMe* and *CBe*, but where for each metallicity bin, two SSPs of age 16 and 18 Gyr are added to our “standard” bases. These extra bases, which we name *GMd* and *CBd*, allow galaxies older than the age of the universe if their bulges are very metal rich. Furthermore, results at very low metallicity also must be taken with care. *MILES* contain only few stars of metallicity below $1/100 Z_\odot$. For this reason, Vazdekis et al. (2010) provide a safe age range for each metallicity bin, being the models with $\log Z_\star(Z_\odot) \leq -1.7$ only valid between 10 and 18 Gyr. This safety margin is provided to avoid the cases when, because of age-metallicity degeneracy, these old metal poor models fit young metal-rich populations, may happen if the base does not include SSP younger than 100 Myr. Our fits do not suffer this problem because bases *GMe* and *CBe* both have spectra of ages as young of 1 Myr.

B.3. Global results and uncertainties associated with SSP models

To evaluate to which extent the spectral synthesis results depend on the choice of SSP models, we now compare the global properties derived with bases *GMe* and *CBe*. Using our pipeline we obtained the radial distribution of the stellar population properties for each galaxy with a spatial sampling of

¹³ The Gallazzi et al. (2005) and Panter et al. (2008) relations have been shifted by 0.25 dex to the right to account for the difference in IMF between their results based on models with Chabrier IMF and ours obtained with Salpeter IMF in the two left panels.

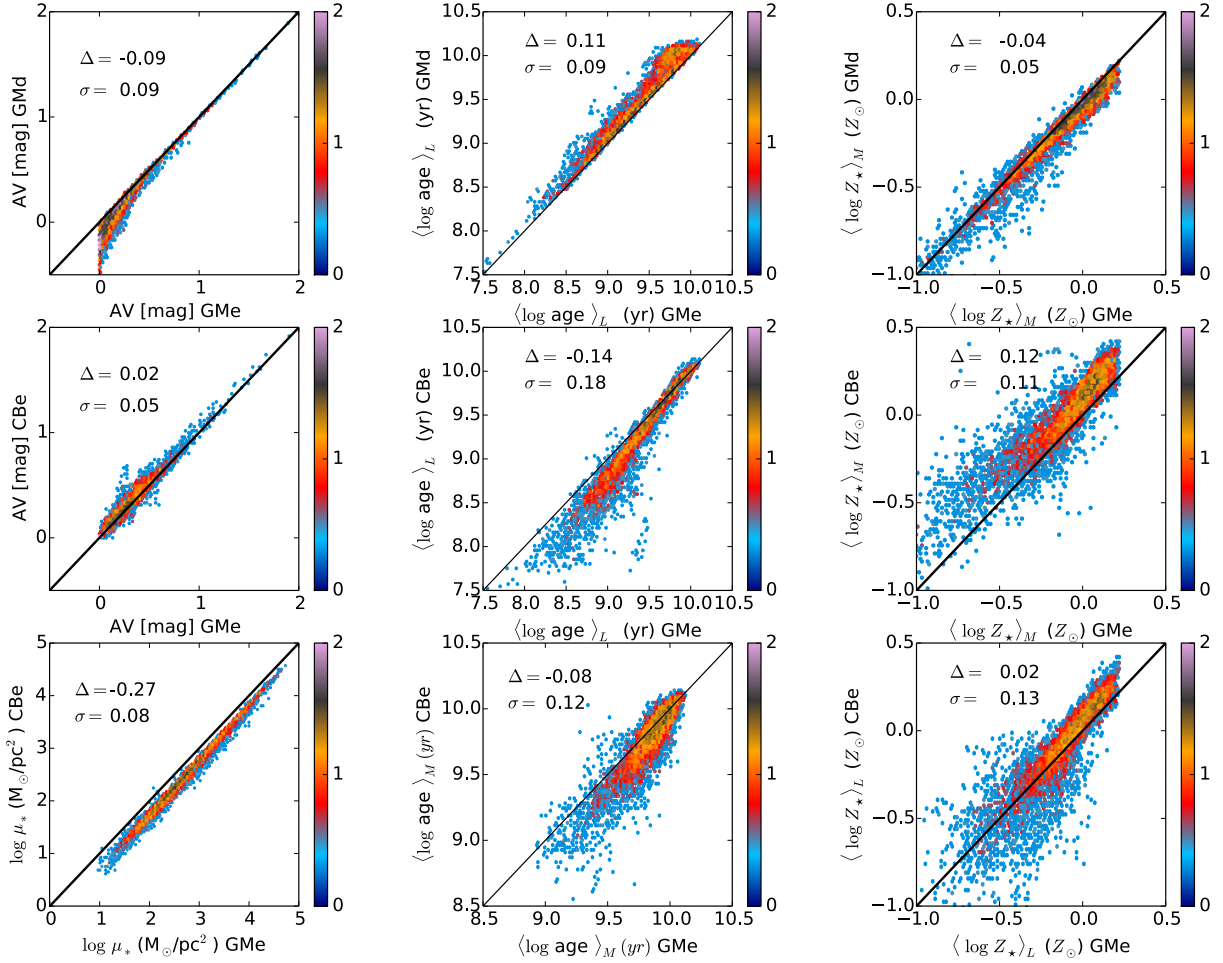


Fig. B.2. Correlation between SP obtained with the *GMe* (*x*-axis) and *CBe* (*y*-axis bottom and middle panels; and *GMe* (*x*-axis) and *GMd* (*y*-axis). The average difference between the property in the *y*-axis and *x*-axis is labeled in each panel as Δ , and the dispersion as (σ) .

0.1 HLR. Here we compare the stellar population properties of the 0.1 HLR radially sampled points, instead of comparing the results obtained from the individual 253 418 fitted spectra. Figure B.2 shows the results for a total of 6000 points corresponding to a maximum of 20 radial points (from nucleus to 2 HLR) for each of the 300 galaxies analyzed in this work. The figure compares the results for base *GMe* in the *x*-axis, with *CBe* in the *y*-axis, in the bottom and middle panels. The upper panels compare the results of *GMe* with *GMd*. Each panel quotes the mean Δ and its standard deviation, where $\Delta = \text{property}(\text{CBe}) - \text{property}(\text{GMe})$ or $\Delta = \text{property}(\text{GMd}) - \text{property}(\text{GMe})$.

GMe-based μ_* -values are higher than *CBe* by 0.27 dex on average, reflecting the different IMF used. Apart from this offset, the two stellar mass surface density agree to within 0.08 dex. Mean extinction is also in good agreement with a dispersion of 0.05 mag. Ages are higher in *GMe* than *CBe* by 0.14 dex for $\langle \log \text{age} \rangle_L$ and 0.08 dex for $\langle \log \text{age} \rangle_M$, with dispersion 0.18 dex and 0.12 dex, respectively. This result is expected since base *GMe* also differs from *CBe* in IMF and isochrones. The differences in opacities in the equation of state between Padova 2000 (*GMe*) and 1994 (*CBe*) tracks produce somewhat warmer stars in the red giant branch in the former. Thus, older ages are expected with *GMe* than with *CBe*. However, the metallicities are lower in *GMe* than in *CBe* by 0.13 dex for $\langle \log (Z/Z_\odot) \rangle_M$ and very similar (on average) for $\langle \log (Z/Z_\odot) \rangle_L$. In both cases, the dispersion is similar, 0.11 and 0.13 dex, respectively. Note that for $Z_* \geq Z_\odot$, the metallicities (weighted in light or in mass)

are always higher with *CBe* than *GMe*, reflecting the saturation effects in the base *GMe* due its limitation to $Z \leq 1.5 Z_\odot$. The shift at under-solar metallicities may be reflecting the age-metallicity degeneracy, *CBe* giving higher metallicity and younger ages.

The upper panels compare the results of *GMe* with the *GMd*. Here, we see two relevant effects. The results of *GMd* also differ from *GMe* in the range of extinctions allowed to . While with *GMe* and *CBe* always assumes $A_V \geq 0$, with *GMd*, can bluer the SSP spectra by up to $A_V = -0.5$ mag. This is allowed to avoid the effect of saturation at $A_V = 0$. The global effect is that ages can be 0.11 dex younger with *GMe* than *GMd*. Metallicity is not affected by this choice of A_V ; but the extension to ages older than the age of the Universe in *GMd* has some effect on the metallicity above Z_\odot , so metallicities are slightly lower and ages slightly older.

Appendix C: 2D maps and tables

C.1. 2D maps of $\log \mu_*$

Figure C.1 shows the M_r vs. $u - r$ CMD for the 300 CALIFA galaxies of our sample. Each galaxy is represented by its 2D map of the $\log \mu_*$ located at the position of its integrated M_r and $u - r$ values. In this plot, the SFH is compressed into the present-day stellar mass surface density, which measures the end product of the SFH. Because our analysis accounts for extinction, these $\log \mu_*$ values and their radial variations are free

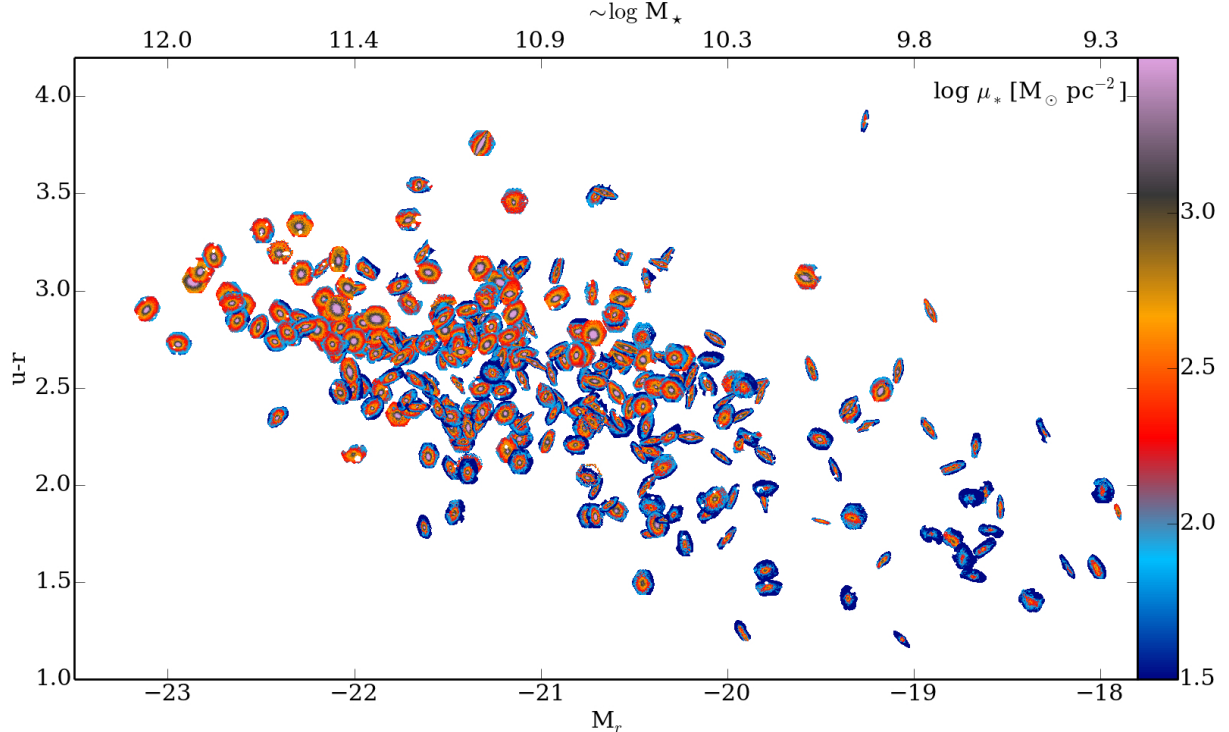


Fig. C.1. 2D maps of stellar mass surface density, μ_* . Each galaxy is placed in its location in the $u - r$ vs. M_r diagram, where color and magnitude correspond to its global values. The 2D maps are shown with north up and east to the left.

from extinction effects. Figure C.1 clearly shows¹⁴ that $\log \mu_*$ correlates with M_r , and spheroids are significantly denser than late-type galaxies by one to two orders of magnitude at the center, and by one order of magnitude at distances 1–2 HLR. At the center, $2.0 \leq \log \mu_* (M_\odot \text{ pc}^{-2}) \leq 4.7$, while $\leq \log \mu_* (M_\odot \text{ pc}^{-2}) \leq 3.4$ at 1 HLR, and $1.0 \leq \log \mu_* (M_\odot \text{ pc}^{-2}) \leq 2.9$ at 2 HLR.

C.2. 2D maps of $\langle \log \text{age} \rangle_L$

Similarly to Figs. C.1, C.2 shows the 2D maps of $\langle \log \text{age} \rangle_L$. It portrays the correlation between the average age of the stellar populations and M_r and colors, with the most luminous and red galaxies being older, while the bluest galaxies are the youngest. Gradients of the stellar population ages are also clearly detected within each galaxy in these 2D maps, and more remarkably in galaxies located in the green valley. At the center, $7.3 \leq \langle \log \text{age} \rangle_L (\text{yr}) \leq 10.1$, while $8.3 \leq \langle \log \text{age} \rangle_L (\text{yr}) \leq 10.1$ at 1 HLR, and $7.5 \leq \langle \log \text{age} \rangle_L \leq 9.9$ at 2 HLR.

C.3. 2D maps of $\langle \log Z_\star \rangle_M$

Similar to Figs. C.1, C.3 presents the 2D maps of $\langle \log Z_\star \rangle_M$. It clearly shows the correlation between the stellar metallicity and galaxy luminosity, equivalent to the mass metallicity

relation. Gradients of the stellar metallicities are more clearly seen in these 2D maps in galaxies with intermediate luminosity ($-22 \leq M_r \leq -20$). The most luminous galaxies have solar or over solar metallicity producing a visual saturation in the 2D maps. The stellar metallicities range from $\langle \log Z_\star \rangle_M = -1.4$ to 0.22.

C.4. 2D maps of A_V

Similarly to Figs. C.1, C.4 presents 2D maps of A_V . Effects of spatial binning are visible in the A_V maps, where all the pixels within a Voronoi zone have the same value. These effects are not noticeable in the μ_* images (Fig. C.1) because μ_* is an extensive property, and the zoning effect was softened by scaling the value at each pixel by its fractional contribution to the total flux in the zone; this is not possible for A_V (Fig. C.4), $\langle \log \text{age} \rangle_L$ (Fig. C.2), or $\langle \log Z_\star \rangle_M$ (Fig. C.3), because these are intensive properties. Figure C.4 shows how A_V changes across the CMD: the most luminous galaxies are little affected by extinction, while A_V is higher in spirals of intermediate type and with blue colors. The mean (dispersion) A_V values at the nuclei, 1 HLR, and 2 HLR are 0.47 (0.37), 0.19 (0.16), and 0.13 (0.13), respectively. 2D maps and the difference in the mean values at different distance indicate that stellar extinction shows radial gradients.

¹⁴ These 2D maps are the results from the GMe SSP base.

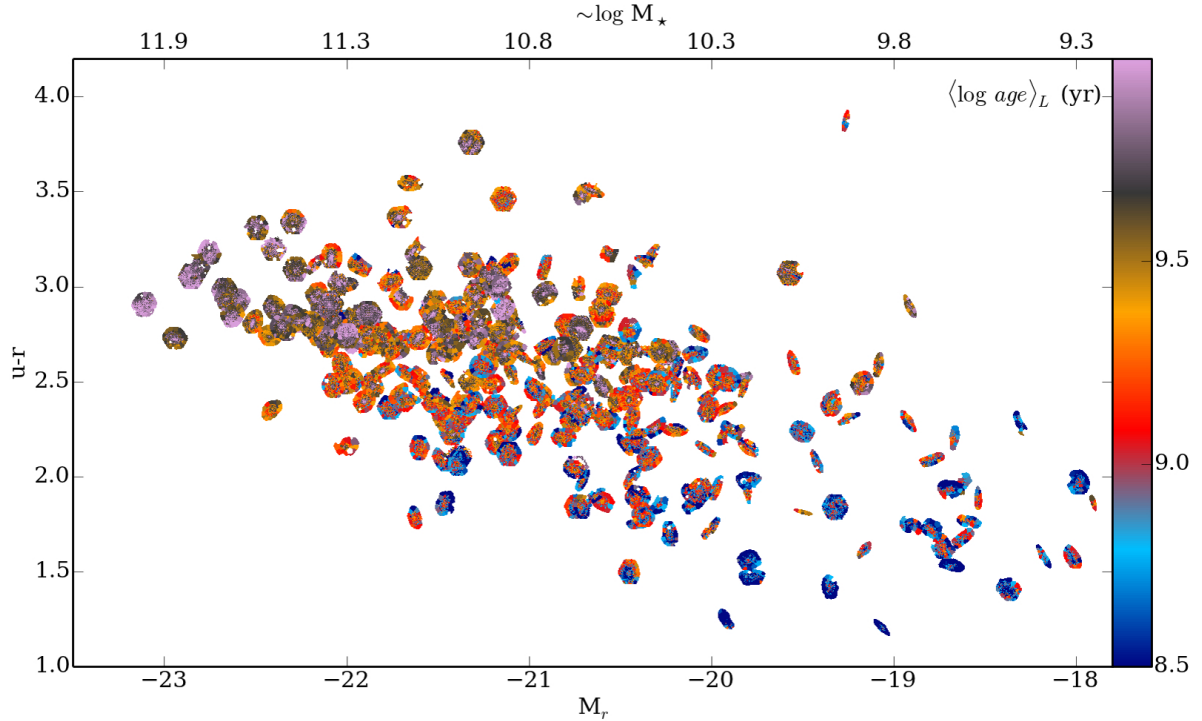


Fig. C.2. As Fig. C.1 except for images of the luminosity-weighted mean age, $\langle \log age \rangle_L$.

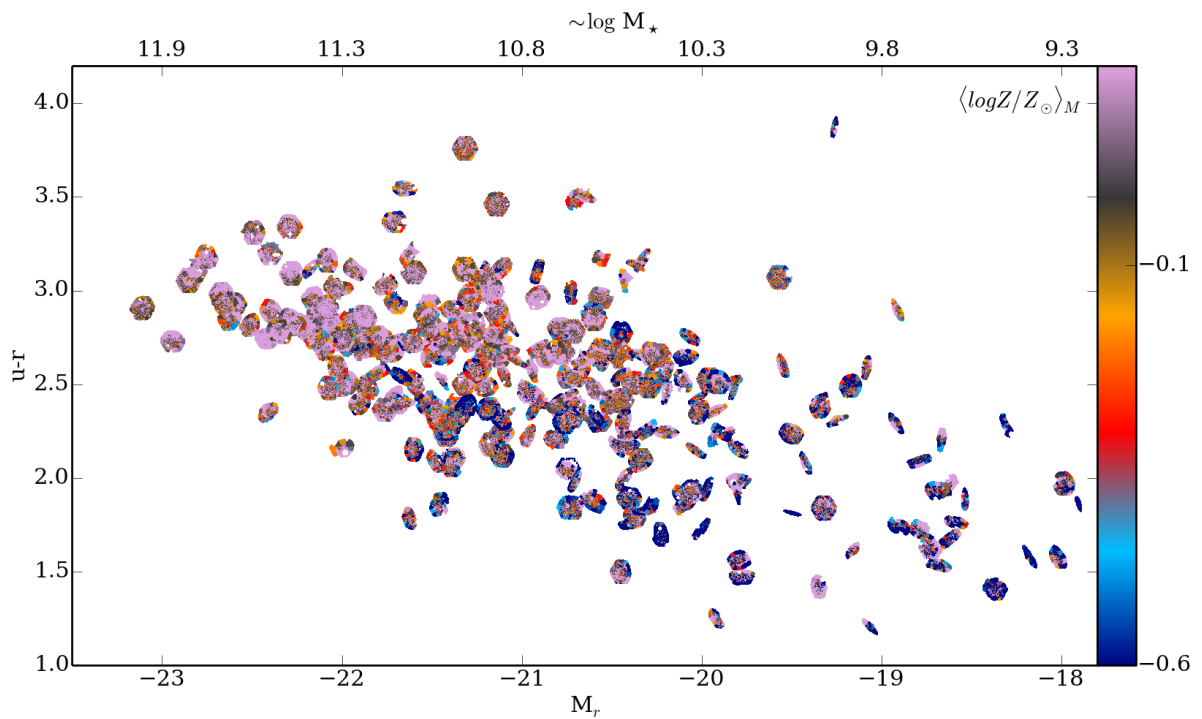


Fig. C.3. As Fig. C.1 except for images of the mass-weighted mean metallicity, $\langle \log Z_\star \rangle_M$.

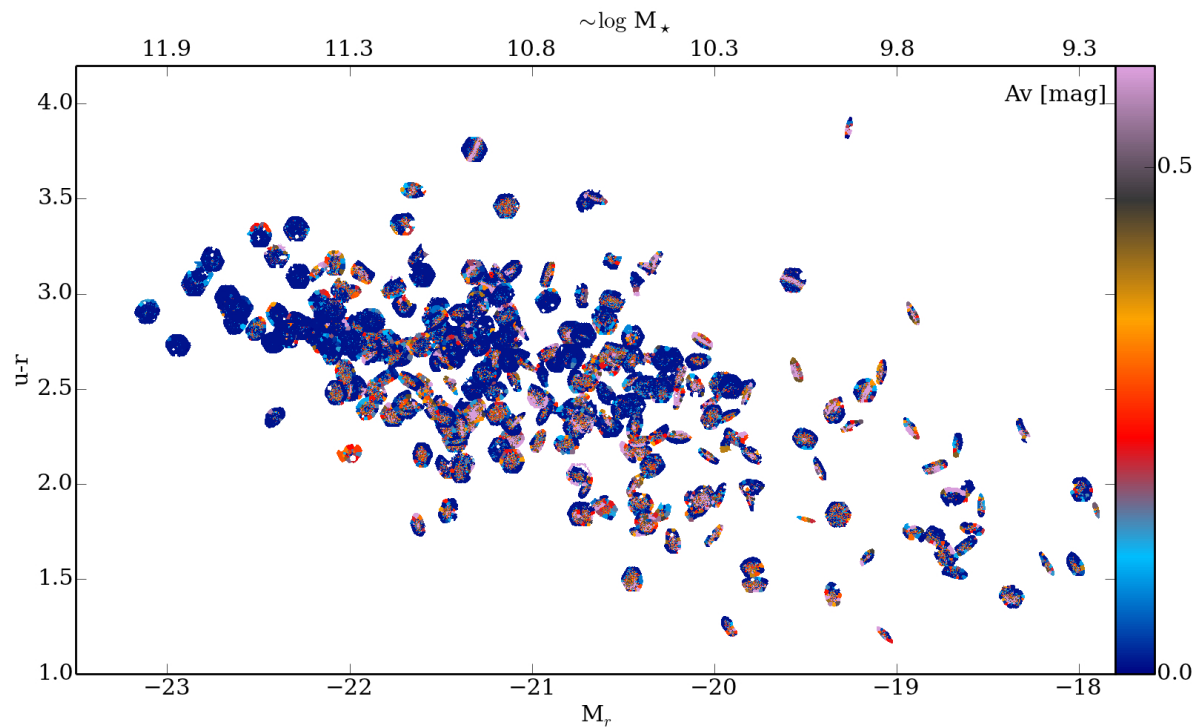


Fig. C.4. As Fig. C.1 except for images of the stellar extinction, A_V [mag].

Table C.1. Stellar population properties: CBe .

R. M. González Delgado et al.: The CALIFA survey across the Hubble sequence

CALIFA ID#	Name	Type morph.	$\log M_\star$	$\log \mu_\star[0]$	$\log \mu_\star[\text{HLR}]$	$A_V[\text{HLR}]$	$\langle \log \text{age}[0] \rangle_L$	$\langle \log \text{age}[\text{HLR}] \rangle_L$	$\langle \log Z[0] \rangle_M$	$\langle \log Z[\text{HLR}] \rangle_M$	HMR	C
	NED		M_\odot	M_\odot/pc^2	M_\odot/pc^2	mag	(yr)	[Z $_\odot$]	[Z $_\odot$]	pc	pc	
001	IC 5376	2 A	10.60	3.87	2.41	0.42	0.53	9.97	9.38	0.25	-0.17	3.3
002	UGC 00005	3 A	10.84	3.29	2.23	0.63	0.41	9.51	8.88	-0.03	-0.04	2.1
003	NGC 7819	4 A	10.04	2.80	1.59	0.63	0.05	8.46	8.86	0.13	-0.27	2.1
004	UGC 00029	-1 A	11.16	3.67	2.49	0.44	0.03	9.89	9.75	0.37	0.14	4.372
005	IC 1528	3 AB	10.09	3.03	1.95	0.80	0.35	8.97	8.64	-0.22	-0.29	4.348
007	UGC 00036	1 AB	10.91	3.89	2.70	0.73	0.19	9.66	9.51	0.39	0.32	4.104
008	NGC 0001	3 A	10.68	3.85	2.53	0.43	0.63	9.55	8.95	0.07	-0.06	2.7142
010	NGC 0036	2 B	11.00	3.71	2.35	0.33	0.34	9.97	9.31	0.05	0.09	1.790
012	UGC 00148	4 A	10.11	2.97	2.20	0.99	0.51	8.86	8.33	-0.62	-0.76	4.820
013	MCG-02-02-030	2 AB	10.29	3.51	2.39	0.50	0.09	9.67	9.26	-0.06	-0.02	3.517
014	UGC 00312	5 B	9.80	2.93	1.51	0.42	0.29	8.59	8.17	-1.33	-0.52	3.659
016	MCG-02-02-040	4 AB	9.85	2.88	1.89	1.24	0.24	8.63	8.75	-0.15	-0.19	2.435
017	UGC 00335NED 02	-1 A	10.58	4.06	2.33	0.46	0.04	10.14	9.78	0.20	-0.10	3.298
019	ESO 540-G 003	2 AB	9.95	3.21	2.21	0.27	0.16	9.70	8.62	-0.19	0.36	2.362
020	NGC 0160	1 A	10.87	4.06	2.47	0.38	0.26	10.03	9.85	0.00	-0.37	4.165
023	NGC 0171	2 B	10.63	3.80	2.26	0.38	0.00	10.02	9.26	0.14	0.18	4.523
024	NGC 0177	1 A	10.27	3.92	1.91	0.96	0.07	9.79	9.12	-0.14	-0.01	3.2268
025	NGC 0180	2 B	10.80	3.46	2.14	0.20	0.08	9.35	9.15	0.21	0.12	4.978
026	NGC 0192	1 AB	10.70	4.14	2.58	1.21	0.32	9.19	9.39	0.12	-0.08	3.2970
027	NGC 0216	5 A	8.90	2.53	1.86	0.29	0.12	8.65	8.54	-0.40	-0.25	1.254
028	NGC 0214	3 AB	10.84	3.84	2.45	0.71	0.35	9.62	8.79	0.12	0.04	4.346
029	NGC 0217	1 A	10.80	4.06	2.63	0.38	0.05	10.13	9.60	0.11	0.22	3.868
030	NGC 0237	4 B	10.15	3.23	2.05	0.09	0.42	9.43	8.66	-0.05	-0.19	3.457
031	NGC 0234	4 AB	10.56	3.20	2.09	0.79	0.42	8.56	8.53	-0.09	0.01	4.4668
032	MCG-02-03-015	1 AB	10.69	3.78	2.43	0.70	0.16	9.65	9.43	0.07	0.01	4.431
033	NGC 0257	4 A	10.81	3.67	2.31	0.61	0.39	9.41	8.73	-0.32	-0.32	6.099
035	NGC 0364	-1 AB	10.79	4.22	2.36	0.59	0.00	10.08	9.68	0.15	0.19	3.2268
036	NGC 0429	1 A	10.71	4.00	2.89	0.00	0.01	9.97	9.76	0.31	0.13	2.564
038	NGC 0447	1 B	11.01	4.03	2.39	0.15	0.03	9.90	9.47	0.42	0.28	4.836
039	NGC 0444	4 A	9.72	2.48	1.51	0.38	0.17	9.12	8.55	-0.34	-0.38	5.690
040	UGC 00809	4 A	9.56	2.51	1.61	0.82	0.23	8.75	8.57	-0.68	-0.06	4.220
041	UGC 00841	3 A	9.98	2.63	1.76	0.76	0.29	9.04	8.79	-0.34	-0.10	4.553
042	NGC 0477	3 AB	10.52	3.15	1.89	0.46	0.15	9.43	8.91	0.16	-0.09	6.329
043	IC 1683	2 AB	10.49	3.42	2.38	1.12	0.43	8.77	9.22	-0.12	0.14	3.098
044	NGC 0499	-1 A	11.24	4.42	3.08	0.09	0.03	10.03	9.94	0.38	0.31	3.210
045	NGC 0496	4 A	10.45	2.75	1.86	0.69	0.10	8.77	8.70	-0.14	-0.30	6.329
046	NGC 0504	0 A	10.48	4.03	2.71	0.01	0.00	10.08	9.74	0.32	0.18	1.838
047	NGC 0517	0 A	10.64	4.07	2.72	0.00	0.00	10.07	9.74	0.27	0.05	2.3323
049	UGC 00987	1 AB	10.71	4.14	2.73	0.34	0.24	10.03	9.57	0.09	0.19	2.922
050	NGC 0528	0 A	10.95	4.17	2.87	0.00	0.00	9.98	9.80	0.35	0.18	2.751
051	NGC 0529	-1 A	11.11	4.37	2.91	0.00	0.00	10.04	9.80	0.37	0.15	2.859
052	NGC 0551	3 AB	10.59	3.25	2.19	0.12	0.14	9.82	9.09	0.14	0.14	5.228
053	UGC 01057	4 AB	10.28	3.11	1.94	0.44	0.24	9.50	8.69	0.28	-0.15	4.918
059	UGC 01271	0 B	10.80	3.98	2.65	0.00	0.01	10.00	9.69	0.37	0.25	3.013
061	NGC 0681	1 AB	10.11	3.89	2.59	0.61	0.24	9.75	9.53	-0.05	-0.17	1.663
062	UGC 01274	1 A	11.11	4.08	3.04	0.36	0.19	10.00	9.78	0.29	0.28	3.791
068	NGC 0741	-1 A	11.48	4.24	2.96	0.14	0.00	10.10	9.90	0.36	0.21	4.620

Table C.1. continued.

CALIFA ID#	Name	Type	$\log M_\star$	$\log \mu_\star[0]$	$\log \mu_\star[\text{HLR}]$	$A_V[\text{HLR}]$	$\langle \log \text{age}[0] \rangle_L$	$\langle \log \text{age}[0] \rangle_L$	$\langle \log \text{age}[0] \rangle_M$	$\langle \log \text{Z}[0] \rangle_M$	$\langle \log \text{Z}[0] \rangle_M$	HMR	C
	NED	morph.	M_\odot	M_\odot/pc^2	M_\odot/pc^2	mag	(yr)	[Z _⊙]	[Z _⊙]	[Z _⊙]	[Z _⊙]	pc	pc
069	NGC 0755	4 B	9.17	2.56	1.83	0.37	0.21	8.86	8.49	-0.05	-0.08	1638	1340 2.2
070	IC 1755	2 A	10.98	3.87	2.58	0.33	0.07	10.08	9.75	0.31	0.14	5650	4152 3.0
071	NGC 0768	4 B	10.58	3.34	1.93	0.10	0.17	9.68	8.89	0.25	-0.09	6604	3796 2.5
072	NGC 0774	0 A	10.77	4.00	2.62	0.35	0.02	10.06	9.70	0.30	0.20	3087	2265 3.0
073	NGC 0776	2 B	10.82	3.79	2.05	0.56	0.17	9.39	9.12	0.38	0.11	4943	2948 2.1
076	NGC 0810	-1 A	11.39	3.96	2.67	0.58	0.02	9.91	9.80	0.41	0.23	5841	4624 3.0
077	NGC 0825	1 A	10.37	4.10	2.77	0.00	0.25	10.10	9.66	0.30	-0.03	1806	1203 3.2
081	UGC 01659	4 B	10.71	3.07	1.85	0.44	0.23	9.80	8.99	0.14	0.04	8576	6249 2.2
087	NGC 0932	0 A	10.97	4.13	2.72	0.13	0.08	9.96	9.77	0.30	0.22	3033	2341 3.2
088	UGC 01938	3 AB	10.39	3.34	2.04	0.54	0.19	9.50	8.75	0.35	-0.23	5081	3097 2.5
100	NGC 1056	1 A	9.94	4.01	2.88	0.96	0.60	8.83	9.23	-0.55	-0.28	958	898 3.2
101	NGC 1060	-1 A	11.61	4.46	3.20	0.15	0.00	10.04	9.88	0.39	0.23	4064	3624 3.0
103	UGC 02222	0 AB	10.71	4.30	2.74	0.24	0.01	10.12	9.77	0.32	0.12	2826	2066 3.1
104	UGC 02229	0 A	10.96	3.72	2.39	0.11	0.10	10.08	9.65	0.21	0.14	5458	3813 3.2
108	NGC 1093	3 B	10.61	3.58	2.24	0.14	0.06	9.88	9.28	0.25	0.15	4252	2838 2.6
115	UGC 02403	2 B	10.42	3.80	2.26	0.23	0.50	9.03	9.05	-0.07	0.04	3747	2232 2.0
116	UGC 02405	3 A	10.44	2.98	1.68	0.35	0.51	9.27	8.00	0.02	0.01	7902	4649 2.2
118	UGC 02465	0 A	10.85	4.20	2.71	0.55	0.10	10.08	9.58	0.39	0.25	3571	2453 2.8
119	NGC 1167	0 A	11.20	4.24	2.64	0.17	0.00	10.08	9.61	0.22	0.17	4277	4083 2.8
127	NGC 1349	-1 A	11.12	3.99	2.36	0.21	0.01	9.95	9.30	0.27	0.29	5199	3502 2.6
131	NGC 1542	1 AB	10.36	3.55	2.50	0.27	0.32	9.66	9.34	-0.03	-0.14	2816	2251 2.5
132	UGC 03038	1 A	10.70	3.50	2.04	0.80	0.39	9.53	8.87	0.23	0.04	6289	4278 2.4
133	UGC 03107	2 A	10.73	3.48	2.32	0.87	0.31	9.42	8.90	0.13	-0.25	7058	4810 2.5
134	NGC 1645	0 B	10.84	3.98	2.70	0.18	0.05	10.03	9.58	0.00	0.16	3379	2361 3.2
135	UGC 03151	1 AB	10.75	3.74	2.61	0.56	0.03	9.71	9.30	0.07	-0.03	4868	3670 2.4
141	IC 2095	4 AB	8.60	1.61	1.06	0.00	0.35	8.01	8.06	0.40	-0.46	2145	1934 2.8
143	NGC 1677	4 AB	9.39	2.88	1.91	0.59	0.21	8.59	8.63	-1.04	0.05	1736	1976 2.5
144	IC 2101	4 AB	10.15	3.04	1.84	0.98	0.37	9.8	8.88	-0.17	-0.24	4783	3546 2.5
146	UGC 03253	2 B	10.52	3.56	2.22	0.40	0.10	9.75	9.06	-0.04	-0.03	3797	2251 2.3
147	NGC 2253	3 B	10.55	3.65	2.29	0.76	0.36	9.05	8.69	-0.14	-0.13	3523	2448 2.1
148	UGC 03539	4 AB	9.79	3.06	1.97	1.28	0.49	9.20	8.73	-0.37	-0.18	3045	2117 2.8
149	NGC 2347	3 AB	10.85	3.91	2.56	0.29	0.35	9.84	8.94	0.17	-0.11	3939	2454 2.6
150	UGC 03899	5 A	9.35	2.63	1.68	0.43	0.34	8.61	8.15	-1.16	-0.48	2253	1760 2.9
151	NGC 2410	2 AB	10.89	3.91	2.56	0.59	0.33	9.78	9.31	0.01	-0.06	4192	2945 3.1
152	UGC 03944	3 AB	9.92	2.87	1.71	0.37	0.07	9.28	8.53	-0.30	-0.13	3851	2534 2.2
153	UGC 03969	2 A	10.69	3.29	2.33	0.88	0.58	9.68	9.08	-0.30	-0.08	6325	5196 2.4
155	UGC 03995	2 B	11.07	4.11	2.51	0.28	0.20	9.99	9.47	0.35	0.21	5286	3309 2.4
156	NGC 2449	1 AB	10.96	3.91	2.75	0.38	0.31	9.96	9.41	0.23	0.14	4073	3150 2.7
157	UGC 04029	4 AB	10.28	3.37	2.03	0.88	0.43	9.51	8.92	0.05	-0.24	4558	3177 2.7
158	UGC 04054	4 A	9.33	2.98	1.77	0.60	0.14	9.50	8.72	-0.47	-0.26	2641	1835 2.7
159	IC 0480	4 AB	10.07	2.55	1.87	1.19	0.40	8.69	8.86	-0.33	0.21	5759	4705 2.3
161	NGC 2480	5 A	9.26	2.37	1.50	0.35	0.15	7.99	8.60	-0.26	-0.14	2662	2397 2.6
165	UGC 04132	3 AB	10.83	3.71	2.35	1.38	0.56	9.22	8.74	-0.21	-0.13	5756	3925 2.3
171	NGC 2513	-1 A	11.22	4.23	2.81	0.01	0.00	10.01	9.70	0.32	0.16	3929	3134 3.1
186	IC 2247	1 A	10.44	3.60	2.25	1.12	0.44	9.48	9.04	-0.01	-0.26	4250	2935 3.0
219	NGC 2639	1 A	11.03	4.19	3.07	0.02	0.20	9.95	9.48	0.25	0.21	2830	2255 2.7
226	UGC 04659	5 A	8.83	2.15	1.28	0.48	0.23	8.17	8.49	-0.93	-0.20	2189	1613 2.2

Table C.1. continued.

CALIFA ID#	Name NED	Type morph.	$\log M_\star$ M_\odot	$\log \mu_\star[0]$ M_\odot/pc^2	$\log \mu_\star[\text{HLR}]$ M_\odot/pc^2	$A_V[\text{HLR}]$ mag	$\langle \log \text{age}[0] \rangle_L$ (yr)	$\langle \log \text{age}[0] \rangle_M$ $[Z_\odot]$	$\langle \log \text{Z}[0] \rangle_M$ $[Z_\odot]$	HLR pc	HMR pc	C
231	UGC 04722	5 A	8.56	1.53	0.99	0.32	0.14	7.79	7.91	-0.87	-0.46	2355 1920 2.1
232	NGC 2730	4 B	10.01	2.67	1.52	0.53	0.23	9.00	8.48	-0.17	-0.32	5584 4705 1.9
272	NGC 2880	-1 AB	10.44	4.55	2.99	0.25	0.00	10.11	9.86	0.22	-0.03	1192 885 3.3
273	IC 2487	4 AB	10.43	3.16	2.18	0.53	0.34	9.59	9.02	-0.30	-0.22	6137 4994 2.5
274	IC 0540	1 AB	9.88	3.34	2.52	0.74	0.37	9.59	9.53	-0.30	-0.18	2154 1812 2.7
275	NGC 2906	3 A	10.44	3.88	2.45	0.58	0.23	9.79	9.10	0.27	-0.01	2932 2185 2.1
277	NGC 2916	3 A	10.67	3.58	2.29	0.09	0.04	9.66	9.07	0.13	0.10	5141 3858 2.2
278	UGC 05108	2 B	10.99	3.81	2.46	1.04	0.18	9.55	9.24	0.32	0.20	4860 3190 2.8
279	NGC 2918	-1 A	11.08	3.87	2.48	0.00	0.00	9.92	9.40	0.17	0.38	4547 2745 3.0
306	UGC 05358	5 B	9.22	1.83	1.28	0.36	0.20	7.97	8.63	0.25	-0.61	4017 3462 2.4
307	UGC 05359	2 B	10.87	3.30	2.12	0.12	0.18	9.93	9.12	0.13	-0.32	8278 5819 2.4
309	UGC 05396	3 AB	10.36	2.98	1.97	0.47	0.43	9.50	8.95	0.09	-0.12	6220 5197 2.1
311	NGC 3106	1 A	11.23	4.06	2.63	0.17	0.02	10.02	9.83	0.10	-0.02	4898 4233 3.1
312	NGC 3057	5 B	8.92	2.09	1.14	0.25	0.08	8.49	8.38	-0.46	0.02	2209 2019 1.9
314	UGC 05498NED01	1 A	10.71	3.49	2.53	0.53	0.26	9.79	9.60	-0.12	-0.14	4434 3654 3.1
318	NGC 3158	-1 A	11.61	4.12	2.88	0.00	0.00	9.99	9.86	0.37	0.18	5293 5626 3.1
319	NGC 3160	1 AB	10.82	3.46	2.44	0.36	0.01	9.92	9.76	0.14	0.11	5313 4260 2.7
326	UGC 05598	2 A	10.21	3.00	1.85	1.13	0.61	8.98	8.54	-0.12	-0.17	4990 4080 2.5
339	NGC 3300	0 B	10.61	3.96	2.54	0.19	0.00	10.00	9.54	0.05	0.17	2939 2356 2.7
341	UGC 05771	-1 A	11.19	3.89	2.62	0.01	0.08	10.07	9.87	0.36	0.14	4503 3136 3.4
353	NGC 3381	5 B	9.47	2.54	1.69	0.28	0.14	7.99	8.59	0.14	-0.09	2402 2180 2.0
361	UGC 05990	4 A	9.17	2.89	2.26	0.59	0.51	8.98	8.61	-1.19	-0.78	1264 1226 2.8
364	UGC 06036	1 A	11.09	3.85	2.88	0.06	0.09	9.99	9.90	0.29	0.26	4847 4367 3.4
381	IC 0674	1 B	11.06	3.92	2.54	0.17	0.09	10.09	9.68	0.21	0.00	4925 3284 2.9
386	UGC 06312	1 A	10.88	3.69	2.48	0.56	0.33	9.87	9.57	-0.02	-0.15	4454 3540 3.0
387	NGC 3615	-1 A	11.34	4.26	2.76	0.00	0.00	10.07	9.72	0.37	0.14	4131 3345 3.3
388	NGC 3614	3 AB	10.13	3.15	1.93	0.32	0.13	9.76	9.12	-0.25	-0.14	3436 2735 2.2
414	NGC 3687	2 B	10.30	3.74	2.23	0.06	0.04	10.01	9.04	0.01	-0.02	2809 1905 2.2
436	NGC 3811	3 B	10.41	3.62	2.19	0.56	0.18	9.20	8.87	-0.01	-0.14	3827 2387 2.1
437	NGC 3815	3 A	10.33	3.43	2.00	0.40	0.24	9.74	8.71	-0.19	0.03	3764 2309 2.6
475	NGC 3991	5 A	9.54	2.38	1.50	0.12	0.14	7.52	8.06	0.10	0.01	3613 4799 1.8
476	NGC 3994	3 AB	10.41	4.25	2.51	0.92	0.51	9.54	8.43	0.01	-0.28	2091 1117 2.7
479	NGC 4003	0 B	11.03	3.78	2.37	0.26	0.01	9.73	9.62	0.38	0.30	5263 3955 2.8
486	UGC 07012	4 AB	9.36	2.49	1.42	0.37	0.23	8.97	8.03	-0.19	0.01	2864 2158 2.7
489	NGC 4047	3 A	10.65	3.53	2.47	0.37	0.40	9.28	8.50	0.14	0.08	3434 2943 2.3
500	UGC 07145	3 A	10.43	2.88	1.83	0.21	0.11	9.81	8.97	-0.27	-0.06	7080 5197 2.3
502	NGC 4149	1 AB	10.26	3.68	2.49	1.22	0.31	9.35	9.32	-0.26	-0.08	3268 2397 2.6
515	NGC 4185	3 AB	10.70	3.28	2.13	0.05	0.03	10.02	9.38	0.00	0.08	5782 5099 2.0
518	NGC 4210	2 B	10.23	3.42	2.10	0.14	0.08	10.01	8.83	-0.10	0.14	3642 2795 1.9
528	IC 0776	5 A	9.12	1.79	1.01	0.01	0.25	8.58	7.96	-0.48	-0.06	3582 3456 2.0
548	NGC 4470	4 A	9.88	2.76	2.01	0.22	0.31	8.80	8.51	-0.04	-0.19	2797 2722 2.0
569	NGC 4644	2 A	10.47	3.50	2.38	0.05	0.25	9.87	9.15	0.08	0.01	3530 2739 2.8
580	NGC 4711	3 A	10.39	3.19	1.99	0.63	0.55	9.48	8.63	-0.02	-0.10	4641 4663 2.0
588	NGC 4816	-1 A	11.25	3.93	2.42	0.07	0.00	10.04	9.77	0.32	0.20	6222 5550 2.9
589	NGC 4841A	-1 A	11.22	4.04	2.49	0.02	0.00	10.00	9.65	0.36	0.23	5003 3823 3.2
592	NGC 4874	0 A	11.49	3.73	2.56	0.00	0.00	9.97	9.79	0.29	0.19	7071 6639 2.7
593	UGC 08107	1 A	11.09	3.46	2.18	0.66	0.45	9.63	8.99	0.11	0.06	8331 6159 2.5

Table C.1. continued.

CALIFA ID#	Name	Type	$\log M_\star$	$\log \mu_\star[0]$	$\log \mu_\star[\text{HLR}]$	$A_V[\text{HLR}]$	$\langle \log \text{age}[0] \rangle_L$	$\langle \log \text{age}[\text{HLR}] \rangle_L$	$\langle \log \text{age}[0] \rangle_M$	$\langle \log \text{Z}[0] \rangle_M$	$\langle \log \text{Z}[0] \rangle_{\text{HLR}}$	HMR	C	
	NED	morph.	M_\odot	M_\odot/pc^2	M_\odot/pc^2	mag	(yr)	[yr]	[Z_\odot]	[Z_\odot]	[Z_\odot]	pc	pc	
602	NGC 4956	-1 A	10.90	4.24	2.60	0.00	0.00	9.98	9.40	0.24	0.23	3026	2290	3.0
603	NGC 4961	4 B	9.51	2.65	1.67	0.36	0.31	8.77	8.17	-0.18	-0.13	2454	2010	2.5
606	UGC 08231	5 AB	9.11	2.25	1.26	0.16	0.07	8.09	8.20	-0.27	-0.41	3114	2596	2.3
607	UGC 08234	0 A	11.15	4.05	2.66	0.09	0.01	9.53	9.33	0.13	0.15	3939	3182	3.3
608	NGC 5000	3 B	10.74	3.59	2.18	0.96	0.13	9.09	9.23	0.29	-0.03	5940	4257	2.2
609	UGC 08250	4 A	9.93	2.54	1.84	0.81	0.49	8.63	8.45	-0.51	-0.23	5609	4712	2.3
610	UGC 08267	2 AB	10.81	3.40	2.37	1.10	0.60	9.50	9.19	0.04	0.07	5862	4582	2.4
611	NGC 5016	3 A	10.28	3.35	2.36	0.47	0.21	9.39	8.77	-0.10	-0.05	2680	2094	2.3
612	NGC 5029	-1 A	11.41	3.91	2.57	0.00	0.00	10.04	9.88	0.37	0.07	6866	5551	3.0
614	NGC 5056	4 AB	10.53	3.54	1.82	0.57	0.19	9.84	8.64	-0.09	-0.04	6011	3038	2.5
630	NGC 5205	3 B	9.80	3.46	2.17	0.14	0.14	9.99	9.13	-0.09	-0.06	1814	1254	2.4
633	NGC 5216	0 A	10.40	3.83	2.43	0.09	0.01	10.09	9.59	0.28	0.15	2207	1689	3.0
634	NGC 5218	1 B	10.52	3.65	2.45	1.65	0.41	9.30	9.10	-0.33	-0.07	3330	2355	2.5
652	UGC 08662	4 A	8.80	2.10	1.38	0.41	0.16	8.32	8.03	-0.84	-0.40	2676	2231	2.2
657	UGC 08733	5 B	9.18	1.88	1.20	0.39	0.17	8.36	8.61	0.03	-0.09	3345	2810	2.1
663	IC 0944	1 A	11.17	3.72	2.58	0.41	0.33	9.82	9.57	0.19	0.15	6635	5272	2.8
664	UGC 08778	2 A	10.06	3.32	2.33	0.55	0.19	9.61	9.33	-0.10	0.04	2850	2258	2.4
665	UGC 08781	2 B	11.07	3.86	2.25	0.07	0.09	10.02	9.48	0.37	0.16	7114	4540	2.5
676	NGC 5378	2 B	10.49	3.77	2.19	0.02	0.02	10.05	9.56	0.11	0.20	3334	2605	2.4
684	NGC 5406	2 B	11.04	3.96	2.35	0.23	0.20	9.87	9.17	0.37	0.22	5563	3992	2.3
708	NGC 5485	-1 A	10.65	4.20	2.91	0.01	0.01	10.05	9.81	0.24	0.13	1914	1488	2.8
714	UGC 09067	3 AB	10.68	3.28	2.06	0.67	0.34	9.26	8.76	0.26	-0.21	6851	4348	2.4
715	NGC 5520	3 A	9.81	3.97	2.13	0.78	0.31	9.35	8.58	0.10	-0.16	1589	721	3.0
740	NGC 5614	1 A	11.21	4.45	2.90	0.44	0.20	9.91	9.50	0.39	0.26	3119	2209	3.1
744	NGC 5631	0 A	10.54	4.44	2.96	0.01	0.04	9.98	9.80	0.27	0.02	1498	1269	3.2
748	NGC 5633	3 A	10.10	3.44	2.41	0.52	0.52	9.39	8.58	-0.21	-0.29	2214	1837	2.1
749	NGC 5630	5 B	9.43	2.32	1.57	0.45	0.25	8.28	8.03	-0.06	-0.34	3530	3045	2.5
754	NGC 5657	3 B	10.33	3.67	2.23	1.10	0.42	9.30	8.92	-0.23	-0.10	3053	1915	3.1
758	NGC 5682	4 B	9.20	2.14	1.62	0.56	0.21	8.23	8.44	-0.32	-0.33	2354	2262	2.6
764	NGC 5720	3 B	11.02	3.60	2.14	0.26	0.28	10.09	9.24	0.07	0.16	7115	4753	2.4
768	NGC 5732	3 A	9.89	2.98	1.75	0.63	0.18	9.07	8.85	-0.31	-0.10	3362	2516	2.3
769	UGC 09476	3 A	10.13	2.95	1.83	0.37	0.12	9.24	8.69	-0.18	-0.17	4273	4053	1.8
774	UGC 09537	2 A	11.18	3.81	2.37	0.81	0.25	9.78	9.56	0.20	-0.08	6566	4783	3.3
775	UGC 09542	4 A	10.28	3.02	1.86	1.09	0.42	9.12	8.40	-0.28	-0.30	5811	4686	2.3
778	NGC 5888	2 B	11.30	3.70	2.34	0.26	0.18	9.98	9.39	0.26	0.18	9098	7201	2.1
791	NGC 5908	1 A	10.98	4.05	2.82	0.73	0.38	9.84	9.69	0.33	-0.03	4099	3047	2.7
795	NGC 5930	1 AB	10.48	3.03	2.11	0.05	0.41	9.74	8.82	0.06	0.06	2436	1888	2.8
797	UGC 09873	2 A	9.99	2.70	1.60	1.11	0.37	8.77	8.92	-0.26	-0.26	5413	4654	2.4
798	UGC 09892	3 A	10.24	3.09	1.97	0.49	0.52	9.55	8.70	-0.20	-0.15	6166	4613	2.5
804	NGC 5971	2 AB	10.38	3.83	2.28	0.49	0.19	10.02	9.49	-0.19	-0.33	2983	1950	3.0
806	NGC 5966	-1 A	10.95	4.00	2.70	0.12	0.00	10.09	9.77	0.23	0.11	3597	2731	2.8
807	IC 4566	2 B	10.86	3.68	2.29	0.37	0.32	9.92	9.35	-0.04	0.16	5242	3762	2.2
809	NGC 5987	1 A	10.89	4.33	2.96	0.49	0.48	9.89	9.75	0.10	0.09	2737	2307	3.0

Table C.1. continued.

CALIFA ID#	Name NED	Type morph.	$\log M_\star$ M_\odot	$\log \mu_\star[0]$ M_\odot/pc^2	$\log \mu_\star[\text{HLR}]$ M_\odot/pc^2	$A_V[\text{HLR}]$ mag	$\langle \log \text{age}[0] \rangle_L$ (yr)	$\langle \log \text{age}[0] \rangle_M$ $[Z_\odot]$	$\langle \log \text{Z}[0] \rangle_M$ $[Z_\odot]$	HLR pc	HMR pc	C
810	NGC 5980	3 A	10.64	3.56	2.46	0.70	0.61	9.61	8.82	-0.08	4507	2957 2.3
813	NGC 6004	3 B	10.57	3.46	2.09	0.62	0.30	9.28	8.94	0.13	0.08	4808 4.383 2.0
814	UGC 10097	-1 A	11.31	4.48	2.87	0.09	0.00	10.11	9.74	0.41	0.32	3473 2295 3.3
815	NGC 6020	-1 A	10.87	3.73	2.77	0.00	0.01	9.61	9.86	0.21	0.08	2765 2195 3.0
816	NGC 6021	-1 A	10.89	4.37	2.70	0.70	0.01	10.06	9.82	0.02	0.07	2679 1586 3.3
818	UGC 10123	1 A	10.32	3.51	2.41	1.11	0.68	9.42	9.08	-0.07	-0.13	3266 2303 2.5
820	NGC 6032	3 B	10.40	3.41	2.01	0.83	0.18	9.43	9.28	-0.15	-0.27	5871 4437 2.0
821	NGC 6060	2 A	10.91	3.88	2.49	0.67	0.52	9.73	9.13	0.18	-0.12	5662 4389 2.2
822	UGC 10205	0 A	10.99	3.82	2.34	1.46	0.27	9.64	9.44	-0.27	-0.14	5579 3630 2.5
823	NGC 6063	3 A	9.98	2.89	1.91	0.25	0.25	9.61	8.96	-0.07	-0.20	3636 2802 1.9
824	IC 1199	2 AB	10.57	3.54	2.30	0.71	0.41	9.61	8.90	0.00	0.05	4917 3533 2.1
826	NGC 6081	0 A	11.00	4.21	2.74	0.90	0.14	9.99	9.81	0.06	0.15	3500 2313 3.4
827	UGC 10297	4 A	9.33	2.65	1.95	0.59	0.26	9.02	8.78	-0.45	-0.17	2654 2286 2.4
828	UGC 10331	4 AB	9.93	2.67	1.84	0.66	0.40	9.01	8.55	-0.65	-0.91	4180 3624 2.4
829	NGC 6125	-1 A	11.24	4.25	2.89	0.00	0.00	10.00	9.90	0.39	0.18	3259 2642 3.2
831	NGC 6132	3 A	10.16	3.16	1.82	0.51	0.48	9.38	8.52	0.10	-0.11	4043 2340 2.5
832	NGC 6146	-1 A	11.53	4.19	2.73	0.18	0.00	10.01	9.80	0.27	0.08	5577 4113 3.4
833	NGC 6154	1 B	11.00	3.84	2.20	0.37	0.07	10.01	9.64	0.26	0.14	6057 3717 2.3
834	UGC 10380	2 AB	10.90	3.36	2.38	0.66	0.35	9.79	9.42	-0.11	0.16	6828 5696 2.8
835	NGC 6150	-1 A	11.30	3.78	2.68	0.01	0.00	10.08	9.80	0.27	0.23	5798 4977 2.9
836	NGC 6155	4 A	9.98	3.06	2.12	0.68	0.43	9.06	8.75	-0.19	-0.19	2491 2567 2.2
837	UGC 10384	2 A	10.28	3.69	2.39	1.60	1.08	9.30	8.50	-0.34	-0.60	4188 2446 2.6
838	UGC 10388	1 AB	10.50	3.86	2.42	0.22	0.06	10.14	9.61	0.18	0.00	3068 2415 3.1
840	NGC 6173	-1 A	11.68	4.15	2.77	0.18	0.00	10.04	9.93	0.31	0.16	6768 5728 3.1
841	NGC 6168	4 AB	9.64	2.85	1.96	0.87	0.56	8.96	8.61	-0.81	-0.43	3244 2754 2.0
842	NGC 6186	2 B	10.46	3.78	2.44	0.85	0.30	9.21	9.30	0.09	0.12	3024 2366 2.4
843	UGC 10650	4 A	9.24	2.35	1.36	0.51	0.29	7.77	8.12	-0.72	-0.44	3578 3852 2.5
844	NGC 6278	0 AB	10.69	4.47	2.85	0.00	0.00	10.09	9.75	0.33	0.21	1868 1412 3.4
845	UGC 10693	-1 AB	11.35	4.00	2.49	0.00	0.00	9.89	9.66	0.31	0.15	6271 5424 3.3
846	UGC 10695	-1 A	11.17	3.81	2.30	0.27	0.01	10.07	9.66	0.29	0.20	6736 4124 2.8
848	NGC 6310	2 A	10.43	3.68	2.47	0.43	0.30	9.92	9.31	0.13	0.19	3861 3220 2.3
849	NGC 6301	3 A	11.04	2.97	2.03	0.30	0.29	9.57	9.01	0.30	0.11	10836 8945 2.0
850	NGC 6314	1 A	10.92	3.84	2.38	0.40	0.37	9.54	9.35	0.21	0.06	4807 3675 3.3
851	NGC 6338	-1 A	11.55	4.11	2.71	0.33	0.00	9.99	9.86	0.33	0.30	6892 5783 2.8
852	UGC 10796	4 AB	9.30	2.40	1.37	0.36	0.33	8.20	8.52	-0.47	-0.37	3325 3467 2.4
854	UGC 10811	2 B	10.86	3.45	2.17	0.19	0.35	9.97	9.24	-0.02	0.00	7769 6226 2.7
856	IC 1256	2 AB	10.43	3.08	2.17	0.72	0.26	9.10	9.08	0.31	0.06	4466 4466 2.2
857	NGC 6394	3 B	10.86	3.18	2.39	0.43	0.38	9.72	9.16	-0.02	0.04	6792 5410 2.1
858	UGC 10905	0 A	11.35	4.01	2.69	0.24	0.28	9.81	9.76	0.22	0.05	5489 4081 3.5
859	NGC 6411	-1 A	10.81	3.75	2.64	0.00	0.00	9.52	9.55	0.28	0.24	3196 2788 3.0
860	NGC 6427	0 AB	10.67	4.49	2.95	0.15	0.00	10.08	9.88	0.33	0.07	1682 1235 3.3
861	UGC 10972	3 A	10.41	3.31	2.07	0.37	0.12	9.87	8.84	0.00	0.14	4887 3390 2.3
862	NGC 6478	4 A	10.99	3.65	2.27	0.61	0.44	9.64	8.76	0.10	-0.01	7164 4767 2.0
863	NGC 6497	1 B	10.89	3.56	2.35	0.00	0.19	9.75	9.31	0.19	0.21	5308 4011 2.7
864	NGC 6515	-1 A	11.11	4.11	2.38	0.11	0.00	9.95	9.64	0.26	0.05	4903 4083 3.1
865	UGC 11228	0 B	10.97	4.19	2.51	0.12	0.00	10.02	9.75	0.36	0.15	3770 2648 3.4
866	UGC 11262	4 A	10.20	2.85	1.54	0.47	0.59	9.47	8.23	-0.46	-0.23	6216 7062 2.2

Table C.1. continued.

CALIFA ID#	Name	Type	$\log M_\star$	$\log \mu_\star[0]$	$\log \mu_\star[\text{HLR}]$	$A_V[0]$	$A_V[\text{HLR}]$	$\langle \log \text{age}[0] \rangle_L$	$\langle \log \text{age}[\text{HLR}] \rangle_L$	$\langle \log \text{age}[0] \rangle_M$	$\langle \log \text{Z}[0] \rangle_M$	HLR	HMR	C
	NED	morph.	M_\odot	M_\odot/pc^2	M_\odot/pc^2	mag	mag	(yr)	[yr]	[Z_\odot]	[Z_\odot]	pc	pc	pc
867	NGC 6762	1 A	10.16	3.55	2.78	0.00	0.16	9.70	9.61	0.09	0.11	1581	1240	2.9
868	MCG-02-51-004	2 A	10.65	3.62	2.22	0.44	0.35	9.93	8.86	-0.07	-0.12	5758	3751	2.2
869	NGC 6941	2 B	10.99	3.60	2.25	0.18	0.25	9.76	9.31	0.28	0.28	6592	4942	2.1
870	NGC 6945	0 B	10.68	4.36	2.68	0.47	0.00	9.90	9.58	0.27	0.14	2442	1787	3.0
871	NGC 6978	2 AB	10.90	3.76	2.45	0.65	0.19	9.78	9.37	-0.10	0.04	5325	4023	2.4
872	UGC 11649	1 B	10.39	3.55	2.14	0.19	0.12	9.84	9.30	-0.03	0.16	3470	2354	2.1
873	UGC 11680NED 01	2 B	11.07	3.68	2.45	0.54	0.24	9.90	9.26	-0.10	0.20	5518	4132	2.5
874	NGC 7025	0 A	11.18	4.46	2.93	0.31	0.07	10.02	9.83	0.35	0.23	3166	2368	3.3
875	UGC 11694	0 A	10.98	4.36	2.53	0.82	0.15	10.02	9.60	0.25	0.19	3689	1829	2.9
876	NGC 7047	3 B	10.67	3.26	2.23	0.13	0.17	9.90	9.15	0.11	0.05	6172	4959	2.0
877	UGC 11717	1 A	10.81	3.69	1.94	0.62	0.13	9.76	9.26	0.30	0.22	6527	3180	2.9
878	MCG-01-54-016	4 A	9.04	2.24	1.40	0.27	0.33	8.89	8.29	-1.22	-0.70	2811	2303	2.3
879	UGC 11740	3 A	10.36	2.78	1.99	0.35	0.52	9.74	8.58	-0.17	0.09	5392	4449	2.4
880	UGC 11792	3 A	10.26	3.21	2.38	1.19	0.60	9.23	9.00	-0.23	-0.18	4178	3690	2.4
881	NGC 7194	-1 A	11.32	4.31	2.73	0.07	0.01	10.08	9.74	0.27	0.23	4377	3336	3.3
883	UGC 11958	0 A	11.27	3.76	2.30	0.17	0.03	10.08	9.82	0.39	0.23	7371	6020	2.8
884	UGC 11982	4 A	9.64	2.67	1.67	0.61	0.47	8.94	8.38	-0.31	0.17	4593	3348	2.3
885	UGC 12054	4 A	8.87	2.86	1.79	0.63	0.44	9.21	8.39	-0.73	-0.14	1277	1006	2.7
886	NGC 7311	1 A	11.09	4.43	2.92	0.34	0.25	9.92	9.50	0.28	0.09	3243	2106	3.1
887	NGC 7321	3 B	11.03	3.66	2.26	0.33	0.31	9.74	9.06	0.35	0.07	6168	3862	2.4
888	UGC 12127	-1 A	11.43	4.01	2.54	0.00	0.00	10.07	9.75	0.30	0.15	5888	5310	3.1
889	NGC 7364	1 A	10.68	3.87	2.46	0.11	0.29	9.59	8.99	0.24	0.12	3126	1981	3.1
890	UGC 12185	2 B	10.68	3.83	2.33	0.17	0.17	10.04	9.27	0.11	-0.06	4498	2832	2.8
891	UGC 12224	4 A	9.91	2.83	1.60	0.34	0.03	9.53	8.81	-0.36	-0.04	4171	3154	1.8
892	VV 488NED 02	2 AB	10.34	3.57	2.31	0.90	0.49	9.68	9.06	-0.39	-0.13	3545	2401	3.1
893	NGC 7436B	-1 A	11.47	4.16	2.64	0.08	0.04	9.96	9.78	0.36	0.15	5955	5228	2.9
894	UGC 12274	1 A	10.99	3.74	2.41	0.23	0.02	10.09	9.71	0.16	0.25	6073	4375	2.7
895	UGC 12308	4 A	8.71	2.47	1.19	0.40	0.06	8.67	7.86	-0.44	-0.09	1982	1226	2.5
896	NGC 7466	3 A	10.74	3.63	2.15	0.99	0.50	9.26	8.96	0.07	-0.27	6059	4131	2.7
898	NGC 7489	3 A	10.51	3.20	1.76	0.84	0.29	8.97	8.21	-0.28	-0.02	6686	3917	2.3
900	NGC 7550	-1 A	11.12	4.12	2.66	0.31	0.00	9.79	9.53	0.21	0.31	3694	2531	2.9
901	NGC 7549	3 B	10.50	3.48	2.06	0.80	0.47	9.26	8.66	-0.23	-0.16	4078	3284	2.1
902	NGC 7563	1 B	10.93	4.32	2.93	0.32	0.01	10.04	9.95	0.31	0.29	2308	1926	3.5
903	NGC 7562	-1 A	11.10	4.47	3.11	0.21	0.00	10.04	9.80	0.25	0.27	2616	2414	3.1
904	NGC 7591	3 B	10.74	3.71	2.46	1.45	0.79	8.92	8.70	-0.22	-0.56	3745	2813	3.0
906	IC 5309	4 AB	10.12	3.22	1.91	0.82	0.49	9.14	8.93	-0.30	-0.14	3694	2570	2.4
907	NGC 7608	3 A	9.90	3.01	2.10	0.61	0.62	9.47	8.83	-0.41	-0.18	3441	2913	2.3
909	UGC 12519	4 AB	10.07	3.06	1.95	0.74	0.45	9.25	8.56	-0.14	-0.08	4521	3204	2.3
910	UGC 12518	2 A	9.98	3.57	2.48	0.85	0.43	9.95	9.53	0.06	0.17	2074	1628	2.8
911	NGC 7619	-1 A	11.25	4.53	3.20	0.03	0.00	9.99	9.82	0.37	0.30	2564	2118	3.3
912	NGC 7623	0 A	10.63	4.04	2.69	0.09	0.01	10.06	9.78	0.04	0.08	2126	1562	3.4
914	NGC 7631	2 A	10.45	3.58	2.47	0.35	0.26	9.79	9.20	-0.04	0.14	3602	2714	2.6
915	NGC 7653	2 A	10.51	3.72	2.16	0.32	0.31	9.72	8.84	-0.11	-0.13	3365	1943	2.7
916	NGC 7671	0 A	10.90	4.57	2.97	0.23	0.04	10.09	9.84	0.38	0.18	2140	1444	3.2
917	NGC 7683	0 A	10.96	4.36	3.07	0.73	0.07	9.67	10.01	0.34	0.27	2273	1863	3.2
919	NGC 7684	0 A	10.83	4.25	2.71	0.34	0.07	9.93	9.76	0.40	0.02	3290	2330	3.1
920	NGC 7691	3 B	10.11	2.77	1.65	0.26	0.11	9.38	8.67	-0.25	-0.34	4901	4146	2.0

Table C.1. continued.

CALIFA ID#	Name	Type	$\log M_\star$	$\log \mu_\star[0]$	$\log \mu_\star[\text{HLR}]$	$A_V[0]$	$A_V[\text{HLR}]$	$\langle \log \text{age}[0] \rangle_L$	$\langle \log \text{age}[\text{HLR}] \rangle_L$	$\langle \log \text{age}[0] \rangle_M$	$\langle \log \text{Z}[0] \rangle_M$	HLR	HMR	C
	NED	morph.	M_\odot	M_\odot/pc^2	M_\odot/pc^2	mag	mag	(yr)	[Z_\odot]	[Z_\odot]	[Z_\odot]	pc	pc	pc
921	UGC 12653	4 A	9.53	2.58	1.32	0.00	0.16	9.47	8.16	-0.24	0.04	4547	3078	2.3
923	NGC 7711	-1 A	10.76	4.35	2.77	0.30	0.00	10.07	9.64	0.29	0.06	2554	1525	3.3
924	NGC 7716	2 A	10.30	4.10	2.46	0.01	0.08	10.05	9.49	0.09	-0.15	1943	1143	2.7
925	NGC 7722	1 A	10.92	4.06	2.75	0.65	0.57	9.77	9.49	0.16	0.25	3097	2560	2.6
926	UGC 12723	4 A	9.69	2.38	1.87	0.79	0.48	7.93	7.93	-0.41	-1.04	5140	4693	2.1
927	NGC 7738	2 B	11.06	3.94	2.27	2.01	0.08	8.69	9.46	-0.32	0.30	6037	3308	3.0
928	UGC 12767	2 B	10.75	3.61	2.07	0.03	0.11	9.95	9.08	0.14	0.32	5670	3800	2.4
929	UGC 12810	3 B	10.78	3.38	1.98	1.19	0.30	9.02	8.59	-0.36	-0.53	8345	5908	2.0
930	UGC 12816	4 A	9.85	2.75	1.46	0.28	0.42	9.13	8.24	-0.45	-0.76	4353	3003	2.4
931	NGC 7782	2 A	11.24	4.02	2.61	0.38	0.13	10.07	9.59	0.38	0.26	6197	4501	2.2
932	NGC 7783NED 01	1 A	11.25	3.64	2.86	0.00	0.01	9.52	9.86	0.32	0.15	5173	4188	3.0
933	NGC 7787	1 AB	10.52	3.52	1.99	1.58	0.34	9.00	9.11	-0.03	0.18	4869	2723	2.6
934	UGC 12857	3 A	9.46	2.86	2.01	0.57	0.47	9.23	8.69	-0.03	-0.24	2041	1783	2.5
935	UGC 12864	4 B	9.92	2.73	1.61	0.46	0.24	8.76	8.48	-0.44	-0.18	5227	4619	2.4
936	MCG-01-01-012	1 AB	10.62	3.37	2.45	0.77	0.20	9.90	9.59	-0.06	0.21	4977	4155	2.6
937	NGC 7800	5 AB	8.98	2.30	1.64	0.37	0.37	8.02	8.23	-0.37	-0.47	1598	1639	2.4
938	NGC 5947	3 B	10.56	3.57	1.76	0.39	0.17	9.45	8.82	0.34	0.07	5225	2688	2.4
939	NGC 4676B	1 B	10.92	3.76	2.58	0.39	0.20	9.89	9.54	0.22	0.18	3912	3032	2.4

Table C.2. Stellar population properties: GMe .

CALIFA ID#	Name	Type morph.	$\log M_\star$	$\log \mu_\star [0]$	$\log \mu_\star [\mathrm{HLR}]$	$A_V[0]$	$A_V[\mathrm{HLR}]$	$\langle \log \mathrm{age}[0] \rangle_L$	$\langle \log \mathrm{age}[\mathrm{HLR}] \rangle_L$	$\langle \log Z[0] \rangle_M$	$\langle \log Z[\mathrm{HLR}] \rangle_M$	HMR	C
	NED		M_\odot	M_\odot/pc^2	M_\odot/pc^2	mag	mag	(yr)	(Z_\odot)	(Z_\odot)	pc	pc	
001	IC 5376	2 A	10.82	4.05	2.64	0.41	0.49	10.00	9.50	0.09	-0.26	3883	2324 3.3
002	UGC 00005	3 A	11.16	3.60	2.54	0.66	0.36	9.58	9.00	0.00	-0.05	6842	5175 2.1
003	NGC 7819	4 A	10.39	3.37	1.91	0.62	0.06	8.59	9.12	0.06	-0.33	5455	3561 2.1
004	UGC 00029	-1 A	11.41	3.90	2.73	0.43	0.05	9.96	9.82	0.17	-0.01	5400	4542 3.1
005	IC 1528	3 AB	10.42	3.49	2.29	0.79	0.27	9.20	8.91	0.01	-0.37	4348	3204 2.1
007	UGC 00036	1 AB	11.13	4.12	2.92	0.77	0.21	9.74	9.59	0.16	0.10	4104	3355 2.7
008	NGC 0001	3 A	10.96	4.13	2.80	0.47	0.61	9.57	9.09	-0.00	-0.18	2781	1871 3.0
010	NGC 0036	2 B	11.21	3.88	2.62	0.38	0.29	9.90	9.46	-0.08	-0.10	5717	4621 2.5
012	UGC 00148	4 A	10.31	3.18	2.39	0.90	0.39	9.01	8.76	-0.63	-1.00	4820	4739 2.2
013	MCG-02-02-030	2 AB	10.57	3.79	2.71	0.50	0.07	9.71	9.36	-0.08	-0.08	3517	2872 2.2
014	UGC 00312	5 B	10.11	2.98	1.87	0.37	0.26	8.56	8.63	-1.14	-0.77	5055	4256 2.1
016	MCG-02-02-040	4 AB	10.21	3.38	2.22	1.21	0.19	8.92	9.09	-0.08	-0.35	3264	2187 2.2
017	UGC 0035NED 02	-1 A	10.77	4.20	2.50	0.51	0.04	10.05	9.74	0.02	-0.19	3298	2205 3.2
019	ESO 540-G 003	2 AB	10.16	3.42	2.44	0.28	0.09	9.74	9.11	-0.34	-0.06	2362	1935 2.6
020	NGC 0160	1 A	11.09	4.26	2.66	0.44	0.27	9.99	9.82	-0.07	-0.38	4165	2985 3.0
023	NGC 0171	2 B	10.88	4.01	2.54	0.40	0.01	10.02	9.35	0.04	0.12	4523	3344 2.0
024	NGC 0177	1 A	10.49	4.09	2.20	1.01	0.08	9.72	9.22	-0.15	0.01	3268	1503 3.8
025	NGC 0180	2 B	11.06	3.77	2.41	0.21	0.09	9.48	9.22	0.07	0.01	6498	5109 2.2
026	NGC 0192	1 AB	10.99	4.43	2.86	1.22	0.31	9.34	9.48	0.02	-0.14	3916	2513 2.6
027	NGC 0216	5 A	9.24	2.78	2.24	0.29	0.13	8.67	8.81	-0.45	-0.35	1254	1360 2.5
028	NGC 0214	3 AB	11.15	4.15	2.71	0.77	0.34	9.71	9.01	-0.01	-0.16	4346	3307 2.4
029	NGC 0217	1 A	11.03	4.23	2.86	0.43	0.06	10.09	9.67	-0.04	0.15	3868	3128 3.0
030	NGC 0237	4 B	10.52	3.50	2.43	0.09	0.36	9.46	8.84	-0.03	-0.14	3457	2542 2.4
031	NGC 0234	4 AB	10.92	3.68	2.45	0.75	0.32	8.83	8.82	-0.02	-0.10	4954	4090 1.9
032	MCG-02-03-015	1 AB	10.95	4.02	2.70	0.70	0.15	9.66	9.51	0.09	-0.08	4431	2530 3.1
033	NGC 0257	4 A	11.02	3.86	2.46	0.66	0.30	9.43	9.05	-0.11	-0.55	6099	4623 2.1
035	NGC 0364	-1 AB	10.99	4.38	2.60	0.64	0.00	10.00	9.69	0.03	0.16	3268	2477 3.1
036	NGC 0429	1 A	10.91	4.12	3.10	0.00	0.01	9.90	9.76	0.19	0.06	2564	1999 3.2
038	NGC 0447	1 B	11.22	4.19	2.60	0.20	0.03	9.89	9.56	0.22	0.13	4836	3509 3.3
039	NGC 0444	4 A	10.12	2.90	1.91	0.32	0.08	9.37	9.02	-0.42	-0.76	5690	4866 2.3
040	UGC 00809	4 A	9.84	2.64	1.89	0.67	0.23	8.83	8.76	-0.15	-0.10	4220	3474 2.3
041	UGC 00841	3 A	10.29	3.10	2.10	0.71	0.27	9.26	8.98	-0.26	-0.23	4555	3450 2.5
042	NGC 0477	3 AB	10.80	3.47	2.18	0.48	0.12	9.52	9.09	0.06	-0.17	6329	4599 2.2
043	IC 1683	2 AB	10.83	3.99	2.68	1.05	0.42	9.13	9.35	-0.16	0.01	3677	2616 2.6
044	NGC 0499	-1 A	11.41	4.58	3.25	0.14	0.03	10.01	9.95	0.21	0.11	3210	2728 3.0
045	NGC 0496	4 A	10.73	3.13	2.11	0.61	0.04	9.07	9.12	-0.25	-0.51	6329	4849 2.0
046	NGC 0504	0 A	10.69	4.21	2.93	0.01	0.00	10.10	9.73	0.13	0.14	1838	1471 3.2
047	NGC 0517	0 A	10.84	4.20	2.97	0.06	0.00	9.97	9.73	0.10	0.03	2323	1780 3.5
049	UGC 00987	1 AB	10.91	4.31	2.97	0.36	0.25	9.99	9.62	-0.06	0.06	2922	2061 3.0
050	NGC 0528	0 A	11.12	4.30	3.04	0.00	0.00	9.94	9.76	0.22	0.14	2751	2046 3.1
051	NGC 0529	-1 A	11.29	4.54	3.08	0.01	0.00	10.03	9.73	0.21	0.20	2859	2505 3.1
052	NGC 0551	3 AB	10.87	3.51	2.49	0.13	0.12	9.85	9.26	0.02	-0.02	5228	4260 2.1
053	UGC 01057	4 AB	10.58	3.39	2.27	0.45	0.24	9.54	8.85	0.07	-0.24	4918	2965 2.4
059	UGC 01271	0 B	10.99	4.14	2.84	0.00	0.01	10.00	9.70	0.17	0.14	3013	2543 3.1
061	NGC 0681	1 AB	10.39	4.17	2.85	0.67	0.22	9.76	9.54	-0.07	-0.16	1663	1174 2.4
062	UGC 01274	1 A	11.28	4.27	3.20	0.39	0.20	9.98	9.80	0.09	0.06	3791	2787 3.1
068	NGC 0741	-1 A	11.64	4.40	3.11	0.16	0.00	10.07	9.82	0.20	0.20	4620	4159 2.8

Table C.2. continued.

R. M. González Delgado et al.: The CALIFA survey across the Hubble sequence

CALIFA ID#	Name	Type	$\log M_\star$	$\log \mu_\star[0]$	$\log \mu_\star[\text{HLR}]$	$A_V[0]$	$A_V[\text{HLR}]$	$\langle \log \text{age}[0] \rangle_L$	$\langle \log \text{age}[\text{HLR}] \rangle_L$	$\langle \log \text{age}[0] \rangle_M$	$\langle \log \text{Z}[0] \rangle_M$	HMR	C
	NED	morph.	M_\odot	M_\odot/pc^2	M_\odot/pc^2	mag	mag	(yr)	(Z_\odot)	(Z_\odot)	(Z_\odot)	pc	pc
069	NGC 0755	4 B	9.54	2.94	2.24	0.42	0.21	8.90	8.74	-0.08	-0.41	1638	1304 2.2
070	IC 1755	2 A	11.19	4.03	2.79	0.35	0.08	10.05	9.76	0.13	0.04	5650	4535 3.0
071	NGC 0768	4 B	10.90	3.60	2.34	0.12	0.17	9.76	9.04	-0.01	-0.11	6604	4297 2.5
072	NGC 0774	0 A	10.99	4.16	2.85	0.37	0.02	10.01	9.71	0.13	0.10	3087	2397 3.0
073	NGC 0776	2 B	11.10	4.07	2.43	0.61	0.16	9.48	9.27	0.19	-0.01	4943	3152 2.1
076	NGC 0810	-1 A	11.58	4.18	2.87	0.56	0.02	9.99	9.81	0.20	0.13	5841	4699 3.0
077	NGC 0825	1 A	10.60	4.26	3.03	0.00	0.24	10.08	9.70	0.15	-0.10	1806	1289 3.2
081	UGC 01659	4 B	10.98	3.25	2.15	0.42	0.24	9.83	9.09	0.01	-0.02	8576	6395 2.2
087	NGC 0932	0 A	11.17	4.29	2.93	0.14	0.08	9.92	9.80	0.18	0.07	3033	2544 3.2
088	UGC 01938	3 AB	10.69	3.60	2.34	0.58	0.15	9.52	9.12	0.16	-0.50	5081	3052 2.5
100	NGC 1056	1 A	10.20	4.24	3.14	0.91	0.54	9.38	9.40	-0.91	-0.43	958	807 3.2
101	NGC 1060	-1 A	11.79	4.65	3.38	0.17	0.00	10.07	9.86	0.17	0.14	4064	3692 3.0
103	UGC 02222	0 AB	10.93	4.43	2.98	0.31	0.01	9.99	9.80	0.15	0.03	2826	2206 3.1
104	UGC 02229	0 A	11.19	3.86	2.61	0.14	0.08	9.99	9.70	0.03	0.03	5458	3907 3.2
108	NGC 1093	3 B	10.87	3.79	2.53	0.16	0.08	9.85	9.33	0.13	0.07	4252	3129 2.6
115	UGC 02403	2 B	10.81	4.25	2.62	0.21	0.42	9.19	9.27	0.21	-0.08	3747	1852 2.0
116	UGC 02405	3 A	10.69	3.32	2.04	0.30	0.41	9.72	8.55	-0.13	-0.27	7902	4987 2.2
118	UGC 02465	0 A	11.04	4.33	2.94	0.62	0.12	9.98	9.63	0.21	0.12	3571	2530 2.8
119	NGC 1167	0 A	11.44	4.42	2.91	0.20	0.00	10.05	9.64	0.06	0.12	4277	4315 2.8
127	NGC 1349	-1 A	11.35	4.17	2.63	0.22	0.01	9.94	9.46	0.10	0.11	5199	3946 2.6
131	NGC 1542	1 AB	10.67	3.86	2.80	0.31	0.27	9.71	9.51	-0.10	-0.22	2816	2146 2.5
132	UGC 03038	1 A	10.99	3.75	2.41	0.79	0.40	9.76	9.05	-0.11	-0.25	6289	4937 2.4
133	UGC 03107	2 A	10.97	3.68	2.53	0.81	0.21	9.68	9.34	-0.10	-0.52	7058	4807 2.5
134	NGC 1645	0 B	11.07	4.20	2.94	0.21	0.06	10.02	9.63	-0.03	0.06	3379	2618 3.2
135	UGC 03151	1 AB	11.03	4.06	2.89	0.57	0.03	9.80	9.41	0.03	-0.05	4868	3653 2.4
141	IC 2095	4 AB	8.98	2.10	1.48	0.12	0.26	8.42	8.49	-0.68	-0.81	2145	1659 2.8
143	NGC 1677	4 AB	9.77	3.09	2.31	0.59	0.24	8.61	8.95	-1.38	-0.17	1736	1654 2.5
144	IC 2101	4 AB	10.47	3.39	2.14	0.99	0.35	9.21	8.98	0.07	-0.32	4783	3253 2.5
146	UGC 03253	2 B	10.79	3.86	2.53	0.42	0.07	9.81	9.18	-0.08	-0.08	3797	2282 2.3
147	NGC 2253	3 B	10.82	4.00	2.57	0.76	0.29	9.33	8.92	-0.26	-0.33	3523	2413 2.1
148	UGC 03539	4 AB	10.11	3.37	2.30	1.27	0.36	9.32	9.08	-0.29	-0.35	3045	2117 2.8
149	NGC 2347	3 AB	11.08	4.09	2.84	0.30	0.27	9.76	9.14	0.06	-0.23	3939	2627 2.6
150	UGC 03899	5 A	9.55	2.73	1.92	0.31	0.29	8.62	8.44	-0.61	-0.68	2253	1805 2.9
151	NGC 2410	2 AB	11.17	4.19	2.85	0.61	0.29	9.79	9.50	0.01	-0.16	4192	2913 3.1
152	UGC 03944	3 AB	10.21	3.19	2.00	0.32	0.04	9.48	8.79	-0.16	-0.31	3851	2526 2.2
153	UGC 03969	2 A	10.97	3.50	2.57	0.88	0.53	9.65	9.28	-0.27	-0.30	6325	4899 2.4
155	UGC 03995	2 B	11.27	4.28	2.77	0.33	0.16	9.99	9.61	0.12	0.01	5286	3636 2.4
156	NGC 2449	1 AB	11.17	4.09	2.96	0.41	0.30	9.91	9.49	0.07	0.02	4073	3343 2.7
157	UGC 04029	4 AB	10.57	3.56	2.32	0.86	0.35	9.77	9.07	-0.25	-0.42	4598	3155 2.7
158	UGC 04054	4 A	9.64	3.26	2.05	0.56	0.15	9.58	8.94	-0.52	-0.39	2641	1802 2.7
159	IC 0480	4 AB	10.45	3.04	2.19	1.15	0.50	8.91	8.99	-0.29	0.04	5759	4316 2.3
161	NGC 2480	5 A	9.71	3.01	2.00	0.28	0.13	8.59	9.04	-0.58	-0.30	2662	2319 2.6
165	UGC 04132	3 AB	11.16	4.08	2.67	1.37	0.45	9.36	9.10	0.04	-0.29	5756	3763 2.3
171	NGC 2513	-1 A	11.42	4.39	3.04	0.02	0.00	9.98	9.70	0.19	0.12	3929	3508 3.1
186	IC 2247	1 A	10.72	3.95	2.57	1.14	0.43	9.59	9.38	0.02	-0.39	4250	2858 3.0
219	NGC 2639	1 A	11.25	4.34	3.32	0.05	0.22	9.87	9.53	0.13	0.06	2830	2486 2.7
226	UGC 04659	5 A	9.11	2.16	1.56	0.31	0.31	8.49	8.82	-0.97	-0.41	2189	1657 2.2

Table C.2. continued.

CALIFA ID#	Name	Type	$\log M_*$	$\log \mu_{\star}[0]$	$\log \mu_{\star}[\mathrm{HLR}]$	$A_V[\mathrm{HLR}]$	$\langle \log \mathrm{age}[0] \rangle_L$	$\langle \log \mathrm{age}[\mathrm{HLR}] \rangle_L$	$\langle \log \mathrm{age}[0] \rangle_M$	$\langle \log \mathrm{Z}[\mathrm{HLR}] \rangle_M$	HLR	HMR	C
	NED	morph.	M_\odot	M_\odot/pc^2	M_\odot/pc^2	mag	(yr)	(yr)	(Z_\odot)	(Z_\odot)	pc	pc	pc
231	UGC 04722	5 A	8.84	2.00	1.38	0.25	0.10	8.38	8.39	-0.73	-0.51	2355	1852 2.1
232	NGC 2730	4 B	10.35	3.06	1.85	0.52	0.22	9.15	8.76	-0.16	-0.49	5584	4505 1.9
272	NGC 2880	-1 AB	10.63	4.70	3.20	0.27	0.00	10.05	9.83	0.08	-0.08	1192	946 3.3
273	IC 2487	4 AB	10.67	3.45	2.38	0.57	0.27	9.62	9.23	-0.22	-0.37	6137	4340 2.5
274	IC 0540	1 AB	10.14	3.63	2.76	0.78	0.33	9.60	9.59	-0.22	-0.30	2154	1851 2.7
275	NGC 2906	3 A	10.72	4.14	2.80	0.61	0.21	9.81	9.20	0.12	-0.09	2932	2261 2.1
277	NGC 2916	3 A	10.96	3.83	2.57	0.10	0.05	9.68	9.18	0.06	-0.00	5141	4291 2.2
278	UGC 05108	2 B	11.23	4.04	2.68	1.06	0.17	9.58	9.40	0.18	0.00	4860	3245 2.8
279	NGC 2918	-1 A	11.31	3.99	2.78	0.00	0.00	9.81	9.49	0.22	0.22	4547	3315 3.0
306	UGC 05358	5 B	9.57	2.38	1.50	0.21	0.16	8.99	8.87	-0.74	-0.69	4017	3325 2.4
307	UGC 05359	2 B	11.05	3.48	2.33	0.09	0.08	10.07	9.60	-0.11	-0.60	8278	5839 2.4
309	UGC 05396	3 AB	10.65	3.25	2.23	0.50	0.35	9.49	9.10	0.07	-0.39	6220	4919 2.1
311	NGC 3106	1 A	11.45	4.27	2.82	0.19	0.02	10.04	9.83	0.01	-0.10	4898	4461 3.1
312	NGC 3057	5 B	9.26	2.49	1.54	0.19	0.13	8.91	8.61	-0.61	-0.37	2209	2011 1.9
314	UGC 05498NED01	1 A	10.97	3.75	2.75	0.60	0.28	9.75	9.64	-0.03	-0.15	4434	3505 3.1
318	NGC 3158	-1 A	11.77	4.30	3.04	0.01	0.00	9.99	9.77	0.19	0.21	5293	5447 3.1
319	NGC 3160	1 AB	11.05	3.74	2.65	0.35	0.01	9.99	9.75	0.02	0.04	5313	4282 2.7
326	UGC 05598	2 A	10.56	3.50	2.19	1.10	0.42	9.28	8.84	-0.15	-0.24	4990	3516 2.5
339	NGC 3300	0 B	10.84	4.20	2.79	0.20	0.01	10.03	9.57	-0.03	0.09	2939	2430 2.7
341	UGC 05771	-1 A	11.39	4.04	2.82	0.06	0.08	10.04	9.88	0.14	-0.02	4503	3261 3.4
353	NGC 3381	5 B	9.85	3.09	2.10	0.28	0.15	8.22	8.75	-0.08	-0.16	2402	2046 2.0
361	UGC 05990	4 A	9.42	3.03	2.52	0.43	0.34	9.14	9.37	-1.42	-1.13	1264	1283 2.8
364	UGC 06036	1 A	11.30	4.06	3.06	0.07	0.10	10.02	9.90	0.10	0.11	4847	4483 3.4
381	IC 0674	1 B	11.26	4.08	2.74	0.17	0.09	10.07	9.67	0.01	-0.04	4925	3618 2.9
386	UGC 06312	1 A	11.10	3.89	2.67	0.62	0.33	9.77	9.61	-0.04	-0.20	4454	3509 3.0
387	NGC 3615	-1 A	11.53	4.43	2.98	0.00	0.00	10.10	9.72	0.13	0.10	4131	3481 3.3
388	NGC 3614	3 AB	10.37	3.39	2.22	0.33	0.08	9.76	9.31	-0.27	-0.27	3436	2899 2.2
414	NGC 3687	2 B	10.55	3.93	2.50	0.08	0.04	9.97	9.20	-0.10	-0.12	2809	2090 2.2
436	NGC 3811	3 B	10.67	3.95	2.48	0.54	0.13	9.37	9.14	-0.07	-0.33	3827	2330 2.1
437	NGC 3815	3 A	10.78	3.74	2.43	0.43	0.17	9.84	9.06	-0.14	-0.16	3764	3458 2.6
475	NGC 3991	5 A	10.03	2.74	1.90	0.25	0.12	7.33	8.25	0.14	-0.25	3613	5230 1.8
476	NGC 3994	3 AB	10.75	4.49	3.06	0.94	0.41	9.51	8.77	0.12	-0.18	2091	1318 2.7
479	NGC 4003	0 B	11.26	3.99	2.61	0.32	0.01	9.74	9.68	0.14	0.17	5263	4032 2.8
486	UGC 07012	4 AB	9.83	3.01	1.91	0.56	0.33	8.89	8.43	0.06	-0.22	2864	2014 2.7
489	NGC 4047	3 A	10.98	3.84	2.80	0.38	0.38	9.40	8.87	0.05	-0.18	3434	2819 2.3
500	UGC 07145	3 A	10.70	3.17	2.12	0.23	0.08	9.83	9.14	-0.21	-0.21	7080	5345 2.3
502	NGC 4149	1 AB	10.58	4.03	2.80	1.27	0.30	9.41	9.39	0.02	-0.12	2797	2460 2.0
515	NGC 4185	3 AB	10.94	3.49	2.41	0.04	0.02	10.04	9.45	-0.13	-0.03	5782	5233 2.0
518	NGC 4210	2 B	10.50	3.64	2.40	0.15	0.09	10.00	9.08	-0.15	-0.05	3642	2990 1.9
528	IC 0776	5 A	9.47	2.13	1.35	0.05	0.24	9.01	8.38	-0.67	-0.42	3582	3019 2.0
548	NGC 4470	4 A	10.28	3.16	2.40	0.29	0.37	8.93	8.64	0.02	-0.22	2797	2460 2.0
569	NGC 4644	2 A	10.74	3.71	2.67	0.02	0.23	9.83	9.30	0.12	-0.07	3530	2896 2.8
580	NGC 4711	3 A	10.75	3.52	2.32	0.65	0.44	9.54	8.93	-0.01	-0.21	4641	4861 2.0
588	NGC 4816	-1 A	11.43	4.11	2.60	0.08	0.00	10.05	9.74	0.10	0.16	6222	5842 2.9
589	NGC 4841A	-1 A	11.43	4.22	2.74	0.04	0.00	10.04	9.70	0.13	0.12	5003	4254 3.2
592	NGC 4874	0 A	11.69	3.90	2.77	0.00	0.00	9.95	9.78	0.16	0.13	7071	6771 2.7
593	UGC 08107	1 A	11.39	3.78	2.49	0.69	0.39	9.73	9.25	0.04	-0.05	8331	5755 2.5

Table C.2. continued.

R. M. González Delgado et al.: The CALIFA survey across the Hubble sequence

CALIFA ID#	Name	Type	$\log M_\star$	$\log \mu_\star[0]$	$\log \mu_\star[\text{HLR}]$	$A_V[\text{HLR}]$	$\langle \log \text{age}[0] \rangle_L$	$\langle \log \text{age}[\text{HLR}] \rangle_L$	$\langle \log Z[0] \rangle_M$	$\langle \log Z[\text{HLR}] \rangle_M$	HMR	C	
	NED	morph.	M_\odot	M_\odot/pc^2	M_\odot/pc^2	mag	(yr)	(Z_\odot)	(Z_\odot)	pc	pc		
602	NGC 4956	-1 A	11.14	4.33	2.90	0.00	9.85	9.46	0.16	0.15	3026	2556 3.0	
603	NGC 4961	4 B	9.96	3.21	2.11	0.36	9.04	8.50	-0.17	-0.42	2454	1891 2.5	
606	UGC 08231	5 AB	9.38	2.48	1.48	0.03	0.06	8.97	8.36	-1.17	-0.52	3114	2396 2.3
607	UGC 08234	0 A	11.40	4.26	2.93	0.15	0.01	9.50	9.43	0.05	0.01	3939	3398 3.3
608	NGC 5000	3 B	10.99	3.88	2.45	0.90	0.12	9.30	9.38	0.03	-0.12	5940	4242 2.2
609	UGC 08250	4 A	10.28	2.79	2.20	0.74	0.34	8.90	9.08	-0.61	-0.48	5609	5107 2.3
610	UGC 08267	2 AB	11.05	3.62	2.63	1.09	0.59	9.60	9.28	0.01	-0.05	5862	4611 2.4
611	NGC 5016	3 A	10.53	3.63	2.59	0.44	0.18	9.49	8.98	-0.21	-0.26	2680	2019 2.3
612	NGC 5029	-1 A	11.61	4.07	2.77	0.02	0.00	10.04	9.86	0.17	0.01	6866	6033 3.0
614	NGC 5056	4 AB	10.86	3.74	2.22	0.59	0.20	9.79	8.80	-0.18	-0.07	6011	3467 2.5
630	NGC 5205	3 B	10.06	3.65	2.46	0.17	0.16	9.86	9.22	-0.10	-0.14	1814	1447 2.4
633	NGC 5216	0 A	10.61	3.99	2.68	0.12	0.01	10.09	9.63	0.02	0.06	2207	1801 3.0
634	NGC 5218	1 B	10.85	3.98	2.80	1.63	0.37	9.45	9.22	-0.20	-0.03	3330	2285 2.5
652	UGC 08662	4 A	9.10	2.38	1.64	0.31	0.14	8.61	8.55	-0.93	-0.47	2676	2274 2.2
657	UGC 08733	5 B	9.57	2.30	1.62	0.47	0.22	8.58	8.84	-0.08	-0.24	3345	2884 2.1
663	IC 0944	1 A	11.41	4.01	2.82	0.46	0.35	9.87	9.63	0.03	0.03	6635	5305 2.8
664	UGC 08778	2 A	10.35	3.63	2.60	0.55	0.21	9.70	9.39	-0.14	-0.07	2850	2227 2.4
665	UGC 08781	2 B	11.29	4.03	2.49	0.12	0.08	10.02	9.53	0.11	0.01	7114	5011 2.5
676	NGC 5378	2 B	10.72	3.96	2.46	0.03	0.03	10.04	9.62	-0.02	0.07	3334	2769 2.4
684	NGC 5406	2 B	11.28	4.17	2.69	0.25	0.18	9.89	9.30	0.19	0.07	5563	4457 2.3
708	NGC 5485	-1 A	10.86	4.36	3.14	0.03	0.01	10.01	9.79	0.10	0.09	1914	1558 2.8
714	UGC 09067	3 AB	11.02	3.62	2.32	0.71	0.20	9.39	9.13	0.13	-0.35	6851	4124 2.4
715	NGC 5520	3 A	10.15	4.19	2.58	0.82	0.24	9.33	8.89	-0.03	-0.20	1589	839 3.0
740	NGC 5614	1 A	11.40	4.63	3.15	0.48	0.21	9.92	9.55	0.17	0.12	3119	2495 3.1
744	NGC 5631	0 A	10.76	4.58	3.18	0.04	0.05	9.90	9.78	0.16	-0.05	1498	1360 3.2
748	NGC 5633	3 A	10.50	3.74	2.87	0.54	0.44	9.41	8.86	-0.10	-0.23	2214	1837 2.1
749	NGC 5630	5 B	9.86	2.77	2.08	0.41	0.25	8.38	8.50	-0.26	-0.65	3530	3056 2.5
754	NGC 5657	3 B	10.66	4.02	2.60	1.08	0.37	9.44	9.10	-0.14	-0.12	3053	1902 3.1
758	NGC 5682	4 B	9.50	2.47	1.90	0.47	0.15	8.70	8.86	-1.14	-0.70	2354	2147 2.6
764	NGC 5720	3 B	11.24	3.79	2.40	0.29	0.26	10.06	9.40	-0.06	-0.04	7115	5424 2.4
768	NGC 5732	3 A	10.24	3.33	2.07	0.59	0.14	9.14	8.98	-0.13	-0.11	3362	2412 2.3
769	UGC 09476	3 A	10.42	3.24	2.16	0.39	0.09	9.31	8.98	-0.20	-0.40	4273	3748 1.8
774	UGC 09537	2 A	11.38	4.07	2.53	0.85	0.27	9.79	9.49	0.04	-0.18	6566	4555 3.3
775	UGC 09542	4 A	10.58	3.38	2.20	1.03	0.32	9.53	9.26	-0.39	-0.79	5811	4418 2.3
778	NGC 5784	0 A	11.32	4.38	2.94	0.19	0.13	9.78	9.57	0.20	0.04	3589	2659 3.4
779	UGC 09598	3 AB	10.75	3.24	2.38	0.06	0.30	9.74	9.02	-0.05	-0.02	5860	4847 2.2
780	NGC 5797	-1 A	10.92	3.87	2.89	0.00	0.00	9.23	9.56	0.20	0.01	2663	2176 3.1
783	UGC 09665	2 A	10.20	3.70	2.56	0.95	0.64	9.61	9.01	-0.36	-0.35	2437	1619 2.4
789	NGC 5888	2 B	11.55	3.92	2.63	0.28	0.17	10.00	9.48	0.09	0.03	9098	7510 2.1
791	NGC 5908	1 A	11.25	4.28	3.11	0.74	0.37	9.88	9.76	0.14	-0.10	4099	3172 2.7
795	NGC 5930	1 AB	10.75	4.28	2.77	1.36	0.11	9.31	9.58	-0.20	-0.11	2436	1725 2.8
797	UGC 09873	2 A	10.28	3.20	1.89	1.01	0.31	9.24	9.07	-0.44	-0.46	5413	3943 2.4
798	UGC 09892	3 A	10.52	3.41	2.25	0.55	0.36	9.59	9.08	-0.12	-0.34	6166	4541 2.5
804	NGC 5971	2 AB	10.57	3.97	2.45	0.46	0.12	9.96	9.54	-0.40	-0.46	2983	1987 3.0
806	NGC 5966	-1 A	11.15	4.16	2.92	0.14	0.00	10.04	9.74	0.08	0.11	3597	2943 2.8
807	IC 4566	2 B	11.12	3.94	2.56	0.42	0.29	9.88	9.43	-0.05	0.06	5242	3897 2.2
809	NGC 5987	1 A	11.13	4.54	3.20	0.52	0.49	9.84	9.78	0.10	-0.00	2737	2392 3.0

Table C.2. continued.

CALIFA ID#	Name	Type	$\log M_\star$	$\log \mu_\star[0]$	$\log \mu_\star[\mathrm{HLR}]$	$A_V[0]$	$A_V[\mathrm{HLR}]$	$\langle \log \mathrm{age}[0] \rangle_L$	$\langle \log \mathrm{age}[\mathrm{HLR}] \rangle_L$	$\langle \log \mathrm{age}[0] \rangle_M$	$\langle \log \mathrm{Z}[\mathrm{HLR}] \rangle_M$	HMR	C
	NED	morph.	M_\odot	M_\odot/pc^2	M_\odot/pc^2	mag	mag	(yr)	(Z_\odot)	(Z_\odot)	(Z_\odot)	pc	pc
810	NGC 5980	3 A	10.98	3.87	2.81	0.74	0.49	9.66	9.07	-0.05	-0.13	4507	3.3
813	NGC 6004	3 B	10.88	3.82	2.42	0.65	0.25	9.41	9.12	0.11	-0.07	4808	4213 2.0
814	UGC 10097	-1 A	11.49	4.63	3.03	0.18	0.00	10.10	9.75	0.12	0.18	3473	2410 3.3
815	NGC 6020	-1 A	11.08	3.92	2.97	0.00	0.01	9.59	9.82	0.22	0.01	2765	2312 3.0
816	NGC 6021	-1 A	11.08	4.56	2.90	0.73	0.01	10.04	9.81	-0.08	-0.01	2679	1683 3.3
818	UGC 10123	1 A	10.65	3.86	2.75	1.13	0.61	9.55	9.38	-0.02	-0.24	3266	2206 2.5
820	NGC 6032	3 B	10.63	3.72	2.27	0.80	0.16	9.55	9.45	-0.19	-0.38	5871	4509 2.0
821	NGC 6060	2 A	11.15	4.09	2.73	0.71	0.50	9.74	9.21	0.07	-0.22	5662	4337 2.2
822	UGC 10205	0 A	11.24	4.08	2.56	1.50	0.25	9.59	9.51	-0.11	-0.22	5579	3500 2.5
823	NGC 6063	3 A	10.29	3.16	2.26	0.25	0.21	9.64	9.16	-0.14	-0.32	3636	2902 1.9
824	IC 1199	2 AB	10.93	3.84	2.74	0.76	0.34	9.67	9.16	0.01	-0.01	4917	3834 2.1
826	NGC 6081	0 A	11.22	4.47	2.94	0.93	0.16	9.98	9.80	0.04	0.01	3500	2342 3.4
827	UGC 10297	4 A	9.58	2.96	2.23	0.53	0.19	9.32	9.01	-0.68	-0.41	2654	2328 2.4
828	UGC 10331	4 AB	10.23	3.02	2.13	0.60	0.22	9.23	9.26	-0.67	-1.23	4180	3470 2.4
829	NGC 6125	-1 A	11.41	4.43	3.06	0.00	0.00	10.03	9.85	0.18	0.10	3259	2775 3.2
831	NGC 6132	3 A	10.46	3.47	2.16	0.50	0.51	9.55	8.61	-0.02	-0.00	4043	2356 2.5
832	NGC 6146	-1 A	11.73	4.37	2.96	0.21	0.00	9.99	9.80	0.08	0.01	5577	4509 3.4
833	NGC 6154	1 B	11.19	4.02	2.42	0.40	0.06	10.01	9.67	0.06	0.03	6057	4066 2.3
834	UGC 10380	2 AB	11.13	3.65	2.61	0.72	0.37	9.86	9.45	-0.10	0.00	6828	5439 2.8
835	NGC 6150	-1 A	11.48	3.95	2.87	0.00	0.00	10.08	9.80	0.06	0.14	5798	5082 2.9
836	NGC 6155	4 A	10.32	3.52	2.46	0.73	0.47	9.12	8.88	-0.07	-0.18	2491	2158 2.2
837	UGC 10384	2 A	10.63	4.01	2.68	1.60	0.90	9.40	8.82	-0.21	-0.58	4188	2380 2.6
838	UGC 10388	1 AB	10.71	4.00	2.62	0.27	0.07	10.03	9.64	0.03	-0.09	3068	2280 3.1
840	NGC 6173	-1 A	11.86	4.31	2.97	0.22	0.00	10.01	9.94	0.11	0.01	6768	6044 3.1
841	NGC 6168	4 AB	9.88	3.10	2.18	0.84	0.44	9.06	8.88	-0.80	-0.57	3244	2549 2.0
842	NGC 6186	2 B	10.75	4.10	2.72	0.86	0.29	9.35	9.40	-0.01	-0.03	3024	2252 2.4
843	UGC 10650	4 A	9.47	2.71	1.57	0.44	0.28	8.46	8.58	-1.22	-0.69	3578	2917 2.5
844	NGC 6278	0 AB	10.89	4.61	3.07	0.07	0.00	10.01	9.74	0.14	0.18	1491	1341 3.4
845	UGC 10693	-1 AB	11.57	4.15	2.75	0.02	0.00	9.85	9.69	0.19	0.07	6271	5659 3.3
846	UGC 10695	-1 A	11.36	3.96	2.54	0.30	0.01	10.07	9.70	0.07	0.05	6736	4807 2.8
848	NGC 6310	2 A	10.70	3.91	2.78	0.46	0.29	9.93	9.45	-0.00	0.00	3861	3313 2.3
849	NGC 6301	3 A	11.35	3.24	2.39	0.33	0.27	9.61	9.15	0.14	-0.06	10836	9716 2.0
850	NGC 6314	1 A	11.21	4.09	2.70	0.42	0.37	9.56	9.40	0.09	0.02	4807	3807 3.3
851	NGC 6338	-1 A	11.72	4.28	2.87	0.36	0.01	10.01	9.84	0.11	0.16	6892	6039 2.8
852	UGC 10796	4 AB	9.55	2.57	1.62	0.36	0.31	8.17	8.65	-0.18	-0.46	3325	3673 2.4
854	UGC 10811	2 B	11.11	3.71	2.45	0.27	0.30	9.94	9.41	-0.10	-0.15	7769	6024 2.7
856	IC 1256	2 AB	10.71	3.50	2.41	0.72	0.21	9.33	9.19	0.16	-0.09	4884	3805 2.2
857	NGC 6394	3 B	11.14	3.47	2.67	0.45	0.34	9.84	9.35	-0.12	-0.11	6792	5471 2.1
858	UGC 10905	0 A	11.55	4.19	2.92	0.26	0.28	9.78	9.80	0.08	-0.04	5489	4385 3.5
859	NGC 6411	-1 A	11.07	3.99	2.91	0.00	0.00	9.56	9.59	0.22	0.14	3196	2925 3.0
860	NGC 6427	0 AB	10.84	4.59	3.16	0.23	0.00	9.92	9.85	0.19	0.03	1682	1386 3.3
861	UGC 10972	3 A	10.64	3.52	2.35	0.35	0.12	9.91	9.21	-0.15	-0.20	4887	3704 2.3
862	NGC 6478	4 A	11.25	3.86	2.58	0.66	0.35	9.60	9.05	0.10	-0.21	7164	5127 2.0
863	NGC 6497	1 B	11.13	3.77	2.60	0.00	0.16	9.73	9.41	0.12	0.04	5308	4345 2.7
864	NGC 6515	-1 A	11.34	4.27	2.64	0.14	0.00	9.91	9.65	0.10	0.01	4903	4519 3.1
865	UGC 11228	0 B	11.17	4.35	2.72	0.17	0.00	10.00	9.73	0.17	0.12	3770	2876 3.4
866	UGC 11262	4 A	10.39	3.07	1.66	0.47	0.26	9.56	8.79	-0.48	-0.76	6216	6729 2.2

Table C.2. continued.

R. M. González Delgado et al.: The CALIFA survey across the Hubble sequence

CALIFA ID#	Name	Type	$\log M_*$	$\log \mu_{\star}[0]$	$\log \mu_{\star}[\mathrm{HLR}]$	$A_V[\mathrm{HLR}]$	$\langle \log \mathrm{age}[0] \rangle_L$	$\langle \log \mathrm{age}[\mathrm{HLR}] \rangle_L$	$\langle \log Z[0] \rangle_M$	$\langle \log Z[\mathrm{HLR}] \rangle_M$	HMR	C
	NED	morph.	M_\odot	M_\odot/pc^2	M_\odot/pc^2	mag	(yr)	(Z_\odot)	(Z_\odot)	pc	pc	
867	NGC 6762	1 A	10.38	3.78	3.00	0.00	0.16	9.68	9.65	0.07	-0.03	1359 2.9
868	MCG-02-51-004	2 A	10.92	3.85	2.48	0.46	0.30	9.93	9.07	-0.10	-0.28	5738 3.2
869	NGC 6941	2 B	11.22	3.84	2.52	0.21	0.24	9.79	9.41	0.12	0.08	6592 2.1
870	NGC 6945	0 B	10.92	4.49	2.94	0.52	0.00	9.79	9.60	0.14	0.09	2442 1949 3.0
871	NGC 6978	2 AB	11.15	3.98	2.69	0.72	0.20	9.74	9.39	-0.12	-0.01	5325 4111 2.4
872	UGC 11649	1 B	10.67	3.85	2.44	0.18	0.11	9.93	9.39	-0.07	0.04	3470 2449 2.1
873	UGC 11680NED 01	2 B	11.32	3.93	2.70	0.59	0.23	9.90	9.41	-0.15	0.03	5518 4081 2.5
874	NGC 7025	0 A	11.38	4.62	3.14	0.35	0.06	10.01	9.85	0.16	0.08	3166 2621 3.3
875	UGC 11694	0 A	11.20	4.53	2.77	0.84	0.14	10.02	9.65	0.04	0.04	3689 2043 2.9
876	NGC 7047	3 B	10.94	3.48	2.51	0.15	0.13	9.88	9.31	-0.02	-0.07	6172 5106 2.0
877	UGC 11717	1 A	11.06	3.98	2.16	0.63	0.12	9.91	9.41	0.08	0.03	6527 3102 2.9
878	MCG-01-54-016	4 A	9.25	2.07	1.69	0.06	0.21	8.94	8.83	-1.18	-0.93	2811 2758 2.3
879	UGC 11740	3 A	10.60	3.03	2.30	0.33	0.41	9.74	8.80	-0.21	-0.01	5392 4369 2.4
880	UGC 11792	3 A	10.56	3.63	2.66	1.20	0.48	9.44	9.31	-0.12	-0.30	4178 3216 2.4
881	NGC 7194	-1 A	11.53	4.47	2.93	0.11	0.01	10.04	9.75	0.07	0.16	4377 3412 3.3
883	UGC 11958	0 A	11.44	3.92	2.49	0.22	0.03	10.08	9.84	0.15	0.08	7371 6319 2.8
884	UGC 11982	4 A	10.01	2.84	2.08	0.51	0.46	9.30	8.88	-0.60	-0.17	4393 3605 2.3
885	UGC 12054	4 A	9.18	3.12	2.07	0.50	0.38	9.31	8.83	-0.70	-0.54	1277 1006 2.7
886	NGC 7311	1 A	11.31	4.61	3.19	0.36	0.27	9.89	9.51	0.11	0.07	3243 2430 3.1
887	NGC 7321	3 B	11.28	3.89	2.59	0.36	0.27	9.78	9.23	0.12	-0.06	6168 4331 2.4
888	UGC 12127	-1 A	11.62	4.18	2.79	0.01	0.00	10.08	9.77	0.06	0.07	5888 5296 3.1
889	NGC 7364	1 A	10.98	4.11	2.84	0.16	0.28	9.56	9.12	0.14	0.03	3126 2132 3.1
890	UGC 12185	2 B	10.91	3.92	2.60	0.23	0.13	9.84	9.45	-0.06	-0.20	4498 3199 2.8
891	UGC 12224	4 A	10.20	3.08	1.89	0.34	0.01	9.52	9.04	-0.37	-0.16	4171 3338 1.8
892	VV 488NED 02	2 AB	10.61	3.79	2.63	0.93	0.45	9.67	9.15	-0.36	-0.13	3545 2525 3.1
893	NGC 7436B	-1 A	11.68	4.34	2.86	0.11	0.05	9.98	9.80	0.14	0.05	5955 5822 2.9
894	UGC 12274	1 A	11.19	3.93	2.59	0.25	0.03	10.09	9.73	-0.03	0.09	6073 4522 2.7
895	UGC 12308	4 A	9.12	2.83	1.66	0.26	0.03	9.23	8.54	-0.92	-0.71	1982 1439 2.5
896	NGC 7466	3 A	11.05	3.97	2.41	1.00	0.44	9.37	9.16	0.04	-0.39	6059 4081 2.7
898	NGC 7489	3 A	10.85	3.53	2.09	0.86	0.22	9.11	8.68	-0.06	-0.22	6686 5822 2.3
900	NGC 7550	-1 A	11.36	4.36	2.93	0.32	0.00	9.84	9.58	0.08	0.19	3694 2866 2.9
901	NGC 7549	3 B	10.78	3.81	2.36	0.84	0.45	9.34	8.77	-0.05	-0.10	4078 2965 2.1
902	NGC 7563	1 B	11.09	4.47	3.09	0.38	0.02	9.98	9.90	0.14	0.17	2308 1969 3.5
903	NGC 7562	-1 A	11.30	4.65	3.31	0.20	0.00	10.06	9.79	0.09	0.19	2616 2439 3.1
904	NGC 7591	3 B	11.03	4.04	2.76	1.43	0.70	9.39	9.10	-0.61	-0.75	3745 2632 3.0
906	IC 5309	4 AB	10.46	3.61	2.20	0.84	0.43	9.28	9.06	-0.15	-0.21	3694 2196 2.4
907	NGC 7608	3 A	10.24	3.25	2.41	0.60	0.54	9.47	9.03	-0.42	-0.20	3441 2889 2.3
909	UGC 12519	4 AB	10.40	3.43	2.28	0.76	0.38	9.35	8.79	-0.07	-0.19	4521 3147 2.3
910	UGC 12518	2 A	10.23	3.78	2.73	0.85	0.43	9.93	9.64	-0.09	0.02	2074 1660 2.8
911	NGC 7619	-1 A	11.43	4.69	3.37	0.05	0.00	9.98	9.81	0.18	0.19	2564 2192 3.3
912	NGC 7623	0 A	10.84	4.24	2.90	0.17	0.01	9.96	9.76	-0.00	0.05	2126 1659 3.4
914	NGC 7631	2 A	10.71	3.88	2.73	0.39	0.24	9.84	9.33	-0.11	-0.01	3602 2780 2.6
915	NGC 7653	2 A	10.75	3.97	2.41	0.37	0.26	9.67	9.00	-0.08	-0.22	3365 2035 2.7
916	NGC 7671	0 A	11.10	4.73	3.17	0.28	0.04	10.08	9.84	0.17	0.08	2140 1562 3.2
917	NGC 7683	0 A	11.15	4.58	3.23	0.76	0.09	9.67	10.00	0.18	0.07	2273 1875 3.2
919	NGC 7684	0 A	11.02	4.39	2.93	0.38	0.08	9.91	9.74	0.22	-0.02	3290 2442 3.1
920	NGC 7691	3 B	10.37	3.00	1.98	0.28	0.04	9.37	8.96	-0.31	-0.51	4901 4184 2.0

Table C.2. continued.

CALIFA ID#	Name	Type	$\log M_\star$	$\log \mu_\star[0]$	$\log \mu_\star[\text{HLR}]$	$A_V[0]$	$A_V[\text{HLR}]$	$\langle \log \text{age}[0] \rangle_L$	$\langle \log \text{age}[\text{HLR}] \rangle_L$	$\langle \log \text{age}[0] \rangle_M$	$\langle \log \text{Z}[\text{HLR}] \rangle_M$	HLR	HMR	C
	NED	morph.	M_\odot	M_\odot/pc^2	M_\odot/pc^2	mag	mag	(yr)	(Z_\odot)	(Z_\odot)	(Z_\odot)	pc	pc	pc
921	UGC 12653	4 A	9.89	2.81	1.71	0.00	0.15	9.53	8.57	-0.25	-0.16	4547	3468	2.3
923	NGC 7711	-1 A	10.98	4.49	3.03	0.01	9.98	9.63	0.16	0.08	2554	1698	3.3	
924	NGC 7716	2 A	10.52	4.25	2.72	0.02	0.07	9.90	9.54	0.15	-0.20	1943	1238	2.7
925	NGC 7722	1 A	11.19	4.32	3.05	0.66	0.53	9.78	9.63	0.12	0.12	3097	2555	2.6
926	UGC 12723	4 A	10.07	2.67	2.27	0.71	0.24	9.07	9.36	-1.07	-1.37	5140	4808	2.1
927	NGC 7738	2 B	11.34	4.38	2.49	1.99	0.08	8.98	9.53	-0.10	0.10	6037	2750	3.0
928	UGC 12767	2 B	11.04	3.82	2.41	0.03	0.10	9.98	9.20	0.02	0.19	5670	4376	2.4
929	UGC 12810	3 B	11.00	3.72	2.15	1.25	0.16	9.32	9.08	-0.29	-0.79	8345	5480	2.0
930	UGC 12816	4 A	10.12	3.02	1.69	0.26	0.26	9.29	8.68	-0.50	-1.00	4353	2984	2.4
931	NGC 7782	2 A	11.42	4.17	2.81	0.43	0.13	10.09	9.65	0.09	0.06	6197	4866	2.2
932	NGC 7783NED 01	1 A	11.47	3.87	3.05	0.00	0.01	9.56	9.86	0.22	0.09	5173	4350	3.0
933	NGC 7787	1 AB	10.85	3.83	2.29	1.58	0.27	9.44	9.31	-0.24	-0.01	4869	2635	2.6
934	UGC 12857	3 A	9.78	3.14	2.33	0.61	0.39	9.17	8.99	0.07	-0.29	2041	1602	2.5
935	UGC 12864	4 B	10.22	3.21	1.86	0.44	0.18	8.94	8.82	-0.37	-0.50	5227	3944	2.4
936	MCG-01-01-012	1 AB	10.88	3.67	2.67	0.80	0.20	9.95	9.65	-0.08	0.02	4977	4080	2.6
937	NGC 7800	5 AB	9.31	2.64	1.99	0.34	0.38	8.12	8.61	-0.34	-0.69	1598	1632	2.4
938	NGC 5947	3 B	10.81	3.77	2.10	0.45	0.14	9.46	8.96	0.18	-0.03	5225	3149	2.4
939	NGC 4676B	1 B	11.11	3.98	2.80	0.40	0.19	9.94	9.56	0.01	0.03	3912	2902	2.4

Referências Bibliográficas

- Abazajian, K. N., Adelman-McCarthy, J. K., Agüeros, M. A., Allam, S. S., Allende Prieto, C., An, D., Anderson, K. S. J., Anderson, S. F. et al. 2009, ApJS, 182, 543
- Asari, N. V., Cid Fernandes, R., Stasińska, G., Torres-Papaqui, J. P., Mateus, A., Sodré, L., Schoenell, W., & Gomes, J. M. 2007, MNRAS, 381, 263
- Ascasibar, Y., Gavilán, M., Pinto, N., Casado, J., Rosales-Ortega, F., & Díaz, A. I. 2015, MNRAS, 448, 2126
- Baldwin, J. A., Phillips, M. M., & Terlevich, R. 1981, PASP, 93, 5
- Barnard, E. E. 1908, Astronomische Nachrichten, 177, 231
- Bolatto, A. D., Wolfire, M., & Leroy, A. K. 2013, ARA&A, 51, 207
- Brinchmann, J., Charlot, S., Kauffmann, G., Heckman, T., White, S. D. M., & Tremonti, C. 2013, MNRAS, 432, 2112
- Bruzual, G. & Charlot, S. 2003, MNRAS, 344, 1000
- Calzetti, D., Kinney, A. L., & Storchi-Bergmann, T. 1994, ApJ, 429, 582
- Calzetti, D., Liu, G., & Koda, J. 2012, ApJ, 752, 98
- Cardelli, J. A., Clayton, G. C., & Mathis, J. S. 1989, ApJ, 345, 245
- Casasola, V., Hunt, L., Combes, F., & García-Burillo, S. 2015, A&A, 577, A135
- Chabrier, G. 2003, PASP, 115, 763
- Charlot, S. & Fall, S. M. 2000, ApJ, 539, 718
- Cid Fernandes, R., Asari, N. V., Sodré, L., Stasińska, G., Mateus, A., Torres-Papaqui, J. P., & Schoenell, W. 2007, MNRAS, 375, L16

- Cid Fernandes, R., Mateus, A., Sodré, L., Stasińska, G., & Gomes, J. M. 2005, MNRAS, 358, 363
- Cid Fernandes, R., Pérez, E., García Benito, R., González Delgado, R. M., de Amorim, A. L., Sánchez, S. F., Husemann, B., Falcón Barroso, J. et al. 2013, A&A, 557, A86
- Cid Fernandes, R., Stasińska, G., Mateus, A., & Vale Asari, N. 2011, MNRAS, 413, 1687
- Cid Fernandes, R., Stasińska, G., Schlickmann, M. S., Mateus, A., Vale Asari, N., Schoenell, W., & Sodré, L. 2010, MNRAS, 403, 1036
- Draine, B. T. 2003, ARA&A, 41, 241
- Gallazzi, A., Charlot, S., Brinchmann, J., White, S. D. M., & Tremonti, C. A. 2005, MNRAS, 362, 41
- García-Benito, R., Zibetti, S., Sánchez, S. F., Husemann, B., de Amorim, A. L., Castillo-Morales, A., Cid Fernandes, R., Ellis, S. C. et al. 2015, A&A, 576, A135
- Garnett, D. R. 2002, ApJ, 581, 1019
- González Delgado, R. M., Cid Fernandes, R., García-Benito, R., Pérez, E., de Amorim, A. L., Cortijo-Ferrero, C., Lacerda, E. A. D., López Fernández, R. et al. 2014a, ApJ, 791, L16
- González Delgado, R. M., García-Benito, R., Pérez, E., Cid Fernandes, R., de Amorim, A. L., Cortijo-Ferrero, C., Lacerda, E. A. D., López Fernández, R. et al. 2015, A&A, 581, A103
- González Delgado, R. M., Pérez, E., Cid Fernandes, R., García-Benito, R., de Amorim, A. L., Sánchez, S. F., Husemann, B., Cortijo-Ferrero, C. et al. 2014b, A&A, 562, A47
- Guiderdoni, B. & Rocca-Volmerange, B. 1987, A&A, 186, 1
- Hubble, E. P. 1925, The Observatory, 48, 139
- Husemann, B., Jahnke, K., Sánchez, S. F., Barrado, D., Bekerait*error*é, S., Bomans, D. J., Castillo-Morales, A., Catalán-Torrecilla, C. et al. 2013, A&A, 549, A87
- Kennicutt, R. C., Calzetti, D., Aniano, G., Appleton, P., Armus, L., Beirão, P., Bolatto, A. D., Brandl, B. et al. 2011, PASP, 123, 1347
- Kennicutt, Jr., R. C. 1998, ARA&A, 36, 189
- Kennicutt, Jr., R. C., Calzetti, D., Walter, F., Helou, G., Hollenbach, D. J., Armus, L., Bendo, G., Dale, D. A. et al. 2007, ApJ, 671, 333

- Kewley, L. J., Dopita, M. A., Sutherland, R. S., Heisler, C. A., & Trevena, J. 2001, *ApJ*, 556, 121
- Kreckel, K., Groves, B., Schinnerer, E., Johnson, B. D., Aniano, G., Calzetti, D., Croxall, K. V., Draine, B. T. et al. 2013, *ApJ*, 771, 62
- Lada, C. J., Lombardi, M., Roman-Zuniga, C., Forbrich, J., & Alves, J. F. 2013, *ApJ*, 778, 133
- Leroy, A. K., Bigiel, F., de Blok, W. J. G., Boissier, S., Bolatto, A., Brinks, E., Madore, B., Muñoz-Mateos, J.-C. et al. 2012, *AJ*, 144, 3
- Leroy, A. K., Bolatto, A., Gordon, K., Sandstrom, K., Gratier, P., Rosolowsky, E., Engelbracht, C. W., Mizuno, N. et al. 2011, *ApJ*, 737, 12
- Leroy, A. K., Walter, F., Sandstrom, K., Schruba, A., Muñoz-Mateos, J.-C., Bigiel, F., Bolatto, A., Brinks, E. et al. 2013, *AJ*, 146, 19
- Lilly, S. J., Carollo, C. M., Pipino, A., Renzini, A., & Peng, Y. 2013, *ApJ*, 772, 119
- Magdis, G. E., Daddi, E., Elbaz, D., Sargent, M., Dickinson, M., Dannerbauer, H., Aussel, H., Walter, F. et al. 2011, *ApJ*, 740, L15
- Marino, R. A., Rosales-Ortega, F. F., Sánchez, S. F., Gil de Paz, A., Vílchez, J., Miralles-Caballero, D., Kehrig, C., Pérez-Montero, E. et al. 2013, *A&A*, 559, A114
- Mateus, A., Sodré, L., Cid Fernandes, R., Stasińska, G., Schoenell, W., & Gomes, J. M. 2006, *MNRAS*, 370, 721
- Osterbrock, D. E. & Ferland, G. J. 2006, *Astrophysics of gaseous nebulae and active galactic nuclei*
- Pagel, B. E. J., Edmunds, M. G., Blackwell, D. E., Chun, M. S., & Smith, G. 1979, *MNRAS*, 189, 95
- Peng, Y. & Maiolino, R. 2014, *MNRAS*, 443, 3643
- Peng, Y., Maiolino, R., & Cochrane, R. 2015, *Nature*, 521, 192
- Pérez, E., Cid Fernandes, R., González Delgado, R. M., García-Benito, R., Sánchez, S. F., Husemann, B., Mast, D., Rodón, J. R. et al. 2013, *ApJ*, 764, L1
- Rémy-Ruyer, A., Madden, S. C., Galliano, F., Galametz, M., Takeuchi, T. T., Asano, R. S., Zhukovska, S., Lebouteiller, V. et al. 2014, *A&A*, 563, A31

- Salpeter, E. E. 1955, ApJ, 121, 161
- Sánchez, S. F., Kennicutt, R. C., Gil de Paz, A., van de Ven, G., Vílchez, J. M., Wisotzki, L., Walcher, C. J., Mast, D. et al. 2012, A&A, 538, A8
- Sánchez, S. F., Rosales-Ortega, F. F., Jungwiert, B., Iglesias-Páramo, J., Vílchez, J. M., Marino, R. A., Walcher, C. J., Husemann, B. et al. 2013, A&A, 554, A58
- Santini, P., Maiolino, R., Magnelli, B., Lutz, D., Lamastra, A., Li Causi, G., Eales, S., Andreani, P. et al. 2014, A&A, 562, A30
- Schmidt, M. 1959, ApJ, 129, 243
- Searle, L. & Sargent, W. L. W. 1972, ApJ, 173, 25
- Stasińska, G., Cid Fernandes, R., Mateus, A., Sodré, L., & Asari, N. V. 2006, MNRAS, 371, 972
- Stasińska, G., Vale Asari, N., Cid Fernandes, R., Gomes, J. M., Schlickmann, M., Mateus, A., Schoenell, W., Sodré, Jr., L. et al. 2008, MNRAS, 391, L29
- Tacconi, L. J., Neri, R., Genzel, R., Combes, F., Bolatto, A., Cooper, M. C., Wuyts, S., Bournaud, F. et al. 2013, ApJ, 768, 74
- Tremonti, C. A., Heckman, T. M., Kauffmann, G., Brinchmann, J., Charlot, S., White, S. D. M., Seibert, M., Peng, E. W. et al. 2004, ApJ, 613, 898
- Zahid, H. J., Dima, G. I., Kudritzki, R.-P., Kewley, L. J., Geller, M. J., Hwang, H. S., Silverman, J. D., & Kashino, D. 2014, ApJ, 791, 130